

Low Cost High Gain Millimeter Wave Planar Antennas

Yazan Al-Alem

A Thesis in
The Department of
Electrical and Computer Engineering

Presented in Partial Fulfillment of the Requirements
For the Degree of Doctor of Philosophy
(Electrical and Computer Engineering)
Concordia University
Montréal, Québec, Canada

June 2019

© Yazan Al-Alem, 2019

CONCORDIA UNIVERSITY
School of Graduate Studies

This is to certify that the thesis prepared

By: **Yazan Al-Alem**

Entitled: **Low Cost High Gain Millimeter Wave Planar Antennas**

and submitted in partial fulfillment of the requirements for the degree of

Doctor of Philosophy (Electrical and Computer Engineering)

complies with the regulations of this University and meets the accepted standards with respect to originality and quality.

Signed by the final examining committee:

Dr. Alex De Visscher Chair

Dr. Aly E. Fathy External Examiner

Dr. Ali Nazemi Examiner

Dr. Robert Paknys Examiner

Dr. Abdel R. Sebak Examiner

Dr. Ahmed A. Kishk Thesis Supervisor

Approved by _____
Dr. Rastko R. Selmic, Graduate Program Director

August 26, 2019

Dr. Amir Asif, Dean
Gina Cody School of Engineering & Computer Science

Abstract

Low Cost High Gain Millimeter Wave Planar Antennas

**Yazan Al-Alem, Ph.D.
Concordia University, 2019**

The advent of the fifth generation of wireless communication systems mandates the use of high gain antennas for transceiver front ends. The use of high gain antennas is very vital in order to compensate for the high path loss of the propagating signals at millimeter wave frequencies. There are many methods to implement high gain antennas; many of those solutions are expensive and complicated in terms of its fabrication process. Here, we emphasize 60 GHz high-gain antennas based on the low cost planar printed circuit board technology. The proposed solutions are low cost with high performance metrics. The proposed antennas suit short range, low power applications, such as wireless personal area networks (WPAN). Nonetheless, the study provided for the proposed structures reveals new physical insights, and new methods for the design procedure, where the design procedure becomes very straightforward.

The first proposed structure utilizes the radiation losses in microstrip line discontinuities to implement an efficient high gain radiator at 60 GHz. The second proposed structure utilizes the diffracted fields from the edges of metal sheets as secondary radiating sources to boost the gain of the element. Also, an increased distance between the antenna elements can be achieved without generating grating lobes; this can be comprehended by visualizing each element as a subarray of radiating sources. Such a concept has a significant implication on the relaxation of the design of feeding networks. The single antenna element realized gain goes up to 11.5 dBi, the 10 dB return loss bandwidth covers the 60 GHz ISM band, and the radiation efficiency goes above 90%.

A Magneto-Electric (ME) dipole is usually designed by superimposing electric and magnetic current elements orthogonally on each other. A new design procedure is proposed, which can transform the radiation characteristics of an electric or magnetic current element to a Magneto-Electric dipole characteristics. The proposed procedure doesn't require the orthogonal combination

of the magnetic and electric current elements. Hence, the procedure possesses a significant advantage, where it avoids the need for a quarter free-space wavelength spacing between the current element and the metallic ground plane. In addition, the proposed design increases the antenna gain dramatically, where the proposed structure has a boresight gain of 11.5 dBi, and a relative bandwidth of 13% centered at 60 GHz. The antenna element has been employed in a planar antenna array to achieve a gain of 22 dBi.

A novel technique is proposed to enhance the gain of a Dielectric Resonator Antenna (DRA) over a wideband range of frequencies. The proposed antenna structure has a relative bandwidth of 27.5% in the 60 GHz band, and a peak realized gain of 12.5 dBi. The peak of the total antenna radiation efficiency is 96%. The proposed antenna is suitable for high data rate short range personal area networks applications. Printed Electromagnetic Band Gap (EBG) technology is used to feed the antenna to eliminate any parasitic radiation from the feed line. The characterization of 60 GHz antennas is very challenging. The end launch connector used to feed the antenna at such frequency is relatively large compared to the antenna dimensions, and that consequently affects the accuracy of the characterization of the antenna, especially if it is in the vicinity of the antenna. EBG surfaces have been used to resolve such characterization impairments.

In a 5G network, the data is communicated at mm-wave frequencies between various communicating entities. The communicated high frequency signal is processed internally within the communicating entity itself. Thus, the data is communicated through electrical interconnects between several chips or between several sub-circuits within the chip. In such a way, those electrical interconnects between various sub-circuits within an Integrated Circuit (IC), or between several adjacent ICs, play a vital role in defining the performance limits of any system. As the frequency of operation gradually increases, the design of interconnects, whether within the IC environment (intra-chip) or between several adjacent ICs (inter-chip), turn into a more challenging task. As the frequencies of operation increase, the proper interconnect guiding structure dimensions become infeasible to realize, or it might exhibit a high level of losses, and large intrinsic RC time delay. Moreover, by the increase of the number of interconnects, the mutual coupling between the interconnect structures become more severe, not to mention the complexity, and associated cost of such design. The wireless interconnects concept (wireless intra-chip/inter-chip communication) emerged as a suggested remedy to the high frequency interconnect problem.

We provide a study of several aspects of wireless inter-chip communication between adjacent ICs at mm-wave frequencies. The symmetrical layers concept is introduced as a general approach to eliminate the destructive interference and redirect the wasted radiated energy to free space towards the receiving antenna. In addition, the use of hard/soft surfaces and EBG structures to focus the radiated energy towards the receiving antenna is studied thoroughly. The use of such concepts has tremendous advantages, in focusing the energy towards the receiving antenna and eliminating the spherical spreading losses introduced by the radiated spherical wave nature. The incorporation of the symmetrical layers with hard/soft surfaces led to novel compact, low-cost wireless inter-chip structures with enhanced link budget performance.

Acknowledgments

First of all, I would like to thank Allah, the most gracious most merciful for His unlimited gifts. I would like to thank my lovely parents and family for their endless help, support, and patience.

I would like to sincerely thank my brilliant mentor and amazing advisor Prof. Ahmed Kishk, a pioneer in the field of Antennas. I am very grateful and thankful for the opportunity he has given me to work in his research group. I am thankful for the vital comments, dedication, and help he provided me in writing this thesis. I am thankful for him being supportive at all stages of my studies at Concordia University both at the academic and personal level. The intensive, practical, and well-designed courses I took with him provided me with a solid foundation in Microwaves and Antennas.

I would like to immensely thank Prof. Raed Shubair, for his unparalleled support both at the personal and academic levels. He is a fantastic friend who is always there for you, in your ups and downs, a friend in need is a friend indeed. I have learned a lot from him, and I owe him a lot of respect.

I would like to thank Prof. Robert Paknys with whom I took Antennas and Advanced Electromagnetic courses. His courses and teaching style are remarkable, and it was essential for me to build my foundation in the area and inspire me with many different ideas.

I would like to thank Prof. Aly E. Fathy, Prof. Abdel Razik Sebak, and Dr. Ali Nazemi for their valuable comments and serving in my examining committee. I would also like to thank Concordia University technical staff, Mr. Jeffery Landry, and Mr. Vincent Mooney-Chopin for their technical advice and help in realizing antenna prototypes.

Dedication

“To my beloved father”

Contents

List of Figures.....	x
List of Tables	xvi
List of Acronyms.....	xvii
1. Introduction	1
1.1 Overview.....	1
1.2 Problem Statement	2
1.3 Motivation.....	5
1.4 Literature Review.....	6
1.5 Proposed Methodology	8
2. Efficient Millimeter-Wave Antenna Based on the Exploitation of Microstrip Line Discontinuity Radiation	10
2.1 Utilizing Microstrip Open Ended Line Radiation	10
2.1.1 Introduction.....	10
2.1.2 Simulation and Experimental Results for the Proposed Structure.....	21
2.1.3 Bandwidth enhancement.....	22
2.1.4 Linear antenna array	27
2.2 Highly Efficient Unpackaged 60 GHz Planar Antenna Array	32
2.2.1 Introduction.....	32
2.2.2 Array Feeding Network Study	33
2.2.3 Proposed Antenna Array	43
2.3 Low-Cost High Gain 60 GHz Superstrate Antenna Array.....	48
2.3.1 Introduction.....	48
2.3.2 Proposed antenna structure	49
3. Dipole Antenna In-Between Two Metallic Sheets “Inspired By the Diffracted Fields” ..	55
3.1 Introduction	55
3.2 Full wave analysis	61
3.3 Linear antenna array.....	63
3.4 Realization at millimeter-wave frequencies.....	64
3.5 Two-element array	67
3.6 Experimental prototyping results	70

4. Magnetic Source Antenna.....	77
4.1 Gain Boost of a Slot Antenna.....	77
4.1.1 Introduction.....	77
4.1.2 Theoretical Qualitative Analysis of the Proposed Structure.....	78
4.1.3 Antenna Feeding Considerations at Millimeter Wave Frequencies	81
4.1.4 Realization at Millimeter Wave Frequencies (60 GHz)	81
4.1.5 Practical Characterization and Prototyping Considerations	85
4.1.6 Array Design.....	88
4.1.7 Experimental Prototyping results.....	97
4.2 Wideband Millimeter-Wave DRA with Gain Enhancement.....	101
4.2.1 Introduction.....	101
4.2.2 Proposed Dielectric Resonator Antenna Structure Qualitative Analysis.....	101
4.2.3 Proposed Dielectric Resonator Antenna Structure	102
5. Enhanced Wireless Inter-Chip Communication Performance Using Symmetric Layers and Soft/Hard Surface Concepts.....	115
5.1 Wireless Inter-Chip Communication	115
5.1.1 Introduction.....	115
5.1.2 Symmetrical Layers Concept.....	116
5.1.3 Different Design Concepts on Wireless Inter-Chip Structures	123
5.1.4 Wireless Inter-Chip Link Budget (Link Losses).....	135
5.1.5 Experimental Prototyping Results	140
5.2 One-To-Two Wireless Inter-Chip Communication Link.....	144
5.2.1 Introduction.....	144
5.2.2 90-Degree Bend Path	144
5.2.3 1:2 Wireless Inter-Chip Link structures.....	147
6. Conclusion and Future Work.....	152
Appendix A.....	155
Appendix B	157
Bibliography	160

List of Figures

Figure 1.1:	Low gain access point antenna coverage.....	3
Figure 1.2:	High gain access point antenna coverage.....	4
Figure 1.3:	Wireless inter-chip communication.....	5
Figure 2.1.1:	Electric current dipole backed by a thin substrate, (A) Isometric view, (B) Side view, and (C) Top view.	11
Figure 2.1.2:	Proposed modifications to the electric current dipole backed by a thin substrate. (A) Side view, (B) Top view, (C) Equivalent image problem of (A), and (D) Proposed duplicated structure.	13
Figure 2.1.3:	Proposed antenna structure.	14
Figure 2.1.4:	Electric field intensity heat map of the proposed antenna at 60 GHz.	14
Figure 2.1.5:	Surface current density intensity heat map of the proposed antenna structure at 60 GHz.....	15
Figure 2.1.6:	Open-ended microstrip line.....	16
Figure 2.1.7:	Approximated equivalent model of the proposed antenna.....	17
Figure 2.1.8:	Vector field current distribution at 60 GHz.....	17
Figure 2.1.9:	Equivalent T-(ABCD) Matrix.....	18
Figure 2.1.10:	Evaluating input impedance from the equivalent T-matrix parameters	19
Figure 2.1.11:	Calculated input impedance from equation (2.1.10) “Normalized to Z_{in} Maximum.”.....	20
Figure 2.1.12:	Proposed narrowband antenna actual prototype model, microstrip feed line length is 21 mm.	21
Figure 2.1.13:	Antenna realized gain, and S11 of the proposed antenna.	22
Figure 2.1.14:	Principal planes radiation patterns, E-plane {Left}, and H-plane {Right}, solid {Simulated}, dashed {Measured}.	22
Figure 2.1.15:	Proposed wideband antenna structure.	24
Figure 2.1.16:	Proposed wideband antenna structure input impedance.	24
Figure 2.1.17:	Electric field intensity and surface current density heat maps at 60 GHz.	24
Figure 2.1.18:	Proposed wideband antenna structure actual prototype.	25
Figure 2.1.19:	Proposed wideband antenna structure realized gain and S11 (dB).	25
Figure 2.1.20:	Principal planes of the wideband antenna at (57, 60, and 63 GHz) from top to bottom, E-plane {left}, H-plane {right}, dashed lines {measured}, and solid lines {simulated}.	26
Figure 2.1.21:	Four-element linear antenna array structure.....	27
Figure 2.1.22:	Four-element linear antenna array structure electric field intensity heat map (Scale is the same as in Fig. 2.1.17, center frequency is 60 GHz).	28
Figure 2.1.23:	Mutual coupling between array elements (ports are assigned (1 to 4) from left to right for the elements shown in Fig. 2.1.22.	28
Figure 2.1.24:	Antenna array structure realized gain and S11 (dB).....	28

Figure 2.1.25:	Principal planes of the linear antenna array at (57, 59, and 61 GHz) from bottom to top, E-plane {left}, H-plane {right}, dashed lines {measured}, and solid lines {simulated}.....	29
Figure 2.1.26:	Four-element linear antenna array feeding network electric field intensity heat map (Scale is the same as in Fig. 2.1.17).	30
Figure 2.1.27:	Antenna array 3D total realized gain radiation pattern, ideal case {left}, connector and feeding network effect {right}.....	30
Figure 2.1.28:	Efficiency of each structure.	31
Figure 2.2.1:	EBG mushroom cell dimensions.....	33
Figure 2.2.2:	Dispersion diagram of the Sievenpiper mushroom cell.	34
Figure 2.2.3:	Printed ridge-gap air microstrip line.	35
Figure 2.2.4:	Printed ridge-gap air microstrip line dispersion diagram.	35
Figure 2.2.5:	Antenna array fed by PRGW power divider.....	36
Figure 2.2.6:	Antenna array fed by packaged microstrip line power divider.	37
Figure 2.2.7:	Realized gain and reflection coefficient for the proposed cases.	39
Figure 2.2.8:	Antenna array with aggregated open microstrip line feeding network, (the distance from the center of the array to the end-lunch connector is the same for all cases. The feed line is only cropped in this figure).	40
Figure 2.2.9:	Electric field heat map for the aggregated open microstrip line fed antenna array at 60 GHz.	41
Figure 2.2.10:	Realized gain and reflection coefficient for both open and aggregated fed microstrip line fed antenna arrays.....	42
Figure 2.2.11:	Electric field heat map in the E-plane for the proposed array structures. ..	42
Figure 2.2.12:	Proposed antenna array structure with aggregated microstrip feeding network.....	43
Figure 2.2.13:	Realized gain and reflection coefficient of the proposed antenna array....	44
Figure 2.2.14:	Realized gain and reflection coefficient of the proposed antenna array (simulated values include substrate permittivity tolerance value).	44
Figure 2.2.15:	Radiation patterns of the proposed antenna array with aggregated microstrip feeding network, E-plane {top}, and H-plane {bottom}.	45
Figure 2.2.16:	Radiation efficiency of the proposed antenna array.	46
Figure 2.3.1:	Proposed antenna array with superstrate structure.	50
Figure 2.3.2:	Proposed antenna array with superstrate structure dimensions.....	50
Figure 2.3.3:	Radiation pattern comparison between the antenna array with and without superstrate, left (H-plane), and right (E-Plane).	51
Figure 2.3.4:	3D Radiation pattern of the proposed superstrate antenna array.....	52
Figure 2.3.5:	S-parameters and gain of the proposed antenna array structure.....	52
Figure 2.3.6:	Radiation pattern in principle planes Left (E-plane), and right (H-plane), top to bottom, 58, 60, and 63 GHz.	53
Figure 3.1:	Dipole antenna between two metal sheets, (a) 3D geometry, and (b) cross-section indicating the diffracted fields.	56
Figure 3.2:	UTD analysis of the dipole antenna between two metal sheets, (a) actual problem, and (b) reciprocal problem.	57

Figure 3.3:	Graphical representation of the complex plane from (3.6)	59
Figure 3.4:	Gain boost (dB) versus Ds/λ	60
Figure 3.5:	Dual electric and magnetic problems	61
Figure 3.6:	Radiation patterns in principle planes, (a) H-plane, and (b) E-plane	62
Figure 3.7:	Two elements array configuration.....	63
Figure 3.8:	Full wave simulation.	63
Figure 3.9:	Radiation pattern in principle planes.....	64
Figure 3.10:	Proposed antenna structure, (a) 3D view, (b) top view, and (c) bottom view.....	65
Figure 3.11:	S_{11} and gain values for the proposed antenna structure.....	66
Figure 3.12:	Principal planes radiation patterns of the antenna structure at 60 GHz, (solid lines refer to a co-polar component (H-plane: Blue, and E-plane: Red), and dashed lines refer to a cross-polar component (H-Plane: Green, and E-plane: Cyan)).	67
Figure 3.13:	Proposed two-element antenna array structure, (a) 3D view, (b) top view, and (c) bottom view.	68
Figure 3.14:	S_{11} and gain values for the proposed two-element antenna array structure.....	69
Figure 3.15:	Mutual coupling between the adjacent elements in the two-element array.	69
Figure 3.16:	Principal planes for the two-element array at 60 GHz, (solid lines refer to a co-polar component (H-plane: Blue, and E-plane: Red), and dashed lines refer to a cross-polar component (H-plane: Green, and E-plane: Orange)).	70
Figure 3.17:	Proposed single element antenna spacer and actual prototype model.....	71
Figure 3.18:	Single element realized gain and reflection coefficient.....	72
Figure 3.19:	Single element radiation patterns in principal planes (solid lines refers to simulated data, and dashed lines refers to measured data) “E-Plane (left) and H-plane (right)”.....	73
Figure 3.20:	Two-element antenna array actual prototype model.....	74
Figure 3.21:	Two-element array realized gain and reflection coefficient.	75
Figure 3.22:	Two-element array radiation patterns in principal planes (solid lines refers to simulated data, and dashed lines refers to measured data) “E-plane (left) and H-plane (right)”.	75
Figure 3.23:	Surface current density heat map and 3D radiation pattern of the two-element antenna array.....	76
Figure 3.24:	Calculated efficiency of the single element and two element array structures.....	76
Figure 4.1.1:	Abstract sketch of the proposed structure.	80
Figure 4.1.2:	Proposed antenna structure.	82
Figure 4.1.3:	Magnetic field heat map and the magnetic vector field distribution for the proposed structure at 60 GHz.....	83
Figure 4.1.4:	3D radiation pattern of the proposed structure at 60 GHz.	84

Figure 4.1.5:	E-plane (solid red) and H-plane (solid blue), and cross-polar (dashed lines) (Frequencies are: 57 GHz, 60 GHz and 64 GHz from top to bottom).	84
Figure 4.1.6:	Proposed antenna structure with the connector body, (a) without using EBG surface, and (b) with the use of EBG surface.	86
Figure 4.1.7:	EBG surface unit cell.....	87
Figure 4.1.8:	Electric field heat map for both structures in Fig. 4.1.6 at 60 GHz.	87
Figure 4.1.9:	Co-polar (solid line) and cross-polar (dashed line) radiation pattern at 60 GHz. E-plane (red) and H-plane (blue). Left side without EBG, and right with EBG.	87
Figure 4.1.10:	Unit cell with a dielectric slab instead of the air gap.....	89
Figure 4.1.11:	Proposed antenna structure with a dielectric slab instead of the air gap....	89
Figure 4.1.12:	Isometric view of the redesigned structure.....	90
Figure 4.1.13:	Co-polar (solid line) and cross-polar (dashed line) radiation patterns at 60 GHz. E-plane (red) and H-plane (blue).	90
Figure 4.1.14:	Realized gain and reflection coefficient of the proposed structure with and without dielectric.	91
Figure 4.1.15:	Proposed antenna array structure.	92
Figure 4.1.16:	Proposed antenna array feeding network, feed lines, and slots locations with respect to the mushroom cells.....	92
Figure 4.1.17:	3D radiation pattern for the proposed antenna structure.....	93
Figure 4.1.18:	Radiation patterns at 58, 60, 64 GHz from top to bottom, respectively....	94
Figure 4.1.19:	Proposed antenna structure with the connector body, without using EBG surface (bottom), and with the use of EBG surface (top).....	95
Figure 4.1.20:	Electric field heat map with and without EBG surface.....	96
Figure 4.1.21:	Actual array fabricated prototype, (a) top, and (b) bottom view.....	97
Figure 4.1.22:	Radiation patterns at 58, 60, 64 GHz from top to bottom respectively (E-plane {left} and H-plane {right}).	98
Figure 4.1.23:	Realized gain, reflection coefficient, and efficiency of the proposed antenna array.	99
Figure 4.2.1:	Sketch of the DRA surrounded by a dielectric ring.....	102
Figure 4.2.2:	Proposed DRA structure.	103
Figure 4.2.3:	Magnetic vector and scalar field heat maps for the proposed DRA structure.....	104
Figure 4.2.4:	Magnetic field heat map for the DRA with/without a dielectric ring (same H-field scale as in Fig. 4.2.3).	104
Figure 4.2.5:	Directivity of the DRA with/without a dielectric ring.	105
Figure 4.2.6:	Radiation patterns with and without the dielectric ring at 60 GHz. (Red) with a dielectric ring, (Blue) without a dielectric ring, right (E-plane), left (H-plane), Solid (co-polar), Dashed (cross-polar), at 60 GHz.....	105
Figure 4.2.7:	Magnetic vector field heat map for the DRA with/without alignment arms (same H-Field scale as in Fig. 4.2.3).	106
Figure 4.2.8:	Top view of the proposed DRA structure.....	107

Figure 4.2.9:	Gain and reflection coefficient of the proposed DRA structure.....	107
Figure 4.2.10:	Red (H-plane), Blue (E-plane), Solid (co-polar component), Dashed (cross-polar component) at 60 GHz.	108
Figure 4.2.11:	(a) Proposed DRA, (b) with single EBG surface, (c) with double EBG surfaces.....	109
Figure 4.2.12:	EBG unit cell dispersion diagram.	111
Figure 4.2.13:	Electric field heat maps for the proposed structures in Fig. 4.2.11.....	111
Figure 4.2.14:	Radiation patterns in the principal planes for the proposed DRA structures shown in Fig. 4.2.11. Red (H-plane), Blue (E-plane), Solid (co-polar component), Dashed (cross-polar component). (a) no EBG, (b) single EBG, (c) double EBG surfaces and (d) 3D radiation pattern of the proposed DRA structure with double EBG surfaces.....	112
Figure 4.2.15:	Actual prototype of the proposed DRA structure.	112
Figure 4.2.16:	Measured and simulated E- and H-plane radiation patterns of the proposed DRA structure. Red (Simulated co-polar), Dashed-Blue (Measured co-polar), Dashed-Purple (Measured cross-polar), Dashed-Green (Simulated cross-polar) right (H-plane), left (E-plane), from bottom to top 65, 60, and 55 GHz.	113
Figure 4.2.17:	Measured S-parameters and gain of the proposed DRA structure.	114
Figure 5.1.1:	Two dipole antennas printed on a dielectric substrate.	117
Figure 5.1.2:	Two dipole antennas printed on a dielectric substrate covered with a top substrate.	118
Figure 5.1.3:	Proposed symmetrical layers analysis configuration.	118
Figure 5.1.4:	Absorbing metamaterials cells bounding the substrate configuration....	121
Figure 5.1.5:	Single substrate layer analysis configuration.	122
Figure 5.1.6:	Parallel plate waveguide reflectors.	122
Figure 5.1.7:	Proposed antenna structure (all dimensions are in millimeters).	123
Figure 5.1.8:	Proposed symmetrical layers wireless inter-chip link structure.	124
Figure 5.1.9:	Balun structure S-Parameters.....	125
Figure 5.1.10:	Proposed symmetrical layers structure electric field intensity heat map at different phases (at 55 GHz).	126
Figure 5.1.11:	Wireless inter-chip link structure with hard surface metallic strips.....	127
Figure 5.1.12:	Proposed mushroom cell structure.	128
Figure 5.1.13:	Proposed mushroom cell dispersion diagram.	128
Figure 5.1.14:	EBG wireless inter-chip link structure.	129
Figure 5.1.15:	Enlarged segment of the proposed structure in Fig. 5.1.14.....	129
Figure 5.1.16:	PEC (soft-surface) wireless inter-chip link structure.....	130
Figure 5.1.17:	Enlarged segment of the proposed structure in Fig. 5.1.16.....	131
Figure 5.1.18:	S-parameters for the proposed structures.	132
Figure 5.1.19:	Electric field heat map comparison at 55 GHz (same scale as Fig. 5.1.10).	134
Figure 5.1.20:	S-parameters with longer separation between transmit and receive dipoles (double distance).	136

Figure 5.1.21:	Doubling the distance, electric field intensity heat map at 55 GHz.....	136
Figure 5.1.22:	Doubling the distance, electric field intensity heat map at 51.7 GHz (Single layer structure).	137
Figure 5.1.23:	Doubling the distance S-parameters (Single layer structure).....	138
Figure 5.1.24:	Electric field heat map in the H-plane for the proposed structures.....	139
Figure 5.1.25:	Actual fabricated prototype, bottom view (left), and top view (right)....	141
Figure 5.1.26:	Experimental setup.....	141
Figure 5.1.27:	Measured S-parameters for the fabricated prototype.....	142
Figure 5.1.28:	Measured Phase and Group Delay	143
Figure 5.2.1:	90-degree bend structures, left (Case (1): Soft Surface), and right (Case (2): EBG).....	145
Figure 5.2.2:	90-degree bend structures electric field intensity heat map at 55 GHz, left (Case (1): Soft Surface), and right (Case (2): EBG).....	145
Figure 5.2.3:	Doubling the distance and the 90-degree bend S-parameters.	146
Figure 5.2.4:	Electric field heat map in the H-plane for the 90-degree bend (soft surface structure case) at 55 GHz, E-Field scale is the same as in Fig. 5.2.2.	147
Figure 5.2.5:	Proposed 1:2 wireless inter-chip link structures, Port 1 is TX, Port 2 and 3 are RXs, (a) EBG T-shape power divider, (b) PEC T-shape power divider, and (c) PEC Y-shape power divider.....	148
Figure 5.2.6:	Proposed 1:2 wireless inter-chip link structures electric field heat maps at 55 GHz. (a) EBG T-shape power divider, (b) PEC T-shape power divider, and (c) PEC Y-shape power divider. E-field scale is the same as in Fig. 5.2.2.	149
Figure 5.2.7:	Proposed 1:2 wireless inter-chip link structures S-parameters.	150
Figure 5.2.8:	Fabricated prototype.	151
Figure 5.2.9:	Proposed 1:2 wireless inter-chip link structure measured S-parameters..	151

LIST OF TABLES

Table 2.2.1:	Line width for different characteristic impedances.....	38
Table 2.2.2:	Comparison with other works	47
Table 2.3.1:	Proposed antenna array with superstrate structure dimensions	51
Table 2.3.2:	Comparison with other antennas operating at 60 GHz in the literature.....	54
Table 3.1 :	Antenna structure dimensions	66
Table 4.1.1:	Structure dimensions in (mm)	82
Table 4.1.2:	Structure dimensions in (mm)	89
Table 4.1.3:	Antenna array feeding network dimensions in (mm)	93
Table 4.1.4:	Antenna array slots dimensions in (mm)	93
Table 4.1.5:	Comparison with other works	100
Table 4.2.1:	Proposed DRA structure dimensions in (mm)	108

LIST OF ACRONYMS

AUT	Antenna under Test
AMC	Artificial Magnetic Conductor
DRA	Dielectric Resonator Antenna
DUT	Device under Test
EBG	Electromagnetic Band Gap
EM	Electromagnetic
ME	Magneto-Electric
PEC	Perfect Electric Conductor
PMC	Perfect Magnetic Conductor
PPW	Parallel Plate Waveguide
PRGW	Printed Ridge Gap Waveguide
RX	Receiver
TE	Transverse Electric
TEM	Transverse Electromagnetic
TM	Transverse Magnetic
TX	Transmitter
HFSS	High Frequency Structure Simulator
WPAN	Wireless Personal Area Network

CHAPTER 1

INTRODUCTION

1.1 Overview

As the future of wireless communication systems is heading towards the fifth generation, whereby operating at higher frequencies, the ability to communicate high data rates would become feasible. Where at such frequencies, designing narrowband front-end systems would allow the communication of high data rates. For instance, a 3% relative bandwidth at the 60 GHz ISM band would result in 1.8 GHz of bandwidth. However, at lower frequencies such as the 2.4 GHz ISM band, it would result in only 72 MHz of bandwidth. This idea motivates the migration of current wireless technologies to operate at millimeter-wave frequencies. Hence, utilizing such higher millimeter-wave frequencies would allow for higher data rates, typically, more than one Gbps [1] [2]. On the other hand, the design of the physical layer becomes very challenging, and the path loss that the electromagnetic waves would encounter becomes considerably significant and consequently limits the range of wireless communication. The design of any 5G communication system operating at mm-wave frequencies includes several aspects, starting from the signal processing at the baseband towards the high-frequency signal launching at the transmitter antenna, and the inverse operation back again at the receiver side. There are several details, and many suggested solutions at each level that would guarantee the signal fidelity, and a low bit error rate wireless communication. In this work, we focus on the antenna design of the system. As mentioned previously, the high path loss is significant at millimeter wave frequencies, and that would eventually limit the operating range. The currently proposed remedy to this issue is to increase the directivity of the transmitting and receiving antennas. This can be simply noticed from the pretty well-known Friis Transmission Equation, whereby increasing the directivity of the antenna, the spherical spreading, and attenuation from the medium can be compensated. Therefore, high gain antennas play an essential role in compensating the high path loss that wireless signals encounter

at such frequencies [1], [2]. The past decade has witnessed many several innovative works in this regard [3]–[10], however, there is still plenty of room for more innovative new solutions that would still satisfy high performance and would be a low cost at the same time.

1.2 Problem Statement

As high gain antennas are an essential part of any 5G system, there is a high motivation for implementing high gain antennas, especially in the 60 GHz band. There are various applications in the 60 GHz band. It can be used for medical imagining, personal wireless area networks (WPAN), and high definition video TV (HDTV). A vast literature exists, and a good start can be found in [2]. Usually, the fabrication of high gain antennas is expensive and requires special fabrication facility due to the tiny dimensions with the highest accuracy possible. In this work, we propose new low cost structures at 60 GHz that can be fabricated in any modest fabrication facility, and at the same time maintain high performance metrics. To shed light on some aspects related to the wireless front end design of the communicating entities in a 5G network, the following discussion is provided.

In wireless communication systems, the received signal level is very crucial in maintaining high throughput. The given example is not unique, as the applications and system architectures can vary. However, it is very beneficial to highlight the important role that high gain antennas play in the transceiver system chain. Fig. 1.1 shows an indoor space to be covered by a 5G wireless service. In the shown scenario, the access point communicates data with the user equipment, the wireless link in such case operates at mm-wave frequencies, which implies that the path loss is high, and the received signal experiences a high level of attenuation. In many cases, asymmetrical bandwidths are assigned for the uplink and downlink channels. As it is usually the case that the end user demand for data download is higher than the upload; however, this could differ depending on the nature of the coverage space requirements. As the downlink is expected to operate at a higher speed (i.e., wider bandwidth) than the uplink, the minimum received signal level by the user equipment is more of a concern than the received signal by the access point, in such case the minimum received signal level by the user equipment should be high enough to maintain an adequate quality of service.

As the signal suffers from high path loss, this suggests that higher gain should be assigned to the transmitter Power Amplifier (PA), which means higher power consumption, and a higher possibility of non-linear distortion. At the receiver side of the user equipment, it suggests a higher gain should be assigned to the Low Noise Amplifier (LNA), and this would result in a high power drain at the user equipment, which could be a critical factor, especially for the battery life of mobile devices. In addition to that, a higher noise factor is expected for high drain current amplifiers, not to mention the increased complexity of the design. Fig. 1.2 shows an alternative scenario where a high gain antenna is employed at the transmitter end of the access point. Employing such high gain antenna would relax the gains of the access point transmitter PA, and the user equipment receiver LNA. In such a case, the increase in the transmitter antenna gain compensates the propagation losses, and maintain an adequate signal level at the receiver side. However, using high gain antenna is associated with a narrower beam-width (comparing the beam-width angles α and β), and would result in smaller coverage, which consequently would increase the number of access points to cover the intended space. Such drawback would still be bearable against the other advantages obtained from relaxing the amplifier gains. In such a scenario, the reduction in the access point cost is highly desirable.

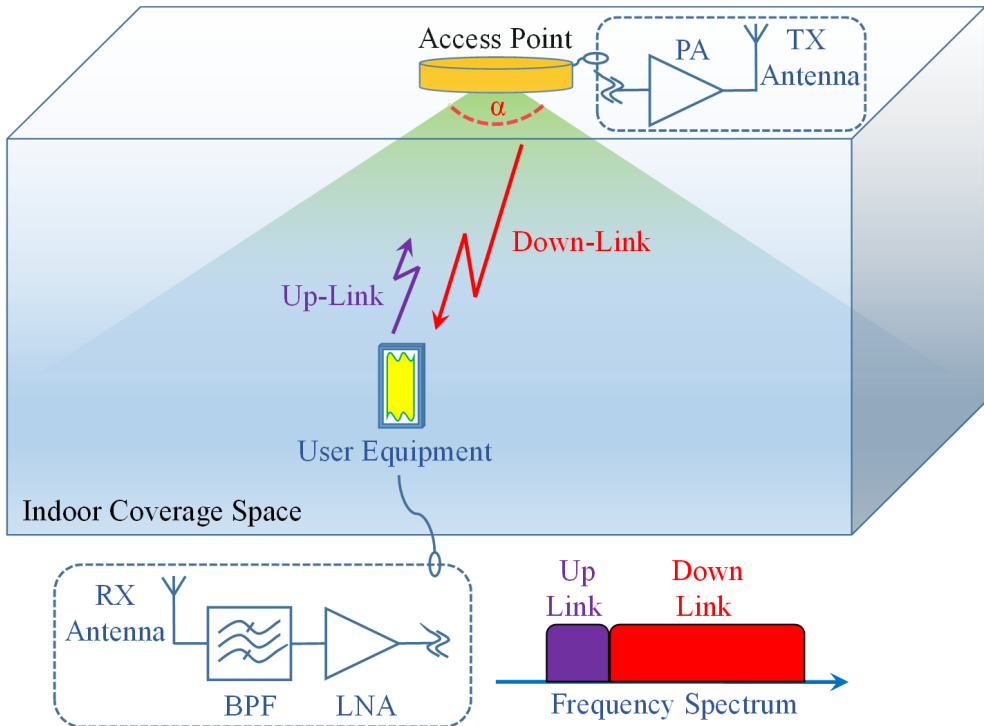


Figure 1.1: Low gain access point antenna coverage.

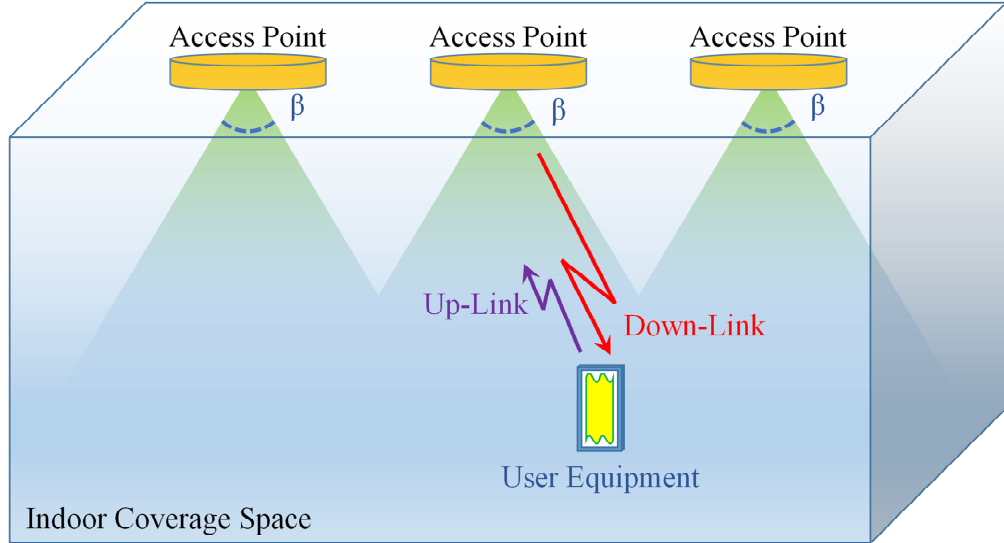


Figure 1.2: High gain access point antenna coverage.

In a 5G network, the data is communicated at mm-wave frequencies between various communicating entities. The high frequency signal is processed internally within the entity. In many cases, the high frequency signal can be transferred between several ICs. A typical scenario is when different technologies are used on a single board, as an example the chosen stack for a power amplifier, and an up-converter circuit are different, where the power amplifier stack could be chosen to handle higher power level than the up-converter stack. Multiple ICs on board with different technologies can be designed to optimize both performance and cost. In such a scenario, the high frequency signal has to be transferred from one IC to another through bonding wires. However, as the 5G wireless system is intended to operate at mm-wave frequencies, the bonding wires will degrade the signal quality. A remedy to this issue is to communicate the data wirelessly between several ICs, as shown in Fig. 1.3. Therefore, this work has been extended to include the design of a novel low-cost wireless inter-chip links structures with enhanced performance metrics. Hence, this thesis investigates low-cost, high-performance antennas for 5G/mm-wave communication, externally between communicating devices/entities, and internally within any device between its internal ICs.

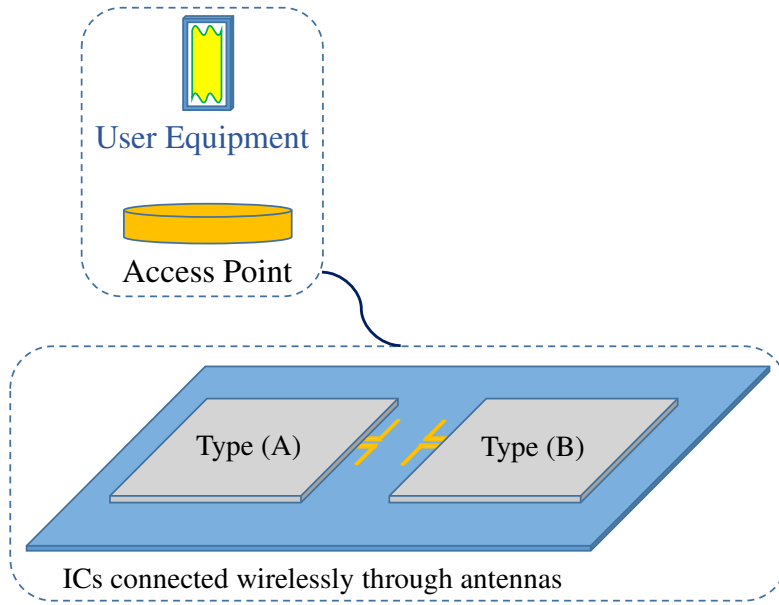


Figure 1.3: Wireless inter-chip communication

1.3 Motivation

The 5th generation migration of the current wireless systems is very valuable, the leap in the data rates of communicating devices that the 5th generation can provide will allow for a higher quality of video calls, high-speed data transfer, and allow for several online and real-time streaming applications. One of the looked for applications is Virtual Reality (VR). Several activities would be possible through VR; it could be used for entertainment, educational, and even medical purposes. For example, hologram models that can describe atoms, human organs, or even electromagnetic problems can be demonstrated with a better understanding and visualization through virtual reality technologies. However, such technologies would require a high amount of data to be communicated in real time; such communication can be only practically realized by having a high data rate communication system such as the sought after the 5G system. Any 5G handset or wireless communicating entity involves a variety of sub-systems, and requires multidisciplinary expertise to be involved, in this work we give more focus on the launching of electromagnetic signals through antennas, targeting new high performance and low cost solutions.

1.4 Literature Review

Various methods were employed to design high gain antennas at millimeter wave frequencies. In [11], an active microstrip antenna integrated with a three-stage pseudomorphic high electron mobility transistor amplifier was designed. Such an active antenna design is suitable for narrowband wireless local and personal area networks (WLAN/WPAN) applications. However, it demands a considerable amount of power consumption, which can constitute some limitations for mobile devices. In [12], a high gain array was comprised of radiating slots that are fed through the substrate integrated waveguide (SIW) power divider network. Such design is very robust in terms of its radiation characteristics because of the SIW feeding network, which is sufficiently shielded/packaged type of feeding networks [13]. On the other hand, it is comparatively expensive due to the required vias as compared with vialess planar structures. In [14], a 60 GHz antenna array with a dual-resonant slot-patch antenna was designed using LTCC technology. The shrinking effect of the LTCC substrates makes it more challenging and expensive in terms of its fabrication process. In [15], a monolithic polymer-based high gain Dielectric Resonator Antenna (DRA) was implemented efficiently. Nevertheless, such design would still require special fabrication process, and might not seem as low profile as printed solutions. In [16] a wideband magneto electric dipole antenna was designed, despite the high bandwidth feature of magneto-electric dipoles, they are still not known for being low profile, and they require several substrate layers. In [17], [18] printed dipole antennas were designed at 30 GHz using printed circuit board technology, the element radiation pattern is an end-fire, and would still be limited to linear array configurations. Moreover, the gain was not maximized for the single element. In contrast, in this work, we investigate the boresight type of elements that would fit well in a planar type of an array. At the same time, we investigate the design at 60 GHz band, where the use of printed circuit boards is still not ubiquitous due to the radiation losses. In [19], [20] SIW fed 60 GHz antennas were implemented as well. In [21] LTCC type of structure was implemented at 60 GHz, the LTCC technology is well suited for a high level of integration, and can push down the size of the structure effectively. However, it is still expensive and more demanding in terms of the fabrication process due to the shrinking effect. In [22], a broadband 60 GHz slot antenna was designed. The bandwidth of the antenna was optimized using a cavity in beneath of the antenna. The EBG feeding provides reasonable efficiency and suitable shielding mechanism. However, the antenna gain was compromised in this

work, not to mention also the cost associated with printed EBG structures. In [23] 60 GHz on-chip antenna using an integrated passive device (IPD) process was implemented. Such a process provides a high level of integration. On-chip designs are known for their low efficiencies due to the silicon substrate. In this IPD process, efficiency is improved due to the use of a glass substrate. In [24], a 60-GHz end-fire fan-like antenna with a wide beam-width was implemented, as this would imply, the wide beam-width reflects a relatively lower gain. Another aspect, is the material characterization at such high frequencies, where the commercial substrates are not fully characterized at mm-Wave frequencies, especially the 60 GHz band, several effects, such as surface-waves and copper roughness become more noticeable at those frequencies. In [25], several commercial substrates were characterized at 60 GHz, taking into account all the aforementioned effects.

Another proposed direction to implement high gain antennas is the use of superstrates to increase the antenna gain. It is well known that arrays are used to achieve high directive radiation characteristics, and a 3-dB gain increase is possible by doubling the number of the elements that double the array size. When the number of elements becomes massive, the mutual coupling between the antenna array elements becomes more severe. Also, the design of the feeding network becomes more challenging, which causes high losses, especially at high millimeter-wave frequencies [26]–[28]. On the other hand, to improve the matching bandwidth, it is common to use a matching circuit (such as Chebyshev and Binomial transformers) [29]. Such matching circuit design would require extra area, and sometimes it would be challenging to accommodate such a matching circuit within the feeding network environment. A different type of antenna called Cavity Resonant Antenna (CRA) (sometimes also known as a Resonant Cavity Antenna, or RCA) is proposed as a solution to the aforementioned issues. The name stems from the fact that the antenna is usually bounded between two substrates (the substrate holding the antenna and the superstrate), similar to the Fabry–Pérot resonator structure, therefore it is also referred to as Fabry–Pérot resonator antennas. The existence of a superstrate in the vicinity of the antenna changes the antenna radiation resistance and reactive impedance, and hence the superstrate can be considered as a design element that can be controlled to control the antenna impedance characteristic, for example lowering the quality factor and increasing the matching bandwidth. The successive in-phase bounces of the trapped waves between the substrate and the superstrate provide a valuable contribution to the boresight direction and increase the directivity [30]–[32]. This suggests that the

use of CRA can eliminate the need for an array to increase the gain. On the other hand, due to the necessity of having a superstrate at free space wavelength distance from the antenna, the structure might get obtrusive and less low-profile. However, as we scale up in frequency, the wavelength becomes physically small, and hence the spacing between the substrate and the superstrate becomes very small in such a way that the antenna would still be considered as a low-profile antenna [33] (for example at 60 GHz, the free space wavelength is 5-mm).

1.5 Proposed Methodology

Adapting to the current requirements for the future generations of wireless technologies at mm-wave frequencies, our designs focus on the design of low cost, low profile, planar, and high gain antennas at 60 GHz. The proposed structures suit short range, low power applications, such as wireless personal area networks (WPAN). The proposed structures can be realized in any modest fabrication facility. The proposed antennas presented in Chapter 2 are based on a new design perspective, which utilizes microstrip line discontinuities radiation, to create an efficient, high gain, 60 GHz low profile antenna. The proposed antenna uses only a single substrate and has a high gain of 11.5 dBi; the antenna can be used in a linear array with the separation distance between the elements to be in the order of a wavelength without generating grating lobes. The compelling feature of the proposed structures is the simplicity, and low cost (single substrate with no vias), while at the same time maintaining a very high gain at the element level and a decent bandwidth. The second proposed antenna in Chapter 3 utilizes the diffracted fields from plane metallic sheets to achieve a gain of 11 dBi. The antenna has a matching bandwidth of 7 GHz (from 57 to 64) to cover the 60 GHz ISM band. The antenna can be employed in a linear array with around one wavelength distance between the feed points without generating any grating lobes. In Chapter 4, a new design perspective is proposed, the proposed design procedure can transform the radiation characteristics of an electric or magnetic current element to Magneto-Electric dipole characteristics. The proposed procedure doesn't require the orthogonal combination of the magnetic and electric current elements [34]. Hence, the procedure possesses a significant advantage. It avoids the need for a quarter free-space wavelength spacing between the current element and the ground plane that makes it a low cost and a high performance solution. In Chapter

4, a novel technique is proposed to enhance the gain of a Dielectric Resonator Antenna over a wideband range of frequencies, producing a high gain and a low cost solution.

In Chapter 5, we provide a study of several aspects of wireless inter-chip communication between adjacent ICs at mm-wave frequencies. The symmetrical layers concept is introduced as a general approach to eliminate the destructive interference and redirect the wasted radiated energy to free space towards the receiving antenna. In addition, the use of hard/soft surfaces and Electromagnetic Band Gap (EBG) structures to focus the radiated energy towards the receiving antenna is studied thoroughly. The use of such concepts has tremendous advantages, in focusing the energy towards the receiving antenna and eliminating the spherical spreading losses introduced by the radiated spherical wave nature. The incorporation of the symmetrical layers with hard/soft surfaces led to novel compact and low cost wireless inter-chip structures with enhanced link budget performance.

CHAPTER 2

EFFICIENT MILLIMETER-WAVE ANTENNA BASED ON THE EXPLOITATION OF MICROSTRIP LINE DISCONTINUITY RADIATION

2.1 Utilizing Microstrip Open Ended Line Radiation

2.1.1 Introduction

Microstrip lines were initially invented as guiding structures. They are abundantly used in the design of passive components such as filters, couplers, and power dividers. Also, they play a vital role in the design of antenna feeding networks [29]. Therefore, the objective is always to minimize any losses as much as possible while carrying out the electromagnetic energy from one point to another. Microstrip line losses are due to dielectric losses, conduction losses, and radiation losses. Radiation losses are usually dominant at discontinuities; such discontinuities would be open stubs, short stubs, T-junctions, and microstrip line bends [35].

Here, an advantage of the radiation losses encountered in microstrip line discontinuities is utilized to create an efficient radiator. To clarify the concept, the radiation mechanism of a printed dipole on a thin substrate, as shown in Fig. 2.1.1 is to be discussed. The substrate thickness is negligible compared to the guided wavelength. According to image theory, such configuration makes an inefficient radiator [36]–[38]. The fringing electric fields at the ends of the dipole and the electric field created by the gap of the antenna constitute aperture fields [27]. Those aperture electric fields can be replaced by equivalent magnetic currents according to the equivalence principle [36]. However, the area of the aperture of the fringing electric fields at the edges and the gap electric field is tiny, and consequently, the antenna gain is expected to be low.

To improve the antenna gain, the following modifications are proposed, as shown in Fig. 2.1.2. First, the gap of the dipole is increased, so that there are now four fringing electric fields at the edges of the dipole strips, which are equivalent to four magnetic currents. Again, this can also be visualized as four magnetic currents antenna array. To have boresight radiation with no grating lobes, the gap distance should be less than a half wavelength. By maintaining a differential feeding to the strips of the dipole, all four magnetic currents are in phase. The differential feeding can be achieved by the 180° phase shifter or a half-guided wavelength delay line. To have an efficient radiator with a high gain, this dipole can be duplicated, as shown in Fig. 2.1.2 (D). This will increase the aperture area of the fringing electric fields at the ends of the dipole strips [39].

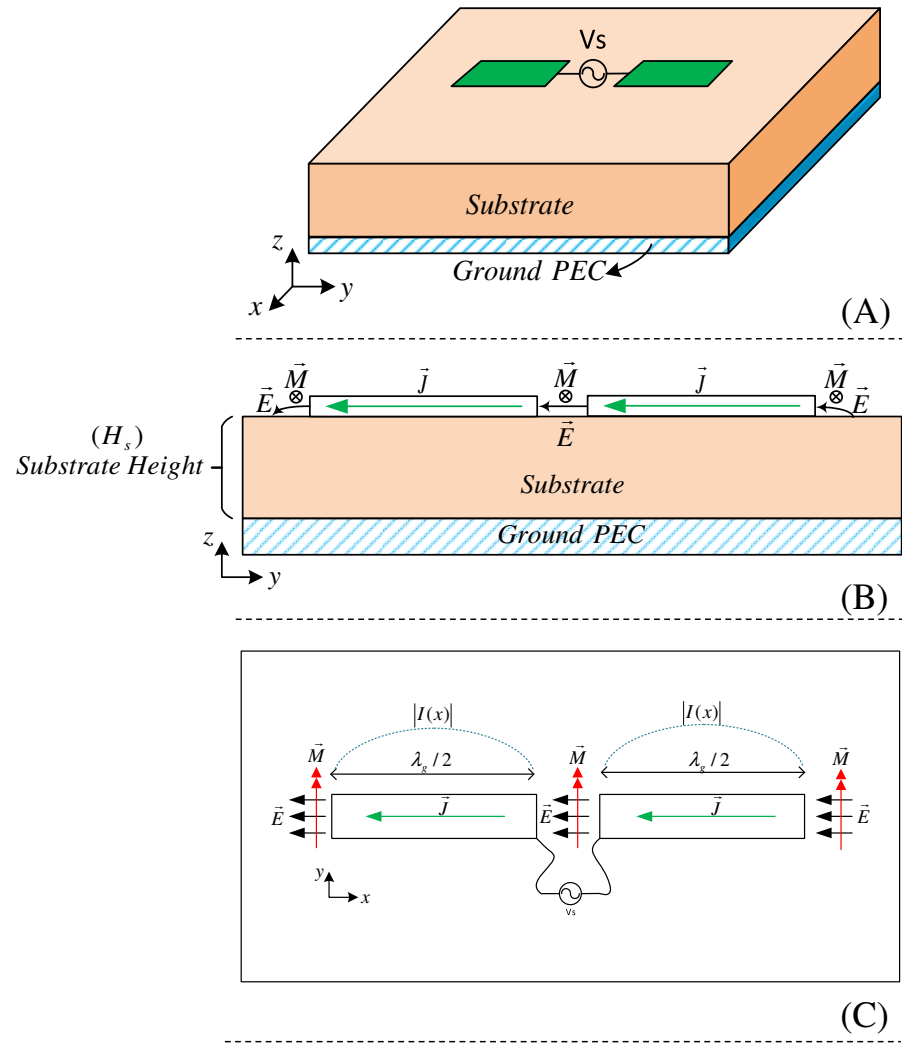


Figure 2.1.1: Electric current dipole backed by a thin substrate, (A) Isometric view, (B) Side view, and (C) Top view.

The configuration shown in Fig. 2.1.3 is a proposed realization. The used substrate is Rogers 5880, the thickness of the substrate is 0.254 mm, the relative permittivity of the substrate is 2.2, and the calculated guided wavelength is 3.37 mm at 60 GHz. As shown in Fig. 2.1.3, there are three dipoles separated by ($E = 0.2$ mm), and they have a gap distance of ($A = 2$ mm). The complete set of dimensions is tabulated in the inset table in Fig. 2.1.3. The microstrip line section denoted by “A” provides the differential feeding.

Fig. 2.1.4 shows the electric field heat map of the proposed structure. The heat map is calculated at 60 GHz. It can be noticed that the fringing fields at the ends of the dipole create an equivalent magnetic current. Also, it can be noticed that those are the only main radiating sources, as other fringing fields in other feeding microstrip lines are out of phase on both sides of each line. Therefore, there is no significant radiation. Another perspective that can be carried out is that the discontinuities are created by the open-ended stubs, and the T-junctions connecting the open-ended stubs to the loop, and those discontinuities radiate.

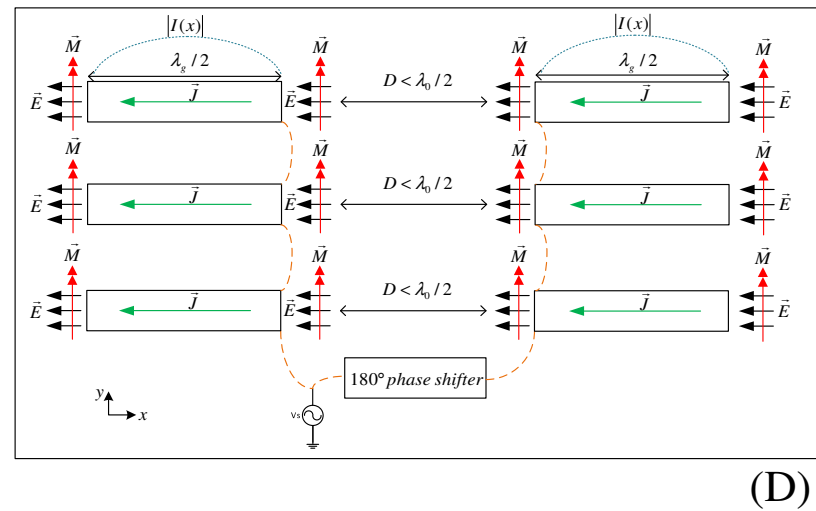
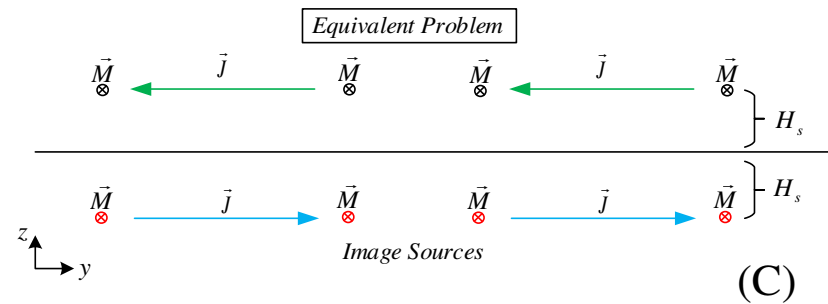
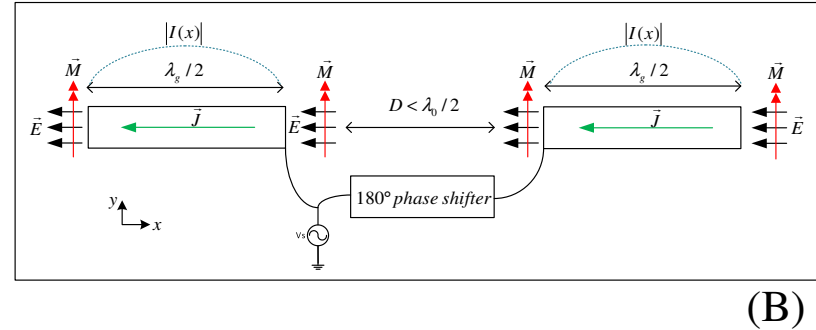
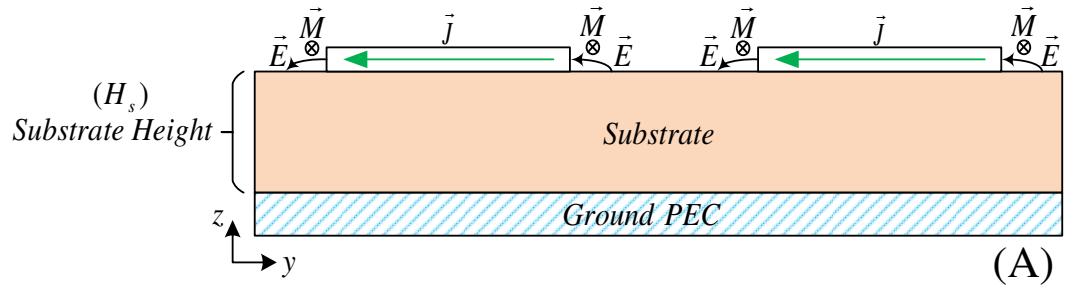


Figure 2.1.2: Proposed modifications to the electric current dipole backed by a thin substrate. (A) Side view, (B) Top view, (C) Equivalent image problem of (A), and (D) Proposed duplicated structure.

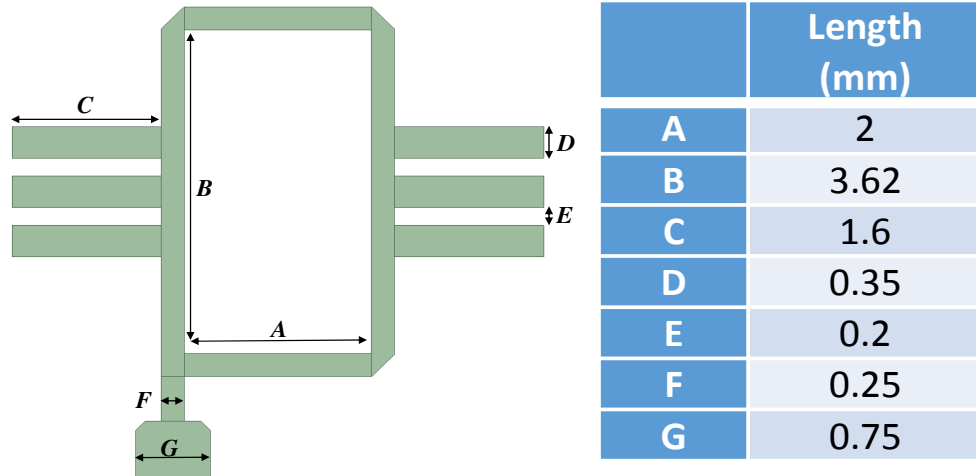


Figure 2.1.3: Proposed antenna structure.

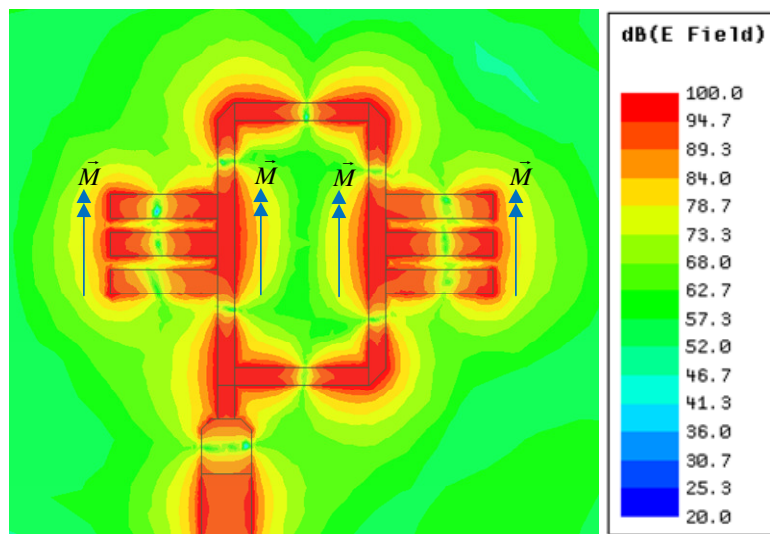


Figure 2.1.4: Electric field intensity heat map of the proposed antenna at 60 GHz.

Fig. 2.1.5 shows the surface current density heat map at 60 GHz. As compared with the electric field intensity, the maximum surface current density locations correspond to the minimum electric field intensity locations as expected. Since the dipole strips are half guided wavelength, their input impedance of the loop is expected to be infinite (i.e., open circuit). The radiation resistance of an open stub is infinite, and that creates a total mismatch. Therefore it is difficult to use an open stub to radiate, even though it has an infinite radiation resistance, and this is due to the total mismatch, where all the energy is reflected back.

There are two types of equivalent circuit models that can be considered to model the structure. The first model is usually referred to as an artificial circuit model, which assumes the structure to be lossless, and only made of LC elements [40]. This type is beneficial to study the dispersion characteristic of various structures. The second type is the typical equivalent circuit model, which includes the losses in the structure (such as radiation, surface waves, dielectric losses, conductor losses, etc.). There have been several studies to obtain equivalent circuit models for microstrip line discontinuities, such as the bends, T-junctions, and open stubs [35]. However, those models' accuracies and validity are not guaranteed at millimeter-wave frequencies.

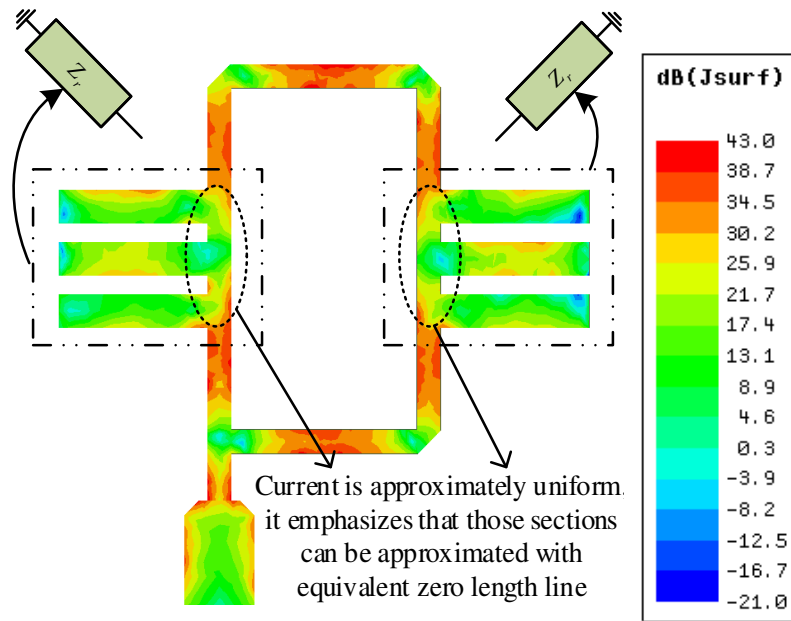


Figure 2.1.5: Surface current density intensity heat map of the proposed antenna structure at 60 GHz.

One of the early approximate equations that evaluate the radiation resistance for the open stub is given in (2.1.1) [41]. This approximate equation is useful in indicating the relation between the radiation resistance of an open stub with frequency. It can be shown that the radiation resistance decreases with the increase of frequency in a nonlinear fashion. Therefore, this indicates that there will be a specific high frequency at which the open stub can be matched to a typical 50Ω impedance, and consequently radiate efficiently. This also backs the idea that microstrip line discontinuities can be utilized for the sake of creating an efficient radiator at higher millimeter-wave frequencies. As shown in Fig. 2.1.6, the radiation resistance is calculated by assuming a

constant aperture field at the end of the line. From the radiated energy, the input impedance can be derived. The reactive part of the energy can be modeled as an additional extension to the line as given by the empirical equation (2.1.2) [40].

$$G_r \approx \frac{(\epsilon_{ref})^{3/2}}{180} \left(\frac{w}{\lambda_0} \right)^2 \quad (2.1.1)$$

$$l_{eo} \approx 0.412h \left(\frac{\epsilon_{ref} + 0.3}{\epsilon_{ref} - 0.258} \right) \left(\frac{w/h + 0.262}{w/h - 0.813} \right) \quad (2.1.2)$$

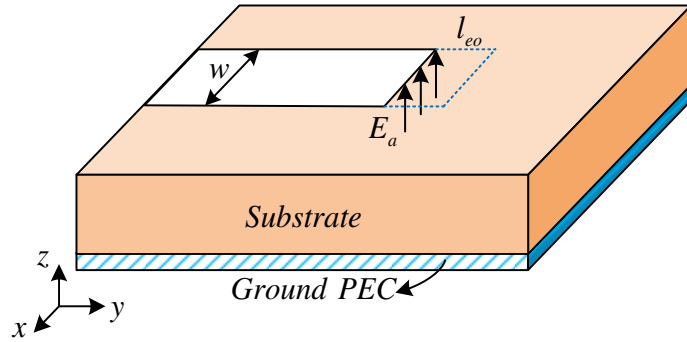


Figure 2.1.6: Open-ended microstrip line.

The three open stubs input impedances are expected to be high (ideally open circuit), the surface current density heat map, shows that the current is minimum at the input of the stubs as expected. Also, it can be noticed from Fig. 2.1.5 that this minimum current value is distributed almost uniformly over the input of the three stubs. Therefore, the dotted section in Fig. 2.1.5 can be approximated by a zero-length line, with the input impedance of the three stubs in parallel. Therefore, having the three stubs in parallel will divide their input impedance by roughly a factor of three. In addition, the other side of the stub (i.e., the T-Junction backside) is contributing to the radiation, and this is equivalent to a parallel impedance to the stub input impedance, and this will also reduce the input impedance further and ease up the matching. The whole structure can be approximated by the model shown in Fig. 2.1.7. Next step is to manifest the advantage of having a loop in the structure. The main idea is to maintain the loop length equal to an integer multiple of a half-guided wavelength to generate impedance resonances at the input. The upper and lower

horizontal sections are already half of a wavelength, where they act as 180° phase shifters to maintain the differential feeding. The length of the vertical sides is chosen to be one guided wavelength. Thus, the current directions in the left and right stubs are the same. Fig. 2.1.8 shows the vector field current distribution.

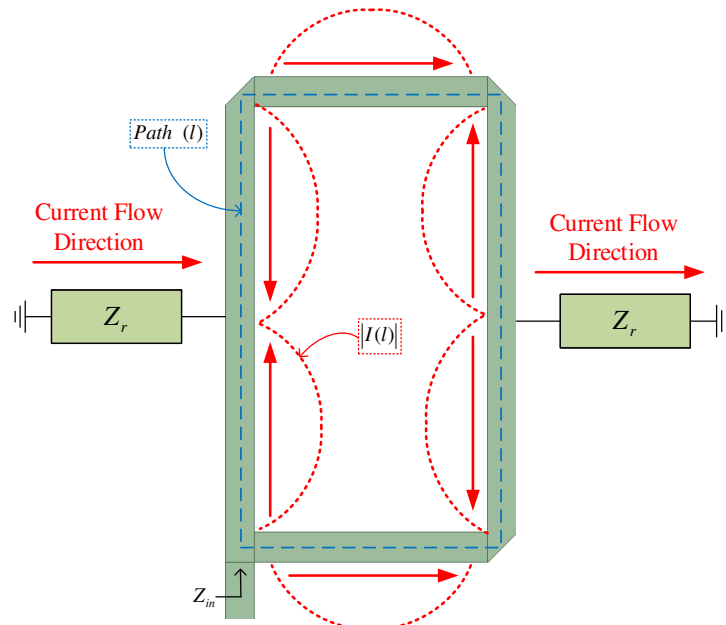


Figure 2.1.7: Approximated equivalent model of the proposed antenna.

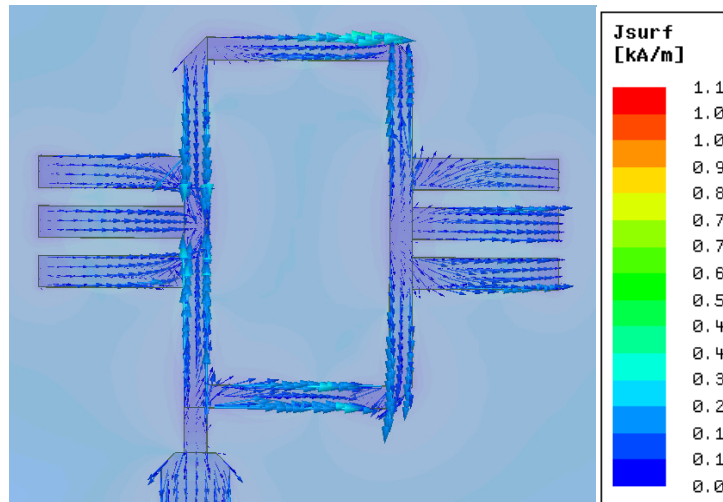


Figure 2.1.8: Vector field current distribution at 60 GHz.

By taking the ABCD-matrix (T-matrix) of each section in Fig. 2.1.7, the equivalent circuit shown in Fig. 2.1.9 can be obtained. Cascading all the T-matrices, an equivalent T-matrix can be obtained, as shown in Fig. 2.1.10, and the input impedance can be derived as follows:

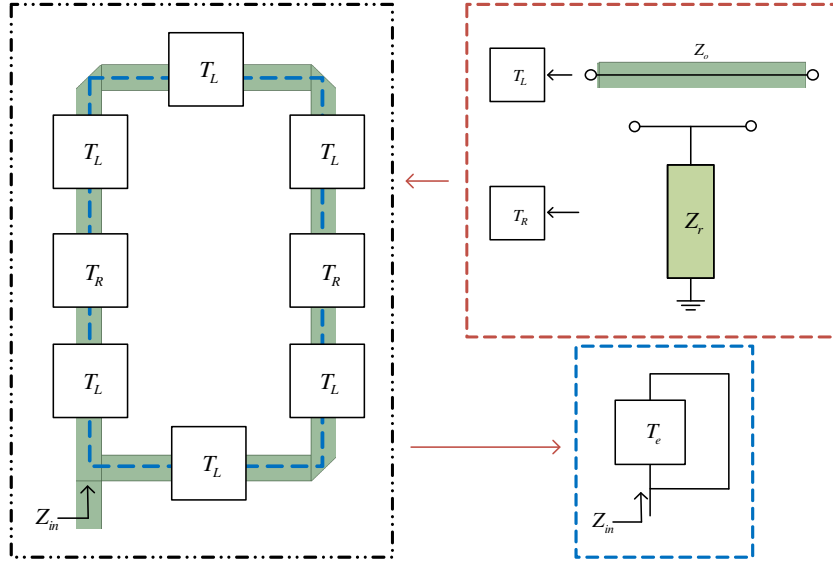


Figure 2.1.9: Equivalent T-(ABCD) matrix.

$$\mathbf{T}_e = \mathbf{T}_L \mathbf{T}_R \mathbf{T}_L \mathbf{T}_L \mathbf{T}_L \mathbf{T}_R \mathbf{T}_L \mathbf{T}_L \quad (2.1.3)$$

$$\mathbf{T}_R = \begin{bmatrix} 1 & 0 \\ Y_r & 1 \end{bmatrix}, \quad Y_r = Z_r^{-1} \quad (2.1.4)$$

$$\mathbf{T}_L = \begin{bmatrix} \cos(\beta l) & jZ_0 \sin(\beta l) \\ jY_0 \sin(\beta l) & \cos(\beta l) \end{bmatrix} \quad (2.1.5)$$

$$\mathbf{T}_e = \begin{bmatrix} A & B \\ C & D \end{bmatrix} \quad (2.1.6)$$

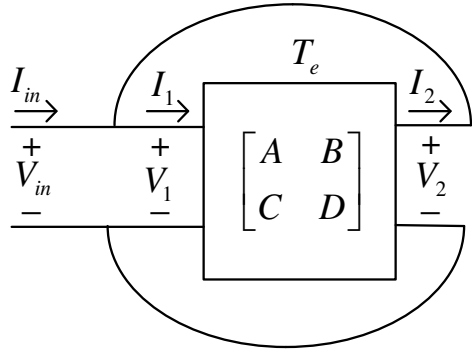


Figure 2.1.10: Evaluating input impedance from the equivalent T-matrix parameters

$$\begin{bmatrix} V_1 \\ I_1 \end{bmatrix} = \begin{bmatrix} A & B \\ C & D \end{bmatrix} \begin{bmatrix} V_2 \\ I_2 \end{bmatrix} \quad (2.1.7)$$

$$\begin{bmatrix} V_{in} \\ I_{in} + I_2 \end{bmatrix} = \begin{bmatrix} A & B \\ C & D \end{bmatrix} \begin{bmatrix} V_{in} \\ I_2 \end{bmatrix} \quad (2.1.8)$$

$$Z_{in} = \frac{V_{in}}{I_{in}} \quad (2.1.9)$$

And hence the input impedance can be written as:

$$Z_{in} = \left(C + \frac{(D-1)(1-A)}{B} \right)^{-1} \quad (2.1.10)$$

Also, by looking only at the center frequency, where;

$$l = \frac{\lambda_g}{2}, \quad \beta l = \pi \quad (2.1.11)$$

$$Z_{in} = \frac{V_{in}}{I_{in}} = \frac{Z_r}{2} \quad (2.1.12)$$

This simple analysis has two main significant observations. (1) The input impedance is half of Z_r , which is the main advantage of having the loop that takes a left and right open stubs impedance combination in parallel and divides the input impedance of the open stubs by two. This helps to

reduce the impedance to match the 50Ω , and basically, manifest the advantage of having a loop in the structure. (2) The input impedance can be easily obtained from (2.1.10). Fig. 2.1.11 shows the input impedance real and imaginary parts for various characteristic impedances for the loop microstrip line. It is noticeable that the quality factor is reduced (bandwidth is increased) by having a higher characteristic impedance of the loop microstrip line.

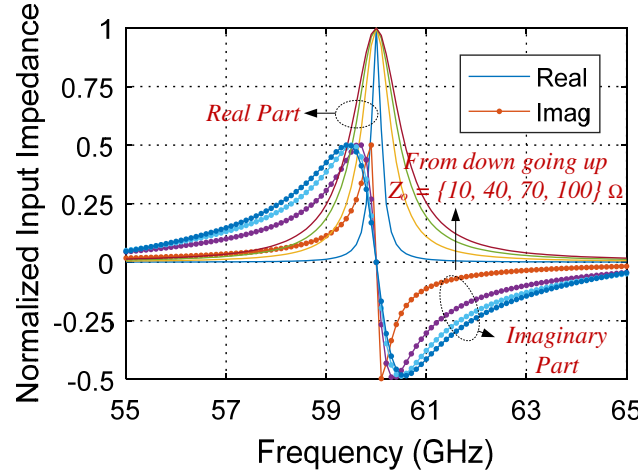


Figure 2.1.11: Calculated input impedance from equation (2.1.10)
“normalized to Z_{in} maximum.”

This analysis is not mathematically rigorous, neither it is accurate in determining the exact input impedance and quality factor due to the lack of accurate equivalent circuit models for each section at such high millimeter-wave frequencies. Those equivalent models ignore various effects, such as the losses due to the substrate surface waves, the mutual coupling between the open stubs, the radiation losses in the loop bends, and most importantly the T-junctions, and open-end exact radiation resistance. Despite this fact, the model is beneficial and very sufficient from an antenna designer's perspective to determine the resonance frequency, tune, optimize and match the antenna properly with the aid of a full-wave solver such as HFSS. The model makes it easy to design such an antenna.

2.1.2 Simulation and Experimental Results for the Proposed Structure

Fig. 2.1.12 shows the proposed antenna structure prototype. Rogers-Duroid 5880 (0.254 mm thickness) substrate is used. The substrate loss tangent is 0.0009. The size of the connector is massive compared to the antenna size. Introducing such a connector for the sake of measurement distorts the radiation pattern, therefore longer feeding microstrip line is used to feed the antenna to reduce the connector effect on the antenna pattern. The extended feeding line introduced higher losses and more surface waves in the substrate. Fig. 2.1.13 shows S_{11} and the realized gain of the antenna versus frequency for both simulated and measured values. Good agreements are observed. A 3.6% relative bandwidth (10 dB return loss bandwidth) is achieved, which is equivalent to 2.2 GHz of bandwidth. Fig. 2.1.14 shows the radiation patterns (both E- and H-plane). The maximum realized gain is 11.5 dBi. The 3dB beam-width is 30° in the E-plane, and 60° in the H-plane. It is important to note that the connector with long feeding line exists only for measurement purposes. However, in the practical integrated system, the antenna is to be connected directly to the next circuitry stages, which could usually be a bandpass filter or an amplifier. Thus, such adverse effects of the connector can be mitigated.



Figure 2.1.12: Photo of the proposed narrowband antenna,
the microstrip line feed length is 21 mm.

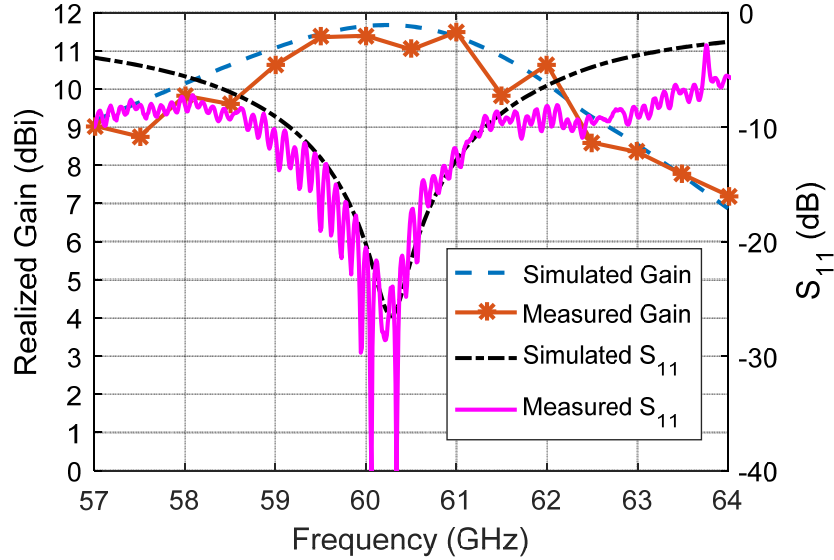


Figure 2.1.13: Realized gain, and S_{11} of the proposed antenna.

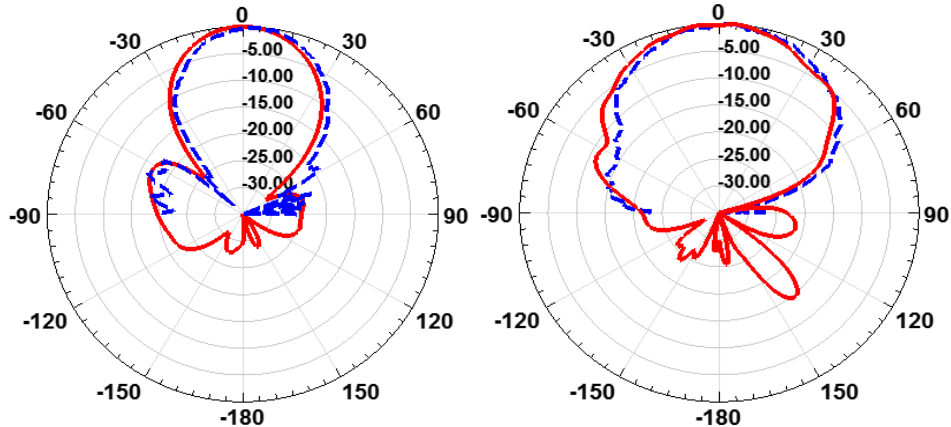


Figure 2.1.14: Principal planes radiation patterns, E-plane {Left}, and H-plane {Right}, solid {Simulated}, dashed {Measured}.

2.1.3 Bandwidth enhancement

One related feature of the proposed antenna structure is its narrow matching bandwidth, and this stems from the high-quality factor introduced by the radiation mechanism of a magnetic current close to PEC. To overcome the limitation of the narrow matching bandwidth, one can think of increasing the substrate thickness in order to reduce the quality factor. However, the price would

be increased surface waves, and losses. Also, the higher level of surface waves, would distort the radiation pattern, and interfere with other circuitry on the same substrate, and would even interfere with the feeding structure of the antenna. Another recommended way to enhance the matching bandwidth is by adding more impedance resonances within the band of operation. In this structure, the open stubs are half wavelength, and the loop is multiple of half wavelengths of the center frequency. Therefore, the structure can resonate at multiples of the center frequency. However, those resonances are far from each other. Also, the structure can resonate when the stubs are quarter of a wavelength. By increasing the number of stubs, the loading impedance of the stubs would differ, and other resonances exist. In such a way, those resonances can be close to each other and lie in the same band of interest. Fig. 2.1.15 shows the modified structure to obtain a broad matching bandwidth. It is worth noticing that by modifying the number of stubs, the mutual coupling between the lines, and their loading impedance to the loop would vary and consequently the input impedance would differ. It is crucial to emphasize that providing a parametric study of the number of stubs with different loop lengths is not quite fair, as it would result in different input impedances. Therefore, the loop length, the phase shift between the left and right stubs, and the length of the stubs were tuned simultaneously to maintain the proper radiation pattern and the required input impedance within the band of interest.

Fig. 2.1.16 shows the input impedance real and imaginary parts, as can be seen, the real part is averaged around 50 ohms, and the imaginary part is averaged around zero. Fig. 2.1.17 shows the electric field heat map of the proposed wideband structure. Fig. 2.1.18 shows the fabricated prototype. The corresponding S_{11} and realized gain versus frequency, for both measured and calculated values, are shown in Fig. 2.1.19. The antenna is covering the band from 57 to 64 GHz (11.67%), with a realized gain of 11 dBi. Fig. 2.1.20 shows the principal planes radiation patterns, both measured and simulated.

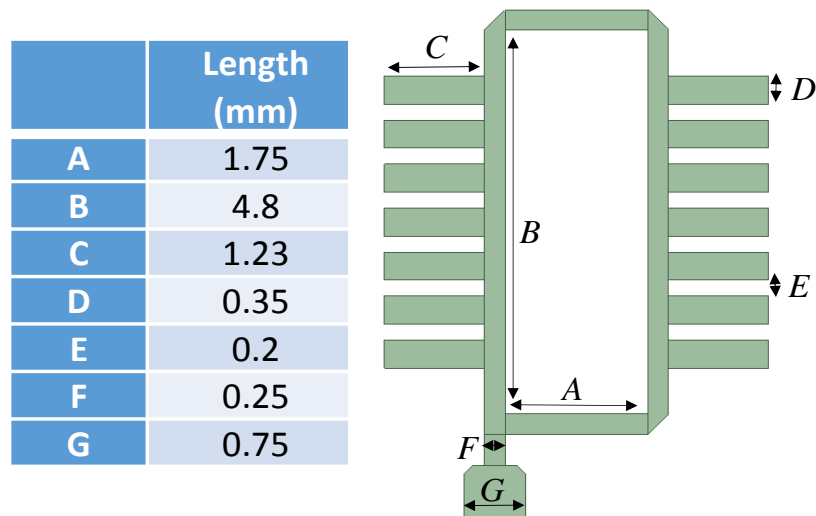


Figure 2.1.15: Proposed wideband antenna structure.

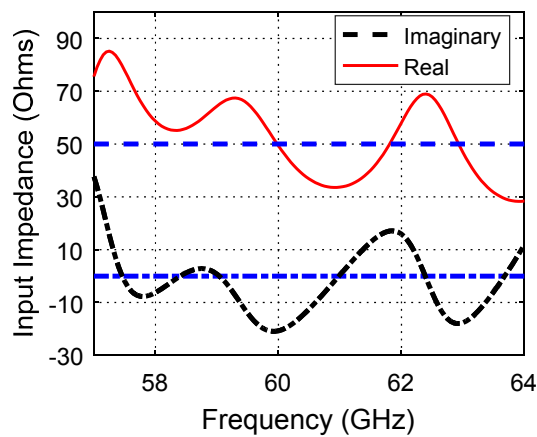


Figure 2.1.16: Proposed wideband antenna structure input impedance.

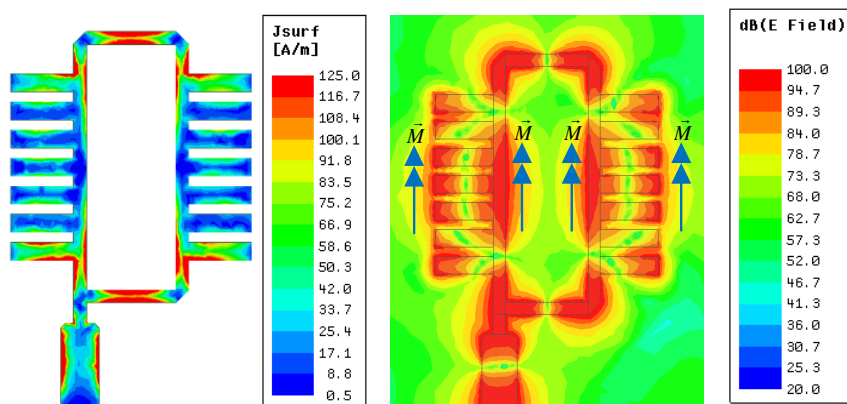


Figure 2.1.17: Electric field intensity and surface current density heat maps at 60 GHz.



Figure 2.1.18: Proposed wideband antenna structure actual prototype.

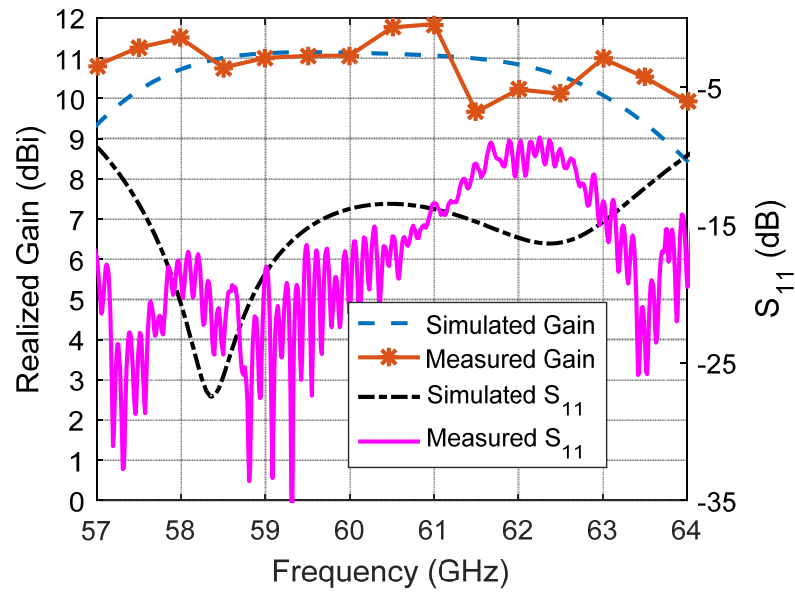


Figure 2.1.19: Proposed wideband antenna structure realized gain and S_{11} (dB).

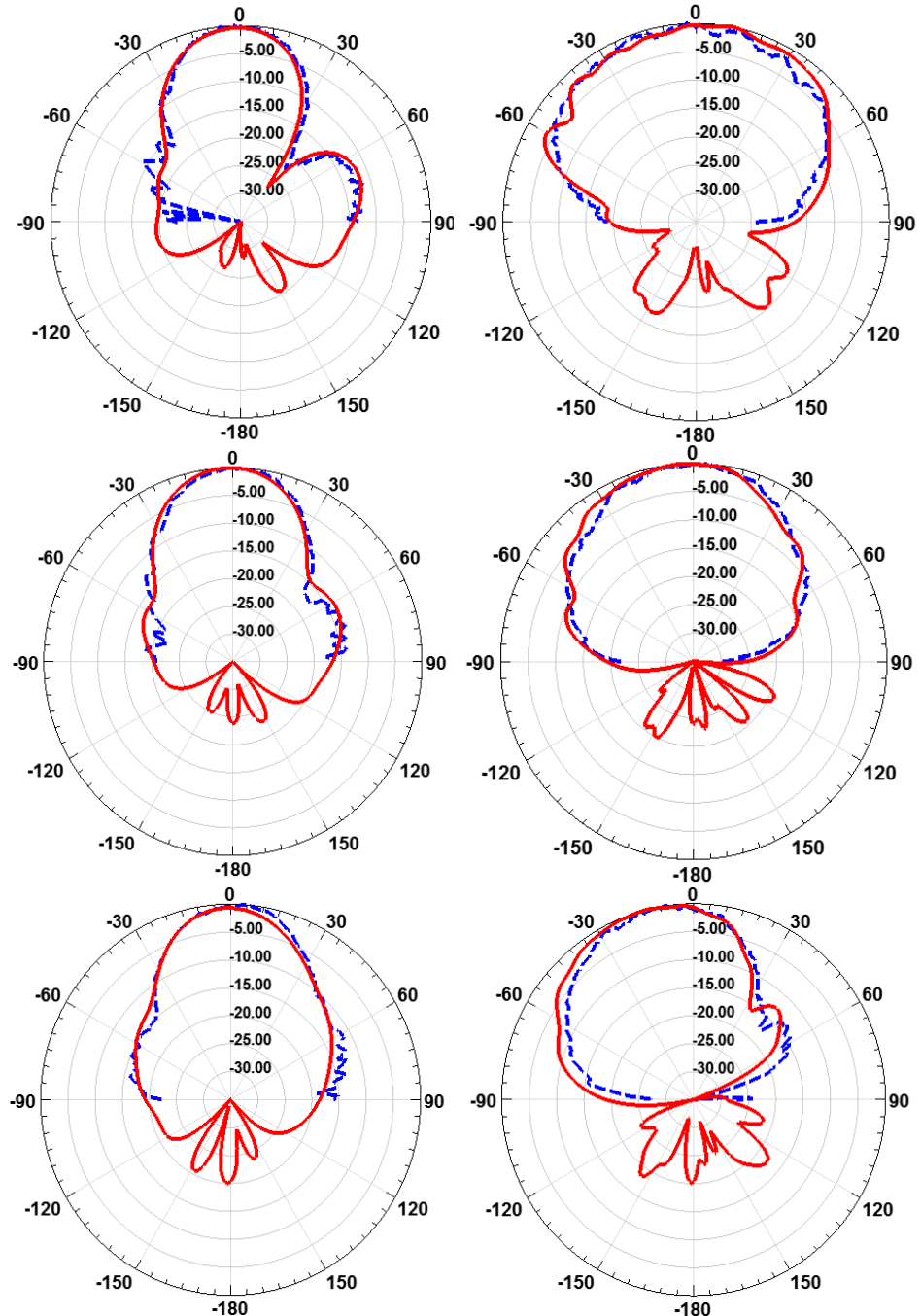


Figure 2.1.20: Principal planes of the wideband antenna at (57, 60, and 63 GHz) from top to bottom, E-plane {left}, H-plane {right}, dashed lines {measured}, and solid lines {simulated}.

2.1.4 Linear antenna array

The proposed antenna structure can be employed in a linear antenna array, with a center to center distance ($D > \lambda_o/2$) between adjacent elements, without generating grating lobes. Fig. 2.1.21 shows the proposed linear antenna array. The center to center distance between the array elements is 7.2 mm (i.e., $1.44\lambda_o$), where the free space wavelength at 60 GHz is 5 mm. This feature of this element is advantageous in a way that reduces the mutual coupling between the elements and feeding lines. Also, it provides further flexibility in the design of the feeding network. The idea originates from the nature of each element, where each element can be thought of as having four magnetic current elements, as shown in Fig. 2.1.22. And therefore, each element can be considered as a subarray, and the distance between the adjacent magnetic current elements satisfies the rule of thumb ($D < \lambda_o/2$), and hence, prevent the generation of grating lobes. Fig. 2.1.23 shows that the mutual coupling between the array elements is less than -30 dB. Fig. 2.1.24 shows S_{11} , and the boresight realized gain vs. frequency, for both calculated and measured values, good agreement is observed.

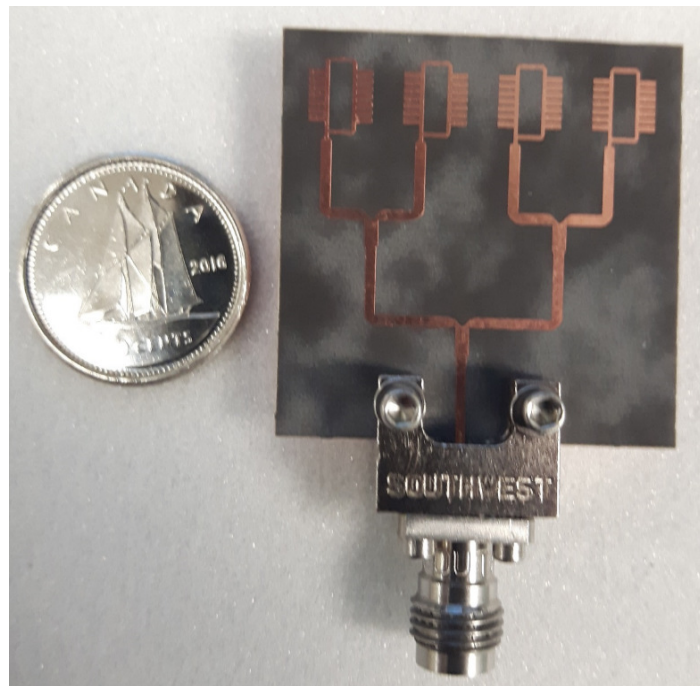


Figure 2.1.21: Four-element linear antenna array structure.

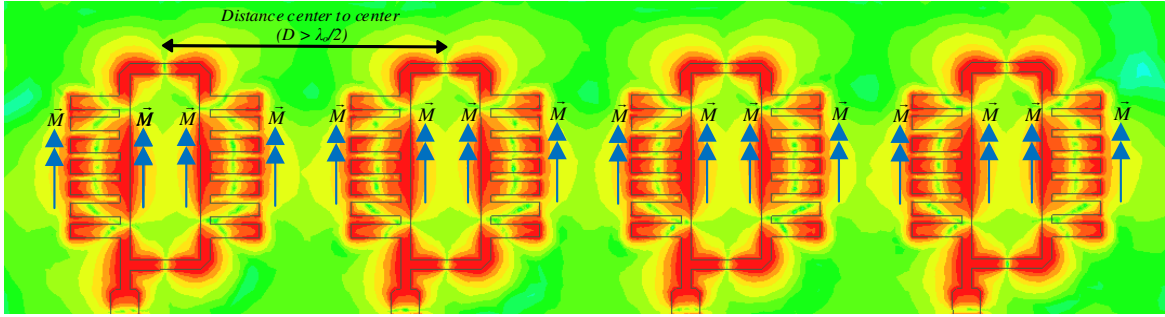


Figure 2.1.22: Four-element linear antenna array structure electric field intensity heat map (Scale is the same as in Fig. 2.1.17, center frequency is 60 GHz).

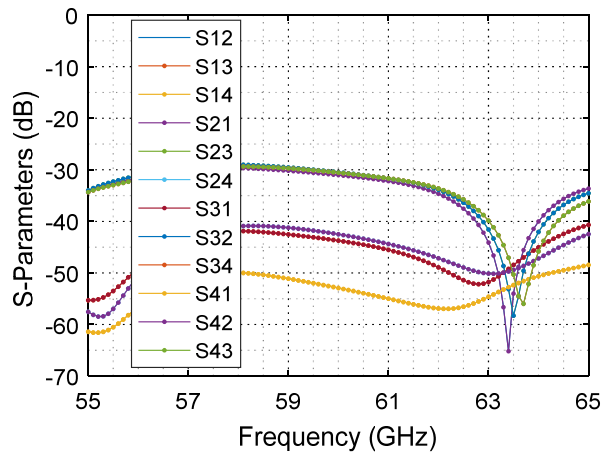


Figure 2.1.23: Mutual coupling between array elements (ports are assigned (1 to 4) from left to right for the elements shown in Fig. 2.1.22).

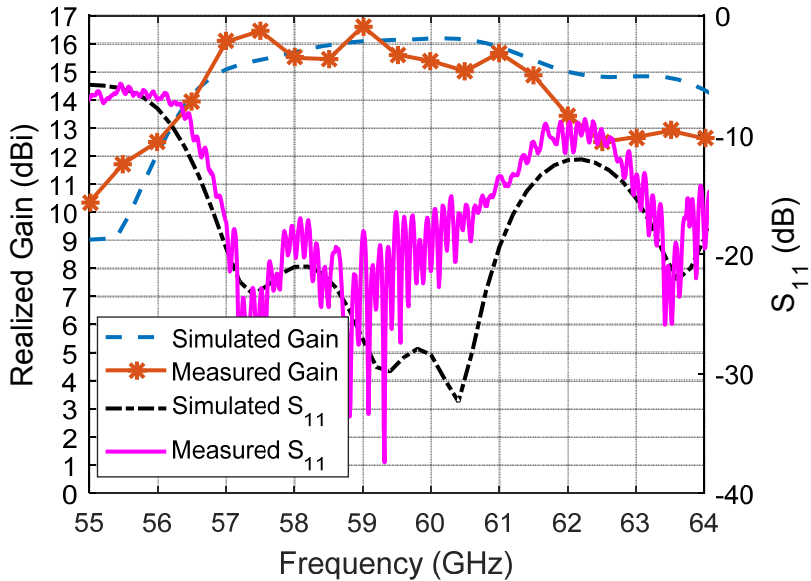


Figure 2.1.24: Antenna array structure realized gain and S_{11} (dB).

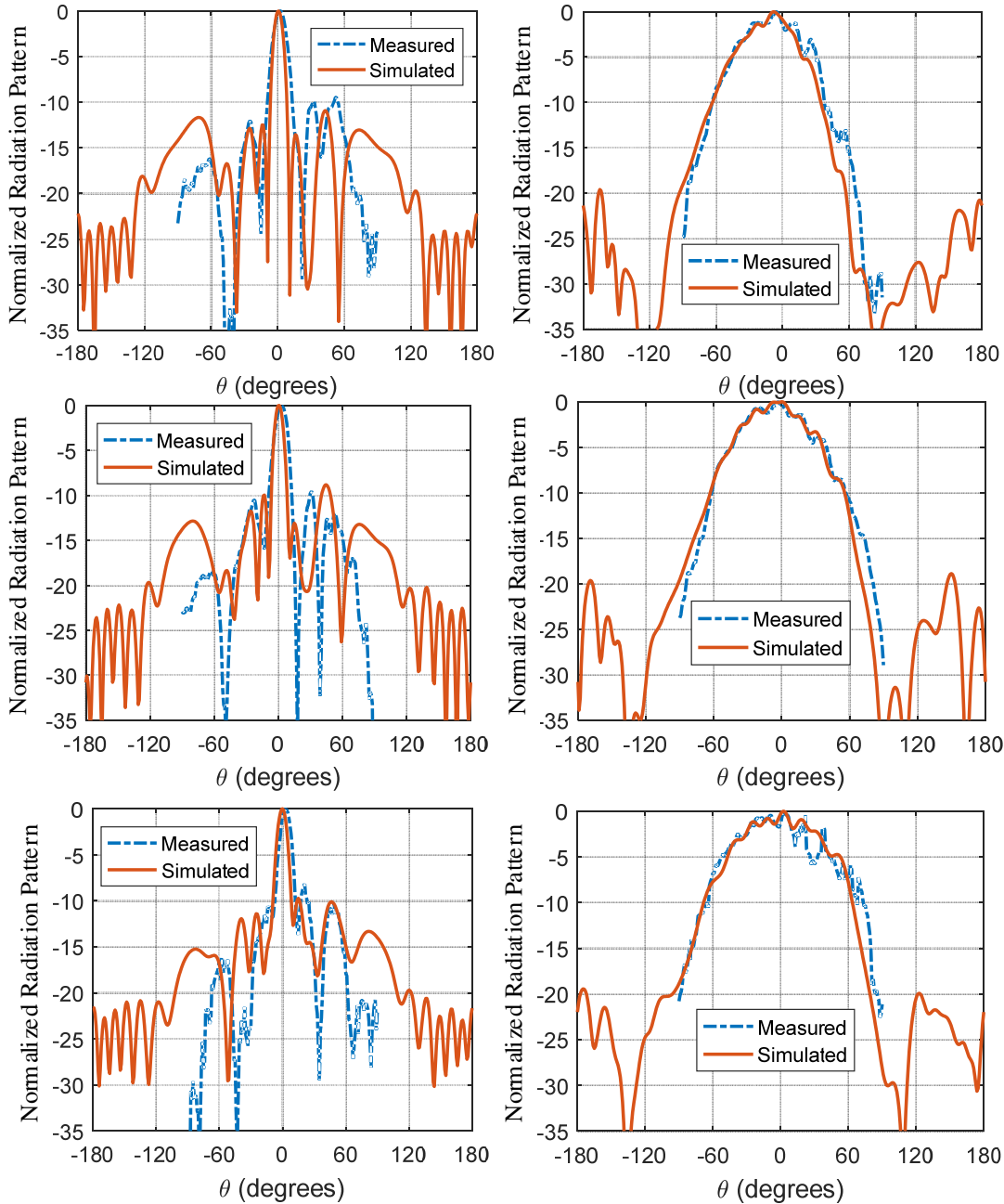


Figure 2.1.25: Principal planes of the linear antenna array at (57, 59, and 61 GHz) from bottom to top, E-plane {left}, H-plane {right}, dashed lines {measured}, and solid lines {simulated}.

Fig 2.1.25 shows the principal planes of the array, as observed, there are no grating lobes. Fig 2.1.26 shows the electric field distribution heat map that indicates a significant amount of surface waves produced by the feeding network, which reflect on the gain with more losses, and distortion of the radiation pattern. In addition, the connector has a considerable effect on the radiation pattern. Fig 2.1.27 demonstrates the effect of the feeding network and connector on the radiation pattern,

but the performance is still acceptable. Some minor asymmetry is noticed in the principal planes due to the offset feeding of the element from the left side instead of the center.

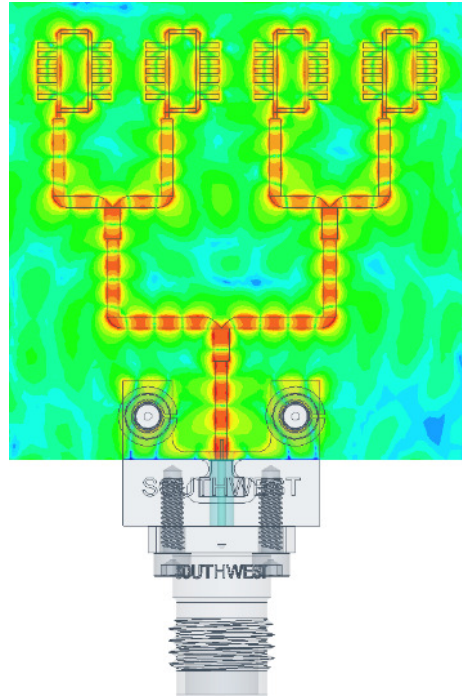


Figure 2.1.26: Four-element linear antenna array feeding network electric field intensity heat map (Scale is the same as in Fig. 2.1.17).

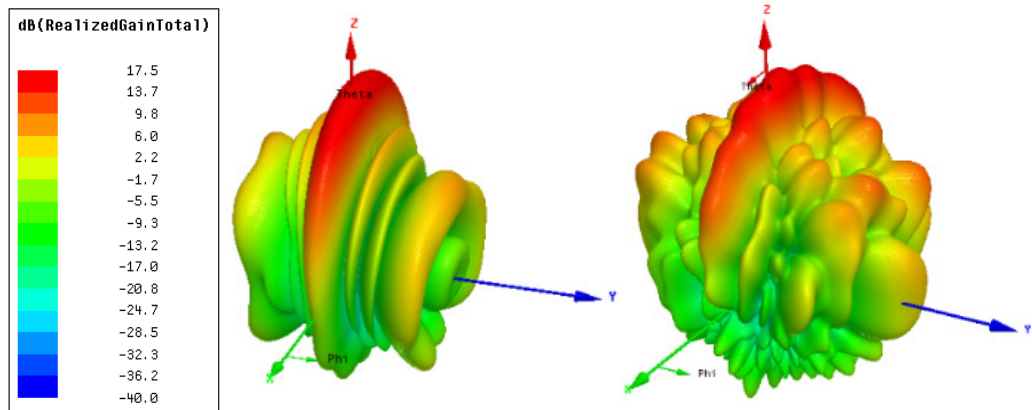


Figure 2.1.27: Antenna array 3D total realized gain radiation pattern, ideal case {left}, connector and feeding network effect {right}.

Antennas realization and characterization at millimeter-wave frequencies is very challenging; this is mainly due to the small physical dimensions of the structure, which requires high precision fabrication process. Such physical dimensions are very susceptible to tolerance errors. Also, the excitation method of the antenna is very critical, as using a large metallic connector near the

radiating structure acts as a large scatterer in the proximity of the antenna environment. Therefore, the induced currents on the connector body interact with the mounting structure and the surrounding measurement apparatus (i.e., parts not covered with absorbers). Such interaction is not considered in the simulation. Therefore, as observed from the measured gain values for the proposed structures, the measured gain fluctuates within ± 1 dB uncertainty around the simulated gain values at some frequencies. Also, as some frequencies have better-measured matching values over others, the measured gain values are relatively higher at those frequencies.

In the linear antenna array radiation patterns, some asymmetry, and some relatively high sidelobe levels are observed at $\pm 70^\circ$; this is attributed to the contribution of the surface waves, edge diffractions, and undesired radiation from the feeding network. Fig. 2.1.26 heat map shows the substrate surface waves. Also, the discrepancy between the measured and simulated sidelobe levels in the linear array radiation pattern is attributed to some tolerance in the uniformity of the thin etched substrate, as seen in Fig. 2.1.21, some areas in the substrate have a bright gray color compared to other regions, and this would introduce some measurement errors for the predicted surface waves, and edge diffractions. This explains why the single element radiation pattern measurement accuracy is better than the array. In such a way, the substrate area is minimized for the single element. Nonetheless, the tolerance and experimental errors are still within an acceptable range, which satisfies the high-performance operation of the proposed structure at such high frequency.

Fig. 2.1.28 compares the calculated efficiencies of the proposed structures within the band of operation, as can be observed, high efficiency of around 98 % is achieved.

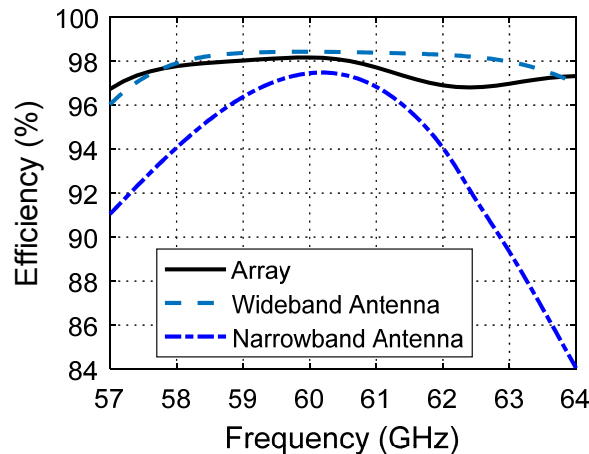


Figure 2.1.28: Efficiency of each structure.

2.2 Highly Efficient Unpackaged 60 GHz Planar Antenna Array

2.2.1 Introduction

In section 2.1, an antenna element that utilizes the microstrip line discontinuity radiation in a constructive way to create an efficient high gain antenna was designed [39]. The structure only used a single dielectric substrate that eases the manufacturability and hence reduces the cost. Also, as the element structure can be perceived as being comprised of four magnetic current elements, the element can be employed in a linear antenna array with elements of center to center separation greater than a free space wavelength with suppressed grating lobes [39]. Such feature of the antenna element can significantly relax the design of the array feeding network. In section 2.1, a linear antenna array fed by a parallel microstrip feeding network was implemented at 60 GHz. However, the open microstrip line feeding network suffered from significant radiation losses. In this section, we investigate the design of a 4x4 high gain antenna array with an efficient feeding network. Where we show that the element proposed in section 2.1 is highly efficient and can be used in several planar array configurations such as series and parallel feeding networks and their combination in a way that even the feeding network does not provide significant losses as one is expecting at these frequencies.

At millimeter-wave frequencies, having a packaged guiding structure is highly desirable to eliminate any possible radiation losses that reduce the antenna efficiency and affect the radiation characteristic of the antenna. Hence, it maintains the radiation characteristics of the antenna only. Packaging, or shielding, in other words, is usually done by surrounding the feeding structure by a metal surface. For a planar feeding network, this can be done by shielding the feeding network from the top and bottom by metal sheets. Such a method is useful for suppressing the radiation from the feeding network. However, such method is undesirable due to the excitation of parallel plate waveguide modes within the shielded package, which eventually constitute a significant source of losses in the feeding structure. Ridge gap waveguide is an example of a new technology that treats such a problem and prevents the propagation of parallel plate waveguide modes [42]. Ridge gap waveguide employs electromagnetic bandgap (EBG) periodic structures, such as Sievenpiper mushroom cells [43], to create the EBG.

2.2.2 Array Feeding Network Study

Fig. 2.2.1 shows the geometry and parameters of a unit cell of the periodic structure. Fig. 2.2.2 shows its corresponding two-dimensional dispersion diagram covering the irreducible Brillouin zone of the cell (Γ is $k_x = 0, k_y = 0$; X is $k_x = \pi/p, k_y = 0$; M is $k_x = \pi/p, k_y = \pi/p$; where k_x and k_y are the wavenumbers in the x and y directions, and “ p ” is the period). The cell is designed to provide the EBG centered at 60 GHz with a bandwidth of 26 GHz (i.e., from 50 to 76 GHz). In [42], a printed ridge gap waveguide (PRGW) with facilitated design properties is proposed. In [44], a similar concept was implemented using a classical ridge gap waveguide and was referred to as an inverted microstrip line. The PRGW in [42], facilitates the design procedure because the guideline lies in a separate layer without a need of plated vias (different level from the textured periodic surface). As such, curved lines can be designed easily once compared to the classical RGW, where the guideline is located on the same surface of the mushroom patches and must be grounded by conducting vias. A detailed discussion of the pros of the structure is provided in [42].

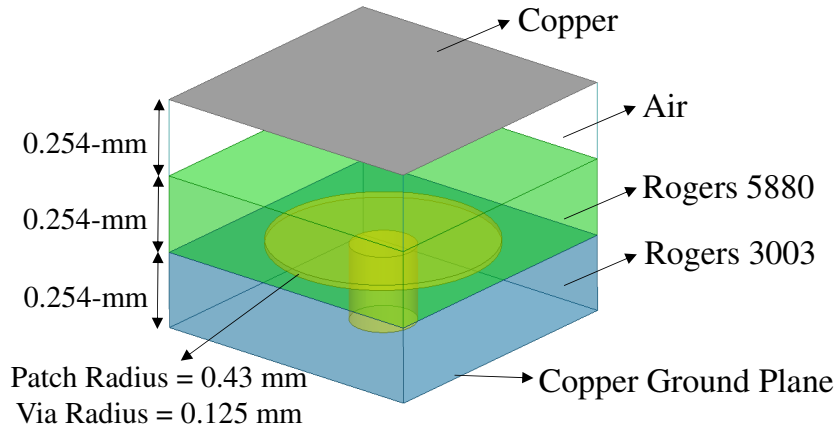


Figure 2.2.1: EBG mushroom cell dimensions.

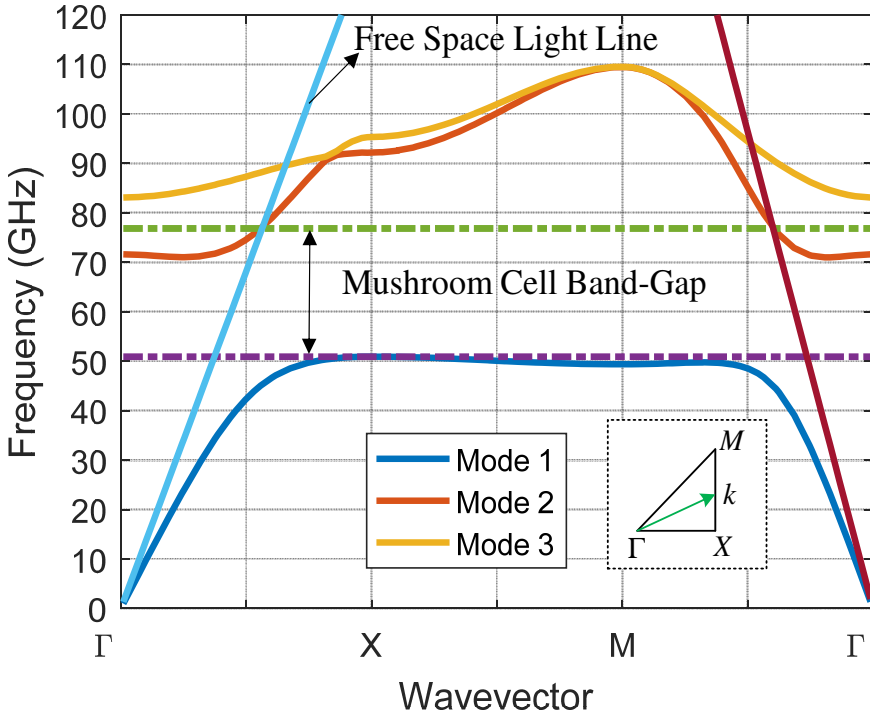


Figure 2.2.2: Dispersion diagram of the Sievenpiper mushroom cell.

Fig. 2.2.3 shows a section of the printed ridge gap waveguide Fig. 2.2.4 shows its corresponding dispersion diagram. A Quasi-TEM mode is excited as expected within the bandgap. A feature of the ridge gap structure is that the guiding bandwidth is a little less than the cell bandgap [42].

Fig. 2.2.5 shows the complete structure of the PRGW antenna array. The elements are arranged to provide boresight radiation by differentially feeding each pair; such an arrangement reduces the cross-polarization level significantly. As shown in Fig. 2.2.5, the left and right side of the array are combined with the PRGW power combiner. Such a packaged solution prevents radiation from this part (power combiner/divider) and any interference with the radiating array. It should be stated that the line widths of the power combiner/divider are different from those of the open microstrip lines, but with the same characteristic impedances.

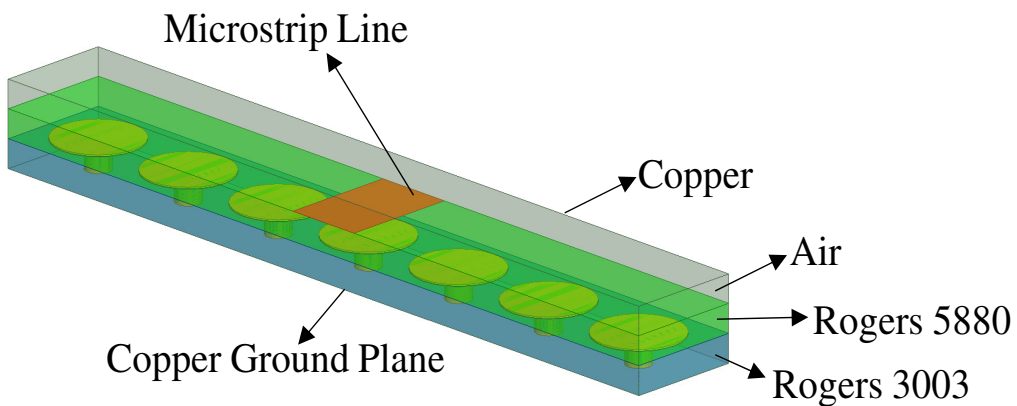


Figure 2.2.3: Printed ridge-gap air microstrip line.

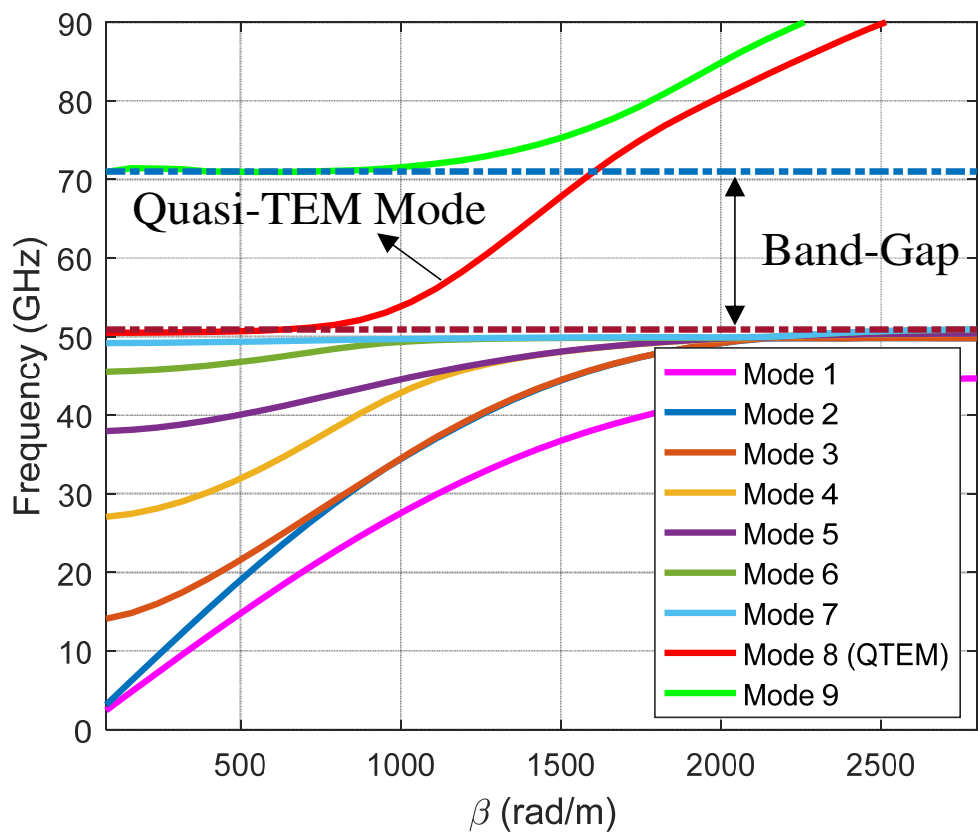
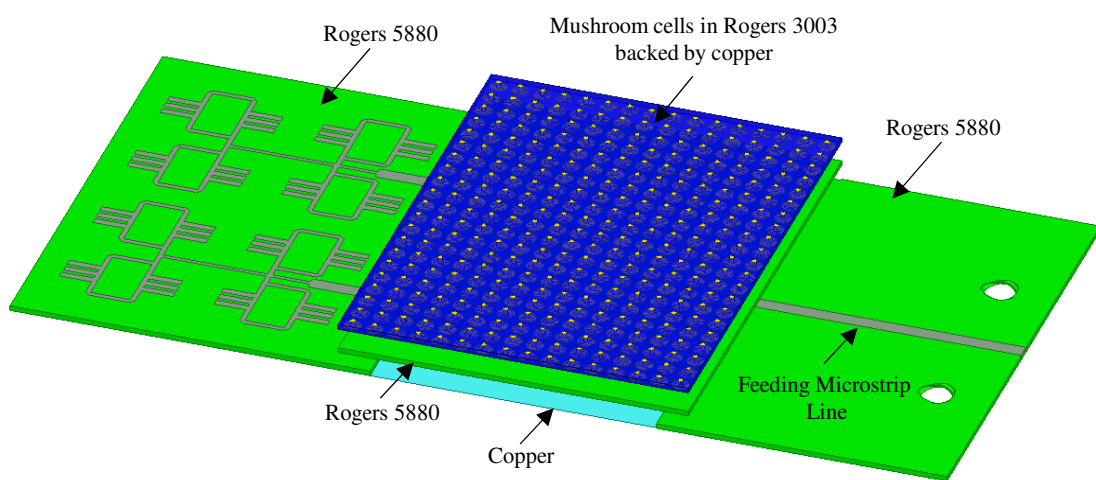
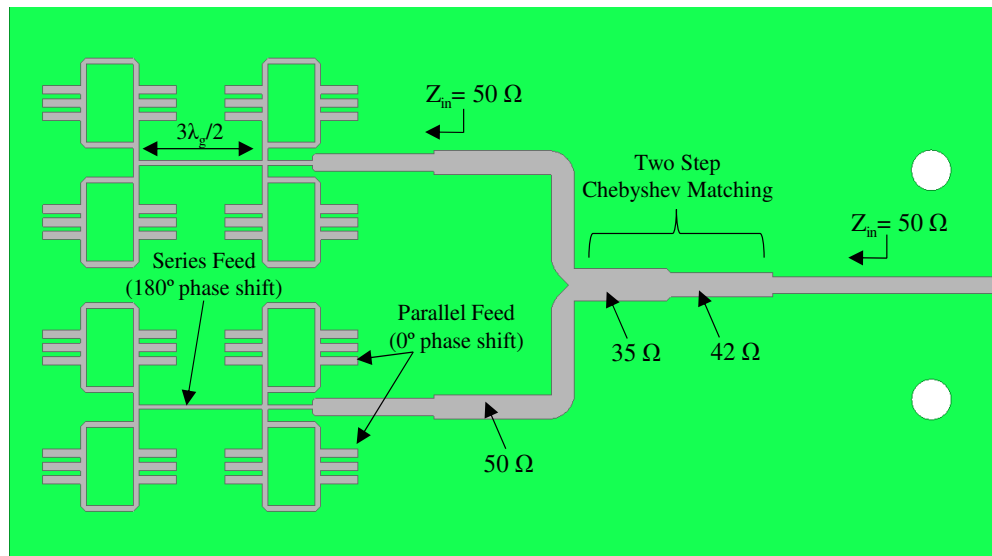
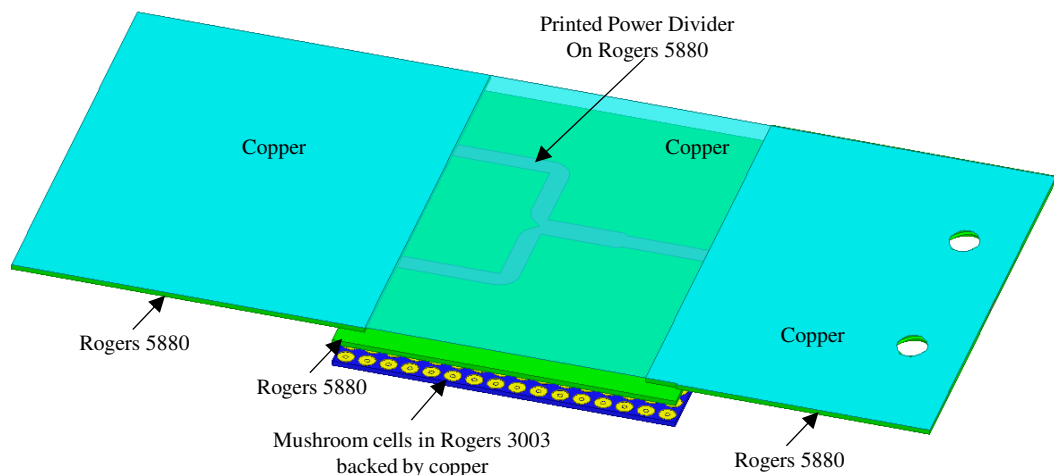


Figure 2.2.4: Printed ridge-gap air microstrip line dispersion diagram.



[Top View]



[Bottom View]

Figure 2.2.5: Antenna array fed by PRGW power divider.

The second feeding network is the same as the above, but its power combiner is made entirely from the same conventional microstrip line feeding the array. Therefore, all the feeding network is an unpackaged open microstrip line network. As the radiating elements section is identical in the two cases, and by guaranteeing that the two structures have equally appropriate matching levels at the main feeding point, the difference in the efficiencies of the two structures indicates the losses level of the feeding network. Since the same type of material is used in both designs, it can be inferred that conduction and dielectric losses are the same. On the other hand, it is well known that packaged PRGW feeding eliminates both surface-waves and radiation losses. However, in open microstrip line technology, such losses can't be avoided. Therefore, studying the PRGW solution is essential to have a reference point regarding the losses attributed to radiation and surface-waves from the feeding network of an open structure. Similar to the PRGW structure, the packaged structure is shown in Fig. 2.2.6. In this case, the feeding network is covered with a mushroom cell layer acting as an AMC (Artificial Magnetic Conductor). The cell size is redesigned with the dimensions shown to operate within the required band. The signal propagates in the air in the PRGW, but it propagates in the dielectric substrate in the packaged solution. Therefore, a higher level of losses is expected in the packaged case due to the dielectric losses. Another difference in the packaged solution is that the signal propagates in the same substrate. Hence, the change in the width of the line is very negligible once compared with the conventional open MSL case. Table 2.2.1 shows the line widths at 60 GHz for the proposed cases.

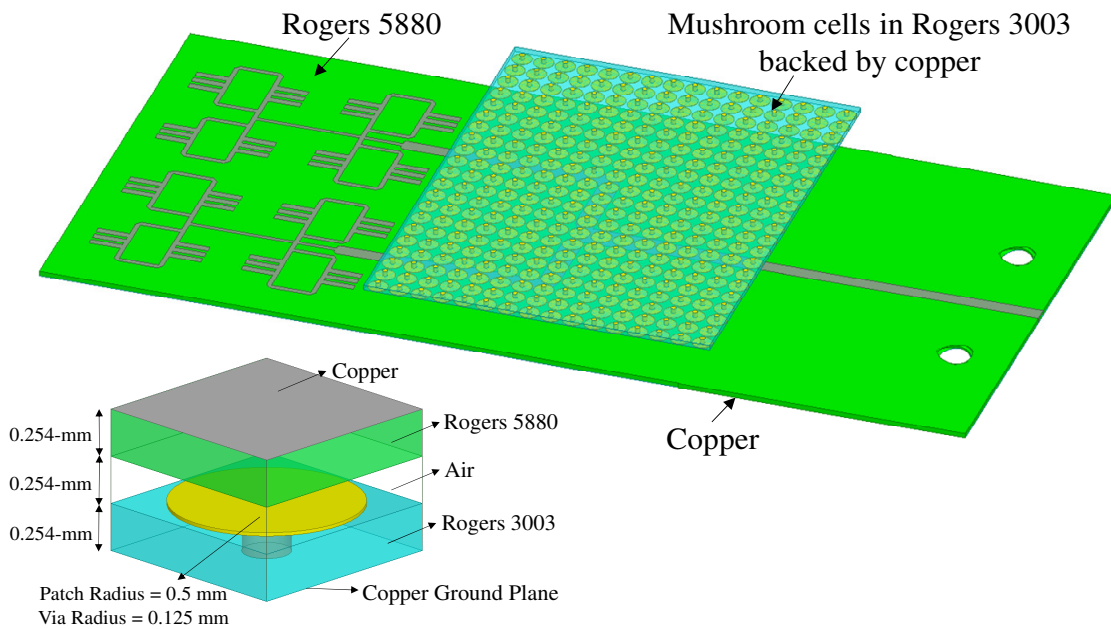


Figure 2.2.6: Antenna array fed by packaged microstrip line power divider.

Table 2.2.1: Line width for different characteristic impedances

Z_0	MSL	PRGW	Packaged
35Ω	1.3 mm	1.7 mm	1.3 mm
42Ω	1 mm	1.4 mm	1 mm
50Ω	0.78 mm	1.05 mm	0.78 mm

As shown in the array structure, two elements are fed in parallel, and the other combined two elements are fed in series. The length of the series feed is $1.5\lambda_g$. This length maintains a 180° phase shift between the feed points. The 180° phase shift at the feed is required to counter the effect of physically flipping the element 180° . Also, the $1.5\lambda_g$ feed maintains one free-space wavelength between the elements. It is clear that the radiating element possesses a high directive nature that allows relaxing the distance between the radiating elements and thus relaxing the feeding network design as well as suppress the grating lobe level. It is worth mentioning that series fed always poses bandwidth restriction in terms of the radiation pattern stability, as the phase shift between elements vary with frequency and hence steer the main beam [26], [37], [38]. However, within a narrowband such effect can be ignored, which is in line with the proposed case.

Fig. 2.2.7 shows the matching bandwidth, and the corresponding realized gain for the three cases, a boresight gain of 20.5 dBi is achieved for the PRGW solution, and the corresponding 10 dB return loss matching bandwidth is almost 3.66% (i.e., 2.2 GHz). The narrow bandwidth is attributed to the high-quality factor and correspondingly narrow bandwidth of the radiating element [39]. The conventional unpackaged microstrip line power divider feeding network is lower in terms of its realized gain level once compared with the PRGW solution; this is expected and attributed to the radiation and surface-wave losses from the open MSL power divider. The packaged solution realized gain level lies in-between the open and the PRGW cases. The packaged solution suffers from additional dielectric losses due to the propagation in the dielectric medium and not air as in the PRGW case. It can be noticed that above 60 GHz, the PRGW has a lower level of matching, which deteriorates the realized gain level. Therefore, the comparison is reasonably drawn only at the center frequency (60 GHz) where all the cases have sufficient matching level.

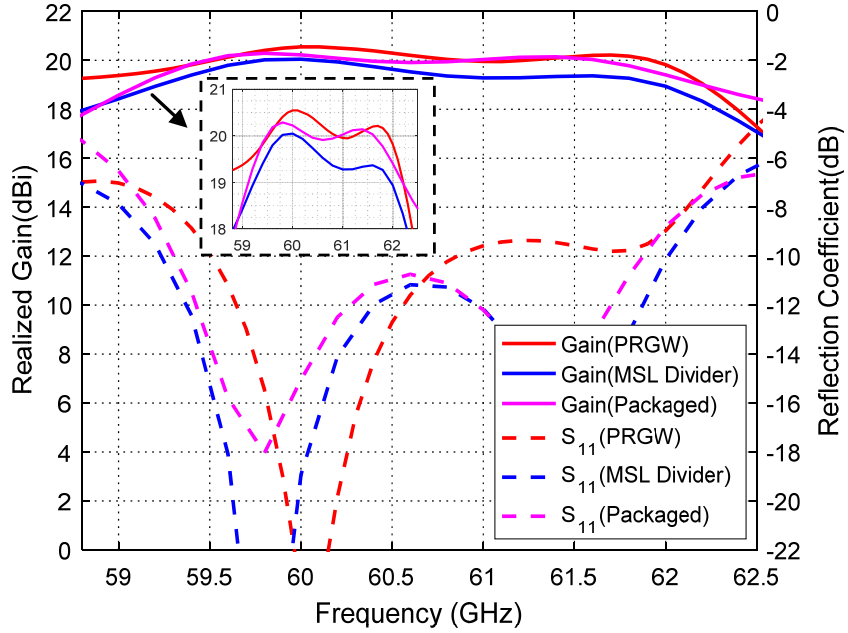


Figure 2.2.7: Realized gain and reflection coefficient for the proposed cases.

PRGW as many packaged solutions necessitates the use of plated vias, those plated vias require a special process to be realized and consume considerable fabrication time. Therefore, the low cost and simplicity features of the open structure solution are obviously spotted once compared with PRGW or other packaged solutions (where it only needs a single substrate layer with no vias). This feature makes it even more desirable for integration purposes. This consequently raises the question, can open microstrip line technology be used with minimal compromise on efficiency and performance? Here, the power divider is eliminated by aggregating all the elements of the configuration shown in Fig. 2.2.8. The typical procedure to design a feeding network for a 2D-array is by using power dividers and quarter wavelength transformers to match the parallel combination of the antenna elements to the desired system impedance. This procedure usually results in transmission lines with different characteristic impedances. Due to the limited space between the antenna array elements, the wide microstrip lines cannot be accommodated, especially in the aggregated configuration shown in Fig. 2.2.8. As an example, in Fig. 2.2.8 the width of the line that can fit between two radiating elements is constrained by the separation distance between them, such distance is fixed by the array design to reduce the grating lobes. Moreover, wide

microstrip lines can have significant radiation effects. Therefore, the feeding network design procedure proposed in Fig. 2.2.8 can provide the required matching impedance by using any arbitrary characteristic impedance. As the procedure is illustrated in Fig. 2.2.8, and by the use of simple transmission line theory, the input impedance at point “A” will always be equal to Z_L as long all the lines (i.e., l_1 , l_2 , and l_3) are multiple of an odd integer of the guided quarter wavelength.

From Fig. 2.2.8, it can be seen that flipping the radiating elements along the y-axis does not require 180-degree phase shift feed to maintain boresight radiation; this is due to the fact that the currents can still run through the open stubs in the same direction as shown in Fig. 2.2.8. Also, the extended distance feature provided by the elements in the E-plane (i.e., along the x-axis) [39], eases off the layout of the feeding lines between the radiating elements.

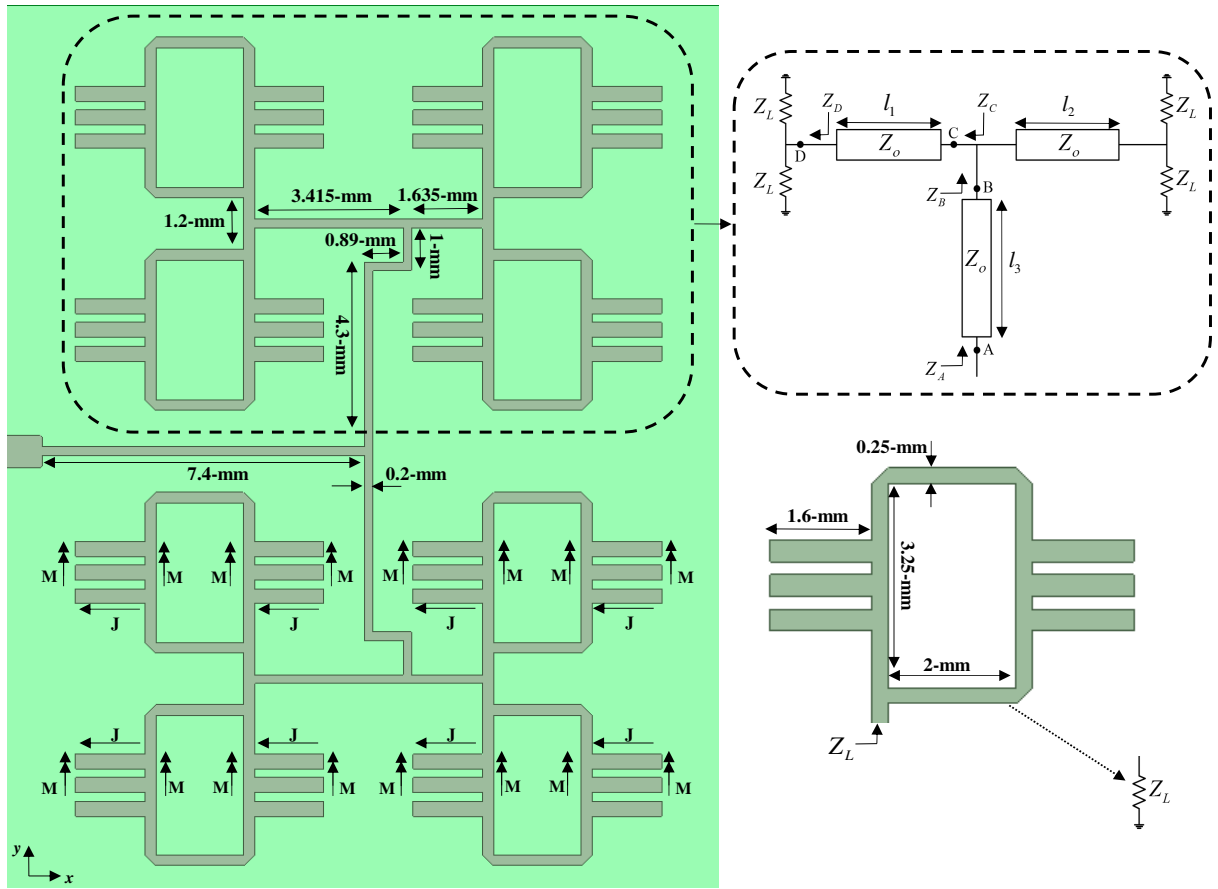


Figure 2.2.8: Antenna array with aggregated open microstrip line feeding network, (the distance from the center of the array to the end-launch connector is the same for all cases. The feed line is only cropped in this figure).

Fig. 2.2.9 shows the electric field heat map, a strong interaction between the feed lines and the antenna array elements due to their proximity is observed. Such strong interaction implies that the proper feeding structure of the array should be designed and tuned simultaneously with the presence of the antennas.

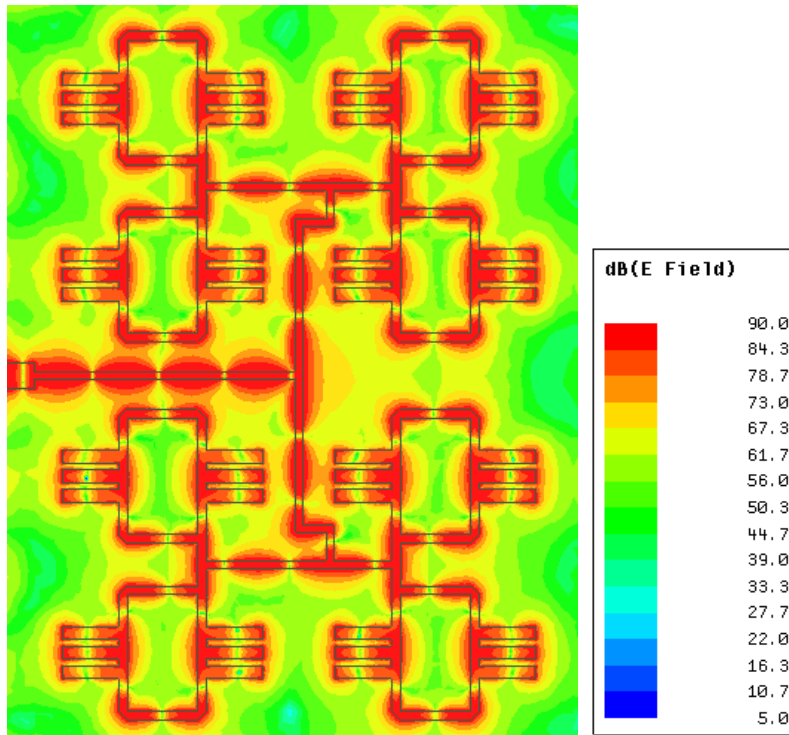


Figure 2.2.9: Electric field heat map for the aggregated open microstrip line feeding network of the antenna array at 60 GHz.

The aggregated proposed design in Fig. 2.2.8 is modular, where the dotted configuration can be reused, and the array can be expanded and doubled easily. Very narrow lines can fit between the radiating elements easily as the matching procedure is independent of the characteristic impedance of the lines. Moreover, the proposed aggregated configuration can reduce the area of the whole array by almost half, where the area needed to accommodate the power dividers has been eliminated by embedding it between the elements. Hence, providing a more compact design. Fig. 2.2.10 shows the matching bandwidth of the array and the corresponding realized gain. As can be noticed, a 0.25 dBi gain enhancement is achieved over the open microstrip line power divider case. Such an enhancement would be more significant with a larger array. The use of narrow lines reduces the bandwidth from 3.66% to 3.2%.

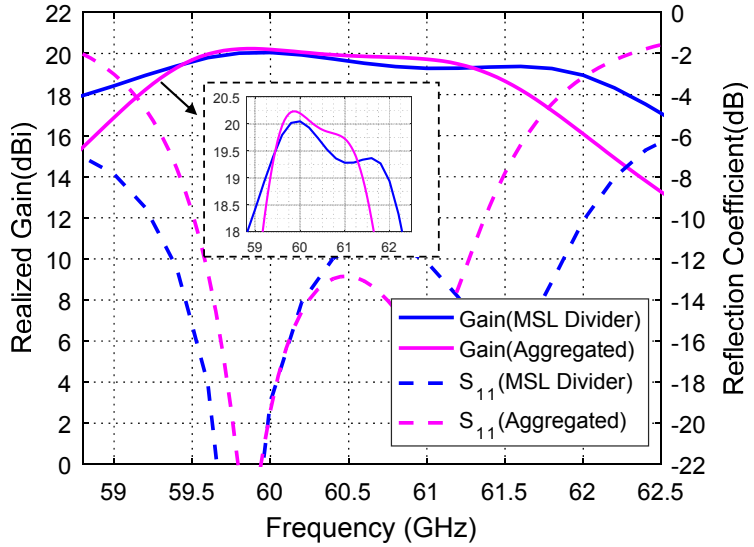


Figure 2.2.10: Realized gain and reflection coefficient of the open and aggregated feeding network of the antenna arrays.

Fig. 2.2.11 shows the electric field heat map in the E-plane for the proposed structures, as can be observed, the packaged cases have neat and stable radiation in the boresight direction. The open MSL case suffers from the undesired power divider radiation; such radiation affects the radiation characteristics of the antenna array and the total gain and efficiency. The aggregated case resolves such issue, and have almost the same neat radiation characteristic as in the packaged case.

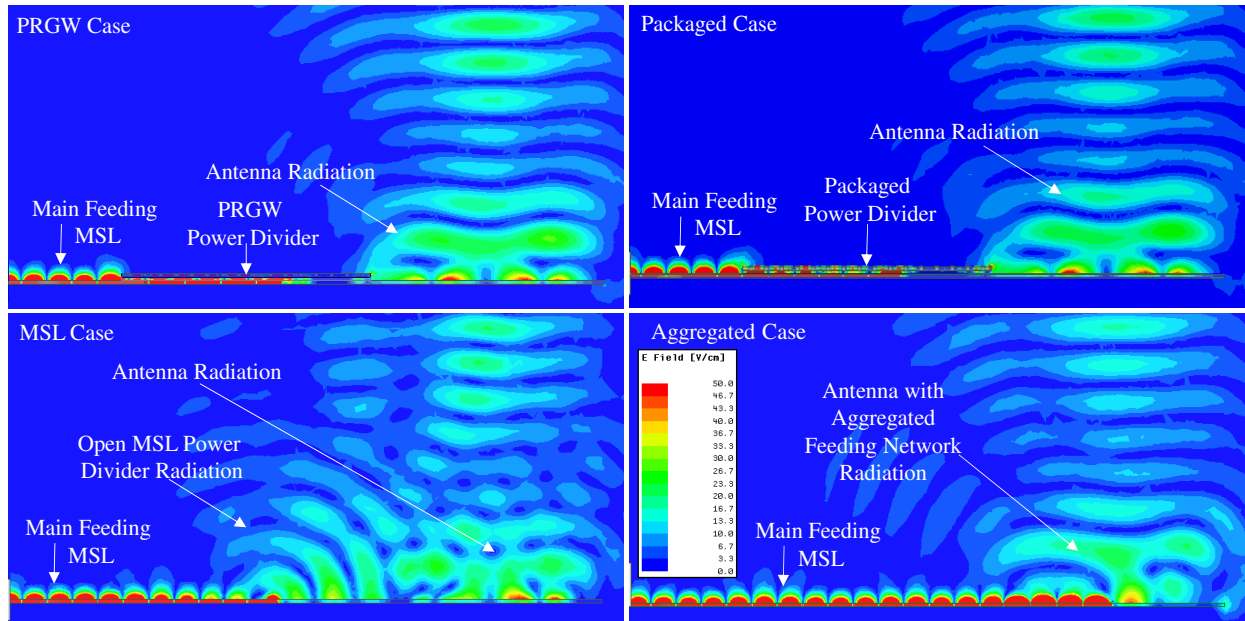


Figure 2.2.11: Electric field heat map in the E-plane for the proposed array structures.

2.2.3 Proposed Antenna Array

The study provided in the last section inspired the design of a high gain array that suits narrowband applications at 60 GHz. Even though the proposed aggregated feeding solution performance cannot fully match the PRGW solution, it still provides a low cost, efficient, and compact solution with minimal compromise on performance. Fig. 2.2.12 shows a photo of the realized expanded version of the proposed array in Fig. 2.2.8, where the array area has been doubled. Interestingly, the array looks from the top as a network of microstrip lines, and at the same time, they are acting in total as a radiating antenna. Fig. 2.2.13 shows the realized gain and the total reflection coefficient of the array. A realized gain of 22.5 dBi is achieved. The 10 dB return loss matching bandwidth is 1.9 GHz (i.e., 3.2 % of relative bandwidth). A 1.7 % shift in the measured resonance frequency over the simulated resonance frequency is observed. This is attributed to the tolerance effects in the fabrication process, the copper roughness, and the fragile substrate small thickness. The sensitivity of the structure to such tolerance errors is noticeable at such high frequencies. To highlight that, when a different value of the dielectric constant of the substrate is varied by just 3.6% to be of the value of 2.28 instead of 2.2, the frequency shift disappears as shown in Fig. 2.2.14.

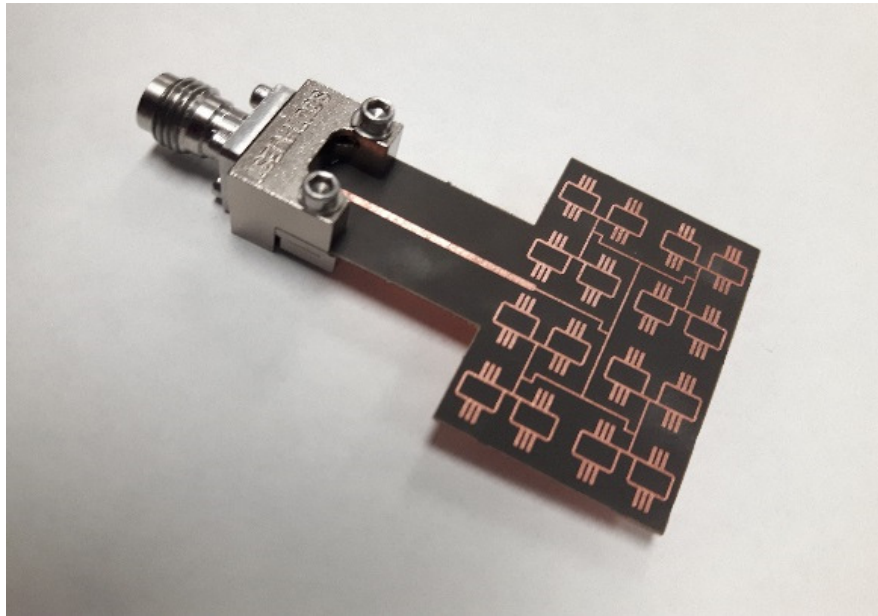


Figure 2.2.12: Proposed antenna array structure with aggregated microstrip feeding network.

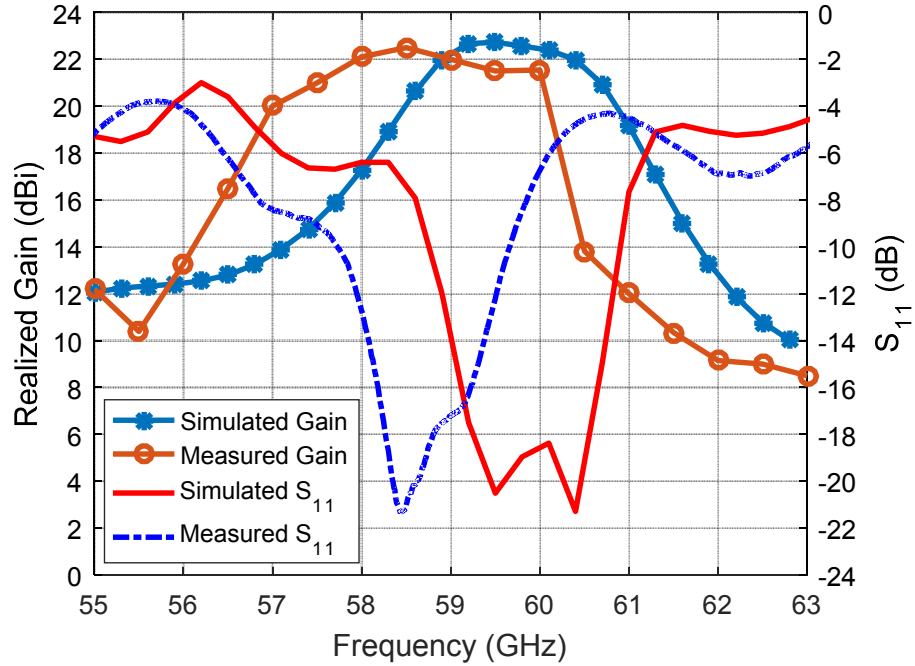


Figure 2.2.13: Realized gain and reflection coefficient of the proposed antenna array.

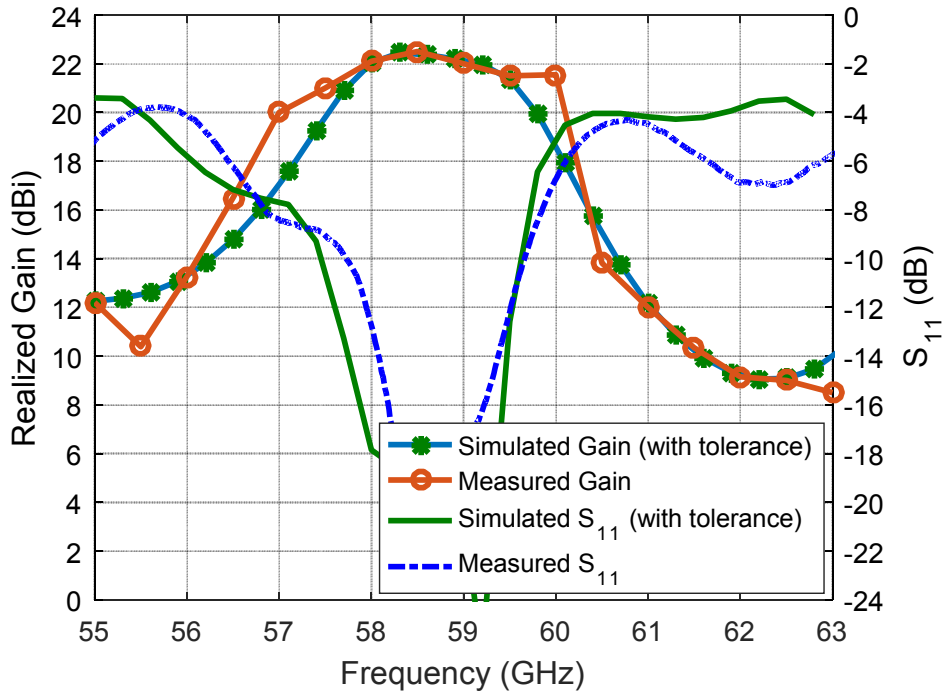


Figure 2.2.14: Realized gain and reflection coefficient of the proposed antenna array (simulated values include substrate permittivity tolerance value).

Fig. 3.15 shows the radiation pattern in the E- and H-plane. Low side-lobe and cross-polarization levels are obtained. The third side-lobe is a suppressed grating lobe.

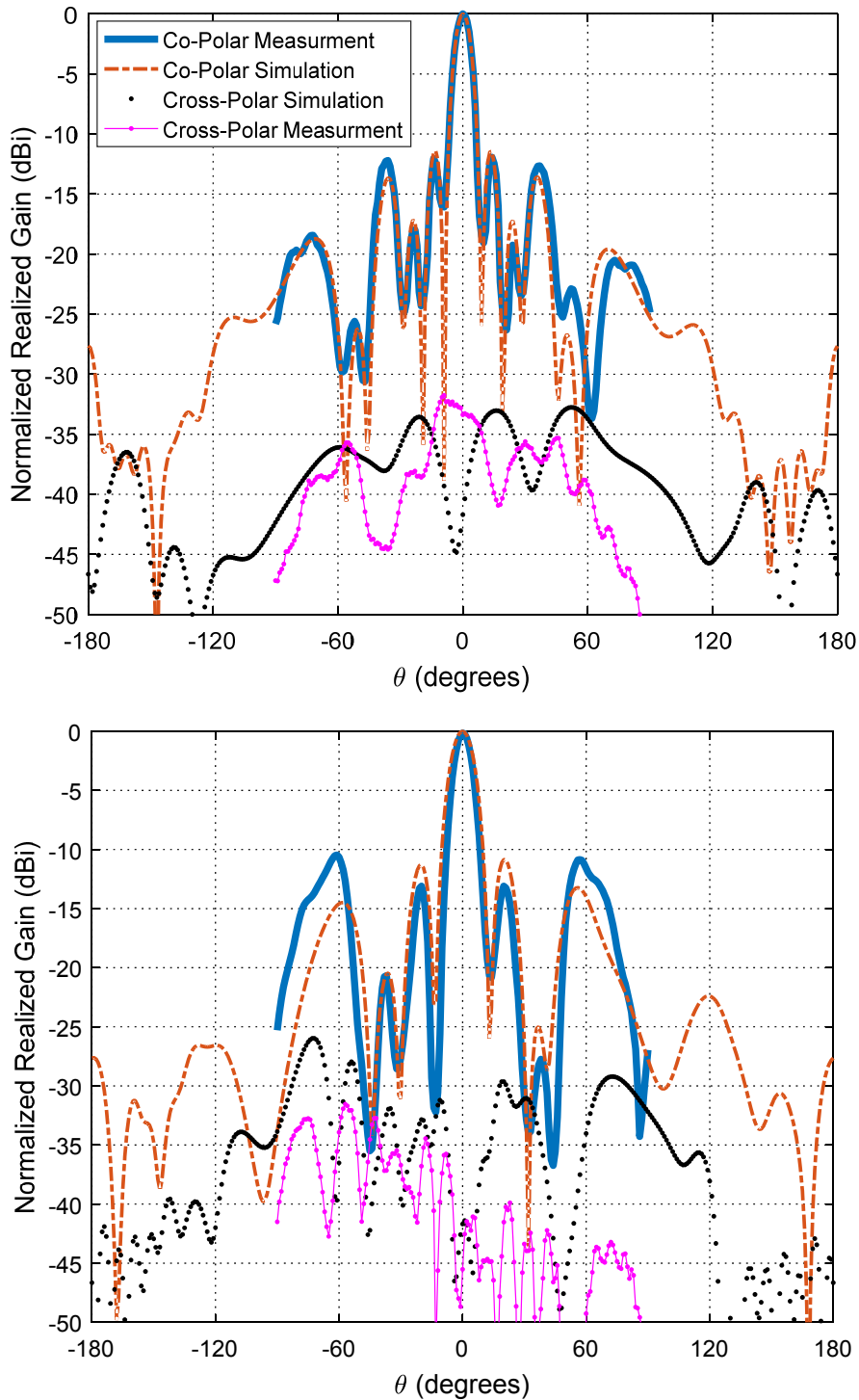


Figure 2.2.15: Radiation patterns of the proposed antenna array with aggregated microstrip feeding network, E-plane {top}, and H-plane {bottom} at 60 GHz.

Fig. 2.2.16 shows the calculated efficiency of the structure, excellent efficiency of 93% is achieved within the matching bandwidth.

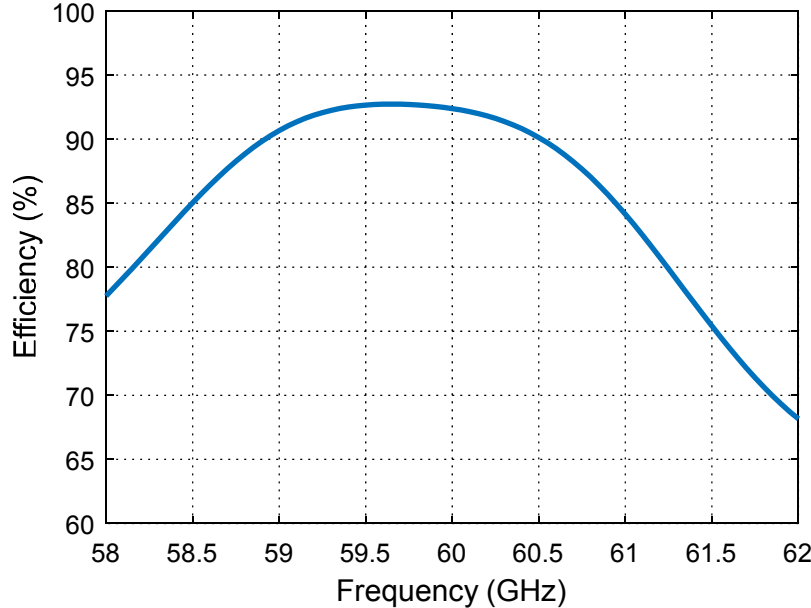


Figure 2.2.16: Radiation efficiency of the proposed antenna array.

Table 2.2.2 compares the proposed antenna array with others in the literature. As can be seen, the gain of the proposed antenna array is higher than any 4x4 antenna array, and this is the main merit of the proposed antenna in this work. As by the feed of only 4x4 elements, the gain of the antenna can be improved dramatically (since each element can be viewed as a sub-array of four magnetic current elements) and can compete with a higher number of elements arrays. This can be easily deduced by the fact that doubling the antenna array size would result in an ideally 3-dB increase in the gain. The bandwidth of the proposed antenna is limited to 3.2 %, which is suitable for many millimeter wave applications. The physical dimension of the array is 28.95mm x 19.3mm, which is equivalent to $5.79\lambda_0 \times 3.86\lambda_0$; the calculated aperture efficiency is 76.3 %.

Table 2.2.2: Comparison with other works

Ref.	Freq.	Array Type	Elements Number	BW (%)	Gain (dBi)
[9]	60 GHz	SIW Fed Slot Array	4x8	2	20.6
[39]	60 GHz	PCB Fringing Fields Ant.	1x4	11.6	16
[28]	60 GHz	PCB Monopoles	1x2	11.6	14
[12]	60 GHz	SIW Slot Antenna Array	12x12	4.17	22
[21]	60 GHz	Patch Antenna Array	4x4	11.6	18
[45]	60 GHz	SIW Slot Antenna Array	4x2	11.6	12
[46]	60 GHz	SIW Slot Antenna Array	8x8	17.1	22.1
[47]	60 GHz	Patch Antenna Array	4x4	9.5	18.2
[48]	60 GHz	Patch Antenna Array	4x4	28	16
[49]	60 GHz	SIW Slot antenna array	4x4	20.8	18.3
[50]	60 GHz	Microstrip Antenna Array	4x4	25.5	15.2
[51]	30 GHz	SIW Slot Antenna Array	4x4	8.5	19.1
[52]	45 GHz	Microstrip Antenna Array	4x4	24.4	18.8
[53]	30 GHz	SIW slot Antenna Array	4x4	4.6	16
[54]	60 GHz	Patch Antenna Array	4x4	18.3	17.5
[55]	60 GHz	Aperture Coupled Microstrip Ant. Array	6x8	1.8	21.6
[56]	24 GHz	Microstrip Antenna Array	8x8	4.1	18
Present	60 GHz	Aggregated Fringing Fields Antenna Array	4x4	3.2	22.5

2.3 Low-Cost High Gain 60 GHz Superstrate Antenna Array

2.3.1 Introduction

Arrays are used to achieve high directive radiation characteristics. Increasing the gain by a 3-dB requires doubling of the array size by increasing the number of elements. Increasing the number of elements increases the feeding network lines length increase, which causes higher losses [26], [27]. In addition, the matching bandwidth decreases due to more accumulation of the reflection from the discontinuities introduced. On the other hand, to improve the matching bandwidth, it is common to use a matching circuit (such as Chebyshev and Binomial multisession transformers) [29]. Such matching circuit design would require extra area, and sometimes it becomes challenging to accommodate it within the feeding network environment as well as the higher insertion losses. A different type of antennas called Cavity Resonance Antennas (CRA) is proposed as a solution to the aforementioned issues. The name stems from the fact that the antenna is usually bounded between two substrates (the substrate holding the antenna and the superstrate), similar to the Fabry–Pérot resonator structure, it can also be referred to as Fabry–Pérot resonator antennas. The existence of superstrate in the vicinity of the antenna changes the antenna radiation resistance and reactive impedance, and hence the superstrate can be considered as a design element that can be controlled to control the antenna impedance characteristic, for example lowering the quality factor and increasing the matching bandwidth. Also, the successive in-phase bounces of the trapped waves between the substrate and the superstrate with a valuable addition in the boresight direction increase the directivity [57], [58]. This suggests that the use of CRA can eliminate the need for an array to increase the gain. On the other hand, due to the necessity of having a superstrate at a minimum half of free space wavelength distance from the antenna, the structure is considered obtrusive and less low-profile. However, as we scale up in frequency, the wavelength becomes physically small, and hence the spacing between the substrate and the superstrate becomes very small in such a way that the antenna would still be considered as a low-profile antenna (for example at 60 GHz, the free space wavelength is 5-mm).

In section 2.1, an antenna element that utilizes the microstrip line discontinuity radiation in a constructive way to create an efficient high gain antenna was proposed [39]. The structure only

used a single dielectric substrate that eases the manufacturability and hence reduces the cost. Also, as the element structure can be perceived as being comprised of four magnetic current elements, the element can be employed in a linear antenna array with the center to center separation between the elements greater than a free space wavelength with suppressed grating lobes [39]. Such feature of the antenna element can significantly relax the design of the array feeding network. The antenna element had a relative matching bandwidth of 3.66% at 60 GHz. In this section, the antenna element is employed in a 2x2 array configuration which is supported by a dielectric superstrate. The employment of the superstrate in the structure enhances the relative bandwidth significantly to become 10.7% and has a positive effect on reducing the side-lobe level. The single element gain is 11-dBi, being employed in a 2x2 array structure, the gain reaches up to 16.5 dBi, and with the addition of the superstrate, the gain goes up to 19.4 dBi.

2.3.2 Proposed antenna structure

Fig. 2.3.1 shows the proposed superstrate antenna array structure. The array configuration is a 2x2 planar structure, and the array element depends on utilizing microstrip line discontinuity radiation as its primary radiation mechanism [39]. Rogers's 6006 substrates with a dielectric constant of 6.15 are used as a superstrate. The superstrate dimensions were optimized to maximize the gain. In [59], it was shown that the finite size of the superstrate could be optimized to maximize the gain enhancement value. The superstrate is held by two rings of Rogers 6006 substrates to hold the superstrate at 5-mm distance from the antenna. The superstrate is held by 4 corner arms of the superstrate itself, in order to keep the optimal size of the superstrate with minimal perturbation. The distance of the superstrate from the antenna can be an integer multiple of a half free space wavelength to obtain gain improvement. However, taking the bandwidth into consideration, it was found that laying the antenna at one wavelength distance (5-mm) from the antenna had an advantage in increasing the bandwidth from 3.66% to 10.7%. Inserting the dielectric superstrate in the vicinity of the antenna alters the near field of the antenna and consequently changes the input impedance of the antenna. Therefore, with different antenna types and different array configurations, the optimal location and size of the superstrate might differ as well. Fig. 2.3.2 shows the antenna array geometry, and the corresponding dimensions are listed in Table. 2.3.1.

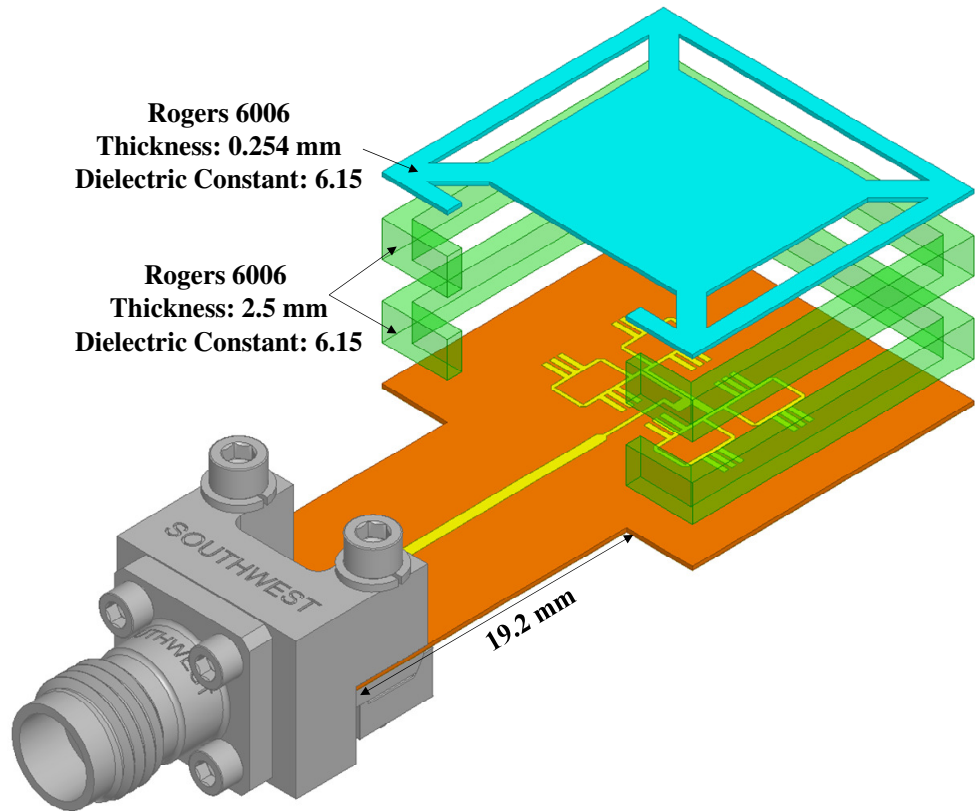


Figure 2.3.1: Proposed antenna array with a superstrate structure.

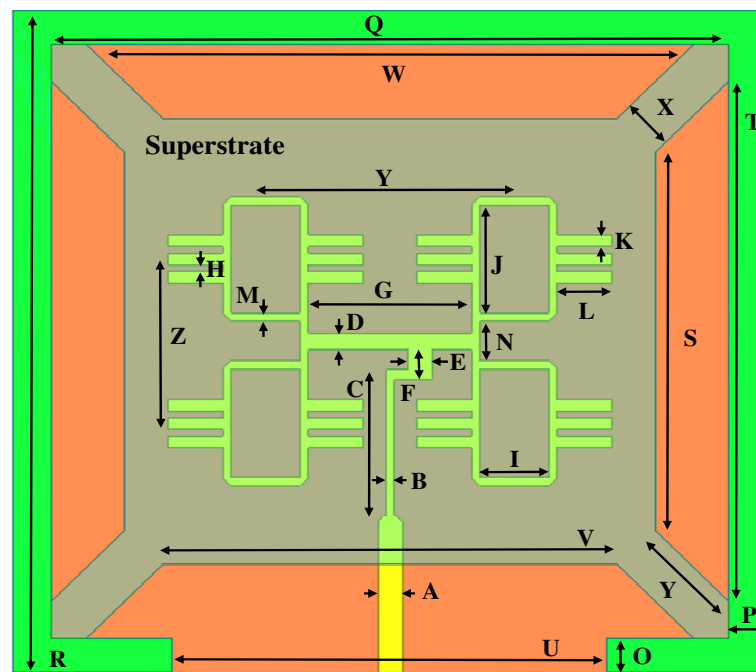


Figure 2.3.2: Proposed antenna array with superstrate structure dimensions.

Table 2.3.1: Proposed antenna array with superstrate structure dimensions

A	B	C	D	E	F	G	H	I
0.7	0.25	4.35	0.5	0.7	0.85	4.75	0.2	2
J	K	L	M	N	O	P	Q	R
3.25	0.35	1.6	0.25	1.2	1.025	1.12	19.67	19.95
S	T	U	V	W	X	Y	Z	
11.4	15.66	12.67	13.26	17.71	1.52	7.25	4.95	

As can be seen from Fig. 2.3.2, the center to center distance between the antenna elements in the E-plane is 7.25-mm ($1.45\lambda_0$), and 4.95-mm ($0.99\lambda_0$) in the H-plane. Even though the separation between the elements is greater than a half free space wavelength, the grating lobes are suppressed as in [39]. Fig. 2.3.3 shows the radiation patterns for the array structure with and without a superstrate, as can be noticed a significant reduction in the side lobe level is obtained with the addition of the superstrate. Fig. 2.3.4 shows the 3D radiation pattern of the proposed superstrate antenna array structure.

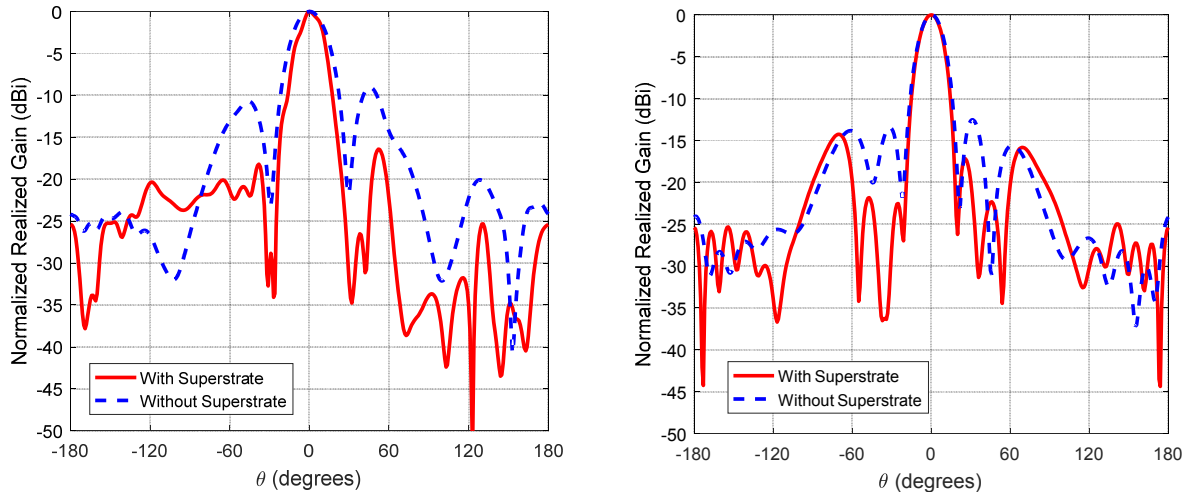


Figure 2.3.3: Radiation pattern comparison between the antenna array with and without superstrate, left (H-plane), and right (E-plane).

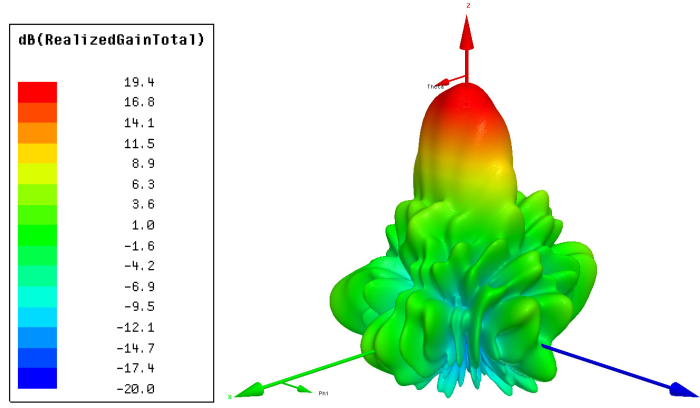


Figure 2.3.4: 3D Radiation pattern of the proposed superstrate antenna array.

Fig. 2.3.5 shows the S_{11} and the realized gain of the proposed superstrate antenna array structure; the gain of the structure goes up to 19.4 dBi with a maximum variation of 1.7 dB over the matching bandwidth. The matching bandwidth is 10.7% centered at 60 GHz. The structure without a superstrate is 2.9 dB less in gain with a maximum gain of 16.5 dBi, and a matching bandwidth of 3.66 %. Due to the interaction between the antenna and the superstrate, the matching of the antenna is affected as can be noticed in Fig. 2.3.5. Fig. 2.3.6 shows the radiation patterns in the principal planes; as can be noticed, a lower side-lobe level is achieved (below -14.8 dB). The total radiation efficiency is shown in Fig. 2.3.5 with a maximum radiation efficiency of 94%. The calculated aperture efficiency is 96%, which is an indication of the uniform aperture distribution.

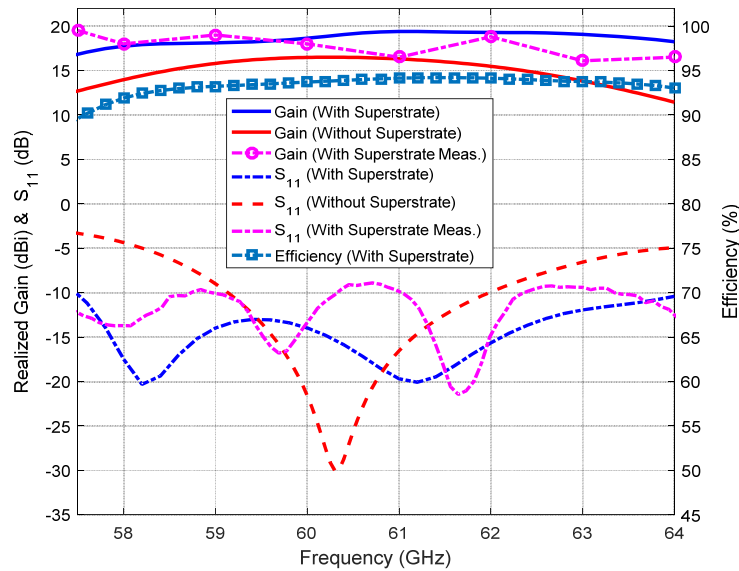


Figure 2.3.5: S-parameters and gain of the proposed antenna array structure.

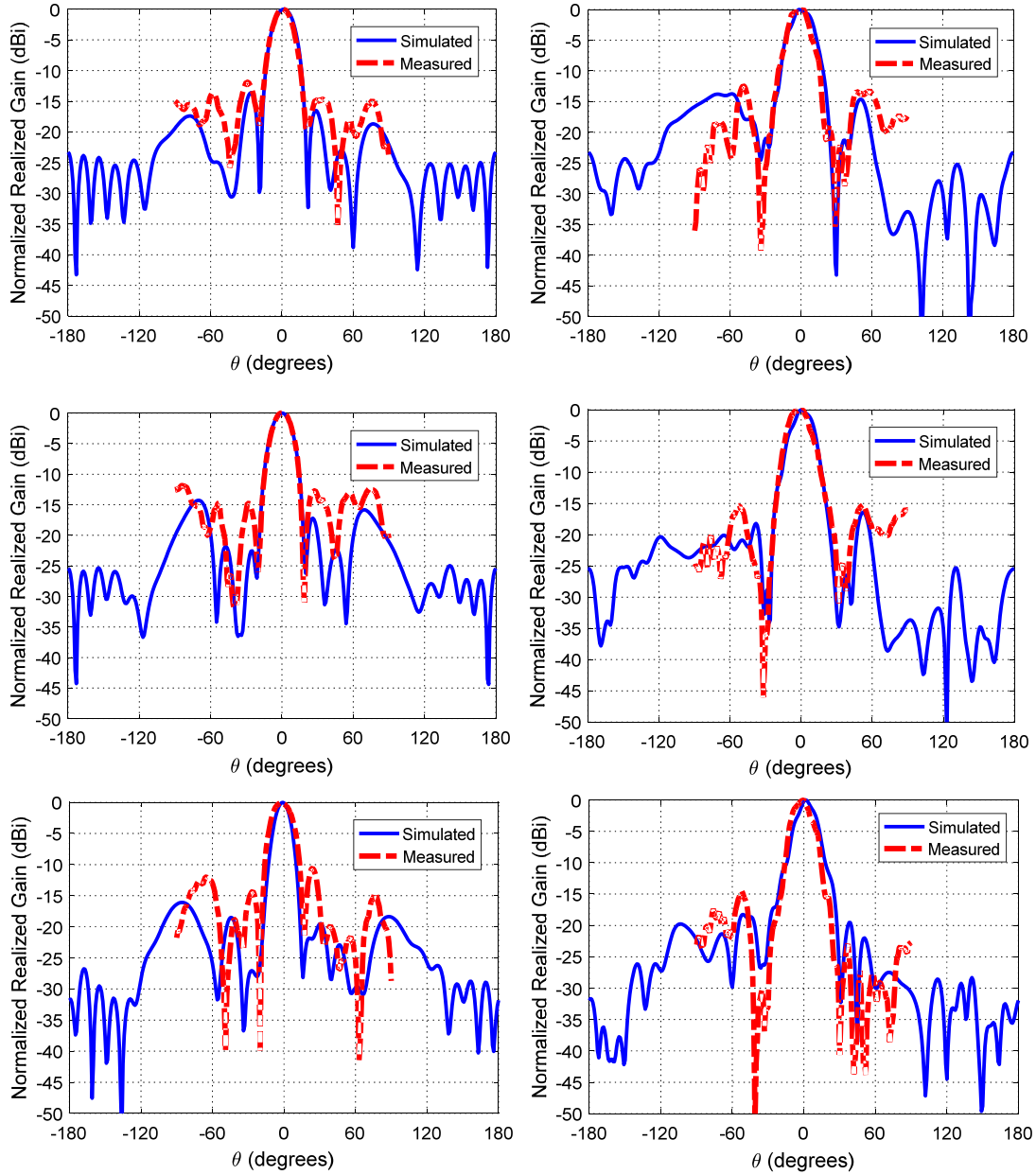


Figure 2.3.6: Radiation pattern in principle planes at different frequencies. Left (E-plane), and right (H-plane), top to bottom, 58, 60, and 63 GHz.

Fig. 2.3.7 shows the fabricated prototype, as can be seen, the prototype is pretty much low profile. The superstrate helps to protect the antenna array underneath as well. At 60 GHz, the physical dimensions are very small, where a slight variation in the height or the flatness of the superstrate has a noticeable effect on the radiation characteristics. The measured results have some deviation; however, it would be acceptable for such low-cost prototyping and characterization.

The merit of the proposed structure is its simplicity and straightforwardness, and a low-cost antenna can be fabricated in any modest fabrication facility. In addition, the antenna is not bulky as it is usually thought when considering the use of superstrate antennas. In addition to that, as the element being used in the array has a high directivity of 11 dBi, the gain is remarkably improved with a simplified feeding network of the 2x2 array to reach up to 19.4 dBi with excellent stability over the matching bandwidth (maximum variation of 1.7 dB). Table 2.3.2 shows a comparison for the proposed superstrate antenna array, as can be noticed the achieved gain performance is superior to other works, with decent bandwidth. At the same time, the structure simplicity is pretty evident, where it doesn't require complicated FSS structures. In addition to that, the back lobe radiation is minimal, for example comparing with [60] it can be noticed that the patch antenna fed by a slot-microstrip line at 60 GHz has high back radiation, in contrast, the proposed structure is entirely backed by copper and doesn't require complicated packaged feeding structures such as PRGW (Printed Ridge Gap Waveguide) and SIW (Substrate Integrated Waveguide). This shows the various possibilities and potential of the fundamental element proposed in section 2.1 [39].

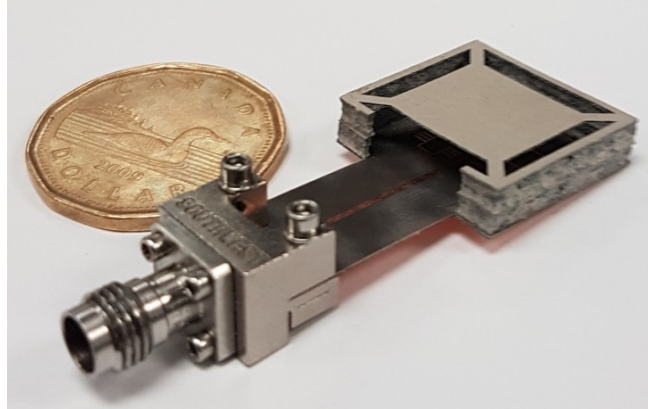


Fig. 2.3.7. Fabricated antenna prototype.

Table 2.3.2: Comparison with other antennas operating at 60 GHz in the literature

Ref.	Gain (dBi)	BW (%)	Superstrate Type	Area (mm x mm) = mm ²	Aperture Efficiency
[61]	15.6	12.2	FSS (Two Layers)	22 x 18 = 396	18.24 %
[60]	14.6	6.7	Dielectric Layer	30 x 30 = 900	6.38 %
[62]	15.5	6.3	FSS (Metal Cap)	22 x 22 = 484	14.6 %
[63]	16.5	2.4	FSS (Slot Array)	18 x 18 = 324	28 %
Present	19.4	10.7	Dielectric Layer	20 x 21.9 = 438	43 %

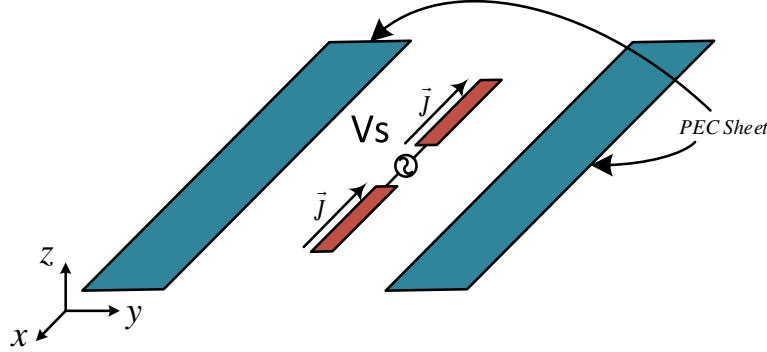
CHAPTER 3

DIPOLE ANTENNA IN-BETWEEN TWO METALLIC SHEETS “INSPIRED BY THE DIFFRACTED FIELDS”

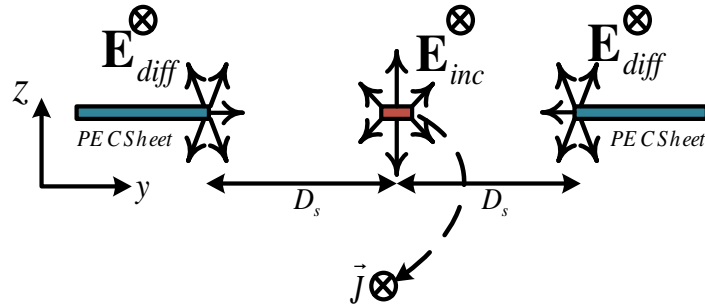
3.1 Introduction

Fig. 3.1 (a) shows a dipole antenna surrounded by two planar metal sheets. The metal sheets can be considered as a special case of a wedge with an exterior wedge angle ($n\pi$) equal to 2π (i.e., $n = 2$). Fig. 3.1 (b) illustrates the structure as an electric radiating current element in the middle of two diffracting edges (TE case). As the dipole radiating fields impinge on the metal sheets edges, the diffracted fields can be modeled as diffraction sources using the uniform theory of diffraction. The wedge problem has been studied intensively in the literature and has been analyzed mathematically by several techniques. Closed form solution can be obtained using eigenfunction series expansions [36]. Full wave numerical methods, such as the method of moments, are capable of providing an accurate solution as well [64], [27]. Uniform theory of diffraction (UTD) is a powerful method that can be used to analyze the wedge problem. UTD is a ray-based method; it treats scattering problems with intuitive ray model for wave propagation. The ray model is very advantageous as it provides physical insight and allows for better visualization of the field interactions in scattering problems. On the other hand, the uniform theory of diffraction requires that the scattering objects to be electrically large, in the order of a wavelength. Also, as line sources radiate cylindrical waves that can be described by Hankel functions, UTD replaces the Hankel function with its asymptotic approximation as given by (3.1). For such approximation, the Hankel function argument should be much greater than 1, and hence ($\rho \gg \lambda/2\pi$), where ρ is the distance from the line source. Therefore, the scattering object should be far enough from the line source and to be electrically large. Therefore, the UTD method is usually referred to as a “high-frequency method” [64].

$$H_0^{(2)}(k\rho) \sim \sqrt{\frac{j2}{\pi k}} \frac{e^{-jk\rho}}{\sqrt{\rho}} \quad (3.1)$$



(a) 3D Geometry.

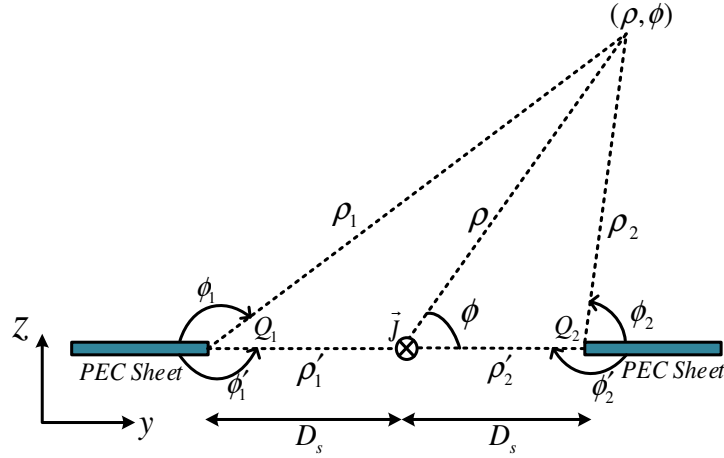


(b) Cross section indicating the diffracted fields.

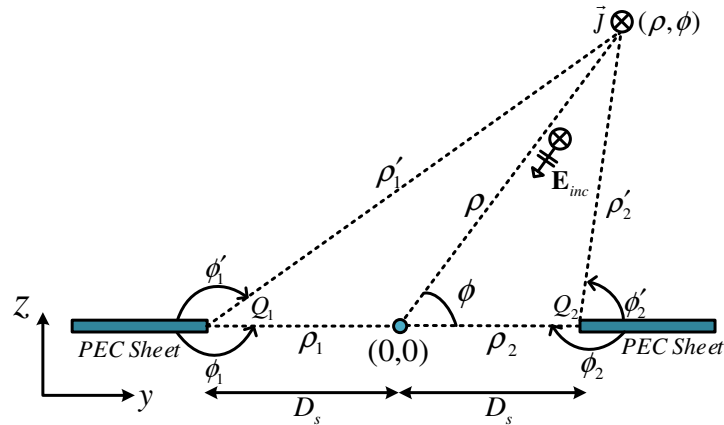
Figure 3.1: Dipole antenna between two metal sheets, (a) 3D geometry, and (b) cross-section indicating the diffracted fields.

We only considered the diffracted fields from the edges close to the electric current source. The metal sheets force the boundary condition of a zero-tangential electric field, and hence the diffracted fields only appear at the inner edges. From another perspective, those metallic sheets act as soft surfaces for the TE polarized wave produced by the dipole. Therefore, it is expected that there will be no propagation in the y-axis direction due to the soft surfaces. Also, it is expected that there will be no propagation in the x-axis direction as well, due to the well-known radiation characteristic of the dipole. Consequently, this intuitively implies that most of the radiation will be concentrated along the z-axis, as can be visualized from Fig. 3.1(b).

Due to the symmetry along the x-axis, the problem can be solved as a 2D problem. Also, further simplification can be obtained by replacing the dipole with a line source. Moreover, the diffractions at the vertices of the metal sheets are ignored. Despite that, those assumptions and approximations reduce the accuracy of the solution. However, the solution is still suitable to provide all the required physical insights needed for the antenna design. Fig. 3.2 (a) shows the actual problem and (b) shows the reciprocal version of the same problem.



(a) Actual problem.



(b) Reciprocal problem.

Figure 3.2: UTD analysis of the dipole antenna between two metal sheets, (a) actual problem, and (b) reciprocal problem.

It is easier to solve the reciprocal version of the problem. In this case, the line source is assumed to be in the far field where it produces an incident plane wave on the metallic sheets. The total

field obtained at the origin (the original location of the line source) will be equal to the radiated field at the same angle of incidence in the original problem. By repeating the calculation for all the angels (ϕ), the radiation pattern is obtained. The total field is given by (3.2). The diffracted field can be calculated by (3.3). The diffraction coefficients D_{soi} are calculated using (3.4) [65], [64] where the subscript ‘s’ refers to the soft case.

$$E_x^{tot} = E_x^{inc} + E_x^{d_1} + E_x^{d_2} \quad (3.2)$$

$$E_x^{d_i} = E_x^{inc}(Q_i) D_{soi} \frac{e^{-jk\rho_i}}{\sqrt{\rho_i}} \quad (3.3)$$

$$\begin{aligned} D_{soi} = & \frac{-e^{-j\pi/4}}{2n\sqrt{2\pi k} \sin(\beta_0)} \times \\ & [\cot\left(\frac{\pi + (\varphi_i - \varphi'_i)}{2n}\right) F(kL_i a^+(\varphi_i - \varphi'_i)) \\ & + \cot\left(\frac{\pi - (\varphi_i - \varphi'_i)}{2n}\right) F(kL_i a^-(\varphi_i - \varphi'_i)) \\ & - \{\cot\left(\frac{\pi + (\varphi_i + \varphi'_i)}{2n}\right) F(kL_i a^+(\varphi_i + \varphi'_i)) \\ & + \cot\left(\frac{\pi - (\varphi_i + \varphi'_i)}{2n}\right) F(kL_i a^-(\varphi_i + \varphi'_i))\}] \end{aligned} \quad (3.4)$$

For the 2D case, $n = 2$, $\beta_0 = \pi/2$, and $a^\pm(\beta) = 2 \cos^2(\beta/2)$, and $F(X)$ is the transition function given in (3.5).

$$F(X) = j2\sqrt{X} e^{jX} \int_{\sqrt{X}}^{\infty} e^{-jt^2} dt \quad (3.5)$$

The structure in Fig. 3.1 can be perceived as three radiating elements (i.e., the dipole and the two diffraction sources). In this case, if the radiation of the three sources adds up constructively in the boresight direction, a high gain can be achieved in the boresight [66]. The problem can be further simplified for the boresight direction ($\phi = 90^\circ$). The total electric field in $\phi = 90^\circ$ direction as a function of D_s is given in (3.6). The derivation details of (3.6) are provided in appendix A.

$$E_x^{tot} = E_0 \left(1 - F \left(2\pi \frac{D_s}{\lambda} \right) \frac{\sqrt{2\lambda/D_s}}{\pi} e^{-j(kD_s + \pi/4)} \right) \quad (3.6)$$

The second term of (3.6) resembles a Lituus spiral. In this case, the trace of the spiral can be roughly approximated with concentric circles centered at the spiral center. Fig. 3.3 shows a graphical representation of (3.6) in the complex plane. Hence, the maximum of (3.6) can be obtained when the second term phase is an odd integer multiple of π . Hence, the peaks in the gain as a function of the distance from the dipole can be roughly approximated as given in (3.7). The derivation details are also provided in Appendix A.

$$D_{smax} = \frac{(4n_o - 1)}{8} \lambda \quad (3.7)$$

where, n_o is a non-zero odd integer number ($n_o = 1, 3, 5, \dots$).

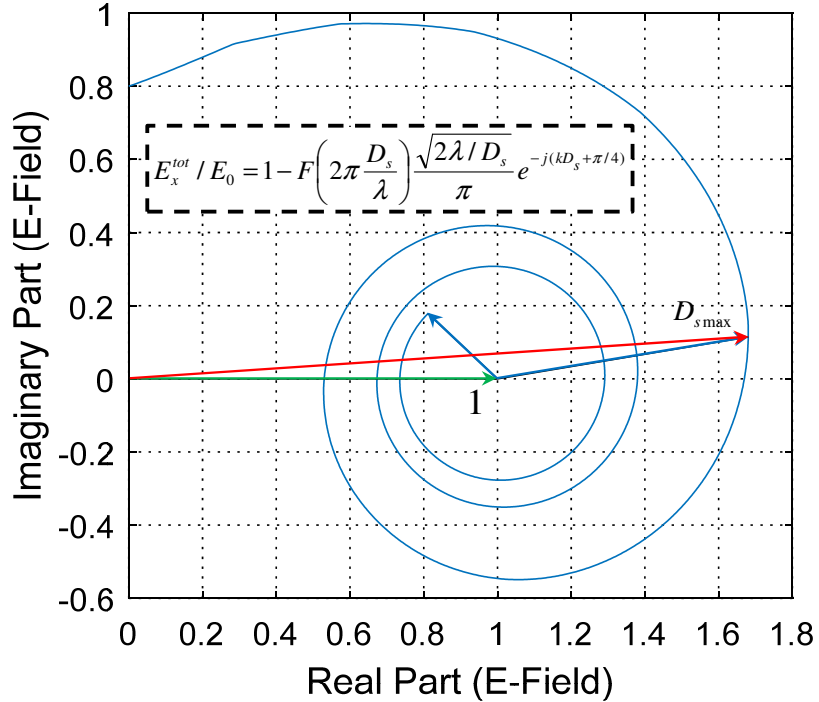


Figure 3.3: Graphical representation of the complex plane from (3.6).

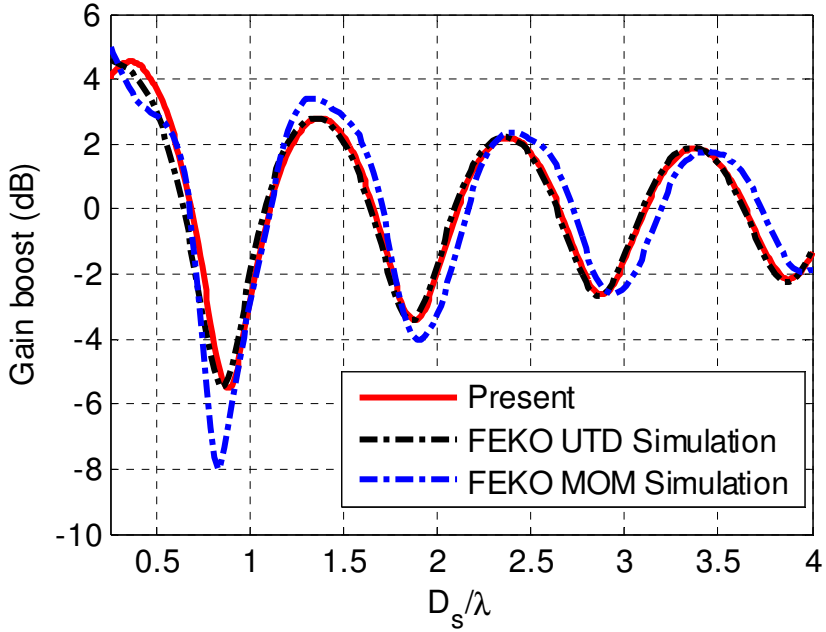
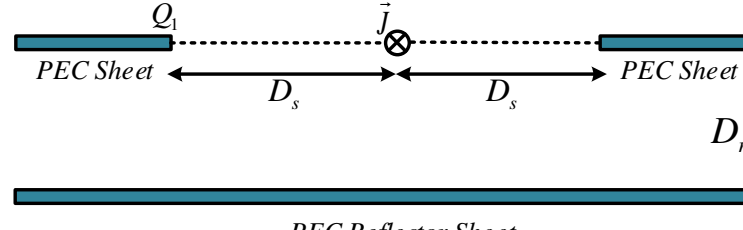


Figure 3.4: Gain boost (dB) versus D_s/λ .

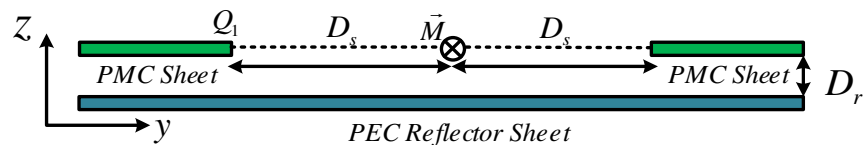
The above analysis indicates that the gain boost due to the diffraction sources adds to the original dipole gain in the boresight direction, which can be calculated easily. Fig. 3.4 shows the gain boost in dB versus the distance D_s . The calculated values have been verified by simulated results using FEKO; the solver settings were adjusted to UTD method. A good match between the calculated and FEKO simulated results is observed, as shown in Fig. 3.4. The oscillatory behavior in Fig. 3.4 is due to the variation of the phase of the induced diffraction sources. As the metal sheets edge separation from the dipole increase, the phase of the induced diffraction sources varies in a periodic fashion. Also, the diffracted sources intensities get weaker as the sheets move further away from the source. This explains the decaying behavior in Fig. 3.4. The peaks of the gain occur when the diffraction sources radiation adds up constructively to the dipole radiation, and the dips happen when they add up destructively.

The peak boost in the gain happens when $\{D_s=0.375\lambda\}$ an increase of 4.54 dB is obtained. On the other hand, the gain boost that can be obtained by having three element array is $\{10 \log_{10}(3) = 4.77 \text{ dB}\}$. Therefore, it seems that the structure is acting as a three-element array (i.e., dipole and two diffracted sources).

To focus the radiation in one direction, a PEC reflector sheet can be used below the radiating structure as shown in Fig. 3.5. This concept can be further generalized for the dual problem where the dipole can be replaced by a magnetic current source (such as a slot antenna). Then, the PEC sheets can be replaced by PMC sheets. As there is no real physical magnetic conductor, periodic structures or high dielectric constant material can realize an artificial magnetic conductor. In the electric case, the reflector distance from the antenna should be a quarter wavelength, and for the magnetic case, it can be placed very close to the antenna [37].



(a) Electric current problem.



(b) Magnetic current problem.

Figure 3.5: Dual electric and magnetic problems.

3.2 Full wave analysis

Fig. 3.6 shows the full wave analysis of the radiation patterns in the principal planes. In the simulation, the width of the sheet used is a quarter wavelength, and the distance D_s is 0.375λ . The structure is backed by a PEC reflector, as proposed in Fig. 3.5 with $D_r = 0.25\lambda$. As it can be noticed in Fig. 3.6, with a single dipole a gain of around 11.5 dBi is obtained, and all the radiation is focused in the boresight direction.

We should emphasize that UTD ray optical field analysis is accurate as long as the observation point is far enough from the transition region and the edge [64], [67]. Therefore, it is noticed in Fig. 3.4 that the smallest D_s value is 0.2λ . Also, as previously stated, the diffraction from the sheet vertices is ignored, and the dipole antenna is approximated with a line source. With all those assumptions and approximations, it is expected that UTD solution to be less accurate once compared with the full wave solution (such as the method of moment solution). Fig. 3.4 shows some deviation for the method of moment solution over UTD solution as we ignored the slope diffraction from the second edge (far edge) and the multiple diffractions of the metal plate between the edges. However, from an antenna designer perspective, the UTD solution is compelling in providing physical insight into the antenna design. For example, even by knowing that the PEC acts as a soft surface for the TE polarization of the dipole, it is still not clear what would be the proper distance of the sheets to achieve maximum boresight gain. Also, UTD intuitive model provides an excellent interpretation of the physical interaction of the fields in the problem through the definition of diffraction sources. Such an interpretation is a bit hard to grasp in other numerical methods. Therefore, with basic UTD analysis, and with the aid of full wave solver, high gain antennas can be designed and optimized easily.

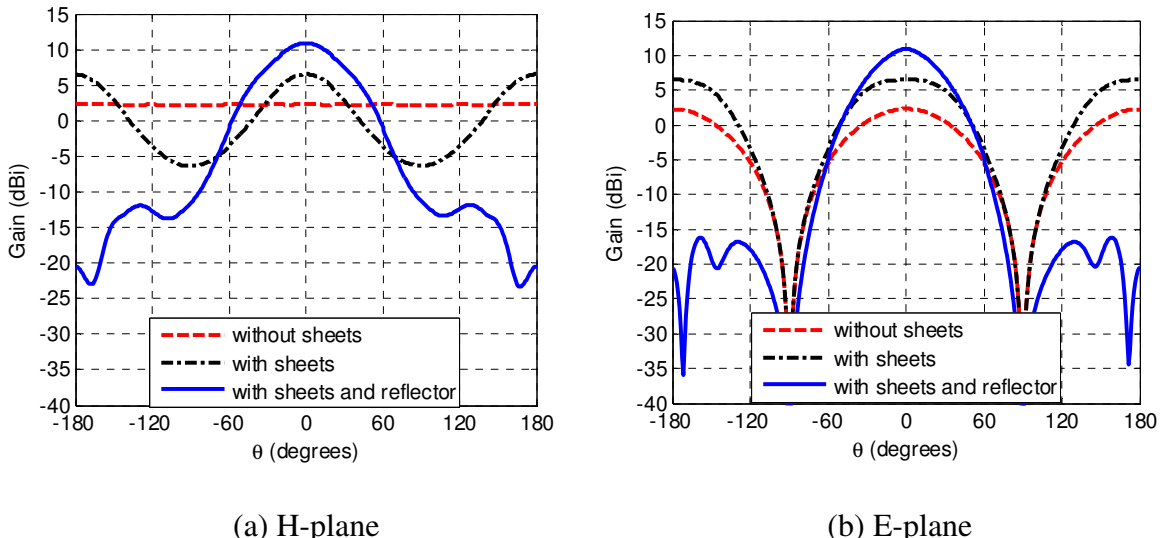


Figure 3.6: Radiation patterns in principal planes, (a) H-plane, and (b) E-plane.

3.3 Linear antenna array

It was shown from the previous analysis that the distance from the dipole to the metal sheet near the edge is 0.375λ , and the sheet width is 0.25λ . Therefore, the width of the antenna is 1.25λ . The question that would arise is it possible to employ this antenna in a linear antenna array without generating grating lobes? The answer is simply, yes. Fig. 3.7 shows the configuration of a two-element antenna array. As can be noticed, the middle sheet is shared between the two elements on the right and left sides. In this case, the diffraction sources, and the real sources (i.e., dipoles) are almost in phase, and all their radiation adds up constructively. Thus, the distance between the radiating elements is less than a half wavelength, where the radiating elements are not only the real sources (i.e., the dipoles) but also include the induced diffraction sources at the edges of the sheet. From another perspective, the two elements are considered overlapping by sharing the quarter wavelength sheet in between.

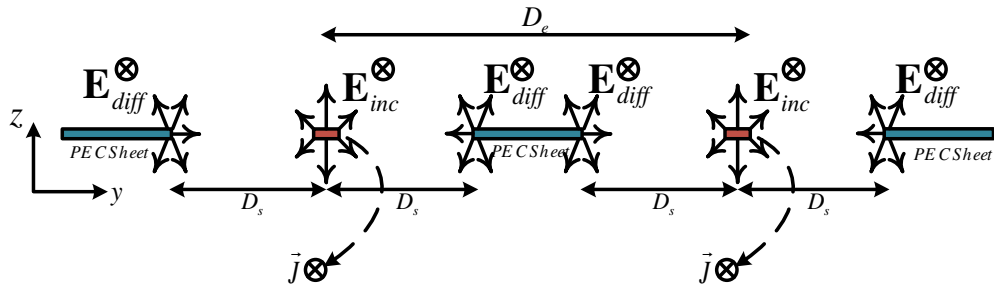


Figure 3.7: Two-element array configuration.

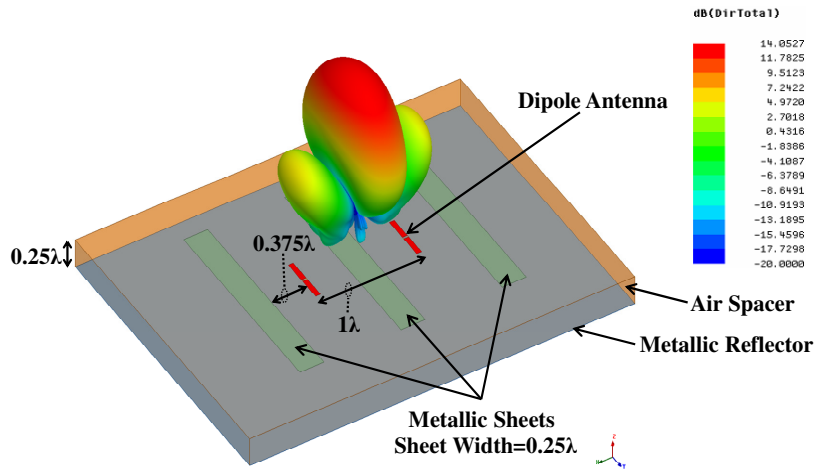


Figure 3.8: Full-wave simulation.

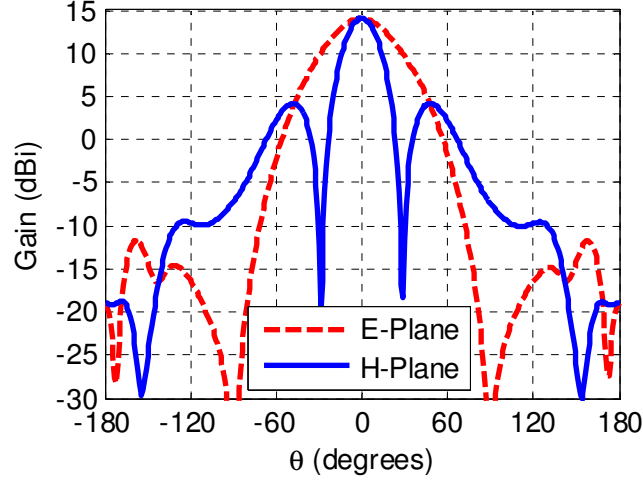


Figure 3.9: Radiation pattern in principal planes.

According to the previous discussion, a tremendous advantage is obtained, where the distance between the elements to be fed can exceed a half wavelength to a one-wavelength. Eventually, this provides higher flexibility in the design of the feeding networks, especially at high frequencies. Fig. 3.8 shows the full wave simulation for two dipoles separated by 1λ (sheet width is 0.25λ , and D_s is 0.375λ). Fig. 3.9 shows the radiation patterns in the principal planes of the same structure. It is noticed that there are no grating lobes. Another advantage is that by having the PEC sheets between the fed dipoles (acting as soft surfaces) [68], a very low mutual coupling is obtained between the array elements.

3.4 Realization at millimeter-wave frequencies

The proposed antenna configuration acts as an excellent candidate to realize high gain antennas at millimeter-wave frequencies. In this case, a planar monopole fed with microstrip-line is used to realize a high gain antenna at 60 GHz. Fig. 3.10 shows the proposed antenna structure. Table 3.1 lists the corresponding dimensions of the proposed structure. Rogers RO-3003 substrate with a dielectric constant of 3 is used. The thickness of the substrate is 0.13 mm. An air spacer of 1.1 mm separates the antenna from a plane metallic reflector. The structure is low profile, fully planar, and

requires no vias. The simplicity of the structure makes it less susceptible to manufacturing tolerances. Also, it makes it very attractive as a low-cost structure.

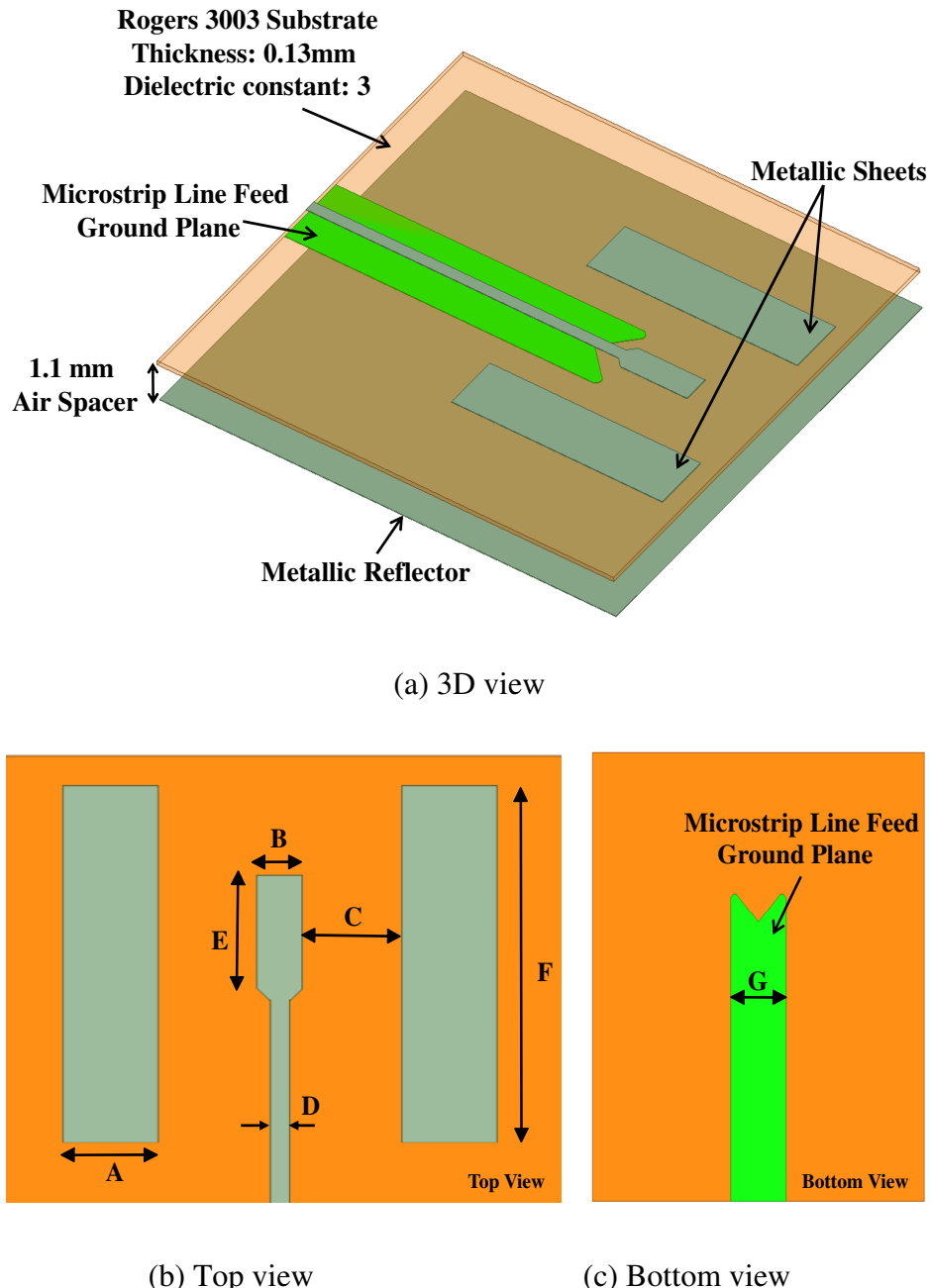


Figure 3.10: Proposed antenna structure, (a) 3D view, (b) top view, and (c) bottom view.

Table 3.1: Antenna structure dimensions

Dimension	A	B	C	D	E	F	G
Value (mm)	1.5	0.71	1.55	0.31	1.9	6	2

Fig. 3.11 shows the corresponding S_{11} and gain values. The antenna is matched over the whole range of the 60 GHz ISM band (i.e., from 57 to 64 GHz). The boresight gain is 11 dBi with excellent stability over the matching bandwidth. Fig. 3.12 shows the radiation patterns in the principal planes. A slight tilt is observed in the beam (i.e., in E-plane) due to the asymmetry of the nature of the printed planar monopole fed by microstrip line instead of a center fed dipole. Also, from Fig. 3.11, the tilt effect can be noticed as the difference between the maximum gain and the boresight gain, which is around 0.5 dB. The radiation pattern is stable over the frequency band with low cross-polarization levels. This makes the antenna, a very suitable low-cost, low profile, and high gain solution for short range high data rate wireless applications at 60 GHz.

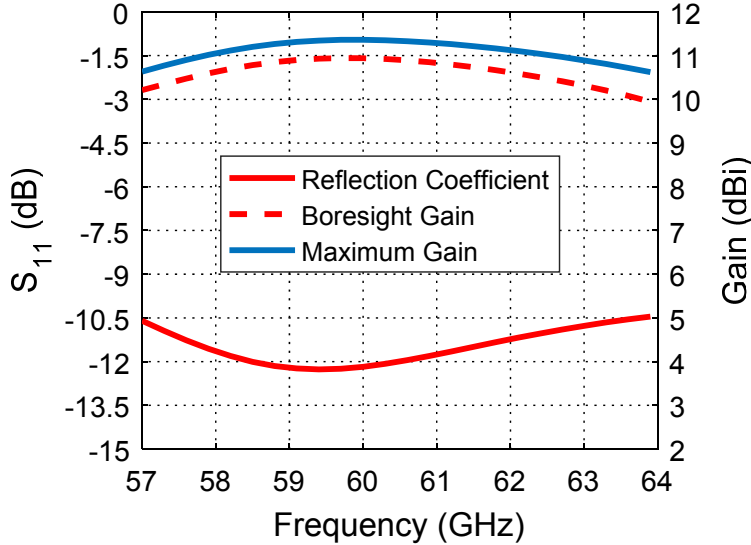


Figure 3.11: S_{11} and gain values for the proposed antenna structure.

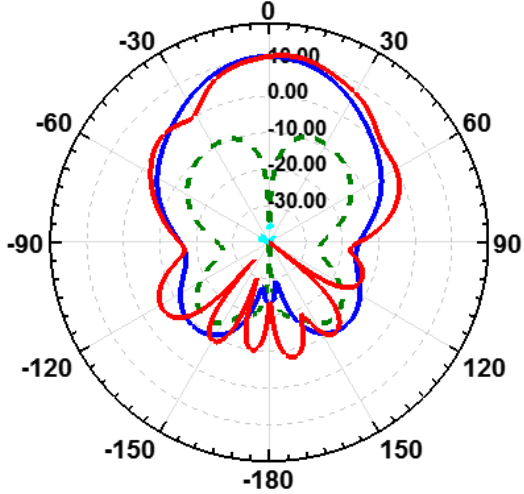
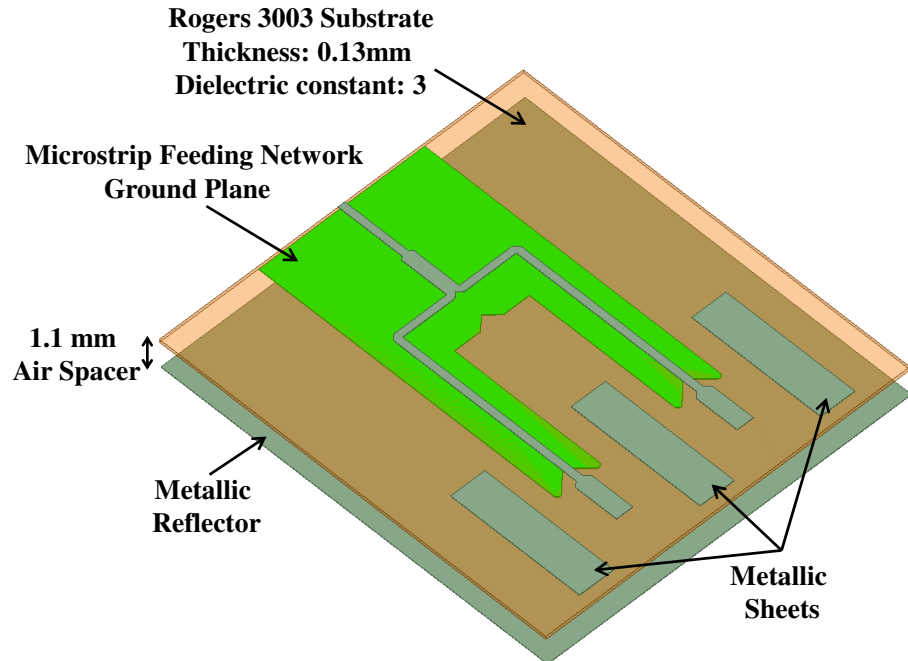


Figure 3.12: Principal planes radiation patterns of the antenna structure at 60 GHz, solid lines refer to a co-polar component (H-plane: Blue, and E-plane: Red), and dashed lines refer to a cross-polar component (H-plane: Green, and E-plane: Cyan {very small < -30 dB}).

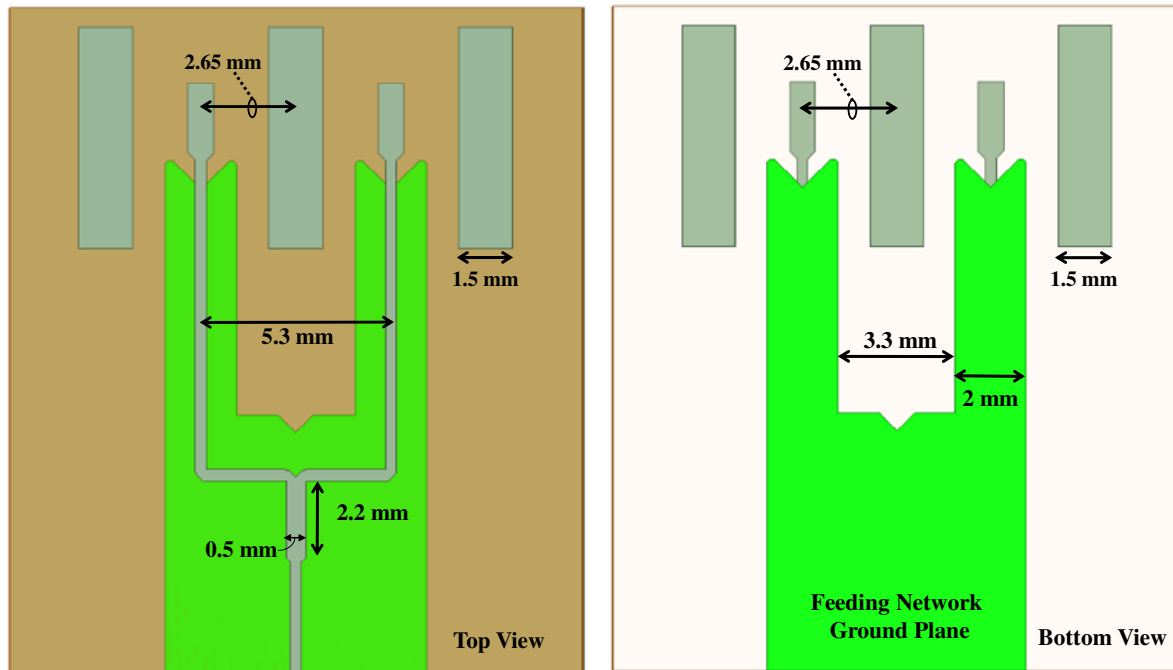
3.5 Two-element array

The proposed antenna design has been employed for a two-element array. Fig. 3.13 shows the two-element array structure. Fig. 3.14 shows the corresponding matching and gain values.

As expected, an extra 3 dB of gain is achieved (i.e., a gain of 14 dBi from the two-element array). The distance between the feeding lines is 5.3 mm, which is 1.06λ . Fig. 3.16 shows the radiation patterns with no grating lobes. This feature makes such a solution very desirable where it provides excellent flexibility in the design of the feeding networks, which is a significant challenge at millimeter-wave frequencies. In such a case, the distance between the feed lines is almost one free space wavelength rather than being half free space wavelength. Also, as the metallic sheets act as soft surfaces, the mutual coupling between the antenna elements is reduced significantly. Fig. 3.15 shows that the coupling between the adjacent elements is less than -30 dB over the whole bandwidth.



(a) 3D view



(b) Top view

(c) Bottom view

Figure 3.13: Proposed two-element antenna array structure, (a) 3D view, (b) top view, and (c) bottom view.

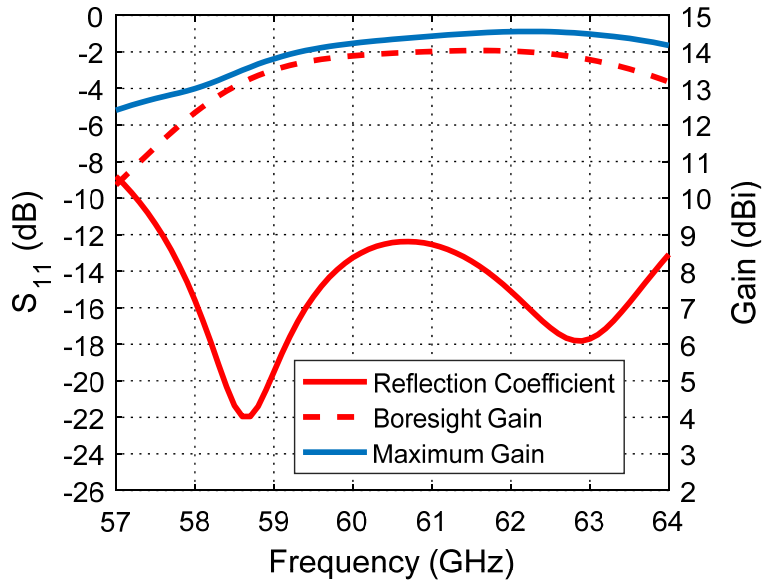


Figure 3.14: S11 and gain values for the proposed two-element antenna array structure.

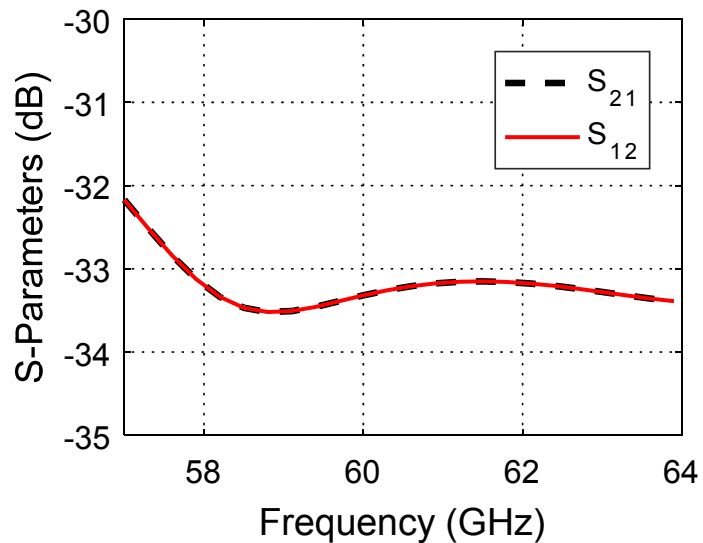


Figure 3.15: Mutual coupling between the adjacent elements in the two-element array.

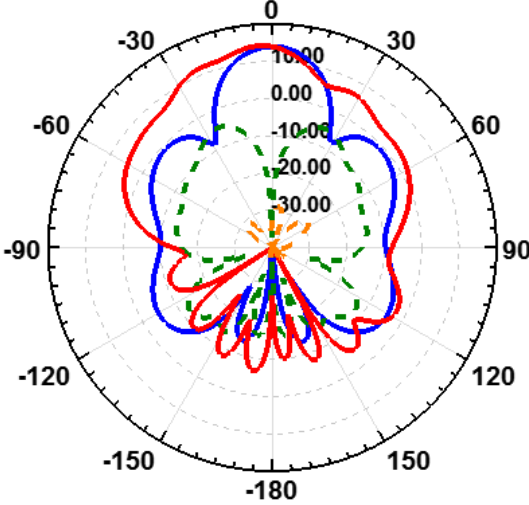


Figure 3.16: Principal planes for the two-element array at 60 GHz, (solid lines refer to a co-polar component (H-plane: Blue, and E-plane: Red), and dashed lines refer to a cross-polar component (H-plane: Green, and E-plane: Orange)).

3.6 Experimental prototyping results

The proposed structures are fabricated and tested in an anechoic chamber. Fig. 3.17 shows the photos of the single element. To realize the reflector, a ring is made of a Rogers-5880LZ substrate, as demonstrated in Fig. 3.17 to provide the spacer needed. The choice of Rogers 5880LZ is attributed to its low permittivity ($\epsilon_r = 2$), the permittivity of the ring is desired to be as low as possible to prevent the excitation of any possible modes in the cavity like region below the antenna (i.e., ring material is desired to be as close to free space as possible). Other ways to realize the spacer is using a dielectric substrate. However, the use of dielectric substrate causes some additional losses in the form of surface waves in the substrate, and hence reduces the gain. Although an AMC reflector can be located in close proximity to the antenna and maintains lower quality factor (i.e., wider bandwidth), the PEC reflector is used that requires a quarter wavelength distance from the antenna that increases the quality factor (i.e., lower bandwidth) as explained thoroughly in [69]. This is justified by the fact that the dimensions of the AMC structure unit cell should be much smaller than the operating wavelength [33], and as the free space quarter wavelength at 60 GHz is 1.25 mm, the design of such unit cell will require much higher precision to fabricate, and will be more susceptible to fabrication tolerances. Also, the PEC reflector has

better performance in terms of gain, once compared with AMC reflectors [69]. From an application perspective, the gain should not be compromised. Moreover, the monopole/PEC-reflector structure matching bandwidth is still wide enough to cover the 60 GHz ISM band.

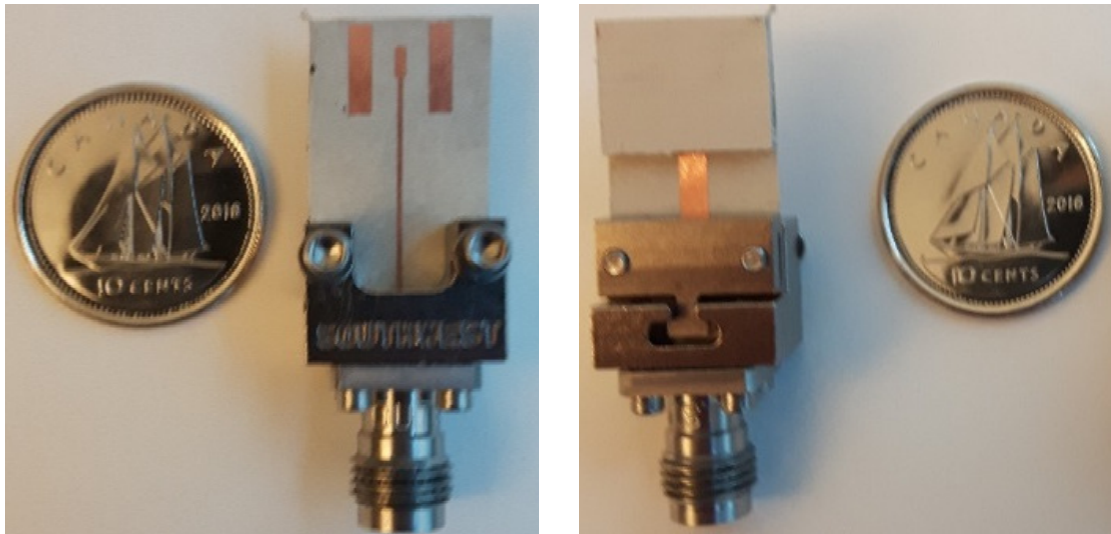
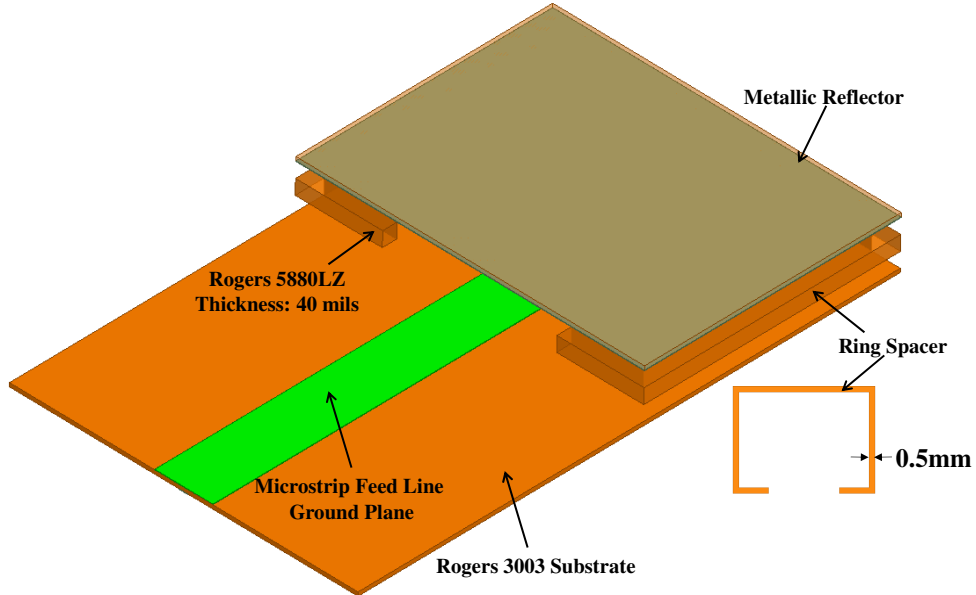


Figure 3.17: Proposed single element antenna spacer and actual prototype model.

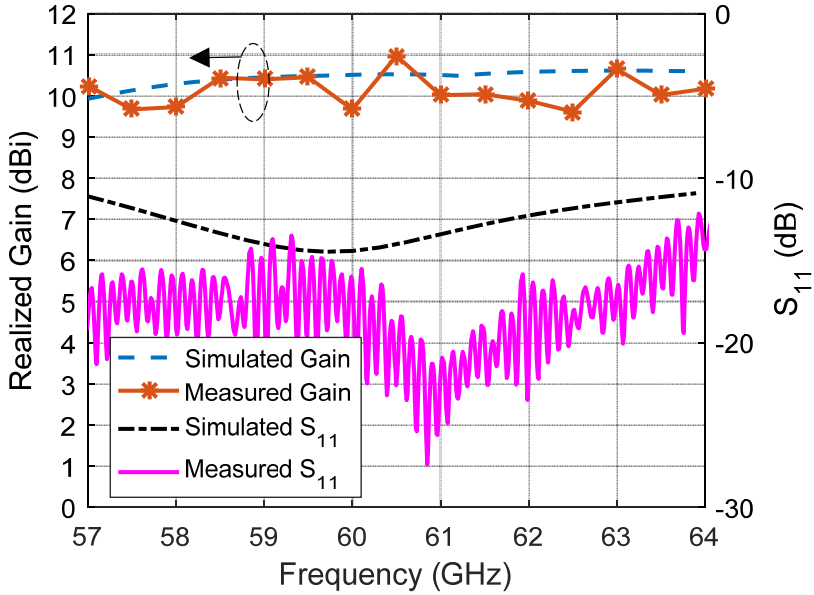


Figure 3.18: Single element realized gain and reflection coefficient.

Fig. 3.18 shows the measured and simulated results of both the realized gain and reflection coefficient. A good agreement between measured and simulated results is observed. Fig. 3.19 shows the simulated and measured normalized radiation patterns in the principal planes. An acceptable agreement is observed as well. It is worth noting that a large number of points was set in the VNA measurement, no smoothing filter was applied in the VNA settings, which caused high ripples in the measured S_{11} .

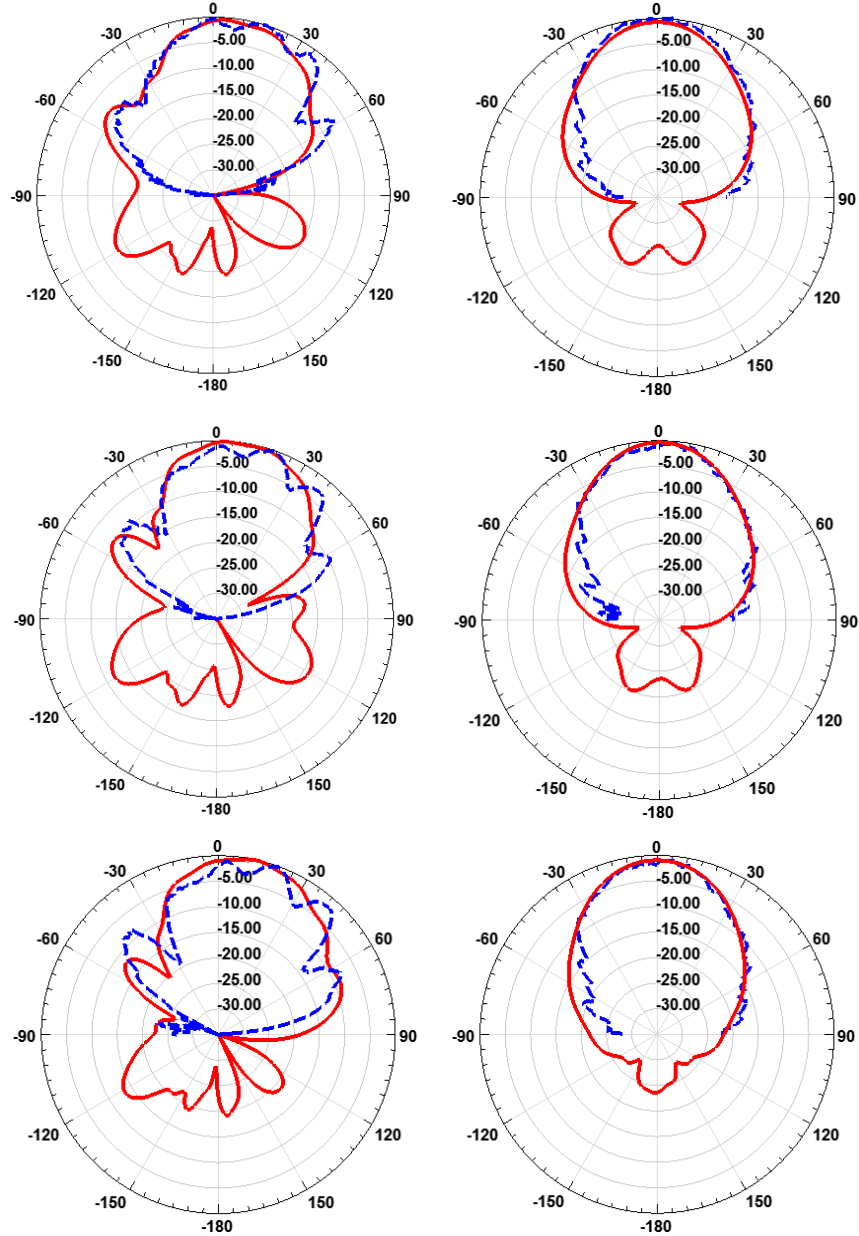


Figure 3.19: Single element radiation patterns in principal planes (solid lines refers to simulated data, and dashed lines refers to measured data) “E-plane (left) and H-plane (right).”

Fig. 3.20 shows the two-element array structure prototype. Fig. 3.21 shows the measured and simulated results of both the realized gain and reflection coefficient. A good agreement between measured and simulated values is observed. Fig. 3.22 shows the simulated and measured normalized radiation patterns in the principal planes. An acceptable agreement is observed.

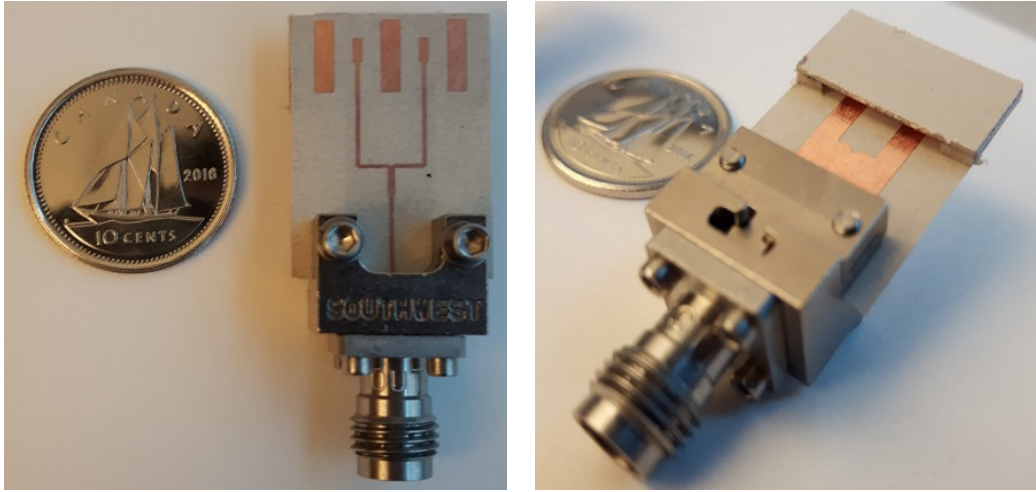


Figure 3.20: Two-element antenna array prototype model.

It was noticed that the reflector ring is a key source of tolerance errors. The substrate thickness is 0.13 mm, which leaves around 1.12 mm distance from the antenna to the PEC reflector, such physical dimension of the ring is a point to consider in terms of the mechanical stability, especially, when attached to a very thin and fragile 0.13 mm substrate. The size of the connector is considerably large, and its existence near the antenna environment can be thought of as a large scatterer. To reduce its effect, the feeding line is extended to have the antenna as far as possible from the connector body. The expense of increasing the feed line length is a higher level of dielectric losses as expected.

Fig. 3.24 shows the induced surface currents from the antenna on the connector body. Also, as the feed line width is very small (0.3 mm), the connector pin alignment of the connector at the center of the line is very critical, in order to have proper excitation of the antenna. Therefore, it is suggested that characterizing the antenna using a probing station can facilitate a more seamless and accurate characterization of such an antenna. It is worth noting that the connector with long feeding line exists only for measurement and characterization purposes. However, in the practical integrated system, the antenna is incorporated directly next to the circuitry stages, which could usually be a bandpass filter or an amplifier. Thus, such deterioration can be mitigated. In the measured radiation patterns, we can see the ripples in the main beam. These ripples are due to the interaction of the antenna with the mounting structure. As seen in Fig. 3.23, the strong current on the connector makes it interact with the surrounding that is not considered in the simulation.

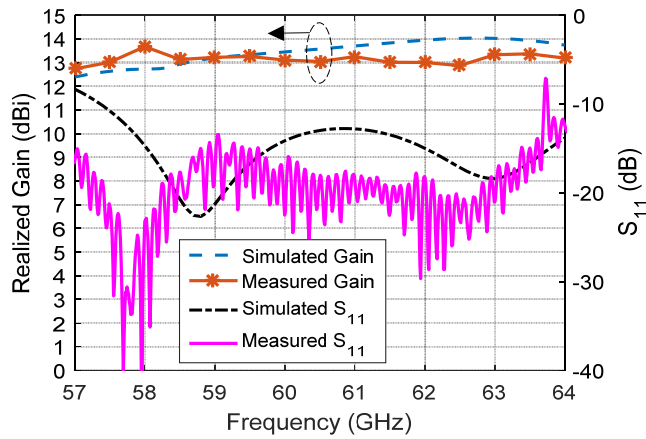


Figure 3.21: Two-element array realized gain and reflection coefficient.

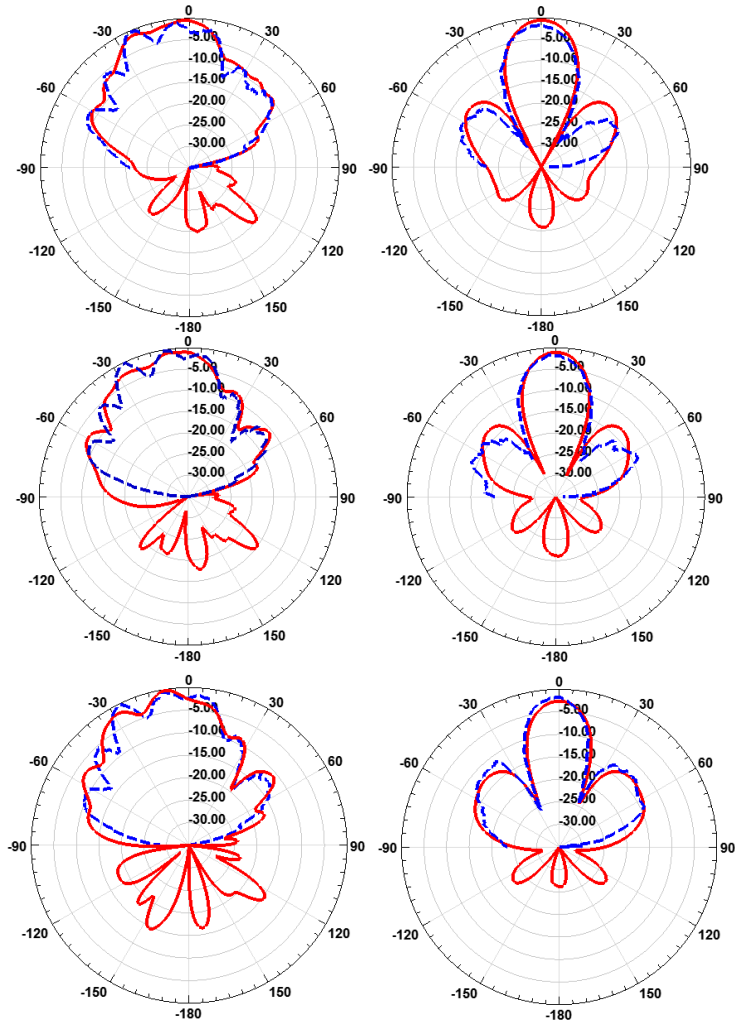


Figure 3.22: Two-element array radiation patterns in principal planes (solid lines refers to simulated data, and dashed lines refers to measured data) “E-plane (left) and H-plane (right).”

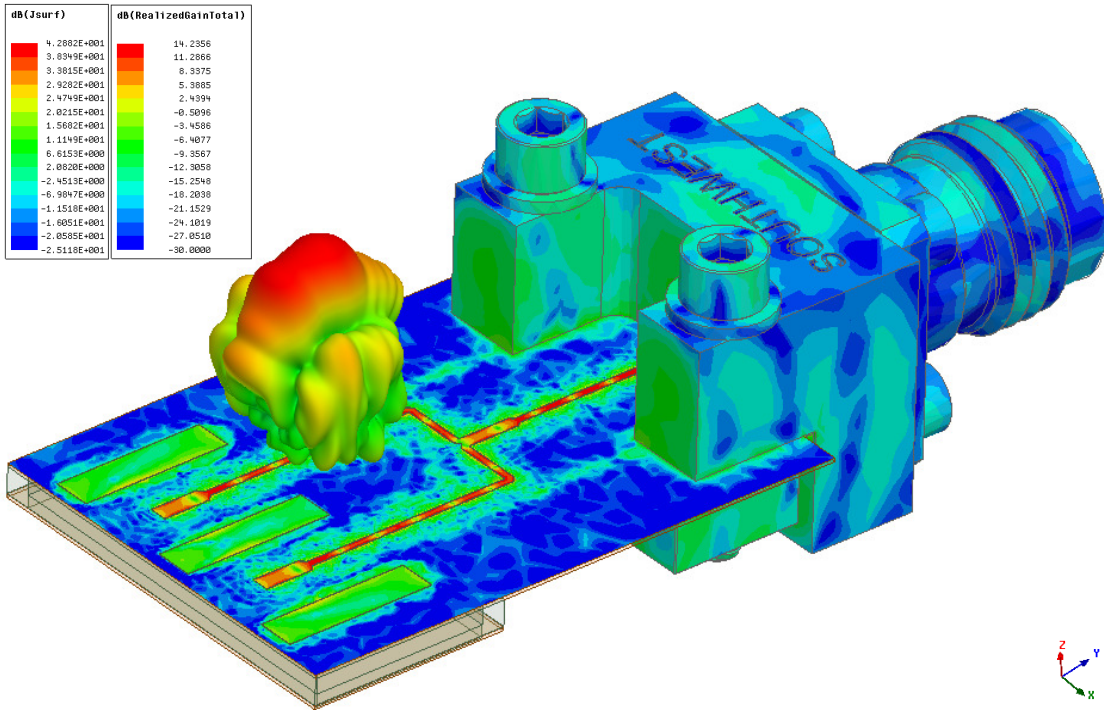


Figure 3.23: Surface current density heat map and 3D radiation pattern of the two-element antenna array.

Fig. 3.24 shows the calculated efficiency of both the single element and array, as expected, the array structure is less efficient due to the higher losses in the feeding structure.

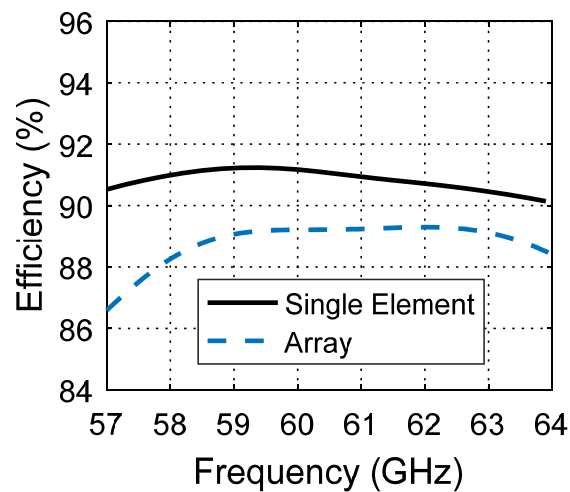


Figure 3.24: Calculated efficiency of the single element and two element array structures.

CHAPTER 4

MAGNETIC SOURCE ANTENNA

4.1 Gain Boost of a Slot Antenna

4.1.1 Introduction

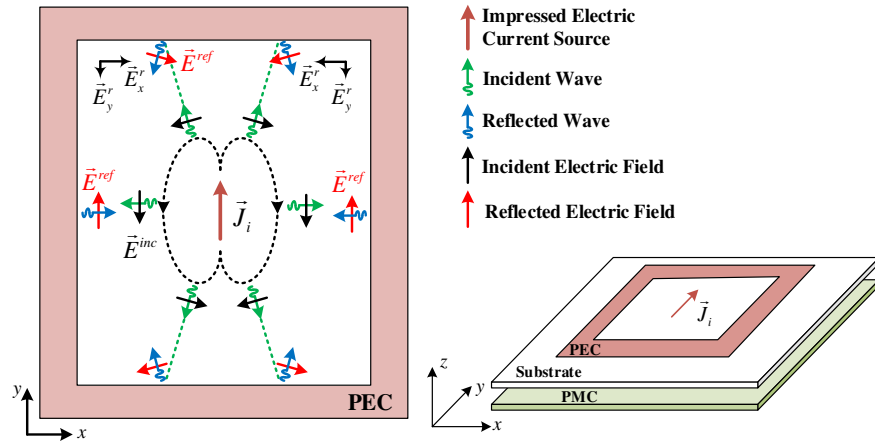
A magneto-electric (ME) dipole antenna is a well-known antenna [34], [70], [71], which provides wideband, low cross-polarization, and symmetric radiation patterns. Such radiation characteristics are essential requirements for most reflector antennas feeds. A ME dipole is usually designed by superimposing electric and magnetic current elements orthogonally on each other. In this chapter, a new design perspective is proposed. The proposed design procedure can transform the radiation characteristics of an electric or magnetic current element to ME dipole characteristics. The proposed procedure doesn't require the orthogonal combination of the magnetic and electric current elements [34]. Hence, the procedure possesses a significant advantage, where it avoids the need for a quarter free-space wavelength spacing between the current element and the metallic ground plane as in [40]. In addition, the proposed design increases the antenna gain dramatically, where the proposed structure has a boresight gain of 11.5 dBi, and a relative bandwidth of 13% centered at 60 GHz. The antenna element has been employed in a planar antenna array to achieve a gain of 22 dBi.

4.1.2 Theoretical Qualitative Analysis of the Proposed Structure

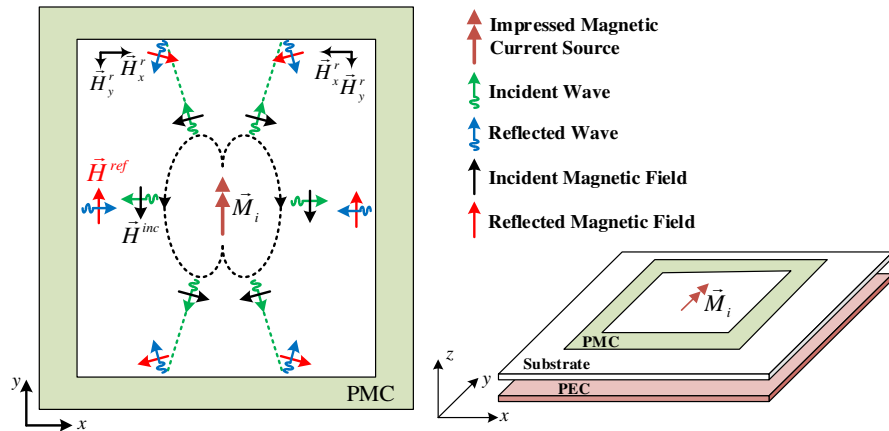
Fig. 4.1.1 shows a simplified sketch, conveying a theoretical abstraction of the proposed structure. Such a sketch is very descriptive and essential in grasping the radiation mechanism of the proposed structure. Part (a) shows the electric current case, part (b) shows the dual magnetic case, and part (c) shows a modified version of the magnetic case with the use of a dielectric material instead of a Perfect Magnetic Conductor (PMC). Fig. 4.1.1-(a) shows an electric current element inserted in the middle of a Perfect Electric Conductor (PEC) rectangular ring, as the electric current element radiates, the radiated wavefront in the vicinity can be approximated by a doughnut shape as denoted by the dotted line in Fig. 4.1.1-(a). As the wave propagates from the current element towards the PEC ring edges, it gets diffracted from the PEC ring inducing a surface current on the ring. In Chapter 3 it was shown that the gain of a dipole could be increased by inserting the dipole between two metallic sheets [28], where the fields diffracted from the edges of the sheets can be utilized to radiate constructively with the dipole radiation, and hence increase the gain of the structure. Further details about the optimal distance of the sheets from the dipole to maximize the gain can be found in Chapter 3 as well. Adding the two sheets parallel to the central dipole allows the control of the radiation pattern in the H-plane. This can be accomplished by controlling the distance of the sheets from the dipole, which consequently determines the phase and the intensity of the diffracted fields. In this structure, however, the current element is enclosed by a rectangular ring rather than being inserted between two sheets. The addition of the two horizontal sheets parallel to the x-axis, will also cause the propagated waves diagonally to be diffracted, and this adds a new degree of freedom in the design, which would allow the control of the shape of the E-plane radiation pattern, and hence obtain a symmetric radiation pattern. The analysis can be simplified by assuming the incidence and reflection of plane waves. The analysis ignores several physical aspects, such as the exact wave-front generated from the dipole and the vertices in the PEC ring. However, such abstract qualitative analysis allows a better physical understanding of the radiation characteristics and provides us with a proper initial rough dimension of the structure. Then, with the aid of a full-wave solver, a practical realization of the structure can be designed and optimized. The diffracted waves from the PEC surface can be thought of as equivalently induced secondary sources. Hence, by controlling the vertical and horizontal dimensions of the ring, the

intensity and phases of these secondary sources can be controlled, in such a way to boost the gain, and maintain the symmetry of the radiation patterns (in other words, to transform the dipole pattern into a ME dipole radiation characteristic with an extra boost to the gain). It is worth noting that, the outside of the principal planes diffracted waves, can be decomposed into two components in the x- and y-direction. Due to the symmetry, the x-components effect cancels out in the boresight, and this consequently reflects positively on maintaining low cross-polarization. The dual case is shown in Fig. 4.1.1-(b), by using the duality principle, the electric current source is replaced by a magnetic current source (which can be realized by a slot). Also, the PEC ring is replaced by a PMC ring.

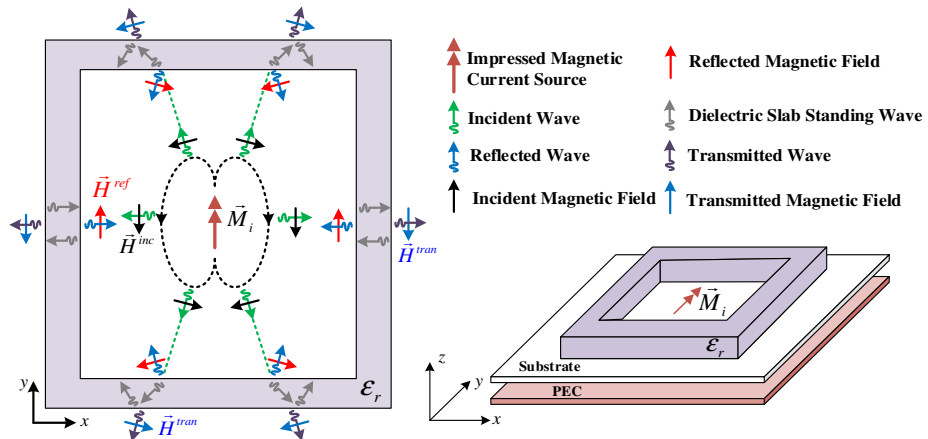
Electric dipoles require a differential feed; such feed can be realized by using a balun circuit. The balun usually increases the complexity of the structure. Also, the balun circuit, along with its geometrical discontinuities contributes to additional losses. On the other hand, the magnetic current radiator case can be realized by a slot, which doesn't require differential feeding. The slot could be backed by a cavity within the EBG structure. Also, in the case of a dipole, a quarter wavelength is a need for a PEC reflector to obtain boresight radiation. Therefore, the realization of the magnetic current source seems to be favorable. On the other hand, the magnetic current source requires the realization of the PMC ring, which does not exist in nature. However, periodic structures can be designed to emulate its characteristics over a specific band of operation (those periodic structures are usually referred to as artificial magnetic conductors "AMC") [72]. The fabrication process of such structures, especially at mm-wave frequencies, requires accurate fabrication due to its small physical dimensions of the periodic structure, which might sometimes be infeasible to fabricate. Moreover, such small dimensions are more prone to tolerance errors. Therefore, a modified version is suggested in Fig. 4.1.1-(c). This version uses a dielectric material rather than the PMC ring. By proper design of the width of the ring to be a quarter guided wavelength, maximum reflection, and minimum transmission from the dielectric ring can be obtained. This can be deduced merely by a simple multi-layer medium analysis; detailed derivation is provided in the Appendix B. Hence, the secondary induced sources would be trapped in the form of a standing wave in the dielectric medium. Eventually, this concludes that the modified magnetic current case is reasonable and straightforward option to be realized.



(a) Electric Case with PEC.



(b) Magnetic Case with PMC.



(c) Magnetic Case with Dielectric Material.

Figure 4.1.1: Abstract sketch of the proposed structure.

4.1.3 Antenna Feeding Considerations at Millimeter Wave Frequencies

Open feeding structures, such as microstrip lines, usually suffer from radiation losses due to the nature of their open structure. Radiation from the feed becomes more noticeable and more severe at mm-wave frequencies [1], [2], [35]. Moreover, the undesired radiation from the feeding structure affects the total radiation pattern of the whole structure adversely. Therefore, packaged feeding structures are highly recommended at such frequencies. Substrate Integrated Waveguide (SIW), and Printed Ridge Gap Waveguide (PRGW) technologies are good examples of packaged feeding solutions that can be incorporated in a low-cost printed circuit board environment. In the present work, we focus on the use of PRGW technology, which packages microstrip lines using a bandgap periodic structures, such as Sievenpiper mushroom cells, where no propagating modes can exist within the bandgap of the periodic structure. The cell dispersion diagram and the PRGW dispersion analysis are the same as in section 2.2.2.

4.1.4 Realization at Millimeter Wave Frequencies (60 GHz)

Fig. 4.1.2 shows the proposed structure, the structure is made of a slot antenna surrounded by a dielectric ring, the ring is made of a Rogers substrate with a thickness of 0.635 mm, and a dielectric constant of 10.2. The slot antenna is fed using a PRGW. Such feeding reduces the back radiation (back lobe radiation is inevitable in open microstrip line feeding). Also, it provides an efficient mechanism for feeding the structure. The complete set of dimensions of the proposed structure is shown in Table 4.1.1. The structure is simulated and optimized using finite element full wave simulator (ANSYS HFSS).

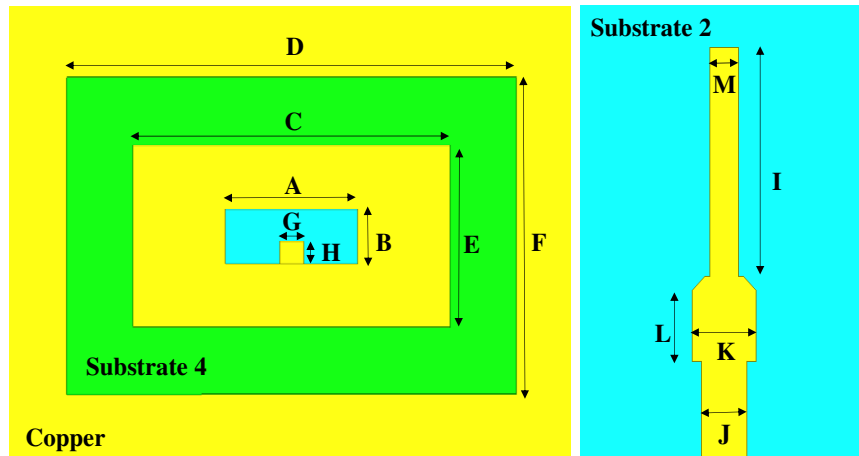
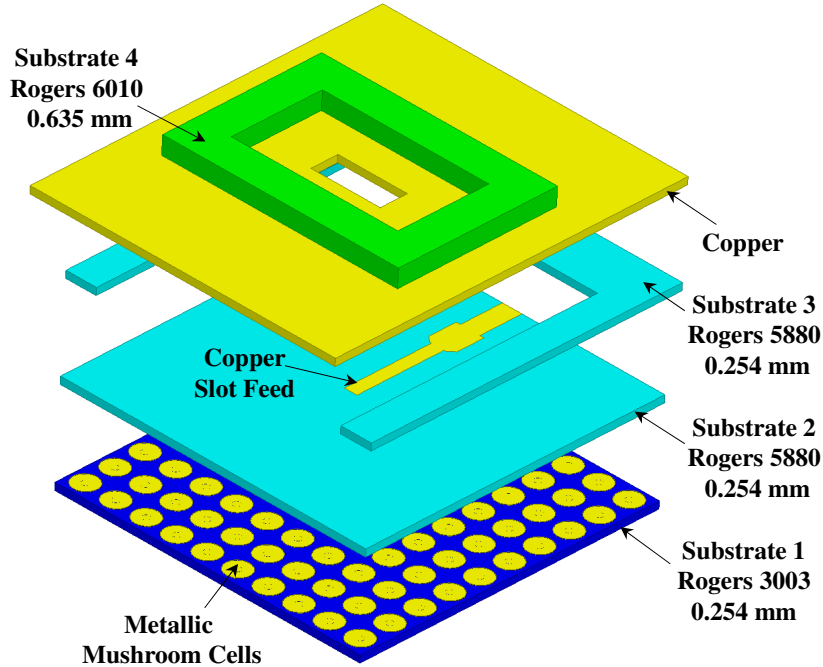


Figure 4.1.2: Proposed antenna structure.

Table 4.1.1: Structure dimensions in (mm)

A	B	C	D	E	F	H	I	J	K	L	G, M
2.5	1	6	8.5	3.35	5.85	0.4	3.2	0.7	1	1	0.45

Fig. 4.1.3 shows the magnetic field heat map and the magnetic vector field distribution for the proposed structure. As can be noticed the slot antenna, acting as the main radiating element, which is equivalent to a magnetic current element. The trapped magnetic fields within the dielectric ring can be visualized as the induced secondary magnetic current element sources. The total radiation

of the structure is the superposition of the radiation of all these elements. By controlling the dimensions of the rectangular dielectric ring, the magnitudes and phases of these secondary sources can be controlled. The dimensions of the dielectric rectangular ring are set to maximize the gain in the boresight direction, and to maintain a symmetric radiation pattern in both the E- and H-plane, in other words, to have a magneto-electric dipole radiation characteristic. The thickness of the dielectric material was set to 1.25 mm, which is approximately equal to three-quarters of a guided wavelength. As can be seen from the heat map, such dimension maximizes the reflectivity from the dielectric ring and traps the wave in the form of a standing wave in the rectangular dielectric ring. Fig. 4.1.4 shows the three-dimensional radiation pattern of the proposed structure. Fig. 4.1.5 shows the radiation patterns in the principal planes. As can be noticed, a good symmetry for both the E- and H-plane is obtained with high gain of 11.5 dBi. Also, the lower level of cross-polarization is achieved. The antenna achieved a 13%, and gain averaged around 11.5 dBi with excellent stability.

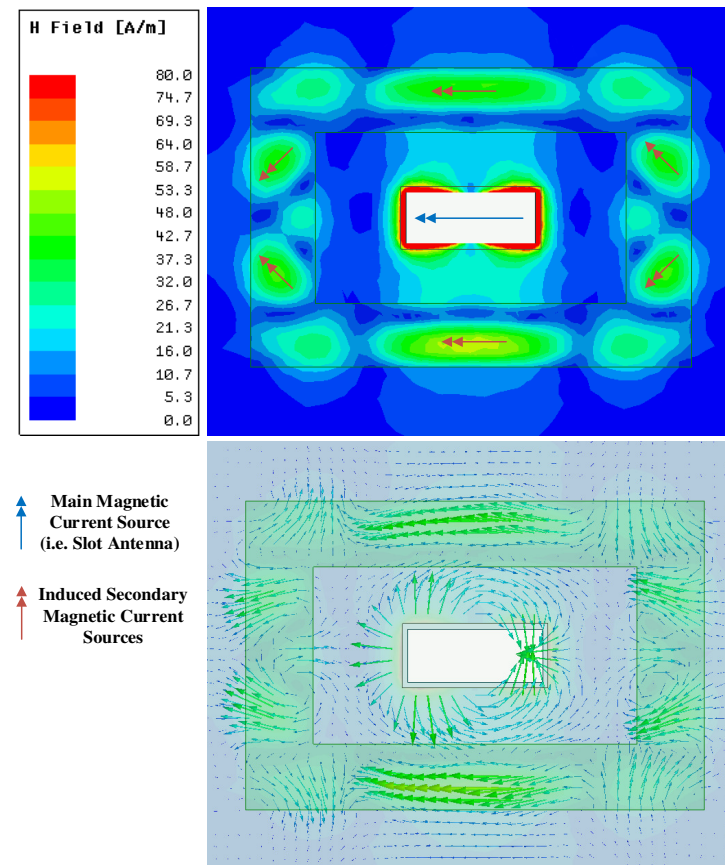


Figure 4.1.3: Magnetic field heat map and the magnetic vector field distribution for the proposed structure at 60 GHz.

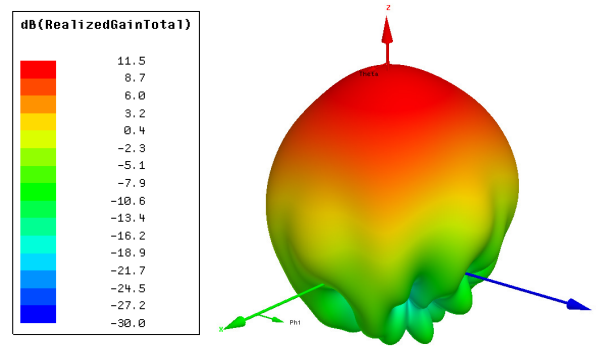


Figure 4.1.4: 3D radiation pattern of the proposed structure at 60 GHz.

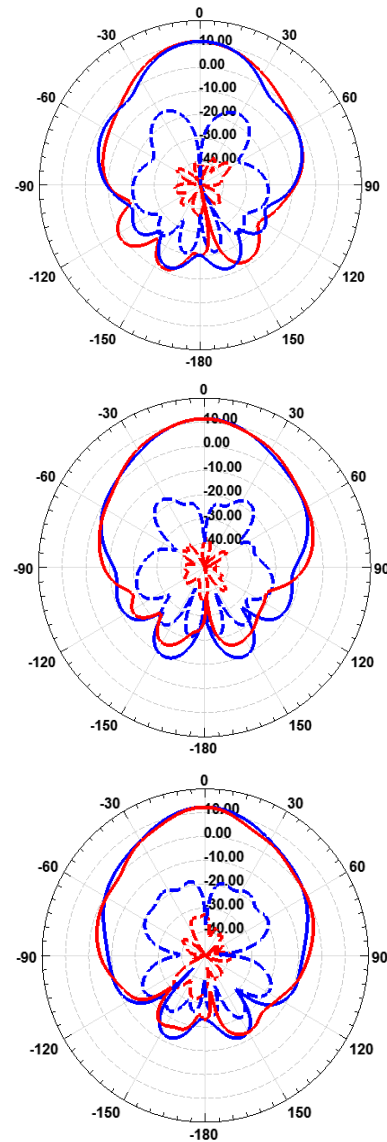
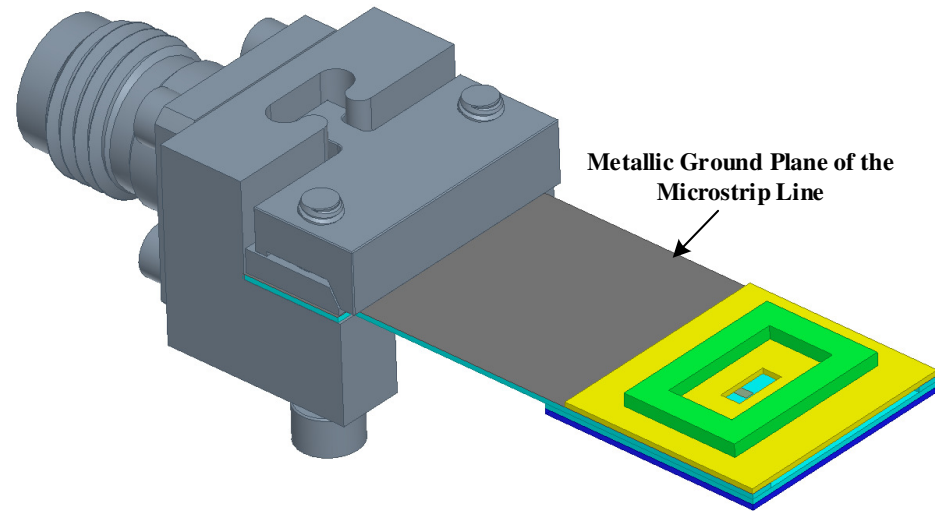


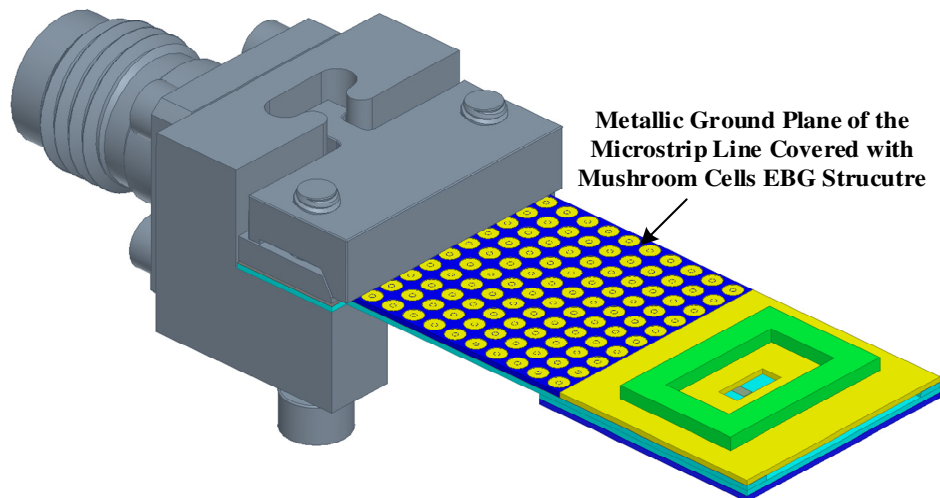
Figure 4.1.5: E-plane (solid red) and H-plane (solid blue), and cross-polar (dashed lines) (Frequencies are: 57 GHz, 60 GHz and 64 GHz from top to bottom).

4.1.5 Practical Characterization and Prototyping Considerations

To characterize the antenna, the antenna must be fed through a coaxial cable connector. Such a connector is very bulky and has a larger relative size compared to the antenna size. Introducing the connector causes asymmetry that affects the symmetry of the radiation pattern in the E-plane. Also, the slot antenna produces a TM surface wave along the transverse direction to the slot. Those TM surface waves couple strongly and propagate along the metallic surface and reflects from the connector body, where the metallic surface acts as a hard surface in this case. To prevent the backward propagation of the TM surface waves and minimize the interaction with the connector body, an EBG surface is inserted on top of the metallic ground plane of the microstrip line. Fig. 4.1.6 shows the two cases (with and without the EBG surface). Fig. 4.1.7 shows the designed EBG cell used on this surface. Its dispersion diagram is removed for brevity that indicated that the EBG band is between 50 to 78 GHz. Fig. 4.1.8 shows the electric field heat map, as can be noticed the case with EBG eliminates the TM surface waves from propagating in the backward direction towards the connector, and hence, minimizes the interaction with the connector body. Fig. 4.1.9 shows the radiation patterns in the principal planes and indicating a more symmetric radiation pattern in the E-plane when the interaction with the connector is reduced.



(a)



(b)

Figure 4.1.6: Proposed antenna structure with the connector body, (a) without using EBG surface, and (b) with the use of EBG surface.

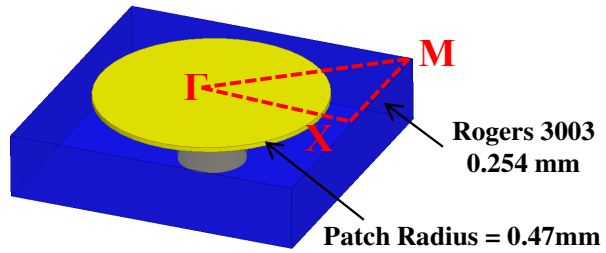


Figure 4.1.7: EBG surface unit cell.

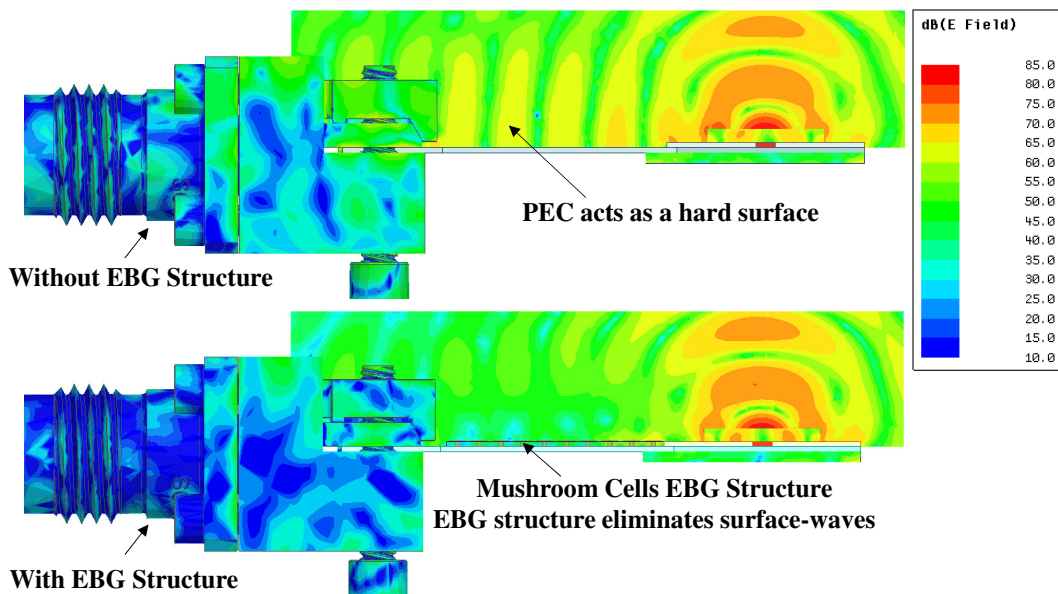


Figure 4.1.8: Electric field heat map for both structures in Fig. 4.1.6 at 60 GHz.

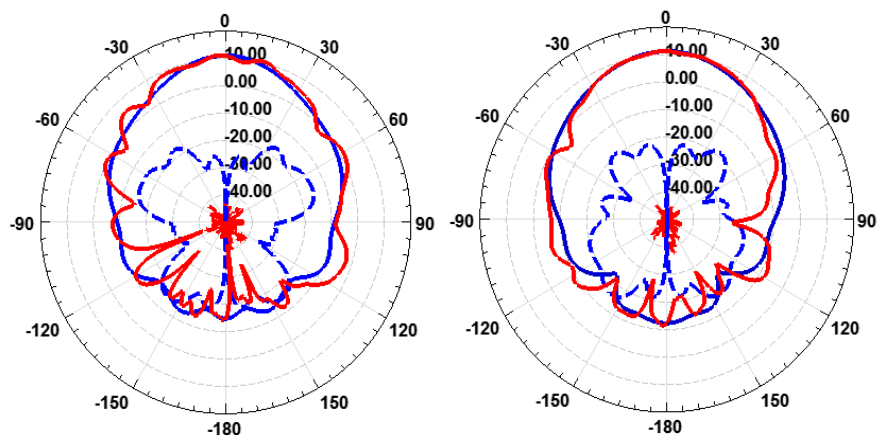


Figure 4.1.9: Co-polar (solid line) and cross-polar (dashed line) radiation pattern at 60 GHz. E-plane (red) and H-plane (blue). Left side without EBG, and right side with EBG.

4.1.6 Array Design

In the previous section, the fundamental aspects of transforming the characteristics of any linear current or magnetic element have been laid out. One realization has been demonstrated by a slot antenna fed by a PRGW feed. Such a realization is not unique. However, it is still advantageous at high millimeter wave frequencies, where the packaged PRGW prevents any spurious radiation from the feeding structure and minimizes the back-lobe radiation as in open microstrip line technologies. In this section, the same previous radiating element is redesigned with Rogers 5880 inserted instead of the air gap. As expected, the dielectric material introduces a higher level of losses, which is more noticeable in the whole structure efficiency at higher frequencies. Also, for long lines, it becomes more significant. The choice of Rogers 5880 is due to its low loss tangent of 0.0009.

The redesign of the previous element with a substrate material instead of the air gap is a cautious step. As for such critical thin dimensions the air gap might suffer from some deformation in its surface uniformity due to some bends in the metal cover sheet which has a thickness of 10 mills. This might be of more concern, even when designing an array with a larger cover sheet. Fig. 4.1.10 shows the cell with the addition of Rogers 5880 instead of the air gap. The dispersion diagram is removed for brevity indicating an EBG between 52 to 74 GHz. Fig. 4.1.11 shows the newly designed antenna and the corresponding dimensions in Table 4.1.2. Fig. 4.1.12 shows an isometric view of the structure, considering the connector effects as detailed out in previous sections. Fig. 4.1.13 shows the radiation patterns for the redesigned antenna. The matching bandwidth and realized gain are shown in Fig. 4.1.14. In Fig. 4.1.14 a comparison between the realized gain and the reflection coefficients of the two cases indicates that the dielectric introduces some losses that affect the gain level. It can be noticed that the level of losses of an additional ~ 1 dB due to the dielectric substrate and the long feed line, including the connector loss effect. Also, the matching bandwidth with dielectric is shifted to the required bandwidth.

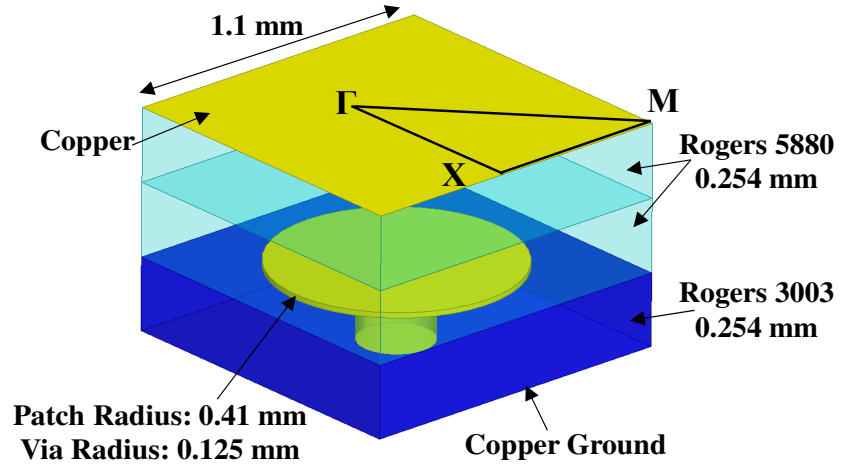


Figure 4.1.10: Unit cell with a dielectric slab instead of the air gap.

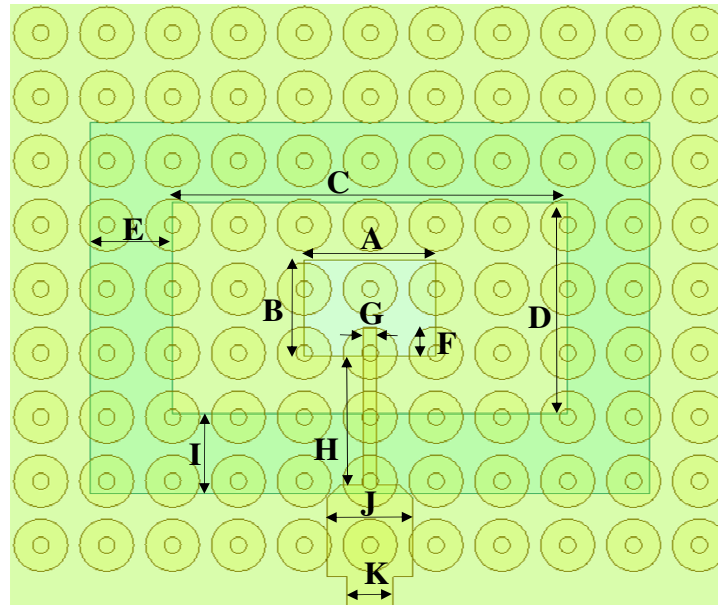


Figure 4.1.11: Proposed antenna structure with a dielectric slab instead of the air gap.

Table 4.1.2: Structure dimensions in (mm)

A	B	C	D	E,I
2	1.5	6	3.3	1.25
F	H	J	K	G
0.44	2	1.3	0.7	0.2

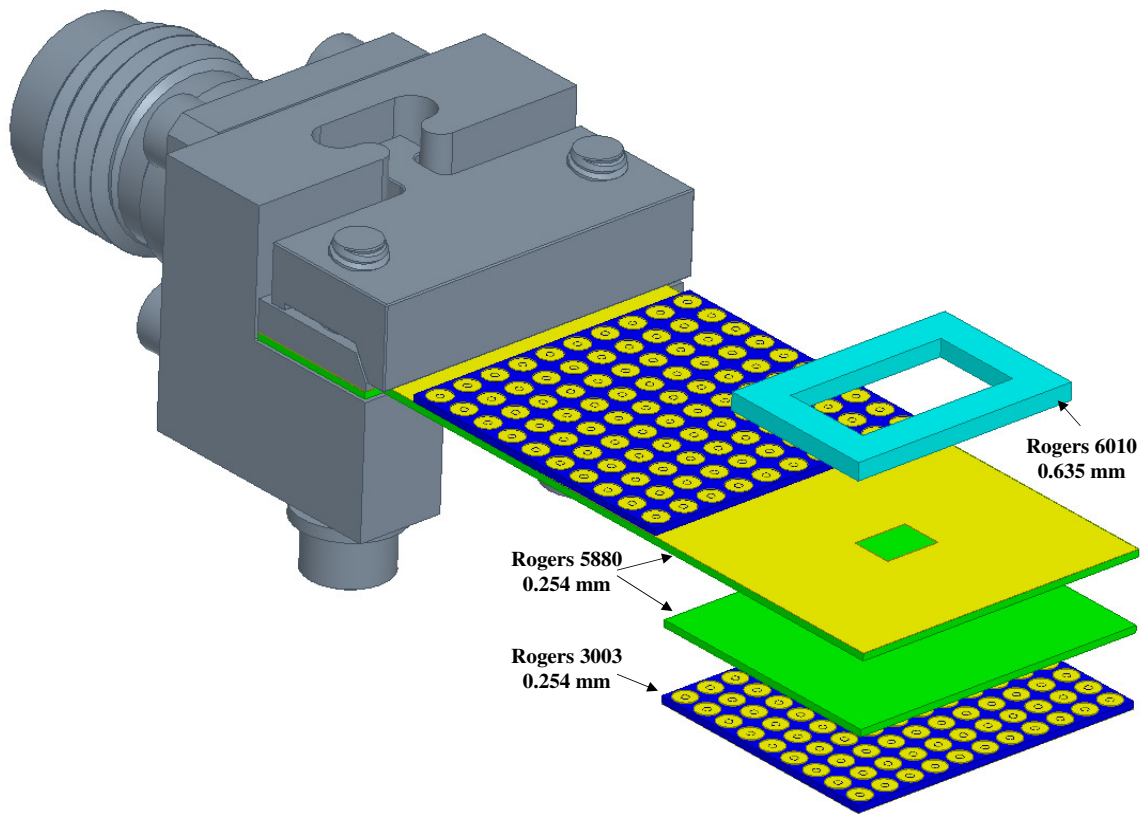


Figure 4.1.12: Isometric view of the redesigned structure.

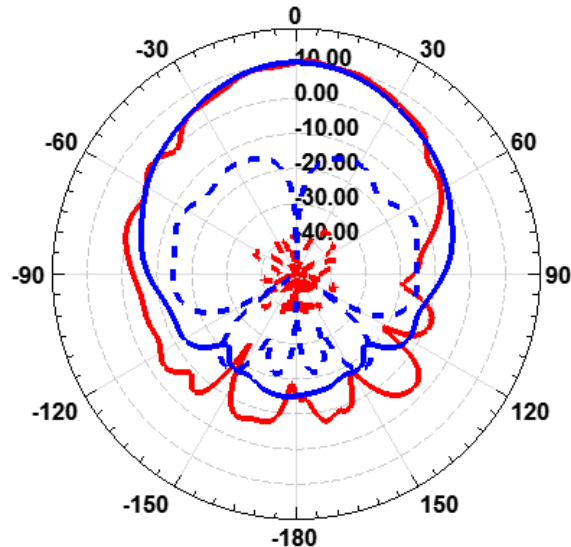


Figure 4.1.13: Co-polar (solid line) and cross-polar (dashed line) radiation patterns at 60 GHz. E-plane (red) and H-plane (blue).

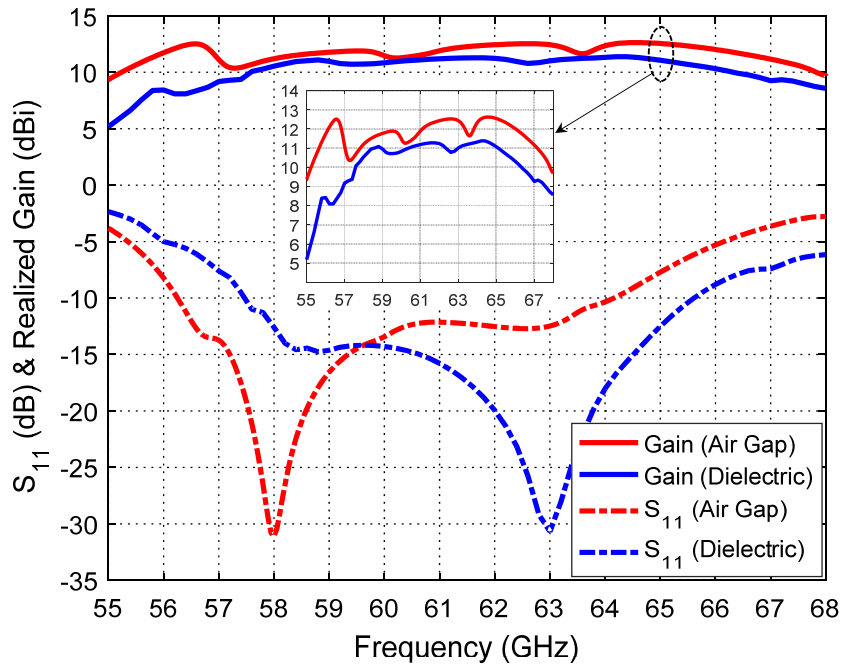


Figure 4.1.14: Realized gain and reflection coefficient of the proposed structure with and without dielectric.

As the element dimension is larger than a wavelength, the use of such element in an array without generating grating lobes is questionable. However, the dielectric ring secondary elements will be shared between adjacent elements, as shown in Fig. 4.1.15, as such, the distance between all the radiating sub-elements of the array, would still be less than half of a wavelength and would prevent the generation of grating lobes. This concept has been detailed out in Chapters 2, and 3 [3], [4]. Another perspective would be noticing the high directivity of the element which suppresses the grating lobes in the array factor. Fig. 4.1.16 shows the feeding network of the structure and its corresponding dimensions in Tables 4.1.3 and 4.1.4.

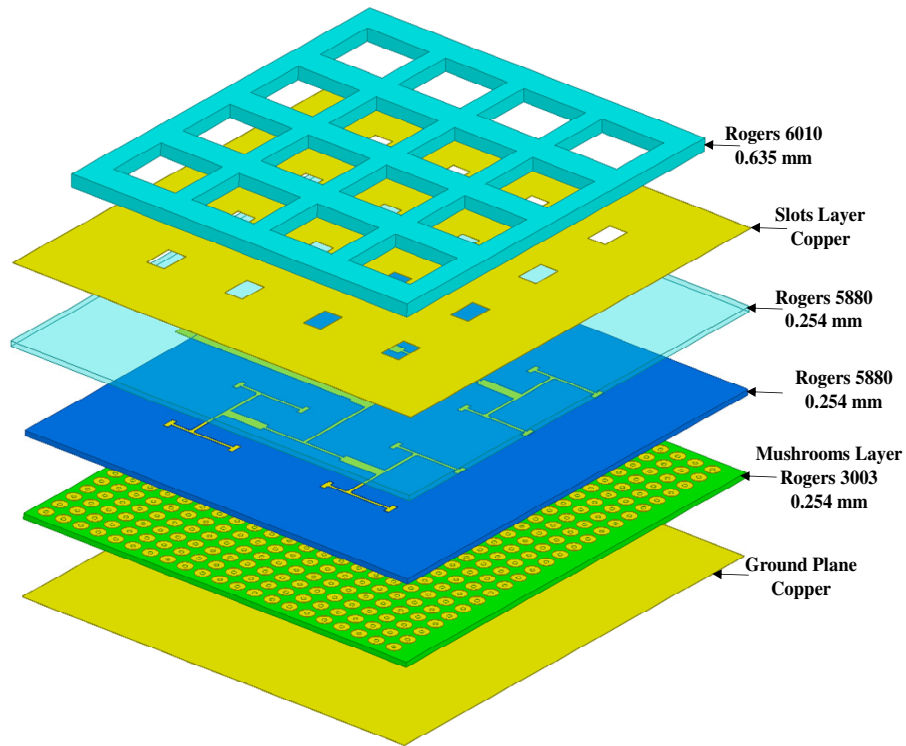


Figure 4.1.15: Proposed antenna array structure.

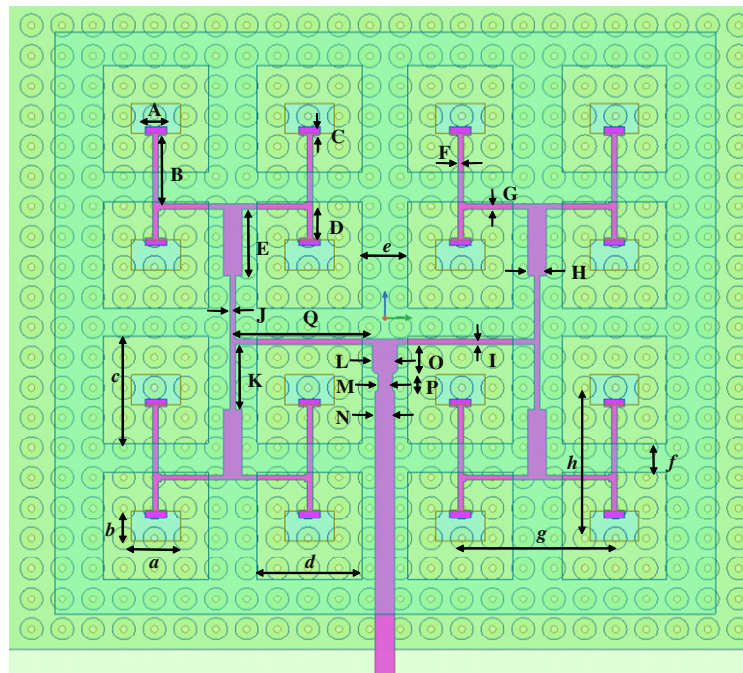


Figure 4.1.16: Proposed antenna array feeding network, feed lines, and slots locations with respect to the mushroom cells.

Table 4.1.3: Antenna array feeding network dimensions in (mm)

A	B	C	D	E	F	G	H	I	J
0.75	2.6	0.3	1.15	2.4	0.2	0.2	0.65	0.2	0.2
K	L	M	N	O	P	Q			
2.45	0.925	0.53	0.68	1.04	0.63	4.89			

Table 4.1.4: Antenna array slots dimensions in (mm)

a	b	c	d	e	f	g	h
1.75	1.1	3.9	3.8	1.7	1.05	5.5	4.95

At this point it's worth mentioning that as the slot dimension has been enlarged to improve the matching bandwidth, and as the slot dimension is large compared to the mushroom cell, the location of the slots and the feed lines with respect to the mushroom cells is very critical in determining the impedance, and consequently the power level at each slot. The feeding network and slots locations were tuned carefully to maintain equal power distribution for each slot, and hence symmetric radiation characteristics in the E and H plane. Also, as the dielectric ring is shared between several slots, the whole thicknesses of the ring slabs were tuned as well in such a way that the induced secondary sources in the dielectric ring would still have the appropriate power level and phase to maintain radiation symmetry and low grating lobes in principal planes. Figs. 4.1.17 - 4.1.18 show the radiation patterns of the proposed antenna array.

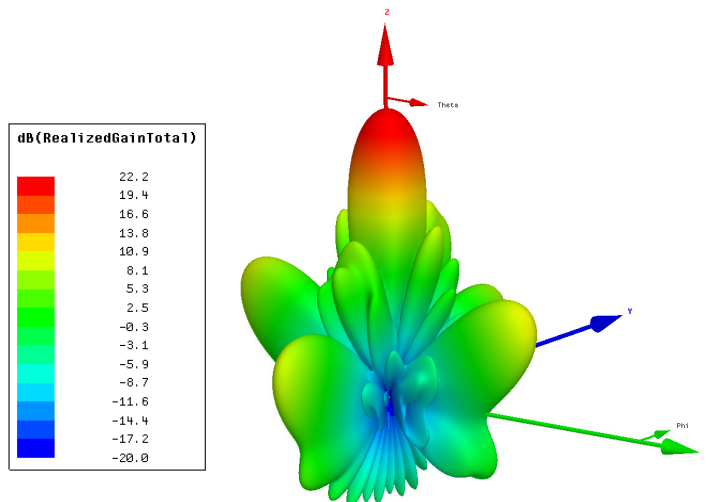


Figure 4.1.17: 3D radiation pattern for the proposed antenna structure.

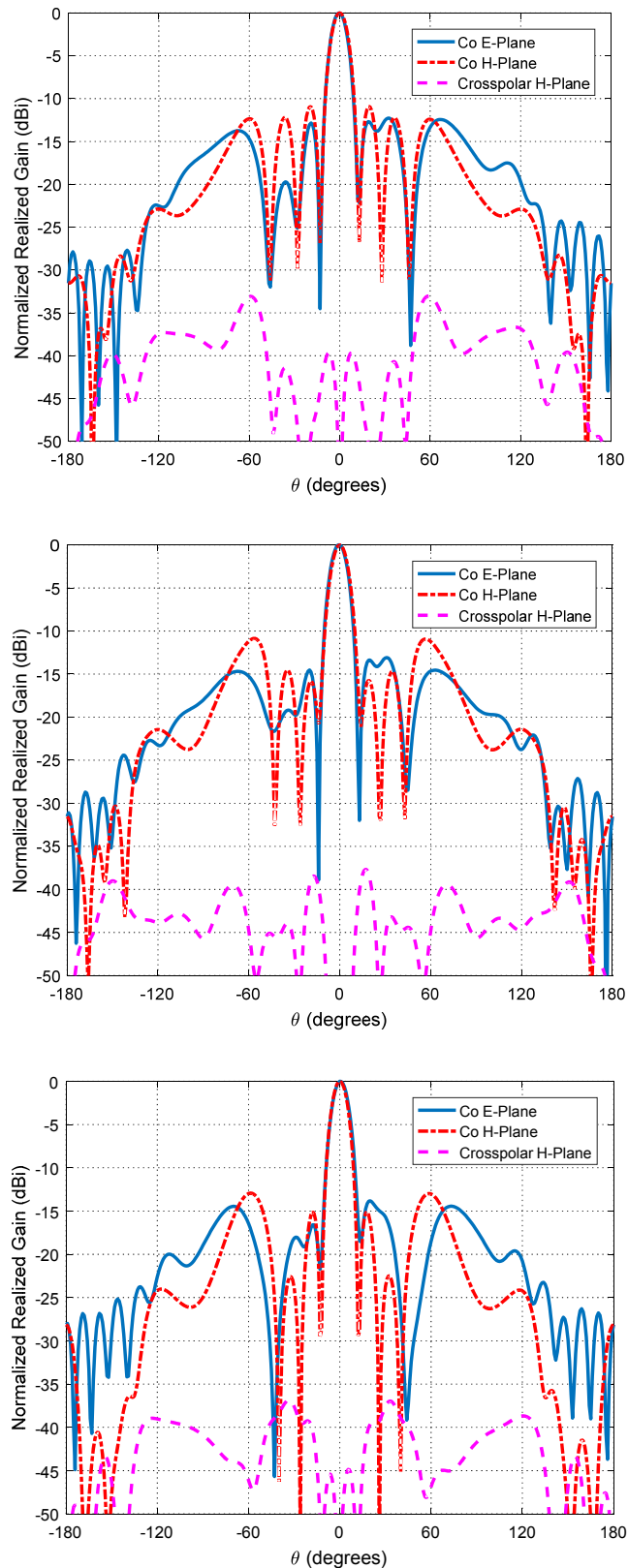


Figure 4.1.18: Radiation patterns at 58, 60, 64 GHz from top to bottom, respectively.

Similar to the previous section, the connector effect has been taken into consideration. An EBG structure has been used to reduce the effect of the backward propagating waves towards the connector body. The introduction of the connector and the longer feed line has some slight effect in reducing the gain and the side lobe level performance. However, it is still within an acceptable range. Also, such connector and long feed line have been introduced for the measurement purposes only, and their existence won't be applicable in the practical integrated transceiver system.

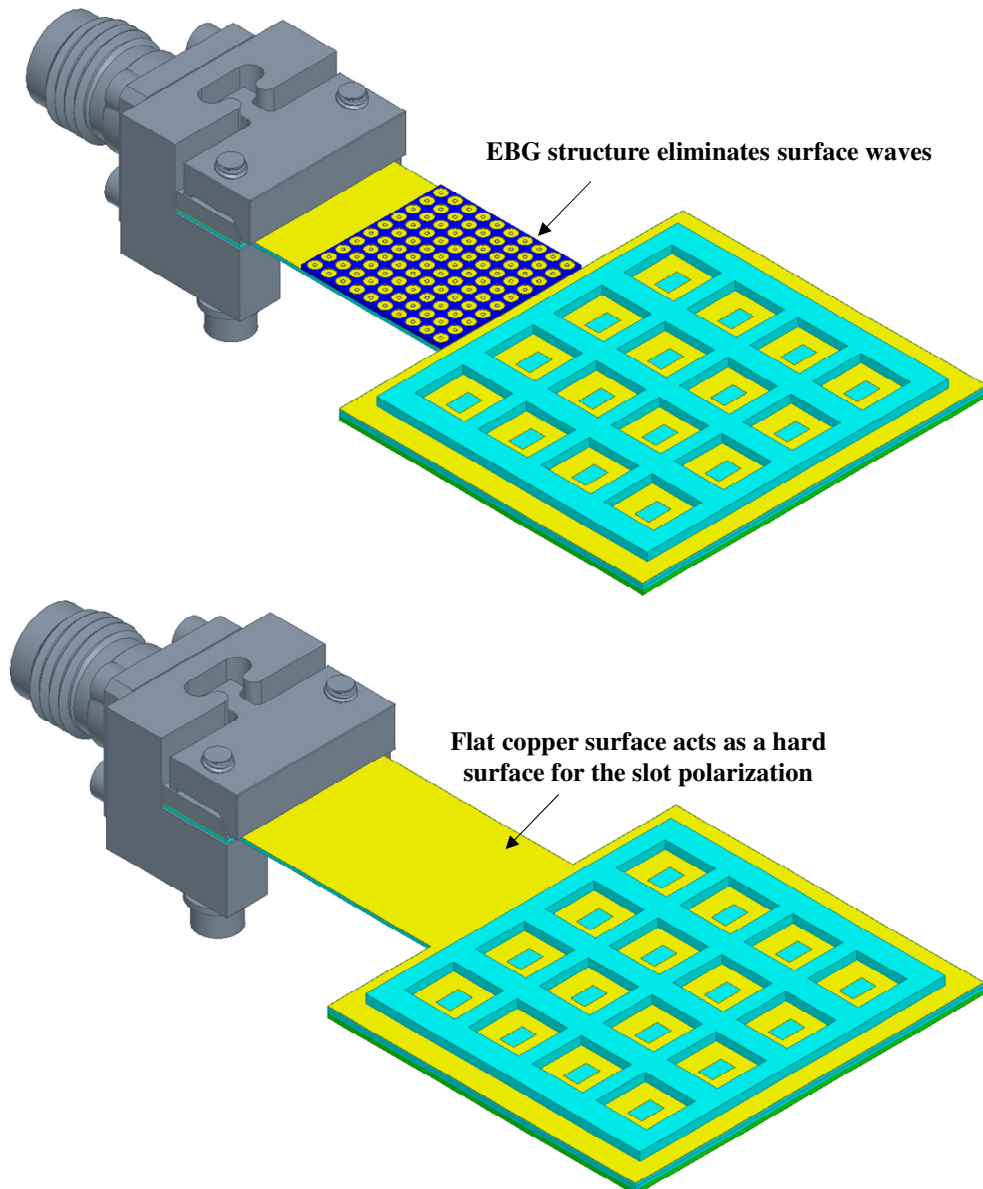


Figure 4.1.19: Proposed antenna structure with the connector body, without using EBG surface (bottom), and with the use of EBG surface (top).

Fig. 4.1.19 shows the array structure with and without the EBG surface that reduces the interaction with the connector at the input of the feeding network. Fig. 4.1.20 shows the heat map for both structures in Fig. 4.1.19. As shown, the EBG structure helps in eliminating the backward propagating waves towards the connector body. However, slight asymmetry and reduction in the side lobe level are expected due to the connector body.

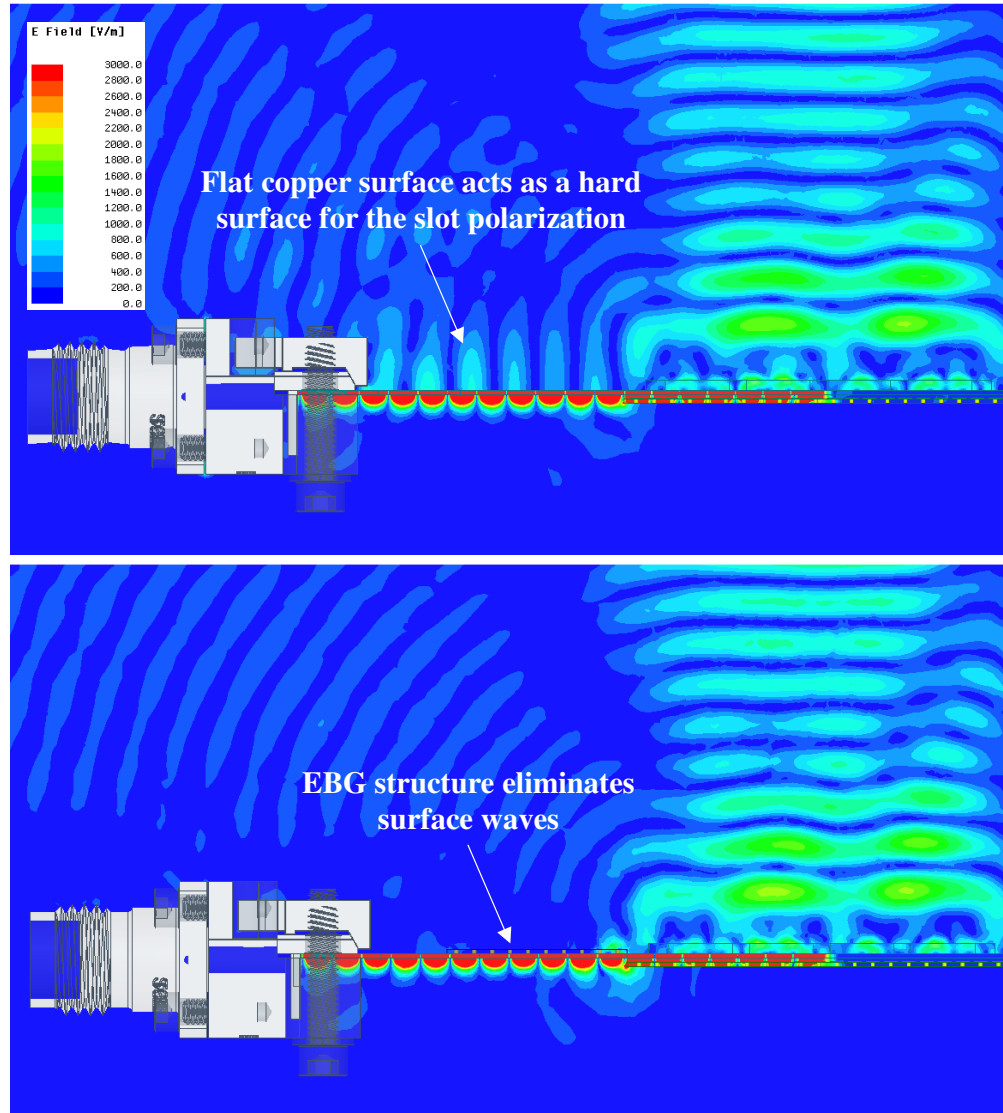


Figure 4.1.20: Electric field heat map with and without EBG surface.

4.1.7 Experimental Prototyping results

Fig. 4.1.21 shows the actual fabricated prototype of the array structure. The size of the connector is massive compared to the antenna size. Introducing such a connector, for the sake of measurement, distorts the radiation pattern. Therefore, a longer feeding microstrip line is used to feed the antenna to reduce the connector effect on the antenna pattern. The extended feeding line introduced high losses. It is important to note that the connector with long feeding line exists only for measurement purposes. However, in the practical integrated system, the antenna is to be connected directly to the next circuitry stages, which could usually be a bandpass filter or an amplifier. Thus, such adverse effects of the connector can be mitigated. Fig. 4.1.22 shows the measured radiation pattern in principal planes. Fig. 4.1.23 shows measured and simulated gain and antenna efficiency as well as the reflection coefficients. A gain of 22 dBi is achieved with a matching bandwidth of 13.3%. As can be seen, an acceptable agreement with simulated results is observed, some drop in the measured gain (21 dBi) over the simulated results is also noticed due to higher losses in the material over the simulated one. One of the main reasons for such losses is the glue used to stack the substrate layers on top of each other.

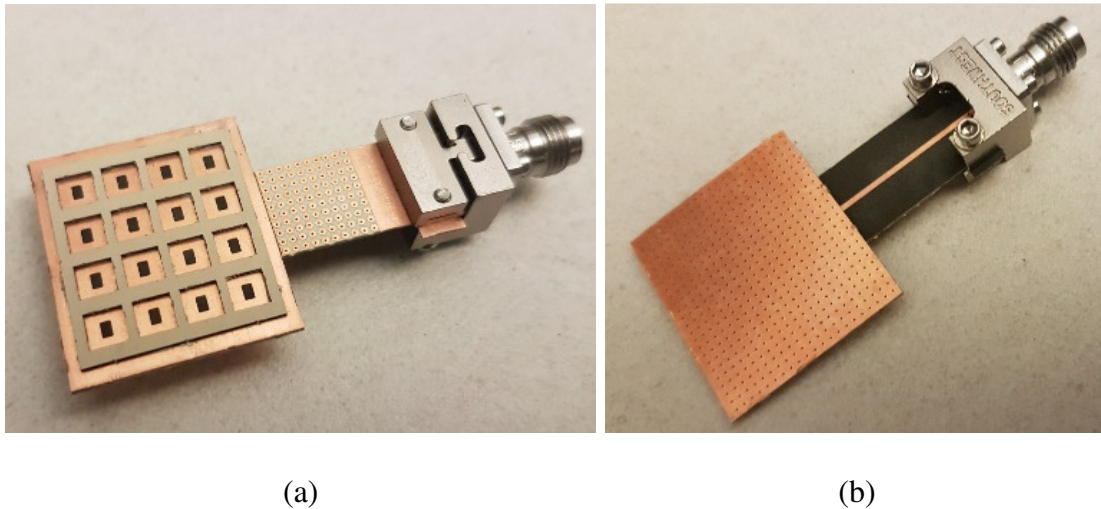


Figure 4.1.21: Actual array fabricated prototype, (a) top, and (b) bottom view.

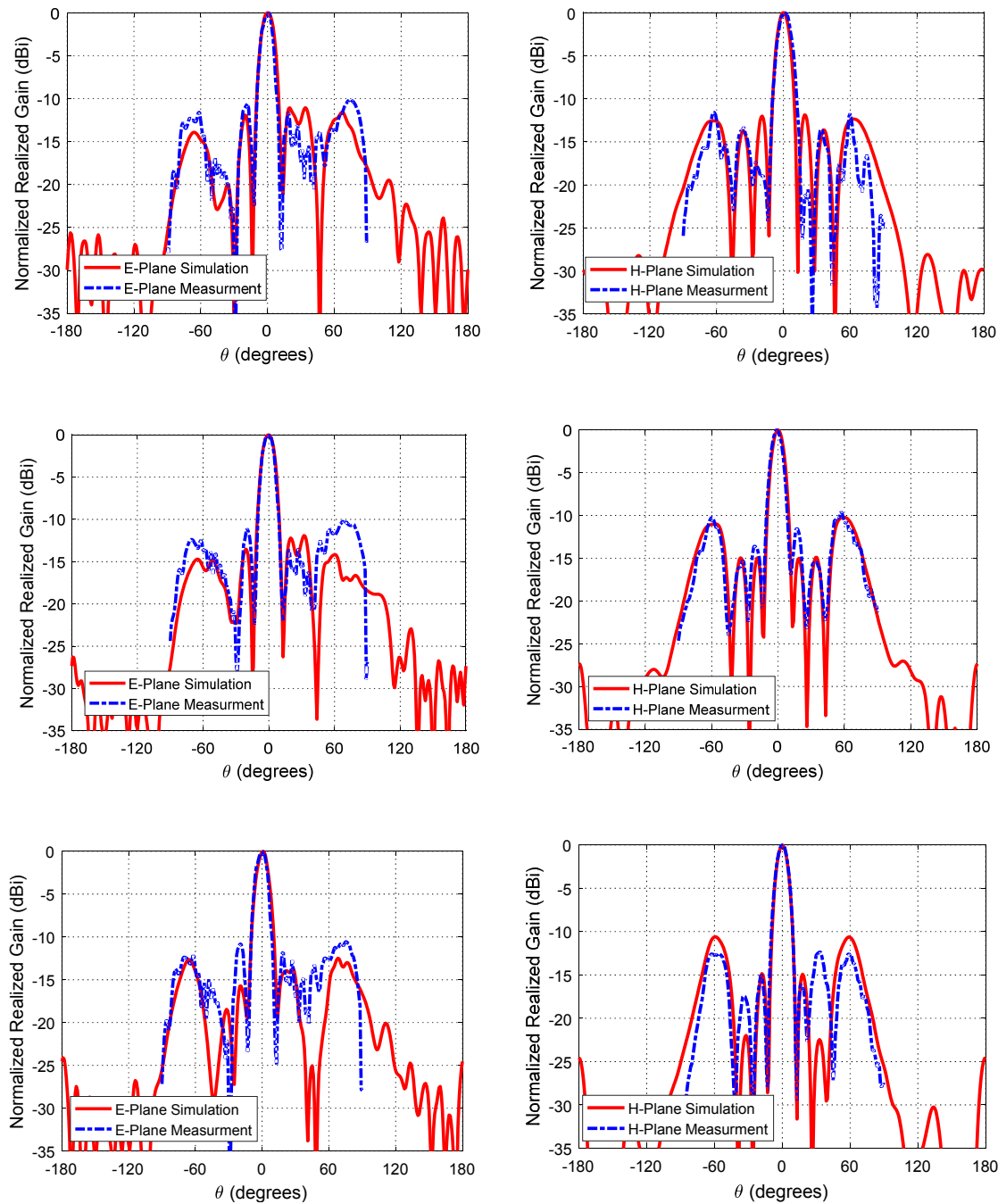


Figure 4.1.22: Radiation patterns at 58, 60, 64 GHz from top to bottom respectively (E-plane {left} and H-plane {right}).

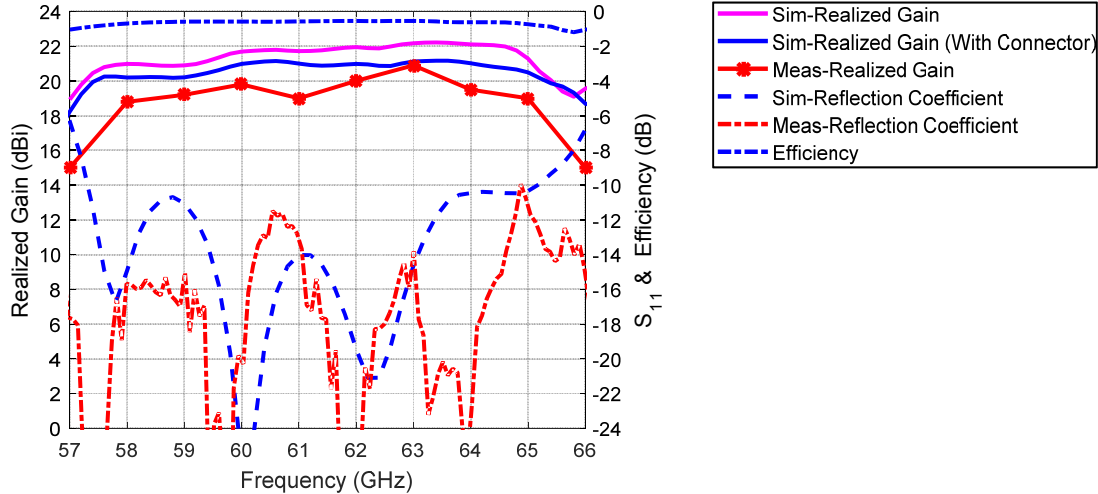


Figure 4.1.23: Realized gain, reflection coefficient, and efficiency of the proposed antenna array.

The efficiency is calculated over the band of interest; the efficiency of the array goes up to 88 %. The efficiency is plotted in dB scale in Fig. 4.1.23, as the figure shows, the efficiency is around -0.55 dB. Table 4.1.5 compares the proposed antenna array with others in the literature. As can be seen, the gain of the proposed antenna array is higher than any 4x4 antenna array, and this is the main merit of the proposed antenna in this work. As by the feed of only 4x4 elements, the gain of the antenna can be improved dramatically and can compete with a higher number of element arrays. This can be easily deduced by the fact that doubling the antenna array size would result in an ideally 3-dB increase in the gain. The use of the induced secondary sources between the elements allows such an increase in the antenna gain. As well, it allows for the considerable distance between the elements without significant high grating lobes. Moreover, the elevated distance allows more freedom in increasing the slot width in order to improve the bandwidth. The bandwidth of the proposed antenna array goes up to 13 %. Nonetheless, the ME dipole elements and excited cavity slots are always superior in their bandwidth performance due to their known low-quality factor feature. The concept of reducing the feed points to obtain the same gain performance level, by the use of the induced secondary sources without generating grating lobes, is very advantageous at millimeter-wave frequencies, wherein such case the design of the feeding network can be relaxed significantly, in such a way to satisfy the gain requirement less number of elements has to be fed, and this reduces the size of the feeding network, and the incorporated losses in the feeding structure.

Table 4.1.5: Comparison with other works

Ref.	Frequency	Array Type	Elements Number	BW (%)	Gain (dBi)
[2]	60 GHz	Gap Waveguide Slot Array	8x8	14	25
[39]	60 GHz	PCB Fringing Fields Ant.	1x4	11.6	16
[28]	60 GHz	PCB Monopoles	1x2	11.6	14
[12]	60 GHz	SIW Slot Antenna Array	12x12	4.17	22
[21]	60 GHz	Patch Antenna Array	4x4	11.6	18
[45]	60 GHz	SIW Slot Antenna Array	4x2	11.6	12
[46]	60 GHz	SIW Slot Antenna Array	8x8	17.1	22.1
[47]	60 GHz	Patch Antenna Array	4x4	9.5	18.2
[48]	60 GHz	Patch Antenna Array	4x4	28	16
[49]	60 GHz	SIW Slot antenna array	4x4	20.8	18.3
[50]	60 GHz	Microstrip Antenna Array	4x4	25.5	15.2
[51]	30 GHz	SIW slot antenna array	4x4	8.5	19.1
[52]	45 GHz	Microstrip Antenna Array	4x4	24.4	18.8
[53]	30 GHz	SIW slot Antenna Array	4x4	4.6	16
[54]	60 GHz	Patch Antenna Array	4x4	18.3	17.5
Present	60 GHz	Slot Antenna Array	4x4	13	21

4.2 Wideband Millimeter-Wave DRA with Gain Enhancement

4.2.1 Introduction

Dielectric Resonator Antenna (DRA) is preferred at millimeter-wave frequencies due to their high efficiency [15], [73]–[79]. Moreover, in the case of millimeter-wave frequencies, the size of the DRA becomes smaller, and with the use of the appropriate dielectric constant, the size of the DRA shrinks more. Therefore, the common bulky feature of DRA is not as severe at millimeter-wave frequencies compared to lower frequencies. For broadside radiation, several gain enhancement techniques were adopted for the DRA such as Yagi-Uda concept [80], superstrate planar lens [81]–[84]. However, these techniques increase the antenna height and have limited bandwidth.

In this section, a novel technique is proposed to enhance the gain of a DRA antenna over a wideband range of frequencies. The proposed antenna structure has a relative bandwidth of 27.5-% in the 60 GHz band and a peak realized gain of 12.5 dBi. The peak of the total antenna radiation efficiency is 96 %. The proposed antenna is suitable for high data rate short-range personal area networks applications. Printed Electromagnetic Band Gap (EBG) technology is used to feed the antenna to eliminate any parasitic radiation from the feed line. The characterization of 60 GHz antennas is very challenging. The end launch connector used to feed the antenna at such frequency is relatively massive compared to the antenna dimensions, and that consequently affects the fidelity of the characterization of the antenna, especially if it is in the vicinity of the antenna. EBG surfaces have been used to resolve such characterization impairments.

4.2.2 Proposed Dielectric Resonator Antenna Structure Qualitative Analysis

Fig. 4.2.1 shows a simplified sketch, conveying a theoretical abstraction of the proposed antenna structure, such sketch is very descriptive and essential in grasping the radiation mechanism of the proposed structure. If a DRA is surrounded by a dielectric ring and the width “d” of the dielectric ring is in the range of a quarter guided wavelength. Then, the ring acts as a reflector [85], where the incident radiated waves generated from the DRA gets trapped within the dielectric ring

material, and a minimal amount of energy leaks beyond the dielectric ring [85]. Therefore, the trapped fields within the dielectric ring are equivalent to radiating secondary sources, as per the equivalence principle presented in [64]. The secondary sources radiate in a constructive way with the main DRA. Therefore, the radiation is boosted significantly in the boresight direction. The phase and magnitude of the secondary sources can be controlled by controlling the vertical and horizontal dimensions of the dielectric ring [85].

In DRAs, it is known that various modes can be excited; each mode has its unique radiation characteristics. In this section, we investigate the TM₃₁ Mode, which is known for having relatively higher gain and bandwidth than the other lower order modes [86].

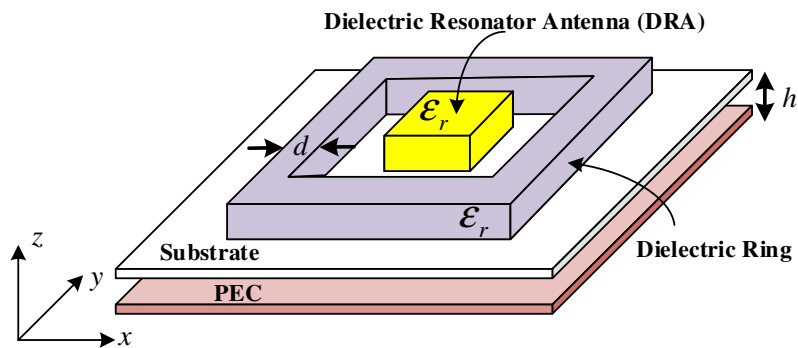


Figure 4.2.1: Sketch of the DRA surrounded by a dielectric ring.

The TM₃₁ mode suffers from a relatively high level of radiation off the boresight direction. In the following section, we show that the proposed technique resolves the off-boresight radiation of the TM₃₁ mode in addition to enhancing the antenna gain.

4.2.3 Proposed Dielectric Resonator Antenna Structure

Fig. 4.2.2 shows the proposed DRA antenna structure. The antenna is fed by a narrow slot. The slot is coupled to a Printed Ridge Gap Waveguide “PRGW” feed line. Rogers 6010, with a dielectric constant of 10.2 and a thickness of 0.635 mm is used for the DRA material. The rectangular ring also uses the same substrate material with the same thickness. The dispersion diagram of the EBG cell is removed for brevity, indicating that the EBG of this cell between 47 to

74 GHz. The patch radius is 0.41 mm, via radius is 0.125 mm, and cell periodicity of 1.1 mm. Further details about PRGW can be found in [87]–[89].

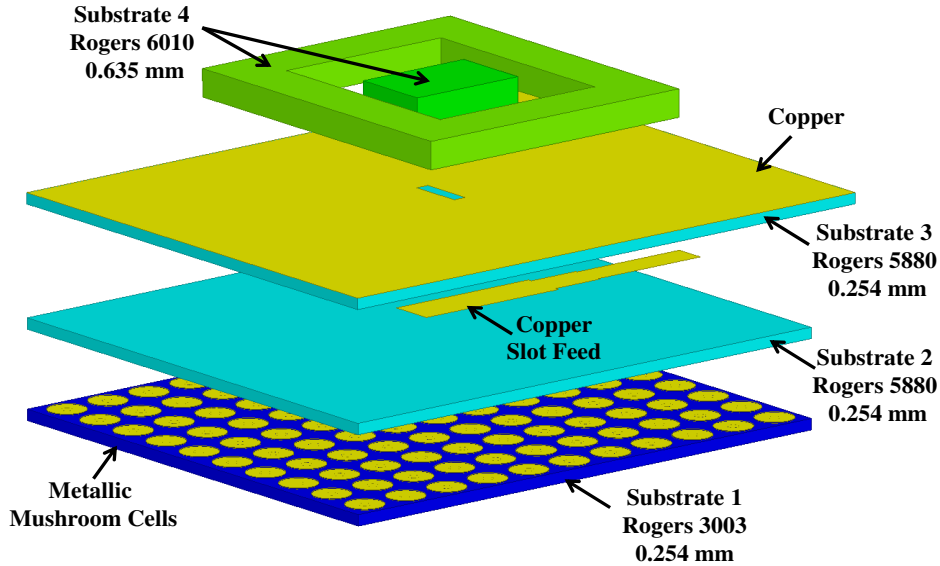


Figure 4.2.2: Proposed DRA structure.

Fig. 4.2.3 shows the magnetic scalar and vector field heat maps of the proposed DRA. As can be noticed from the heat maps, the DRA is excited with TM₃₁. The main sources are located within the DRA, and the excited secondary sources are trapped within the rectangular dielectric ring. All together radiate in phase in the boresight direction. As also noticed from the vector field heat map in Fig. 4.2.3, the electromagnetic waves are trapped in the dielectric ring as a standing wave and have minimal propagation beyond the ring. Also, it is to be mentioned that the DRA modes are excited by the slot antenna, and the dimensions of the DR determines the resonance and the modes excited within the cavity, and as the DRA radiates, the wave impinges on the dielectric ring and gets trapped in the dielectric ring as a standing wave, in such a case the ring field distribution depends on the wave-front of the impinging waves generated from the DRA, as can be seen from the vector field heat map, the front of the wave spreads almost similar to a dipole pattern, and this explains the spread of the mode along the horizontal direction. However, the vertical direction is governed by the quarter wavelength width to minimize the wave propagation beyond the dielectric ring. In simple words, the rectangular DRA is usually excited internally by a slot. Therefore, it is governed by the DR resonances, but the ring is excited externally by the impinging waves on it. It

is not also governed by the ring cavity resonances, but by the quarter wavelength width to maximize reflectivity.

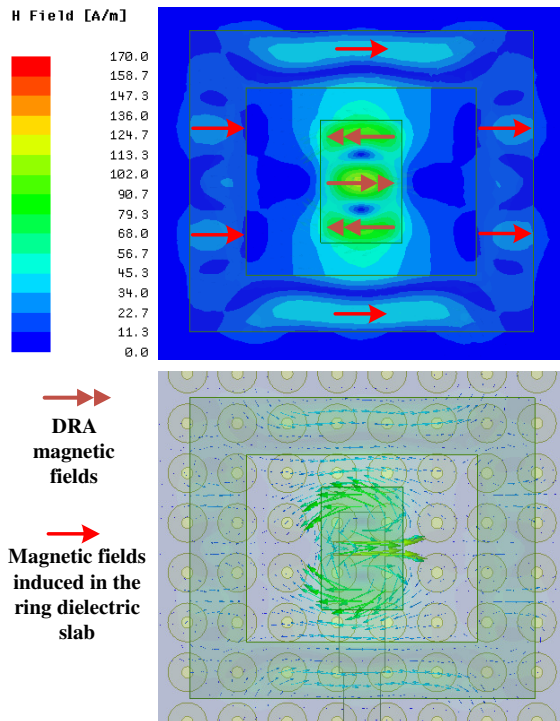


Figure 4.2.3: Magnetic vector and scalar field heat maps for the proposed DRA structure.

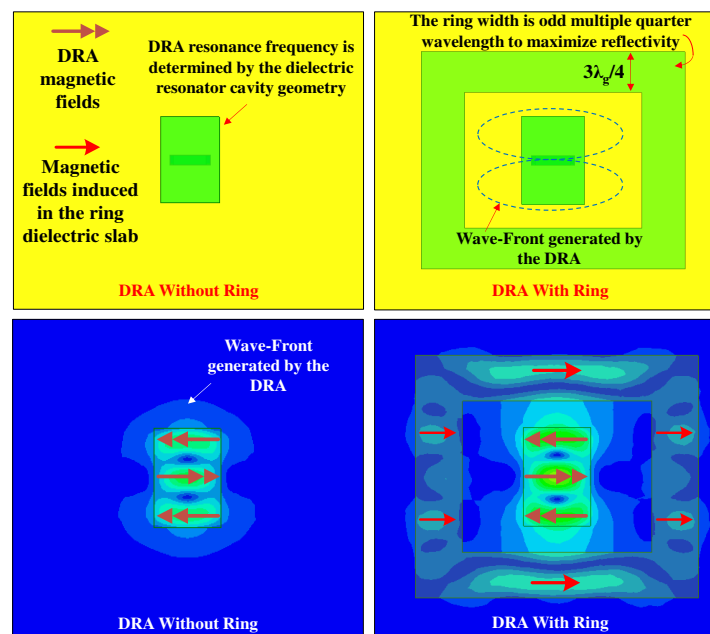


Figure 4.2.4: Magnetic field heat map for the DRA with/without a dielectric ring (same H-field scale as in Fig. 4.2.3).

The DRA TM_{31} mode is known to have high relative bandwidth. However, it has relatively high radiation off the boresight direction. This can be illustrated by comparing Figs. 4.2.4-4.2.6. Fig. 4.2.4 shows the heat map of the DRA with and without the dielectric ring. Fig. 4.2.5 compares the directivity in each case, which shows a significant gain enhancement. Fig. 4.2.6 shows the radiation patterns in each case, as can be seen, the gain is enhanced, and the radiation level off boresight is reduced for the ring case, in addition to the cross polarization reduction.

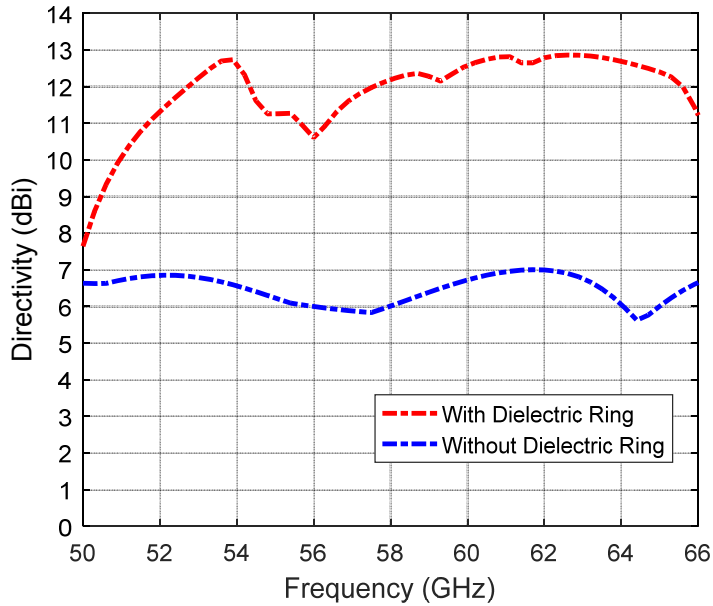


Figure 4.2.5: Directivity of the DRA with/without a dielectric ring.

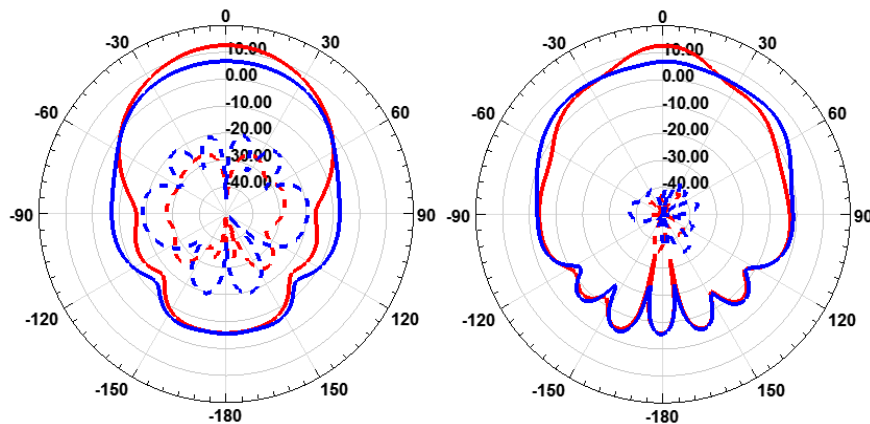


Figure 4.2.6: Radiation patterns with and without the dielectric ring at 60 GHz.
(Red) with a dielectric ring, (Blue) without a dielectric ring, right (E-plane),
left (H-plane), Solid (Co-polar), Dashed (Cross-polar), at 60 GHz.

In the process of realizing the structure, the rectangular DRA must be aligned in the middle of the dielectric ring. The alignment of the DRA is very critical in such case, especially for a DRA operating at 60 GHz, where the dimensions can go in the order of sub-millimeters. Therefore, as the antenna can couple weakly in the H-plane, the insertion of a dielectric slab, as shown in Fig. 4.2.7 along the x-axis will not have any significant effect on either the antenna impedance or radiation characteristics. Therefore, the second structure shown in Fig. 4.2.7 is preferred over the first one. In such a case, the DRA and the rectangular ring are connected to reduce the misalignment possibility between them. From the heat map shown in Fig. 4.2.7, it can be seen that the connecting part has no effect. The coupling through the alignment slabs is very week. Fig. 4.2.8 shows a top view of the proposed antenna structure, and the corresponding dimensions are shown in Table 4.2.1. Fig. 4.2.9 shows the reflection coefficient and the realized gain for both structures (with/without alignment arms), as can be noticed from the figure, the differences between the two structures are minimal as expected. The antenna has a relative bandwidth of 27.5 % (16 GHz bandwidth). The peak realized gain goes up to 12.6 dBi with stable performance over the frequency band. Fig. 4.2.10 shows the radiation pattern in the principal planes for the DRA structure with the alignment arms.

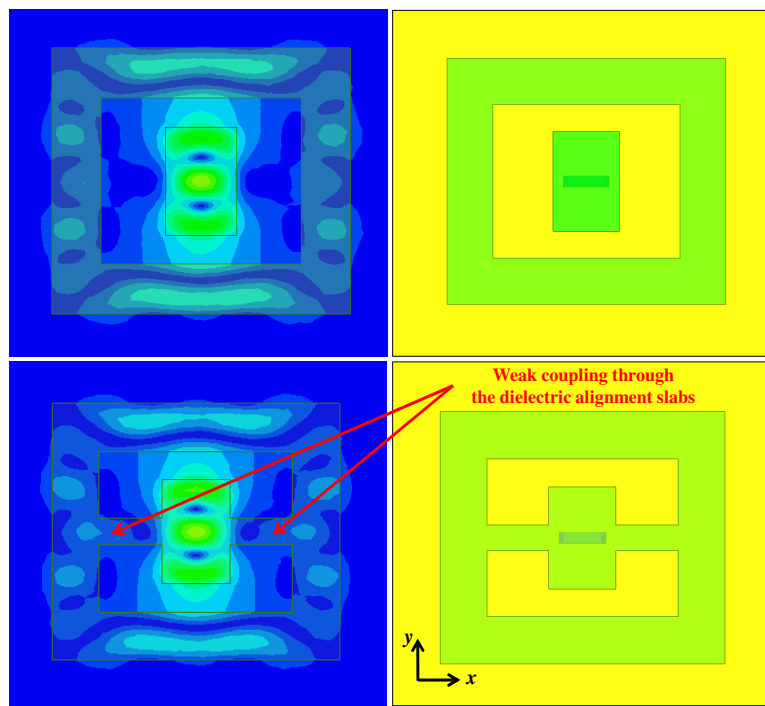


Figure 4.2.7: Magnetic vector field heat map for the DRA with/without alignment arms (same H-field scale as in Fig. 4.2.3).

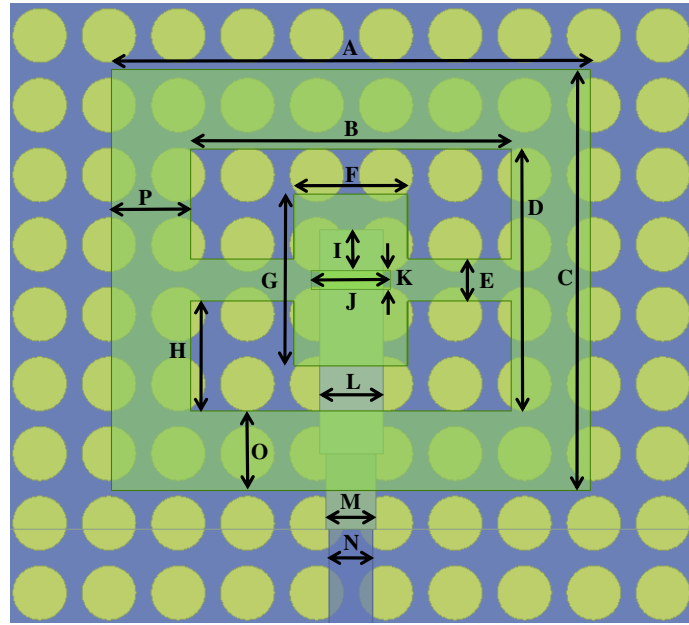


Figure 4.2.8: Top view of the proposed DRA structure.

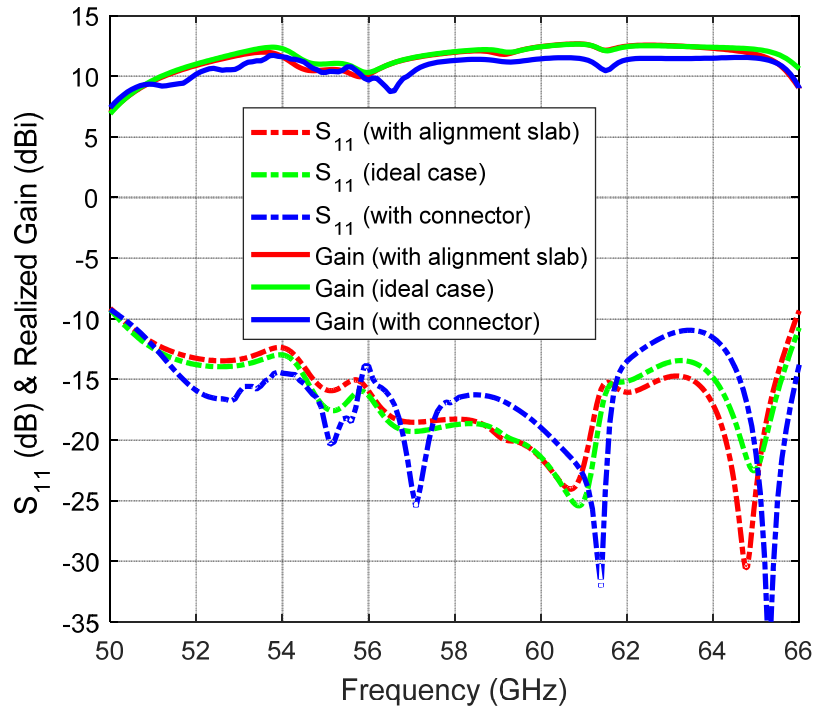


Figure 4.2.9: Gain and reflection coefficient of the proposed DRA structure.

Table 4.2.1: Proposed DRA structure dimensions in (mm)

<u>A</u>	<u>B</u>	<u>C</u>	<u>D</u>	<u>E</u>	<u>F</u>	<u>G</u>	<u>H</u>
7.6	5.1	6.55	4.05	0.675	1.8	2.7	1.6875
<u>I</u>	<u>J</u>	<u>K</u>	<u>L</u>	<u>M</u>	<u>N</u>	<u>Q</u>	<u>P</u>
0.65	1.25	0.3	1	0.8	0.7	1.25	1.25

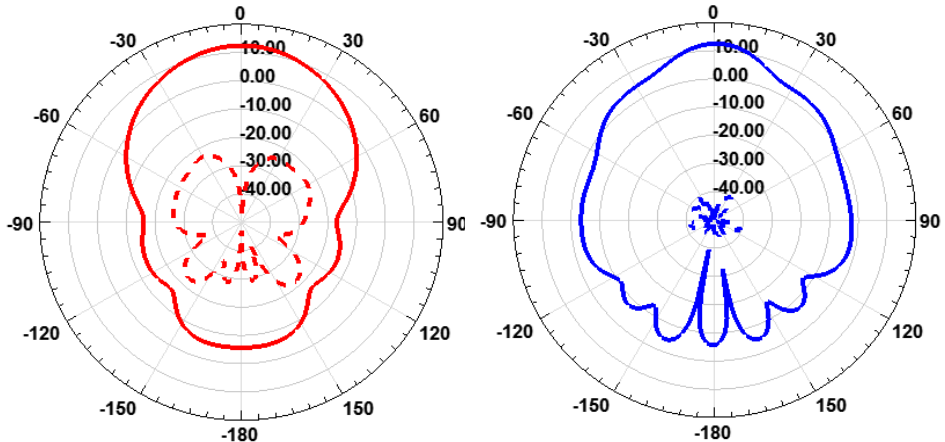


Figure 4.2.10: Red (H-plane), Blue (E-plane), Solid (co-polar component), Dashed (cross-polar component) at 60 GHz.

For measurements, the antenna must be connected to an end launch connector. The connector size is massive compared to the antenna size. Fig. 4.2.11-(a) shows the antenna connected to the end launch connector.

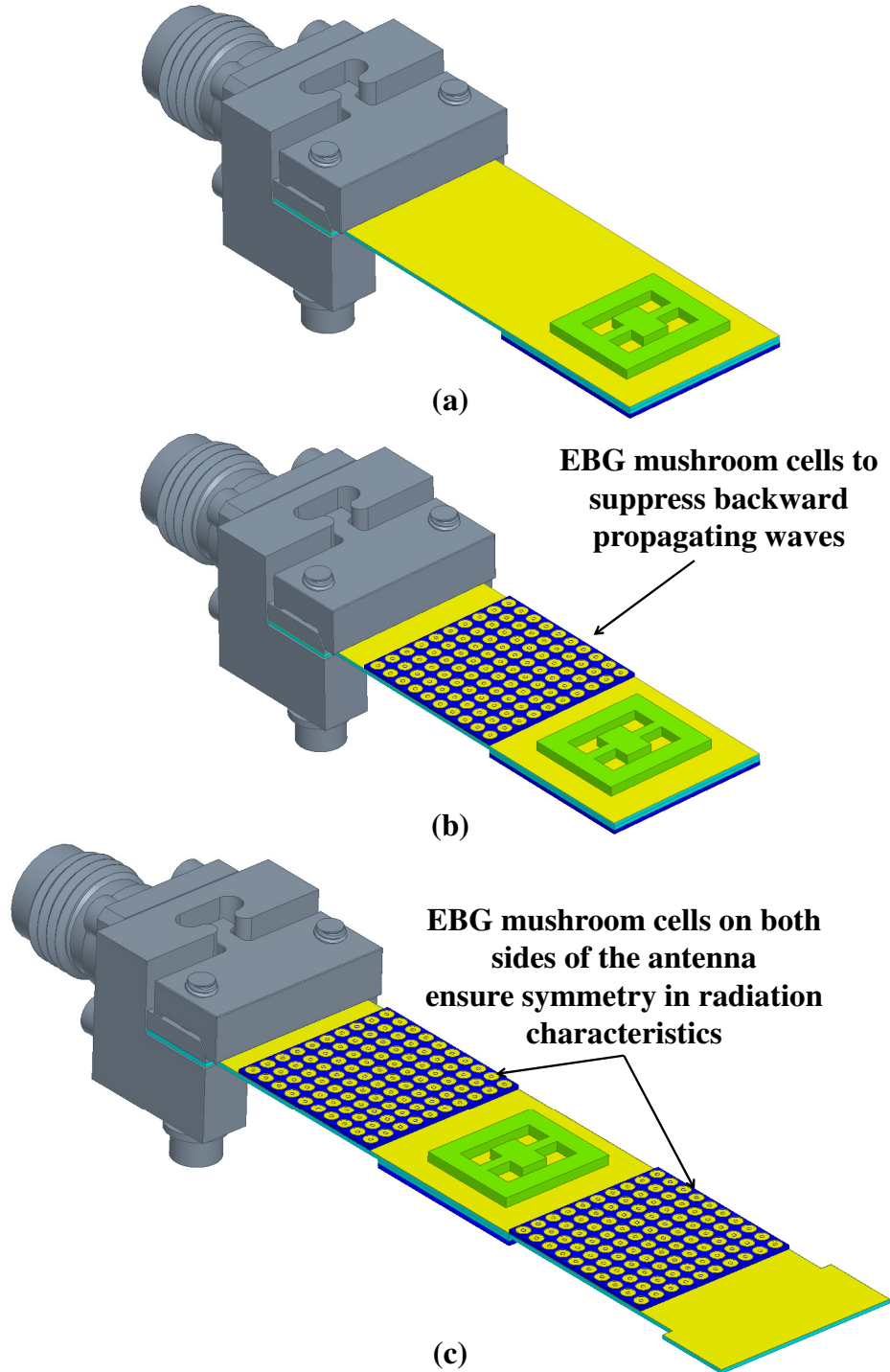


Figure 4.2.11: (a) Proposed DRA, (b) with single EBG surface, (c) with double EBG surfaces.

The copper surface acts as a hard surface to the normal component produced by the antenna. Therefore, the backward propagated waves towards the connector will be scattered from the connector body that distorts the radiation characteristics of the antenna. To prevent the backward waves from propagating towards the connector body, an EBG surface can be inserted as shown in Fig. 4.2.11-(b). The used mushroom cell is a circular mushroom cell with a patch radius of 0.47-mm, a via radius of 0.125-mm, a Rogers 3003 substrate material of 0.254 mm thickness. The cell dispersion diagram is shown in Fig. 4.2.12.

It can be noticed that the antenna still has significant radiation in the end-fire direction, which can be easily observed from the radiation pattern shown in Fig. 4.2.10. In such a case, diffracted fields have a significant level. As one side of the antenna diffracts the fields from the PEC edge, the other edge diffracts the fields from the EBG edge. Therefore, the asymmetry between the two edges type shows its effect on the radiation pattern. To resolve this issue, a double EBG surface on both sides is used, as shown in Fig. 4.2.11-(c). Fig. 4.2.13 shows the corresponding electric field heat map for the proposed structures in Fig. 4.2.11.

Fig. 4.2.14 shows the radiation patterns for each structure. As can be seen from Fig. 4.2.14 the double EBG surface structure has the lowest cross-polarization level and the best front to back ratio as expected. Also, the heat map in Fig. 4.2.13 shows clearly the effect of the diffracted fields from the edges in higher back-lobe radiation and asymmetry of the radiation pattern. Fig. 4.2.14-(d) shows the 3D radiation pattern of the double EBG surfaces structure.

Fig. 4.2.15 shows the fabricated prototype for the proposed DRA. Fig. 4.2.16 shows the measured radiation patterns in the principal planes and Fig. 4.2.17 shows the measured gain and S-parameters. Good match with the simulated results is observed. The measured gain goes up to 12.6 dBi. The 10 dB return loss bandwidth is 27.5 %. Some slight differences within an acceptable limit are observed due to the glue and tolerances of the used materials and dimensions. Such results show that the proposed EBG and alignment techniques are adequate in countering the measurement challenges at 60 GHz. The total simulated radiation efficiency is also shown in Fig. 4.2.17, maximum efficiency of 96% is achieved.

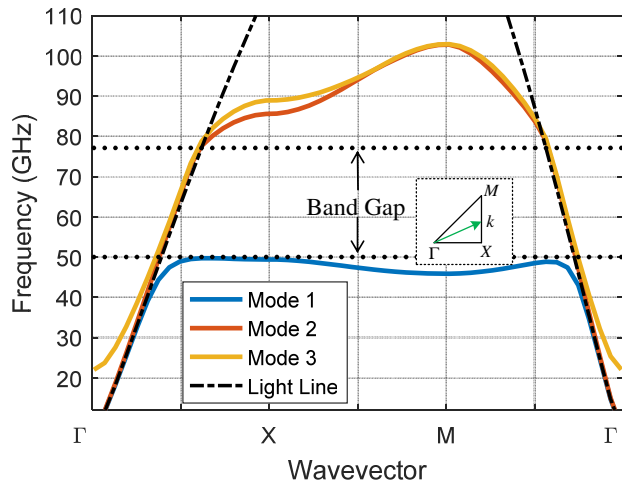


Figure 4.2.12: EBG unit cell dispersion diagram.

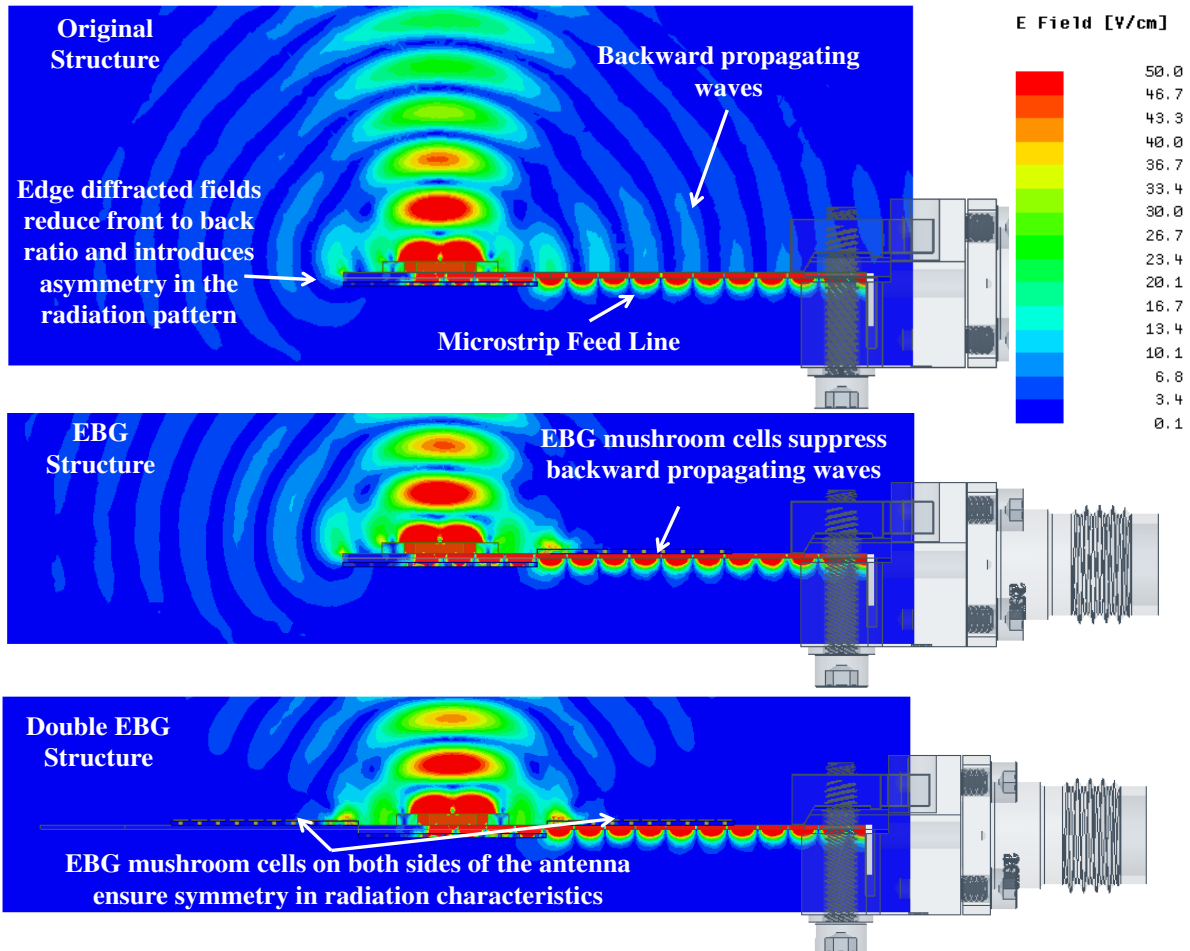


Figure 4.2.13: Electric field heat maps for the proposed structures in Fig. 4.2.11.

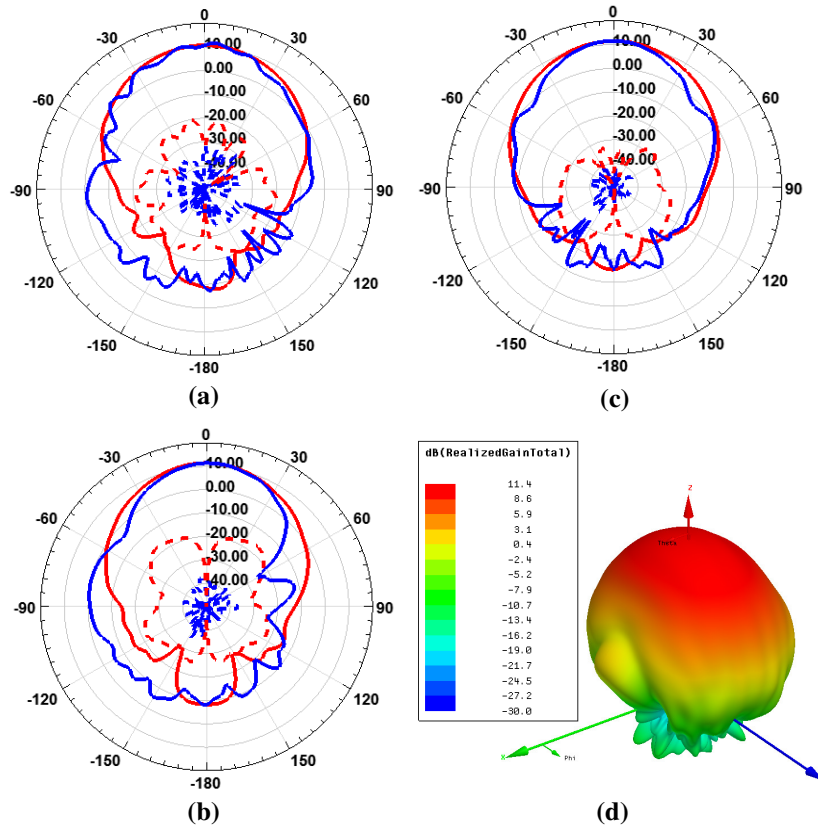


Figure 4.2.14: Radiation patterns in the principal planes for the proposed DRA structures shown in Fig. 4.2.11. Red (H-plane), Blue (E-plane), Solid (Co-polar Component), Dashed (Cross-polar Component). (a) no EBG, (b) single EBG, (c) double EBG surfaces and (d) 3D radiation pattern of the proposed DRA structure with double EBG surfaces.

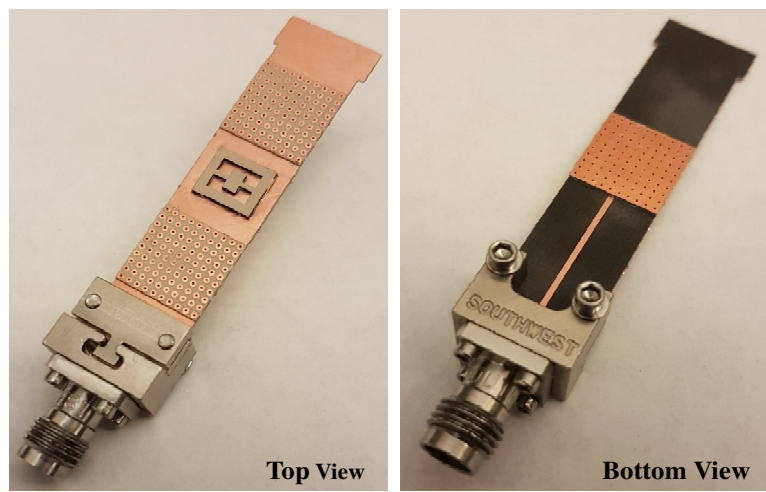


Figure 4.2.15: Actual prototype of the proposed DRA structure.

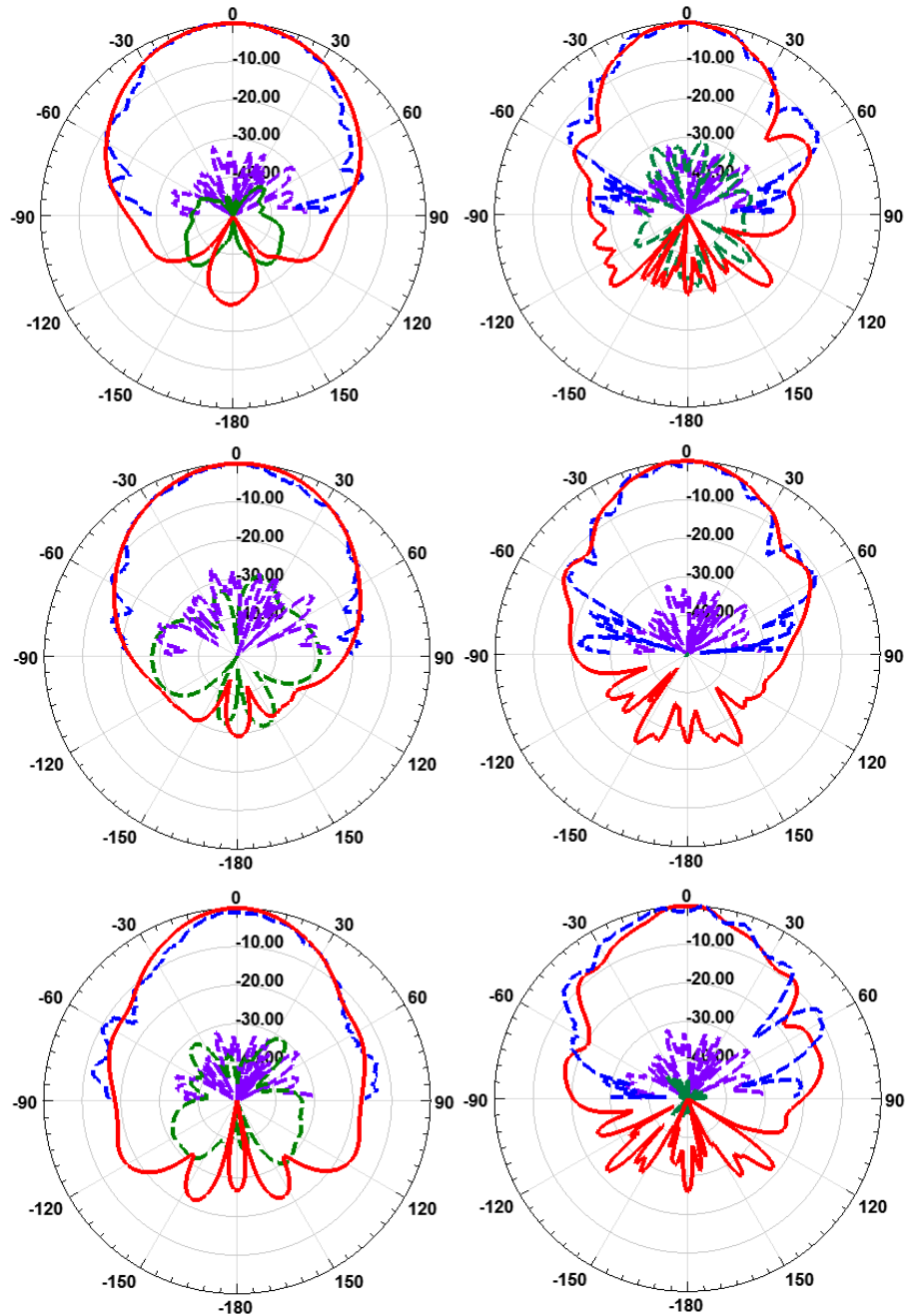


Figure 4.2.16: Measured and simulated E- and H-plane radiation patterns of the proposed DRA structure. Red (Simulated Co-polar), Dashed-Blue (Measured Co-polar), Dashed-Purple (Measured cross-polar), Dashed-Green (Simulated cross-polar) right (H-plane), left (E-plane), from bottom to top 65, 60, and 55 GHz.

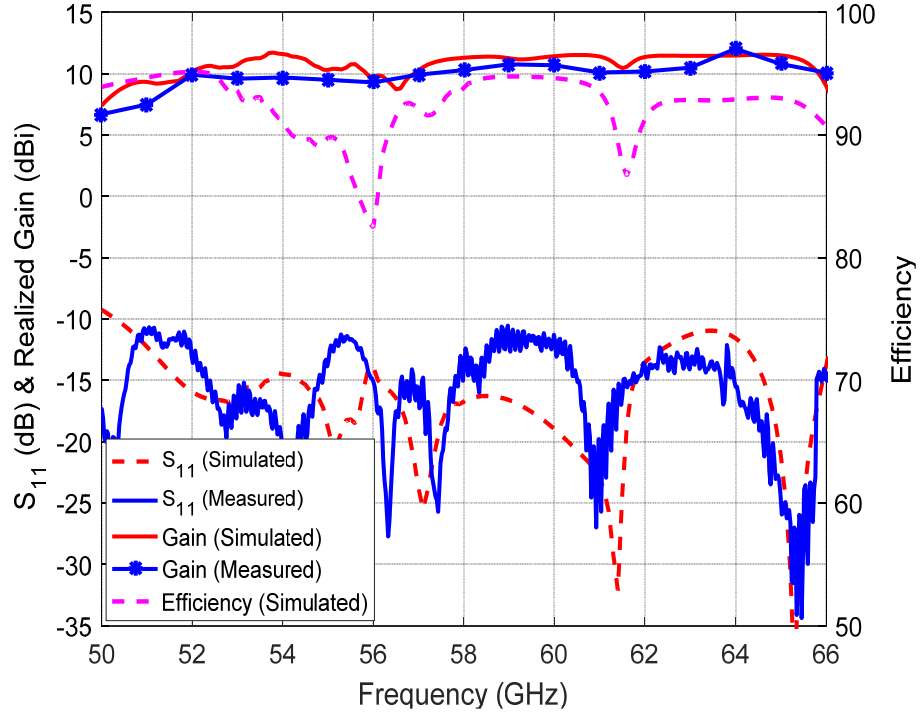


Figure 4.2.17: Measured S-parameters and gain of the proposed DRA structure.

It is worth emphasizing that the ring is governed by the guided quarter wavelength width as contrast to [90], where a patch parasitically excites higher order modes in an annular ring. The proposed design possess an advantage, where it minimizes the off-boresight radiation and maintains a neat radiation pattern in the boresight. The design procedure is straightforward. The ability to employ the element in a planar array without generating grating lobes is possible by sharing the ring sides as explained in the previous chapter.

CHAPTER 5

ENHANCED WIRELESS INTER-CHIP COMMUNICATION PERFORMANCE USING SYMMETRIC LAYERS AND SOFT/HARD SURFACE CONCEPTS

5.1 Wireless Inter-Chip Communication

5.1.1 Introduction

Electrical interconnects between various sub-circuits within an IC, or between several adjacent ICs, play a vital role in defining the performance limits of any system. As the frequencies of operation have been into a gradual increase, the design of interconnects, whether within the IC environment (Intra-chip) or between several adjacent ICs (Inter-chip), turn into a more challenging task [91]–[93]. As the frequencies of operation increase, the proper interconnect guiding structure dimensions become infeasible to realize, or it might exhibit a high level of losses, and large intrinsic RC time delay [94]. Moreover, by the increase of the number of interconnects, the mutual coupling between the interconnect structures become more severe, not to mention the complexity, and associated cost of such design. The wireless interconnects concept (wireless intra-chip/inter-chip communication) emerged as a suggested remedy to the high frequency interconnect problem [95], targeting several potential applications, such as wireless clock distribution [96]. In [97], several fundamental aspects and concepts related to wireless inter/intra-chip communication were laid out. It introduced the actual gain formula to characterize the link quality between communicating antennas. It also identified the main paths of propagation between the transmitting and receiving antennas [94], which consequently led to the study of several substrate materials to reduce the indirect wave destructive interference effect, and correspondingly enhance the link

budget between communicating antennas. In [98] unbalanced on-chip fed meander antenna was prototyped at 22-28 GHz, it used high resistivity substrate to increase the received signal level. In [99], an FR4 PCB substrate channel was bounded by metamaterial absorbing cells to improve the link quality between communicating monopoles. In [100] vertical quarter wavelength monopoles surrounded by a 3D printed dielectric distribution were prototyped at 60 GHz, the special designed 3D printed dielectric distribution enhanced the communication quality and provided a higher energy focus in the desired direction.

In this section, we provide a study of several aspects of wireless inter-chip communication between adjacent ICs. The symmetrical layers concept is introduced as a general approach to eliminate the destructive interference and redirect the wasted radiated energy to free space towards the receiving antenna. In addition, the use of hard/soft surfaces and EBG structures to focus the radiated energy towards the receiving antenna is studied thoroughly. The use of such concepts has tremendous advantages, in focusing the energy towards the receiving antenna and eliminating the spherical spreading losses introduced by the radiated spherical wave nature. The incorporation of the symmetrical layers with hard/soft surfaces led to novel compact wireless inter-chip structures.

5.1.2 Symmetrical Layers Concept

In [97], the primary propagation paths between the transmitting and receiving antennas for wireless intra/inter-chip communication were identified, the primary path is the direct line of sight path between the transmitting and receiving antennas. The other paths trace the reflected waves at the interfaces between different layers. It was shown in [97] that the reflected waves from the interfaces destructively interfere with the direct wave, and consequently lessen the received signal strength. The original case of the problem is shown in Fig. 5.1.1, as the figure shows, two dipole antennas are printed on a dielectric substrate, the first antenna is a transmitting antenna (i.e., connected to a transmitter circuitry), and the second antenna is a receiving antenna (i.e., connected to a receiver circuitry). The transmitting dipole antenna radiates its electromagnetic energy in an omnidirectional fashion. The radiated energy can be divided into the following: (1) portion of the radiated energy is radiated to free space, (2) another portion is radiated directly towards the receiving antenna, and (3) some of the energy is radiated within the substrate and reflected towards the receiving antenna. The receiving antenna is only capable of capturing the radiated energy

towards it, either directly from the transmitting antenna, or reflected through the substrate. The rest of the radiated energy is wasted and cannot be captured by the receiving antenna. This has a crucial implication on lowering the link budget of such wireless link.

To tackle this issue, another top substrate can be used to cover the previous structure, as shown in Fig. 5.1.2. By doing so, the wasted radiated energy to free space is directed back to the receiver antenna from the reflection from the top substrate-air interface.

The solution of a dipole antenna excitation in a dielectric substrate layer is a straightforward problem; such problem can be either solved analytically using Green's functions or numerically by various methods, such as the finite element method (such problem can be easily solved with a full wave analysis solver such as HFSS). However, in [94], [97], [98], [101], it was shown that using a ray model has a significant advantage in providing a physical understanding and a simple approximation in analyzing such a problem. The ray model is based on physical optics approximation, which provides a compelling physical insight, and better visualization of the interaction of the fields within the structure, such visualization is useful through the design process of the structure.

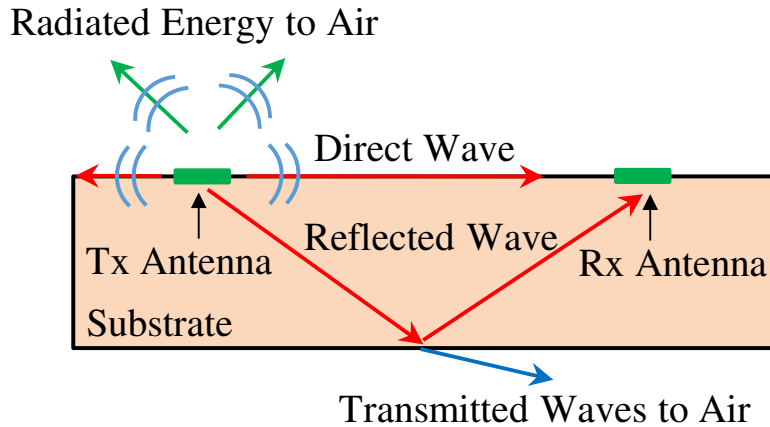


Figure 5.1.1: Two dipole antennas printed on a dielectric substrate.

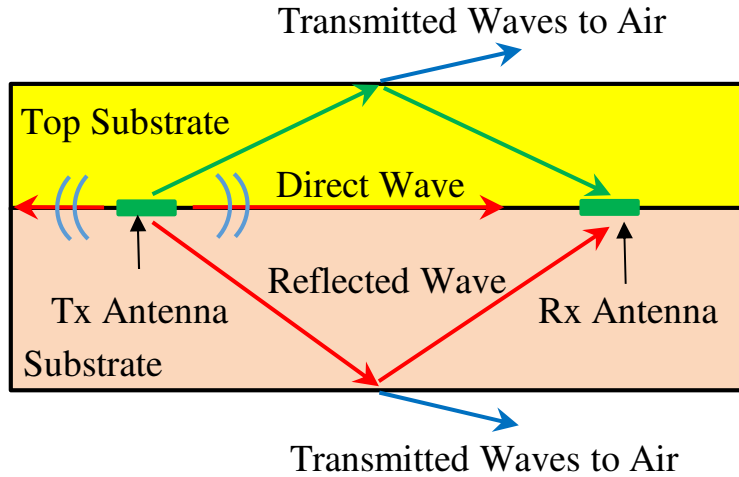


Figure 5.1.2: Two dipole antennas printed on a dielectric substrate covered with a top substrate.

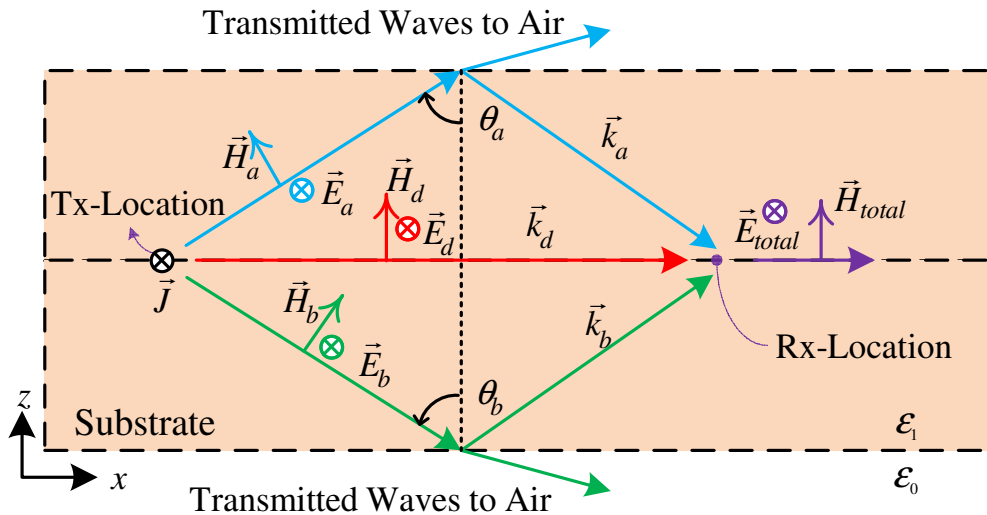


Figure 5.1.3: Proposed symmetrical layers analysis configuration.

In [94] it was shown that the reflected waves from the bottom of the substrate and the direct waves interfere at the receiver antenna location, such interference can be destructive, in such a way that deteriorates the link budget of the wireless link. In [97], different substrate thicknesses were used in order to minimize the destructive interference problem. A parametric study is provided in [97]. As it was shown in [97], the destructive interference effect is more severe for a thicker substrate, this can be easily attributed to the difference between the path lengths (i.e., time

delays) for both the direct and reflected propagating waves, also as the substrate thickness gets higher, the reflected wave and direct wave propagation directions deviates more from each other. On the contrary, when the substrate thickness is low (i.e., thin), the direct wave and reflected wave directions are almost parallel, and the paths' lengths are almost the same. Therefore, the effect of destructive interference won't be significant in such a case. The case of interest is when the substrate is thick, or more generically for any arbitrary substrate thickness. In the proposed solution in Fig. 5.1.2, not only the direct wave from the substrate interferes with the reflected wave from the bottom substrate-air interface, but it also interferes with the reflected waves from the top substrate-air interface. This adds another degree of freedom that can geometrically eliminate the destructive interference and direct the energy towards the receiving antenna, without resorting to any modification in the substrate material electrical properties and thickness, the only required condition to ensure the elimination of the destructive interference, is by having equal substrate thicknesses for the top and bottom substrates (i.e. symmetrical layers).

Fig. 5.1.3 shows the analysis configuration of the proposed symmetrical layers concept. The transmitting antenna is modeled as an injected current element source. The receiving antenna is assumed to be located on the line of sight at a distance D_x away from the transmitting antenna. Both transmitting and receiving antennas are sandwiched by the same substrate material. It is to be shown that if the thicknesses of the upper and lower substrates are equal, then the effect of destructive interference can be eliminated. The following assumptions are followed in the analysis of the proposed concept. Surface waves at the interfaces between different materials are ignored. The radiating source is assumed to be an ideal line current source (TE - 2D case), where physical optics approximation is assumed for the radiated cylindrical wave from the source, the accuracy of this approximation increases by increasing the substrate thickness (i.e., when the dielectric-air interface is electrically far from the source). It is important to emphasize that even though this might differ from an accurate full-wave solution for the electric dipoles within the same configuration, the analysis provides compelling insights into the structural, physical characteristics, which can be efficiently utilized with the aid of a full-wave simulator tool, such as HFSS, to optimize the wireless inter-chip link performance. As shown in Fig. 5.1.3, the transmitted waves from the source split into three paths. The first is the direct path from the transmitter to the receiver, shown in red, with a path length equal to D_x . The second and third paths are the reflected wave's paths', shown in blue and green, with path lengths equal to l_a and l_b , respectively. The total

electric field at the receiver is equal to the sum of the direct field component, and the reflected waves components, as expressed in (5.1.1), k is the wavenumber given by $k = 2\pi / \lambda_d$ and λ_d is the wavelength in the dielectric medium. The reflection coefficients for such TE polarization are given by (5.1.2). From Snell's law, the refraction angles of the transmitted waves are given by (5.1.3) [36].

$$E_y^{tot} = E_0 e^{-jkD_x} + E_0 \Gamma_a e^{-jkl_a} + E_0 \Gamma_b e^{-jkl_b} \quad (5.1.1)$$

$$\Gamma_{a,b} = \frac{\sqrt{\epsilon_r} \cos(\theta_{a,b}) - \cos(\theta_{a,b}^t)}{\sqrt{\epsilon_r} \cos(\theta_{a,b}) + \cos(\theta_{a,b}^t)} \quad (5.1.2)$$

$$\theta_{a,b}^t = \sin^{-1} \left(\sqrt{\epsilon_r} \sin(\theta_{a,b}) \right) \quad (5.1.3)$$

In the case of the symmetrical layers, the thicknesses of the upper and lower substrates are equal, which implies that the reflected angles, reflection coefficients, and the lengths of paths of the reflected waves are equal, and correspondingly (5.1.1) can be rewritten as:

$$E_y^{tot} = E_0 e^{-jkD_x} \left(1 + 2\Gamma_a e^{-jk(l_a - D_x)} \right) \quad (5.1.4)$$

If the dielectric constant of the substrate is high enough, high reflectivity is expected at the interface. Also, in the critical angle scenario, the reflection coefficient magnitude of Γ_a is maximum equal to 1, and by tuning the distance D_x , the direct and reflected waves can add up in phase and (5.1.4) can reduce to (5.1.5).

$$E_y^{tot} = 3E_0 e^{-jkD_x} \quad (5.1.5)$$

As (5.1.5) points out, three times increase over the direct wave is obtained (equivalent to 9.5 dB). This approach requires that the transmitting and receiving antennas to be sandwiched between two identical substrates to eliminate the destructive interference and redirect the wasted radiated energy to free space towards the receiving antenna. Other proposed solutions can be derived from this approach. For example, the use of absorbing metamaterial cells bounding the substrate [99], as illustrated in Fig. 5.1.4, forces $\Gamma_a = 0$, and eliminates any possible reflected waves to interfere with the direct wave. However, in such a case, the energy absorbed by the metamaterial cells is

lost. Hence, the received signal strength is reduced, and correspondingly the signal to noise ratio (SNR).

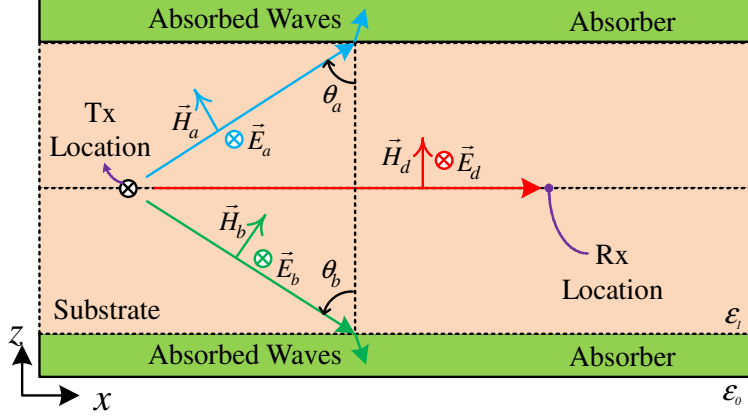


Figure 5.1.4: Absorbing metamaterials cells bounding the substrate configuration.

On the other hand, the use of other substrate materials with different electrical properties and thicknesses is only a matter of controlling the magnitude of the reflected waves. The main advantage of the symmetrical layers concept is that it ensures redirecting the waves from the substrate-air interface towards the receiving antenna in a constructive way. Moreover, it allows high flexibility in material selection by being independent of the used material.

At this point, it is worth comparing the symmetrical layers structure with the single substrate layer structure. The single substrate layer analysis configuration is shown in Fig. 5.1.5. The total electric field at the receiver point is given by (5.1.6) and (5.1.7). As can be deduced from (5.1.7), a constructive addition can still be possible in this case, however, the superposition of the direct and reflected waves will result in a total wave propagating towards free space. In addition to that, the radiated energy from the antenna to free space is wasted. Hence, lowering the link budget of the wireless inter-chip link. Therefore, the enhancement for the link budget of the symmetrical layers structure is attributed to: (1) redirecting the wasted energy to free space towards the receiving antenna, and (2) eliminating the destructive interference at the receiver antenna location.

$$E_y^{tot} = E_0 e^{-j k D_x} + E_0 \Gamma_b e^{-j k l_b} \quad (5.1.6)$$

$$E_y^{tot} = E_0 e^{-j k D_x} \left(1 + \Gamma_b e^{-j k (l_b - D_x)} \right) \quad (5.1.7)$$

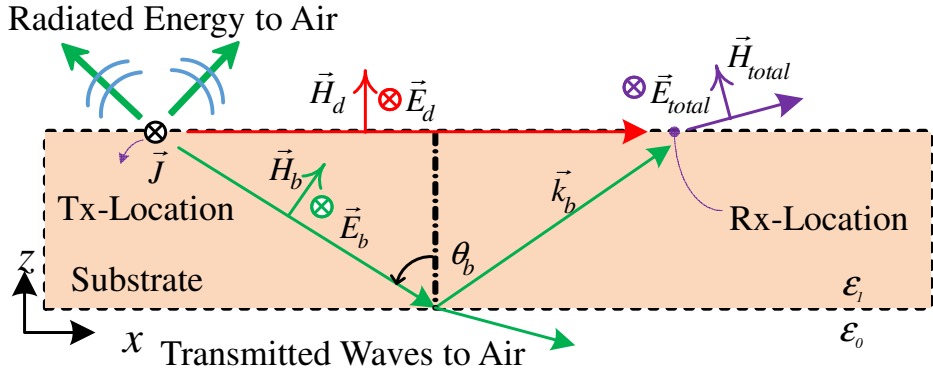


Figure 5.1.5: Single substrate layer analysis configuration.

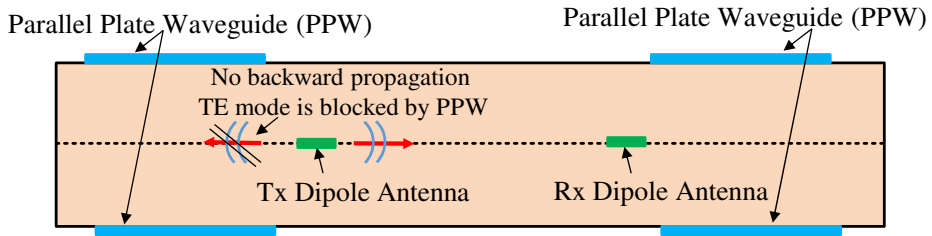


Figure 5.1.6: Parallel plate waveguide reflectors.

To further enhance the link budget of the wireless inter-chip link, the dipole antenna is backed by a reflector, as shown in Fig. 5.1.6, where a metallic sheet can be located at the top and bottom of the substrate. Such an arrangement can be viewed as a parallel plate waveguide. The parallel plate waveguide TE cut-off frequency is much higher than the operating frequency of the antennas, and as the antennas are producing only TE polarization, non-of the backward waves can propagate in the parallel plate waveguide. Therefore, the parallel plate waveguide acts as a reflector.

5.1.3 Different Design Concepts on Wireless Inter-Chip Structures

A. Symmetrical Layers Wireless Inter-Chip Link Structure

Fig. 5.1.7 shows the proposed antenna structure and lists the dimensions in millimeters. Fig. 5.1.8 shows the proposed symmetrical layers wireless inter-chip link structure. The structure operates in the frequency range 50-60 GHz. The structure is composed of three substrates, all using Rogers 3003, with a dielectric constant of 3. The antennas are dipoles fed differentially through baluns. The three substrates allow the antenna to be symmetrically located in the middle as if it was equivalently sandwiched between two equal thickness substrates. Substrate 2 is used for the balun and the feed of the antenna. The balun ground plane is tapered to provide a smooth matching transition; the tapered ground plane also assists in increasing the aperture area of the antenna by capturing more energy at the edge discontinuity of substrates 1 and 3. The dipoles are also backed by reflectors. The reflector sheets are located on top of substrate 1 and bottom of substrate 3. From another perspective, they can be considered as a parallel plate waveguide, with its TE cutoff frequency to be much higher than the operating frequency of the proposed wireless interconnect, which accordingly prevents the radiated energy from the antenna to propagate back towards the feed, and focuses it towards the receiving antenna.

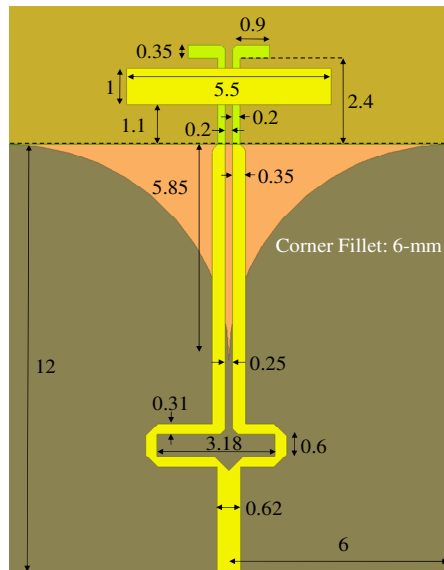


Figure 5.1.7: Proposed antenna structure (all dimensions are in millimeters).

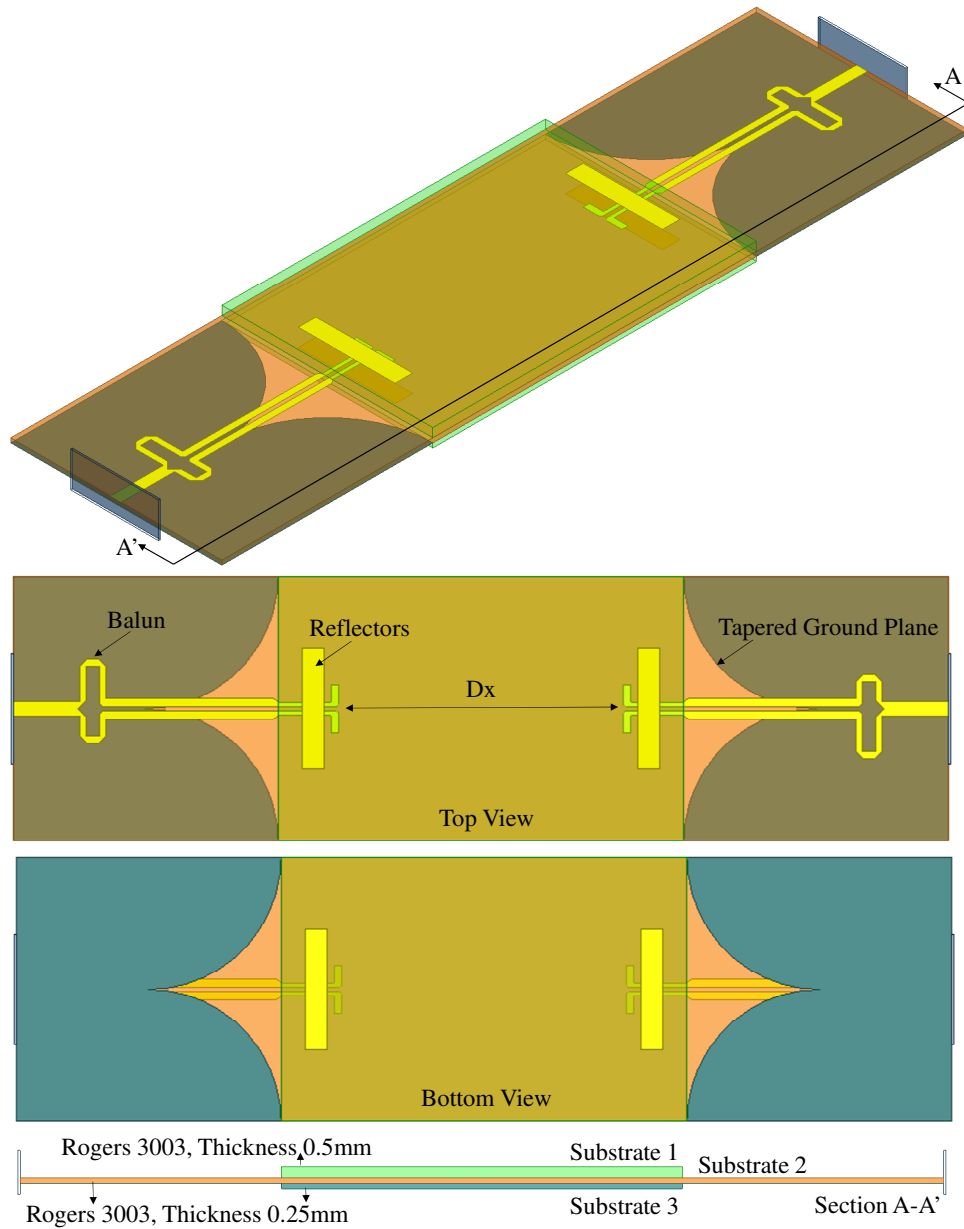


Figure 5.1.8: Proposed symmetrical layers wireless inter-chip link structure.

The asymmetric single layer structure is similar to the symmetrical layers structure. However, it only excludes substrate 1 to produce asymmetry. The designed balun exhibits around 1-dB loss for the differential mode, as shown in Fig. 5.1.9. This is equivalent to the 2-dB loss in the link budget when counting for both baluns at the transmitter and receiver sides. Such loss in the balun takes the form of radiation losses, and this is expected, especially for microstrip line technology, at such high frequency (i.e., 60 GHz).

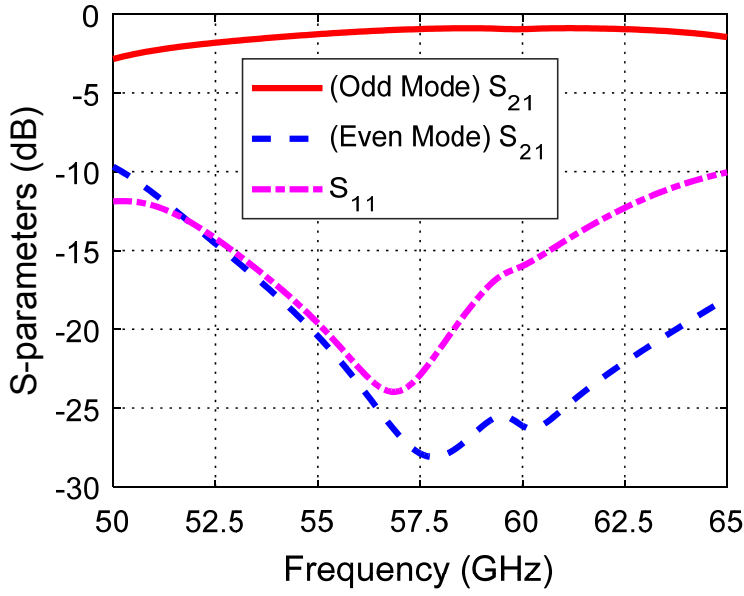


Figure 5.1.9: Balun structure S-Parameters.

The tapered ground plane is crucial in matching the antenna over the desired bandwidth. In addition to that, it helps in transmitting, and reciprocally receiving/capturing some of the radiated energy, as if the tapered ground plane is acting as a secondary antenna. The receiving problem can be looked at as follows: (1) the dipole antenna along with its reflector constitutes an antenna aperture area, this aperture captures the incident wave on it, and direct the energy to the differential feed, none of the energy can bypass the dipole-reflector aperture. (2) Outside the aperture of the dipole-reflector structure (i.e., on the upper and lower sides), the energy is guided by the edges of the tapered ground plane towards the differential feed. Thus, the tapered ground plane acts as a secondary aperture. (3) As the propagating wave is TE polarized, it can't propagate beyond the ground plane, since the ground plane forces the tangential electric field component to be zero (soft surface for TE polarization), and therefore it can only propagate along the edges of the ground plane in the form of a normal component, which is perpendicular to the edge of the tapered ground plane, and hence guided towards the feed lines. Fig. 5.1.10 shows the electric field heat map intensity at different phases. As can be noticed from the heat map, the waves located at the upper and lower sides of the heat map are captured by the tapered ground plane, while the waves in the middle are captured by the dipole-reflector antenna.

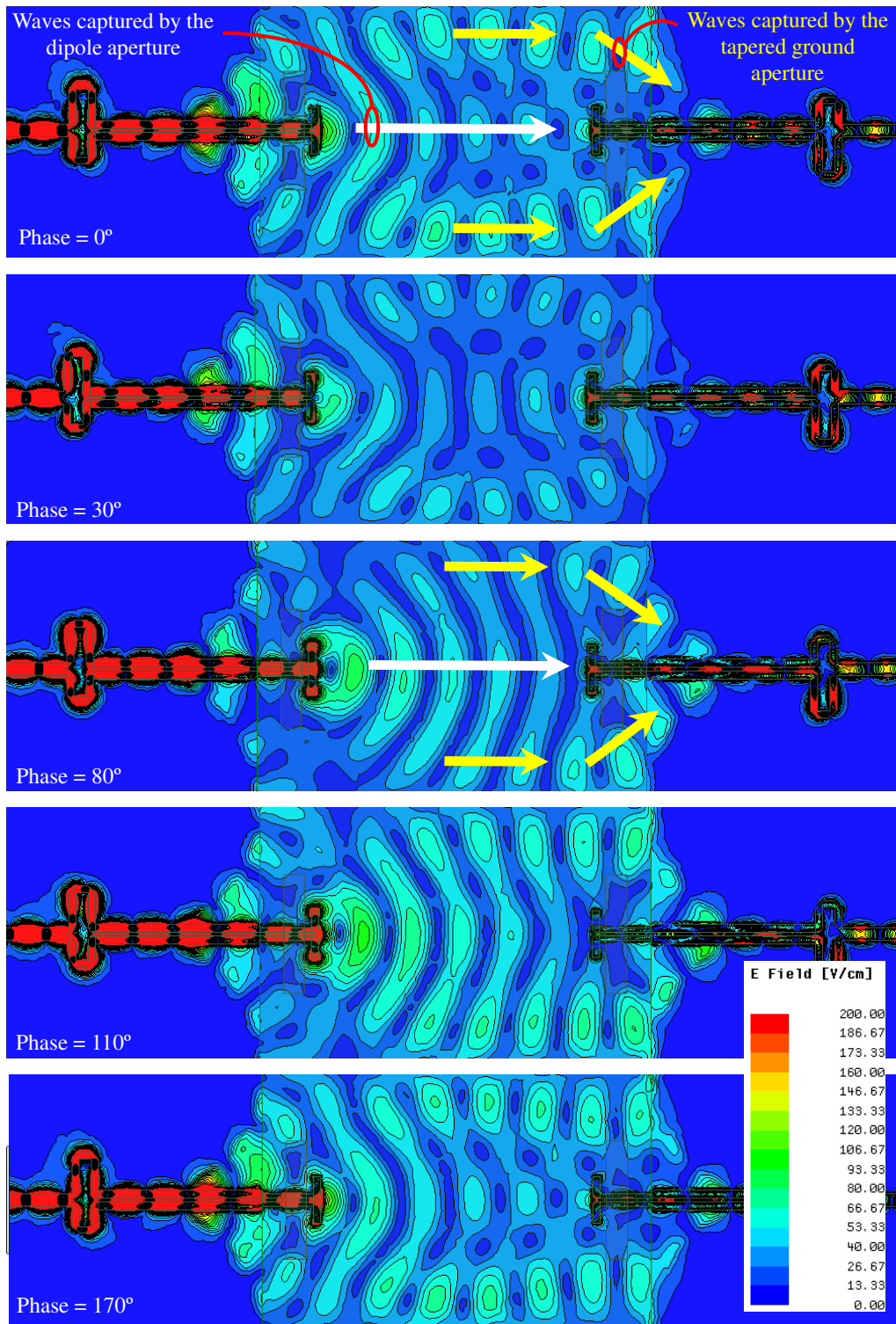


Figure 5.1.10: Proposed symmetrical layers structure electric field intensity heat map at different phases (at 55 GHz).

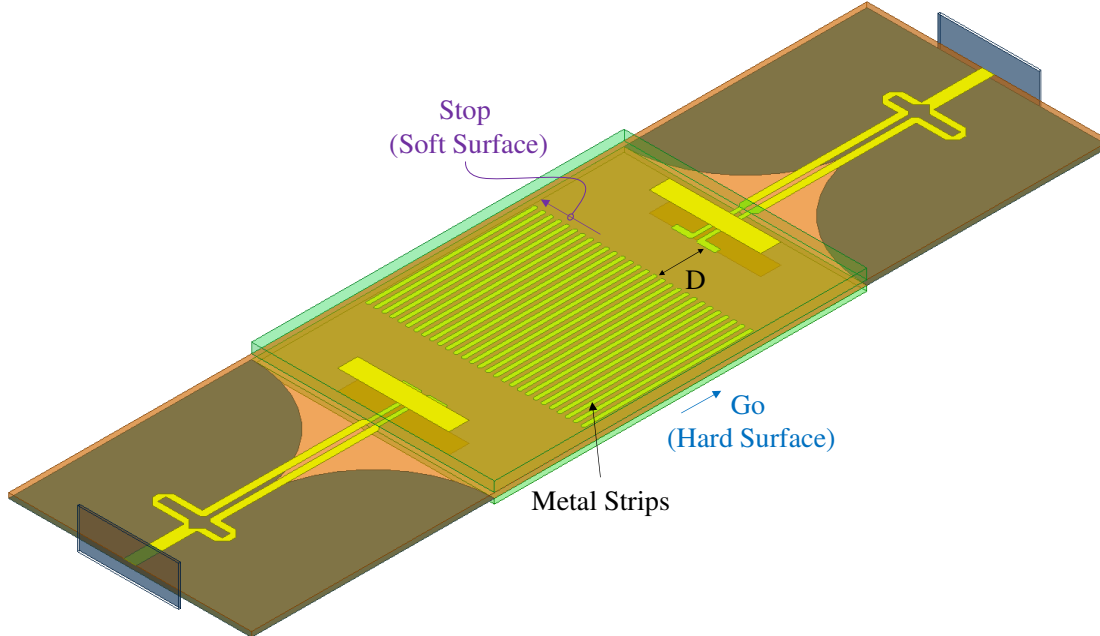


Figure 5.1.11: Wireless inter-chip link structure with hard surface metallic strips.

B. Soft/Hard Surfaces Wireless Inter-Chip Link Structure

The dipole antenna E-plane is parallel to the substrate, and the H-plane is perpendicular to both the substrate and the antenna. The objective of inter-chip wireless communication is to focus the radiated energy as much as possible in both planes. Ideally to squeeze the radiation beam to a zero beam-width, focusing all the energy from the transmitter to the receiver, similar to the case of point to point laser communication. However, this ideal scenario is far-fetched at microwave frequencies. To increase the focusing in the E-plane, metallic strips are aligned between substrate 1 and 2, as shown in Fig. 5.1.11. The metallic strips act as a hard surface (*go*) in the direction of propagation for only the antenna polarization. Further explanation of the mechanism by which hard and soft surfaces function is provided in [102], [68]. Using such metallic strips (hard surface) increases the directivity in the E-plane, where it allows the wave to only propagate in one direction, which is the *go* direction (i.e., towards the receiving antenna). The dimension “D” in Fig. 5.1.11 is 2.4 mm, the width of the strip is 0.2 mm, and the spacing between the strips is 0.193 mm.

C. EBG Wireless Inter-Chip Link Structure

Another approach to increase the directivity and focus the energy further in the E-plane is to block the wave from propagating in all undesired directions. This can be achieved by using electromagnetic bandgap (EBG) structures. EBG structures can provide a stopband, where no propagating waves (modes) can exist within the structure [37]. The EBG cell used is a circular mushroom type, as shown in Fig. 5.1.12. The cell dispersion diagram is shown in Fig. 5.1.13. A bandgap of 33 GHz bandwidth exists from 42 GHz to 75 GHz. Fig. 5.1.14 shows the proposed EBG structure for wireless inter-chip communication. The mushrooms are located in substrate 1, and its copper cover is laid at the bottom of substrate 3. Fig. 5.1.14 shows the boundary of the mushrooms, which is everywhere, except the line of sight direction between the antennas. Fig. 5.1.15 shows an enlarged segment of the proposed structure in Fig. 5.1.14, the corresponding dimensions are in millimeters.

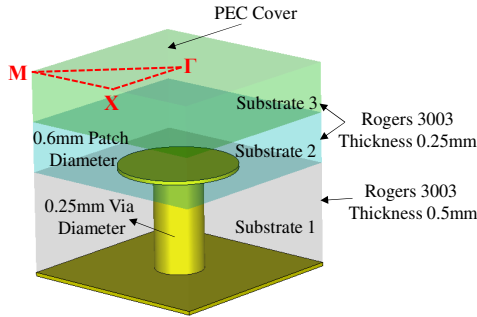


Figure 5.1.12: Proposed mushroom cell structure.

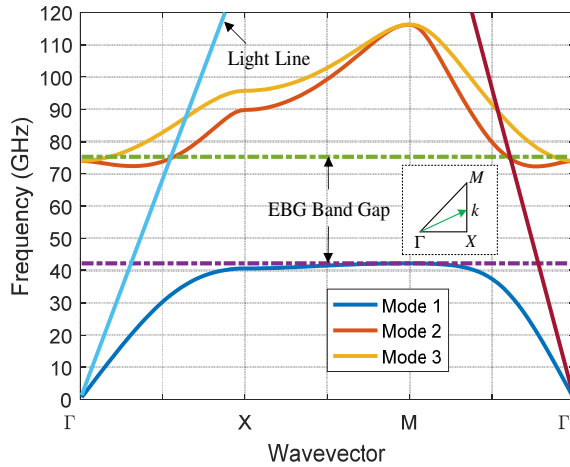


Figure 5.1.13: Proposed mushroom cell dispersion diagram.

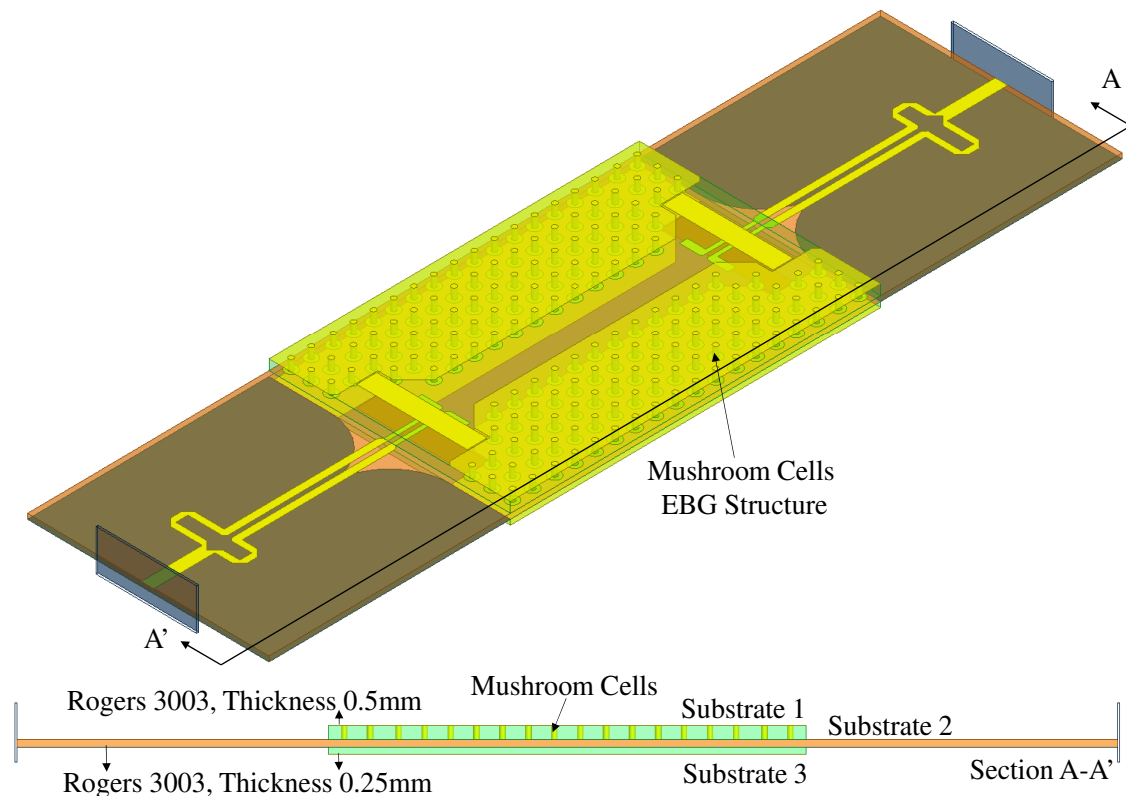


Figure 5.1.14: EBG wireless inter-chip link structure.

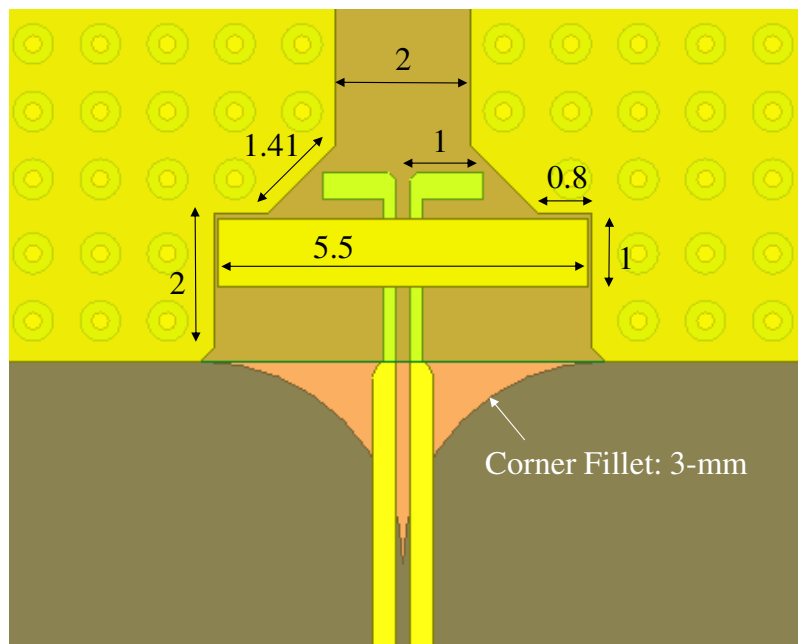


Figure 5.1.15: Enlarged segment of the proposed structure in Fig. 5.1.14.

D. PEC (Soft-Surface) Wireless Inter-Chip Link Structure

The dipoles in the previously proposed structures are oriented to produce TE polarization. Any PEC surface will act as a soft surface by forcing the tangential electric field component to zero. This observation inspired the structure shown in Fig. 5.1.16. In this figure, a metallic copper surface is put in-between substrate 1 and 2 everywhere except the line of sight direction between the antennas. This structure has the same objective of increasing the directivity and focus the energy in the E-plane by blocking the wave from propagating in all undesired directions. The merit of such structure is its simplicity in being planar, and the avoidance of the metallic vias which might not be feasible to realize at higher frequencies (due to their tiny dimensions). As such, it is low-cost as compared to the EBG structure. In addition, the simplicity of the structure makes it less susceptible to manufacturing tolerances once compared to EBG structures. Furthermore, the conductor edges act as a hard surface for the antenna polarization while the flat surface is soft for this polarization. It should be stated that the cross-polarization component will be the only leaking polarization that sees the flat conducting surface as a hard surface. Fig. 5.1.17 shows an enlarged segment of the proposed structure in Fig. 5.1.16, the corresponding dimensions are in millimeters.

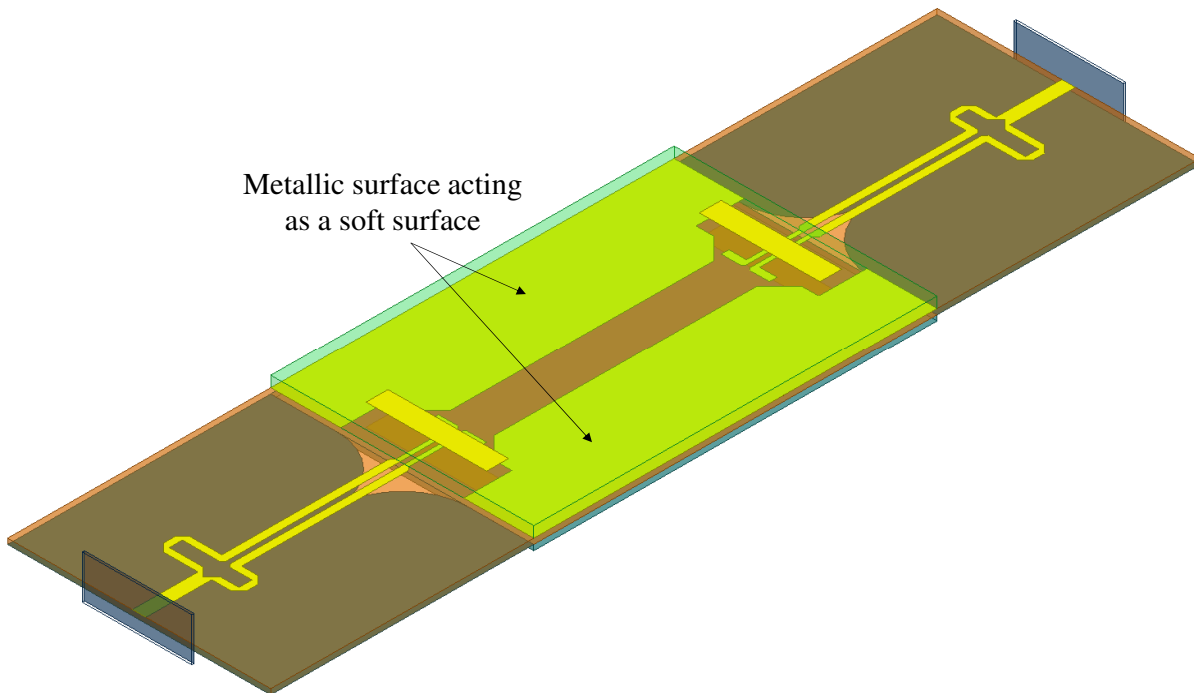


Figure 5.1.16: PEC (soft-surface) wireless inter-chip link structure.

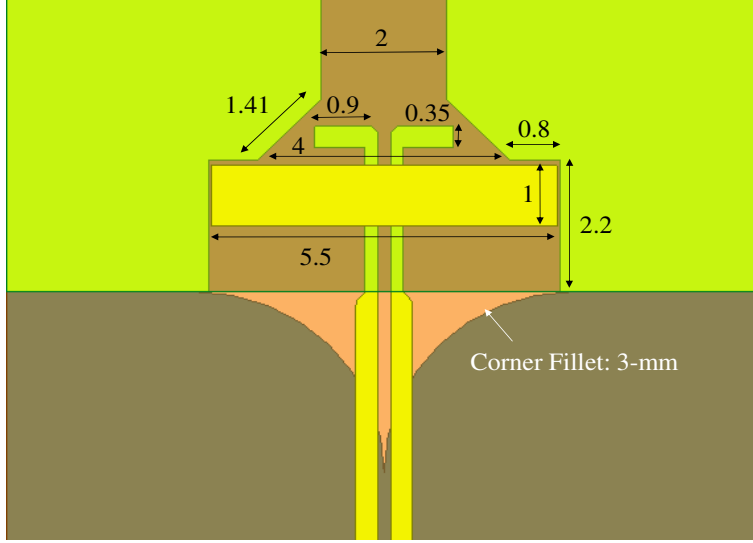


Figure 5.1.17: Enlarged segment of the proposed structure in Fig. 5.1.16.

Fig. 5.1.18 shows the S-parameters of the proposed wireless inter-chip link structures. As it can be observed, there is a considerable leap in S_{21} value for the symmetrical layers structure over the single layer structure (around 9 dB). Also, by adding the strips, further improvement in S_{21} value is achieved. The EBG structure and the PEC soft surface solution have higher S_{21} value over the strips solution. It is noticed that the S_{21} level of the EBG case is remarkably stable over the desired band. However, it is still more expensive than the PEC soft surface solution; the PEC soft surface structure can provide the same S_{21} value with less stability over the matching bandwidth, the PEC soft surface structure requires no vias, which makes it advantageous because of its simplicity and low cost as compared to the EBG solution. All proposed solutions are matched with a return loss greater than 10-dB from 50 to 60 GHz, with an equivalent relative bandwidth of 20 %. A -5.6 dB S_{21} value can be achieved over a distance $D_x = 12$ mm, between the transmitter and the receiver. It is important to point out that the S_{21} value considers the balun losses at both ends, which is around 2-dB. The extra losses can be avoided if the differential feeding is provided directly from the IC, which is usually very common to have such balanced output (i.e., differential) from the IC output pins. Fig. 5.1.18 shows the S_{21} phase for all proposed structures. It is noticed that all structures have a linear phase, assuring a dispersive free communication channel.

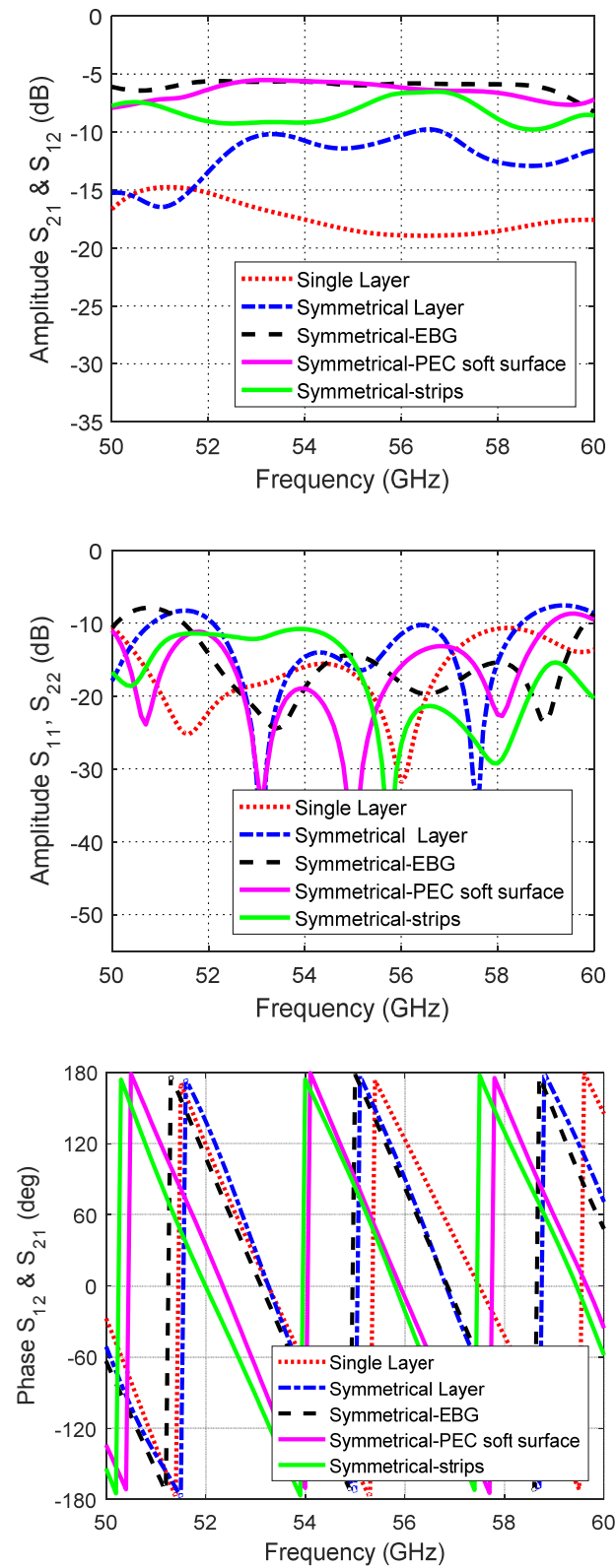


Figure 5.1.18: S-parameters for the proposed structures.

Fig. 5.1.19 compares the electric field intensity heat maps for the proposed structures. The heat maps are provided at the antennas' level, and the scale is unified for all structures, as shown in the same figure. The heat map gives visual insights into the propagation mechanism of each solution. The first heat map shows the single layer electric field intensity, the spherical spreading of the wavefront in the E-plane is noticeable. Also, it can be noticed that the tapered ground plane helps in capturing some of the radiated energy, as explained previously. The second heat map refers to the symmetrical layers structure. It can be noticed that the electric field intensity is higher than the single layer as expected due to the proposed symmetrical layers. The third shows the strips hard surface structure, as it shows, the E-field intensity is higher in the middle, which implies that the directivity is higher in the E-plane. Also, as the heat map shows, the inclusion of the strips hard surface has increased the received signal level over the symmetrical layers structure as expected. The fourth and fifth heat maps refer to the PEC (soft surface), and EBG structures. As the heat map shows, the radiated energy from the antenna is confined in the area lacking the PEC soft surface, or the EBG structure, in other words, the radiated energy can't propagate within the EBG or the soft surface region, and this consequently led to higher levels of directivity in the E-plane. Also, the spherical wave spreading in the E-plane is eliminated by adding the EBG/PEC soft surface structure, where the structures tend to behave in a similar fashion to guided structures. However, the antenna is still unbounded by any metallic structures, and radiation losses to free space are not negligible as in the traditional guided structures.

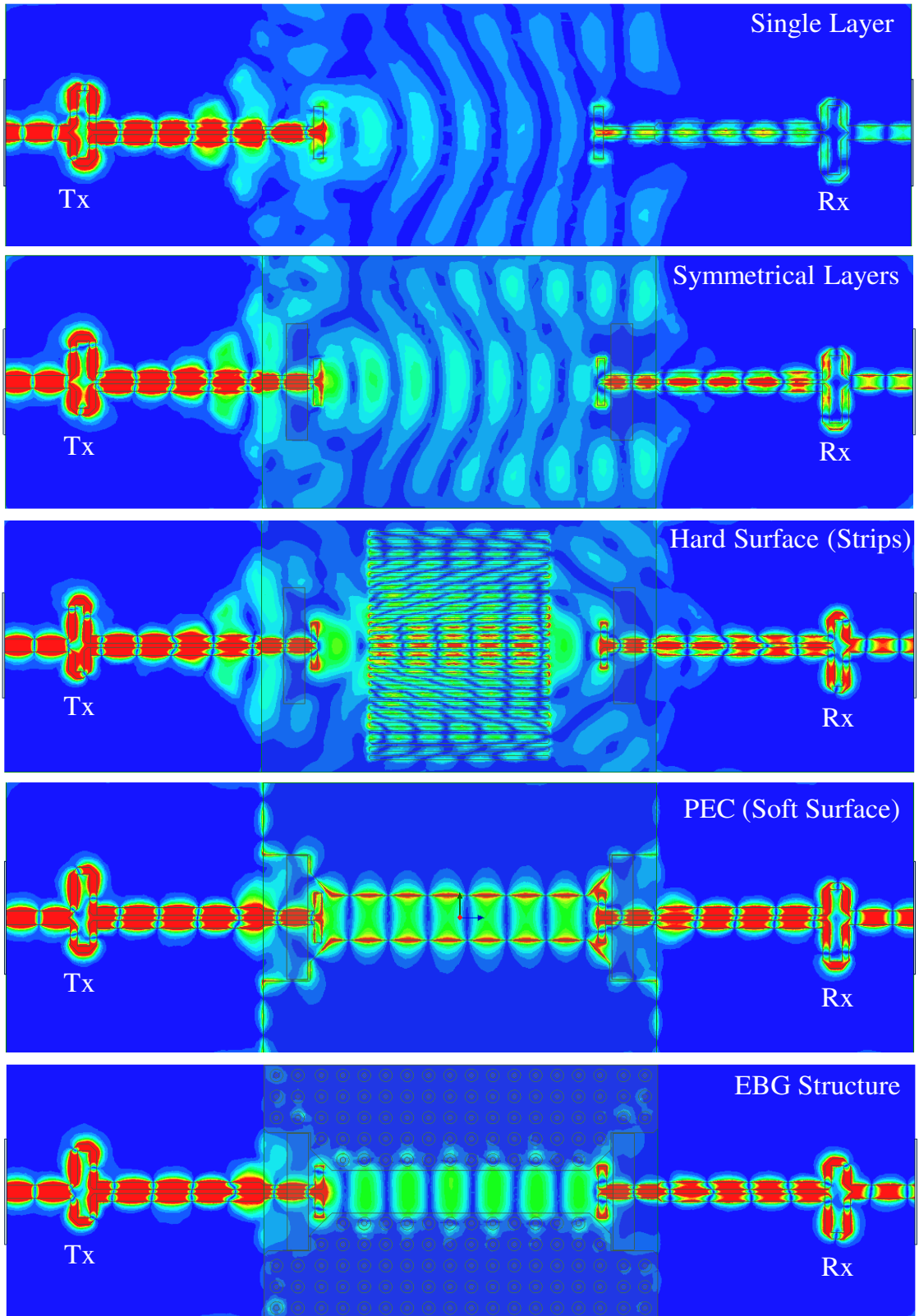


Figure 5.1.19: Electric field heat map comparison at 55 GHz (same scale as Fig. 5.1.10).

5.1.4 Wireless Inter-Chip Link Budget (Link Losses)

In [97], a key figure of merit to benchmark the inter-chip wireless communication link quality was proposed. The key figure of merit is referred to as the actual gain formula; the actual gain formula is given by (5.1.8) [97]. The formula is a sort of modified version of Friis equation, which quantifies the total power loss along the path from the transmitting to the receiving antennas. The formula given in (5.1.8) assumes that the transmitting and receiving antennas are in perfect alignment, and there are no polarization losses. This equation considers the boost due to the transmitter and receiver gains, G_t and G_r , respectively. It also takes the spherical spreading loss of the radiated waves into account. Such spreading loss is modeled by the term $(\lambda / 4\pi R)^2$. It can be inferred from the spherical spreading loss term that an extra loss of 6-dB in the actual gain occurs for each doubling in the distance. The dielectric loss is modeled by $e^{-2\alpha R}$, where α is the attenuation factor in Np/m.

$$G_a = \frac{|S_{21}|^2}{(1 - |S_{11}|^2)(1 - |S_{22}|^2)} = G_t G_r \left(\frac{\lambda}{4\pi R} \right)^2 e^{-2\alpha R} \quad (5.1.8)$$

The PEC soft surface performance is studied at two distances D_x and $2D_x$. The S-parameters are shown in Fig. 5.1.20. The E-field heat map is shown in Fig. 5.1.21 for both cases. It is noticed that the losses are almost negligible between the two cases, and this is because the losses are only attributed to the dielectric losses, which are negligible at such distance for the used substrate. The spherical spreading loss is not there anymore, as the PEC soft surface prevents the wave from spreading in a spherical nature, and confines it to the line of sight region only as shown in Fig. 5.1.21. This has a tremendous advantage where the expected loss due to doubling the distance in S_{21} value is eliminated. It is noticed that some of the S_{21} values for the longer distance are better than, the shorter version of the structure at some off-centre frequencies. This can be explained by noticing that the matching level of the antennas at these frequencies is lower for the shorter distance version.

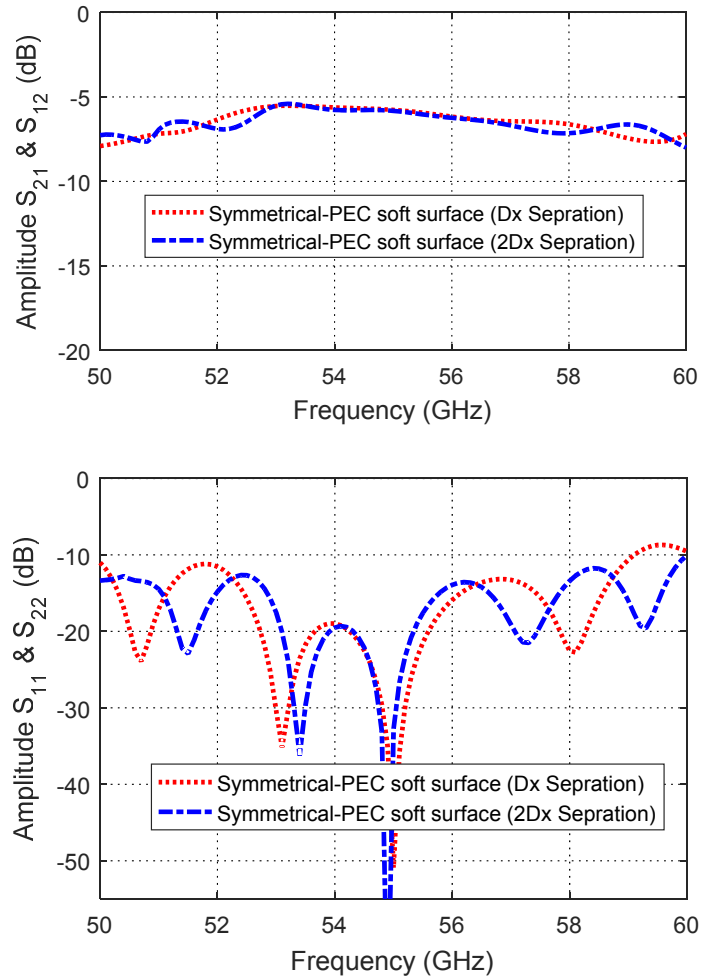


Figure 5.1.20: S-parameters with longer separation between transmit and receive dipoles (double distance).

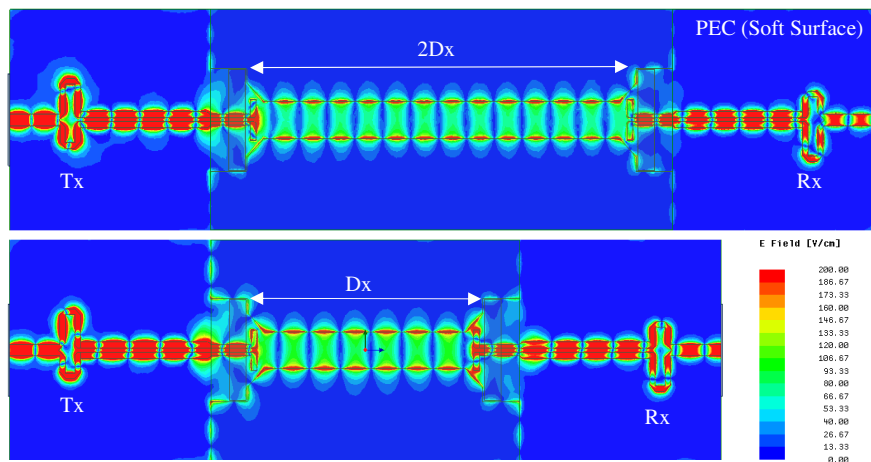


Figure 5.1.21: Doubling the distance, electric field intensity heat map at 55 GHz.

In the single layer structure, one significant effect is the reflected waves from the side edges of the substrate in the E-plane, as can be seen from Fig. 5.1.22. The reflected waves which are mostly captured by the tapered ground plane can interfere destructively with the direct wave between the two dipoles as seen from S₂₁ level in Fig. 5.1.23 at 51.7 GHz. This suggests that the width of the substrate should be increased to shift such destructive behavior outside the band of interest, which is not practical. However, when the PEC (soft surface for this polarization) is used on the sides, as shown in Fig. 5.1.21, these waves are suppressed, and the substrate width is not of concern. Aside from the destructive behavior, the 6 dB loss due to the spherical spreading waves can be noticed with the double distance structure. It should be clear that the antenna is not radiating in a homogeneous medium. Therefore, variation in the 6 dB difference value is expected.

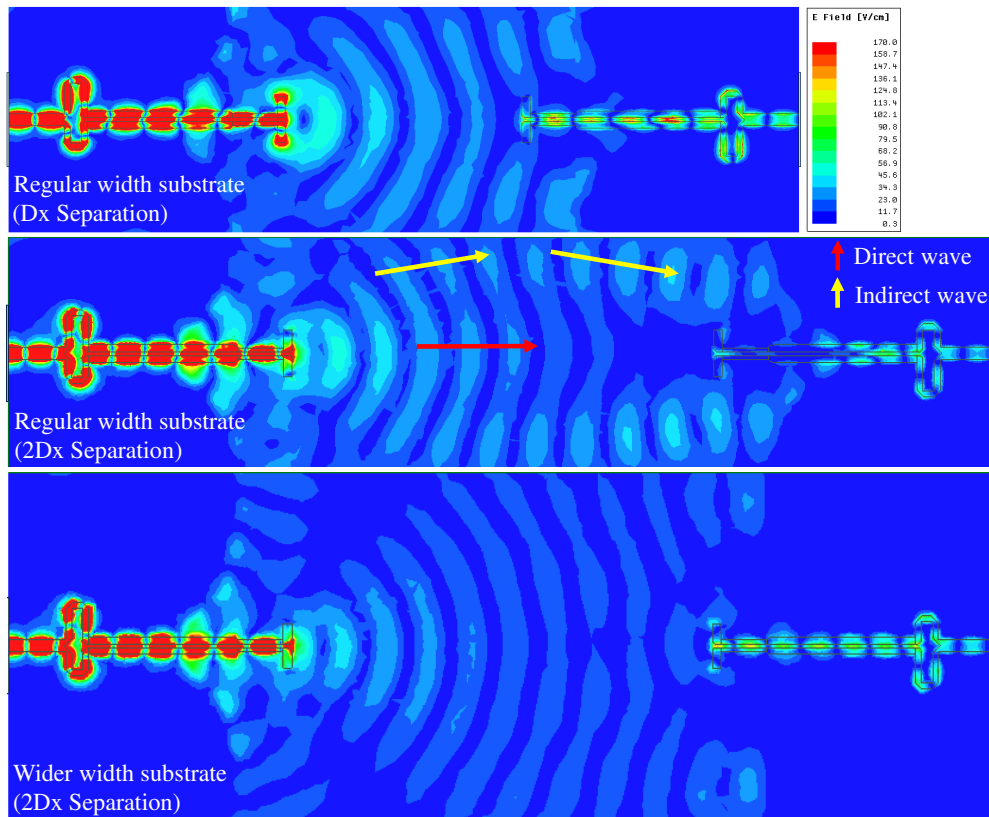


Figure 5.1.22: Doubling the distance, electric field intensity heat map at 51.7 GHz (Single layer structure).

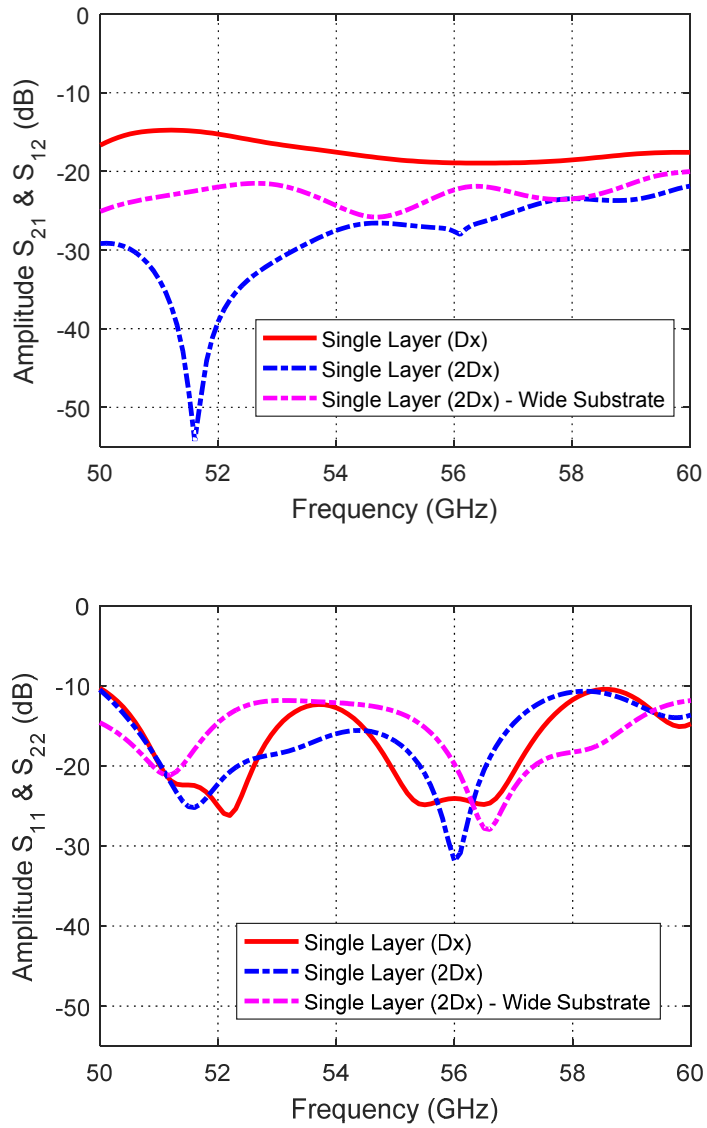


Figure 5.1.23: Doubling the distance S-parameters (Single layer structure).

Fig. 5.1.24 shows the heat map of the electric field in the H-plane for the proposed structures. It is noticed that the symmetrical layers structure has less radiation loss to free space once compared with the single layer structure as expected. Also, the radiation loss at the balun location is noticeable. The radiation losses at the discontinuity locations are also evident.

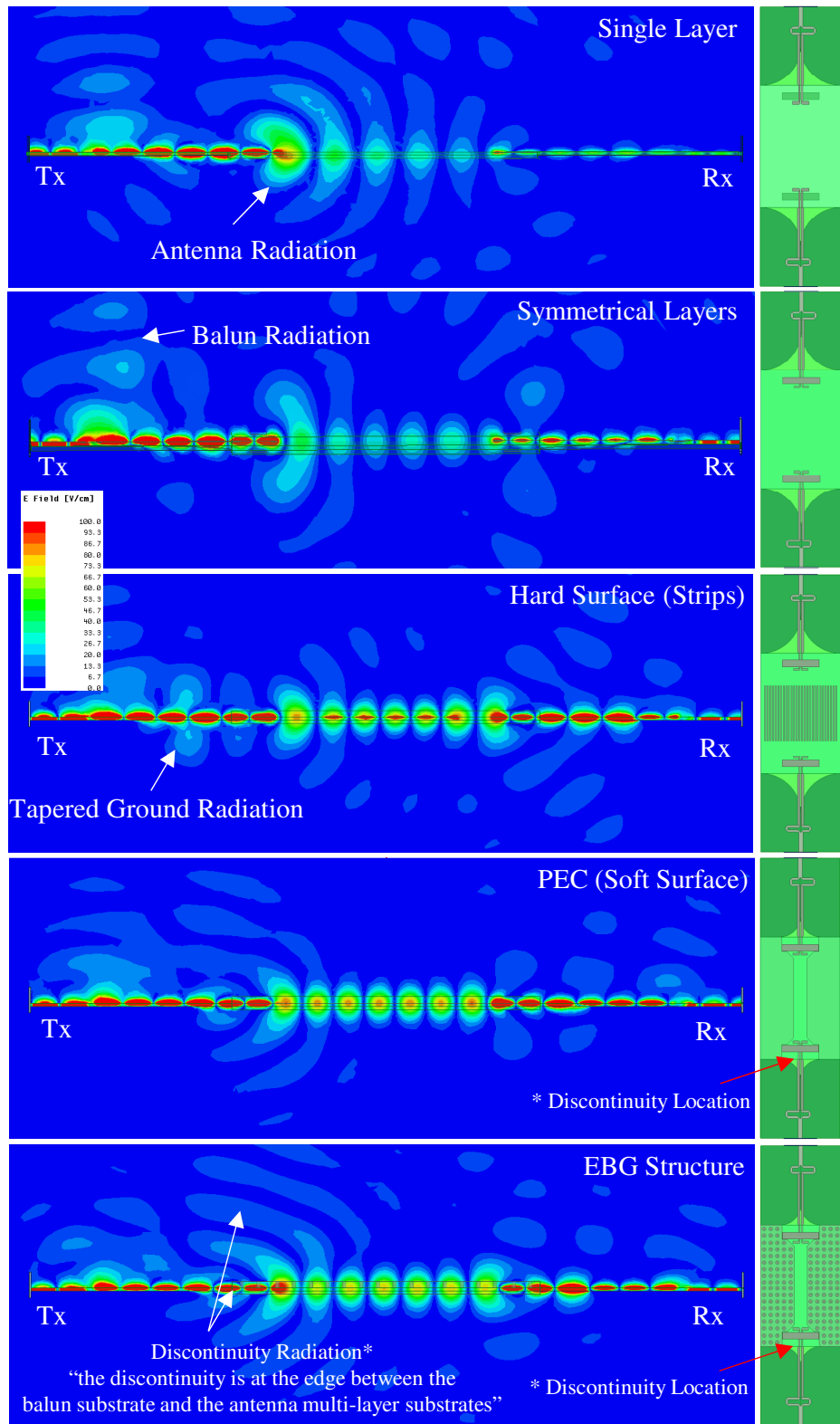


Figure 5.1.24: Electric field heat map in the H-plane for the proposed structures.

It is also noticed that for the EBG and the soft surface structures, the discontinuity radiation at the edge between the balun substrate and the multi-layer substrates sandwiching the antennas is more severe. This is attributed to the proximity of the vertices and edges of the EBG and PEC surface structures. The vertices and edges are strong sources of diffracted fields.

5.1.5 Experimental Prototyping Results

From the previous sections, it was concluded that the soft PEC surface structure is optimal in terms of its cost and performance. Therefore, the soft PEC surface structure is fabricated, as shown in Fig. 5.1.25 shows the actual fabricated prototype for this structure. Fig. 5.1.26 shows the experimental setup. The fabricated structure is the same structure previously studied and detailed in Figs. 5.1.16 and 5.1.17. The experimental setup consists of a Vector Network Analyzer (VNA), to measure the S-Parameters of the Device under Test (DUT). Anritsu testing fixture is used to measure the S-parameters of the device. The testing fixture has been calibrated using the well-known TRL (Thru, Reflect, and Load) method. The reference planes were set at the edges of the microstrip line input-output of the DUT. Fig. 5.1.27 compares the measured S-parameters to the simulated ones, an acceptable agreement between simulated and measured results is observed. The wireless inter-chip link covers the frequency range from 50 to 60 GHz, with a relative bandwidth of 20%. It is worth emphasizing that the baluns introduce around 2-dB loss in the link budget as concluded from the balun structure simulation in Fig. 5.1.9. Such losses can be avoided if the differential feeding is provided directly from the integrated circuit output pins.

It is also worth noting that in wireless inter-chip communication, the antennas can be either integrated within the chip, or can be kept outside the chip, and printed on the board holding the chips. Integrating the antenna inside the chip will have a great advantage in mass production. However, lower efficiencies are expected in such a case. Depending on the frequency, the antenna size would play a role in increasing the cost as well. In [32], the antennas were integrated within the chip, but to enhance the communication link, directors were printed on the Rogers substrate board holding the two chips. In contrast, our proposed solution, the whole antenna structure is printed on the Rogers substrate.

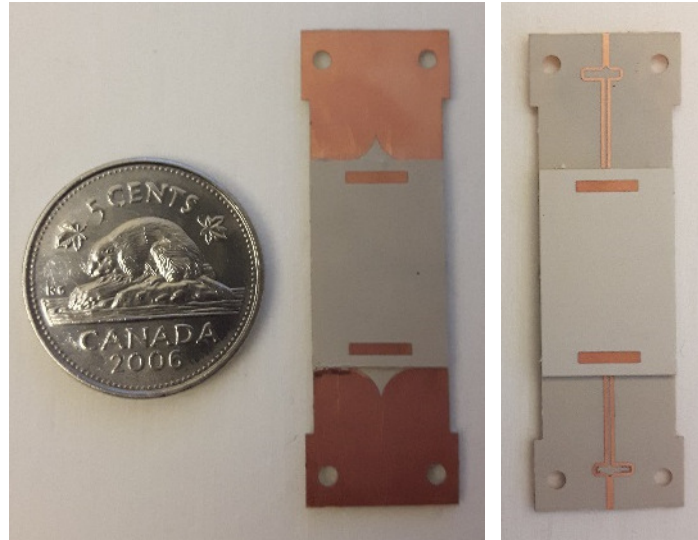


Figure 5.1.25: Actual fabricated prototype, bottom view (left), and top view (right).

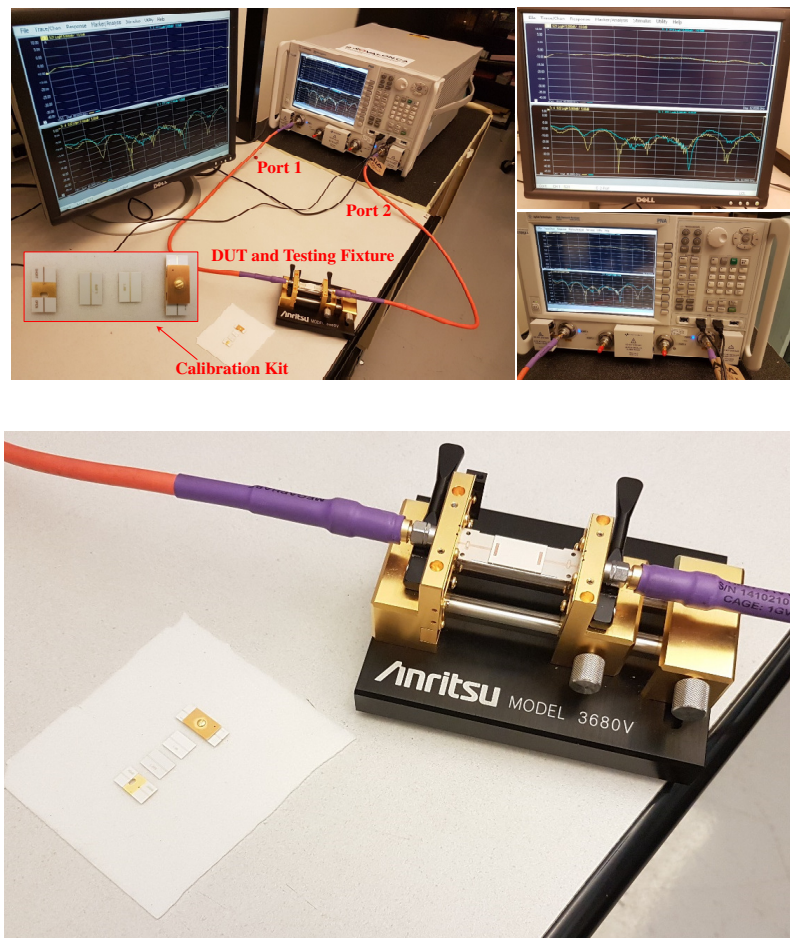


Figure 5.1.26: Experimental setup.

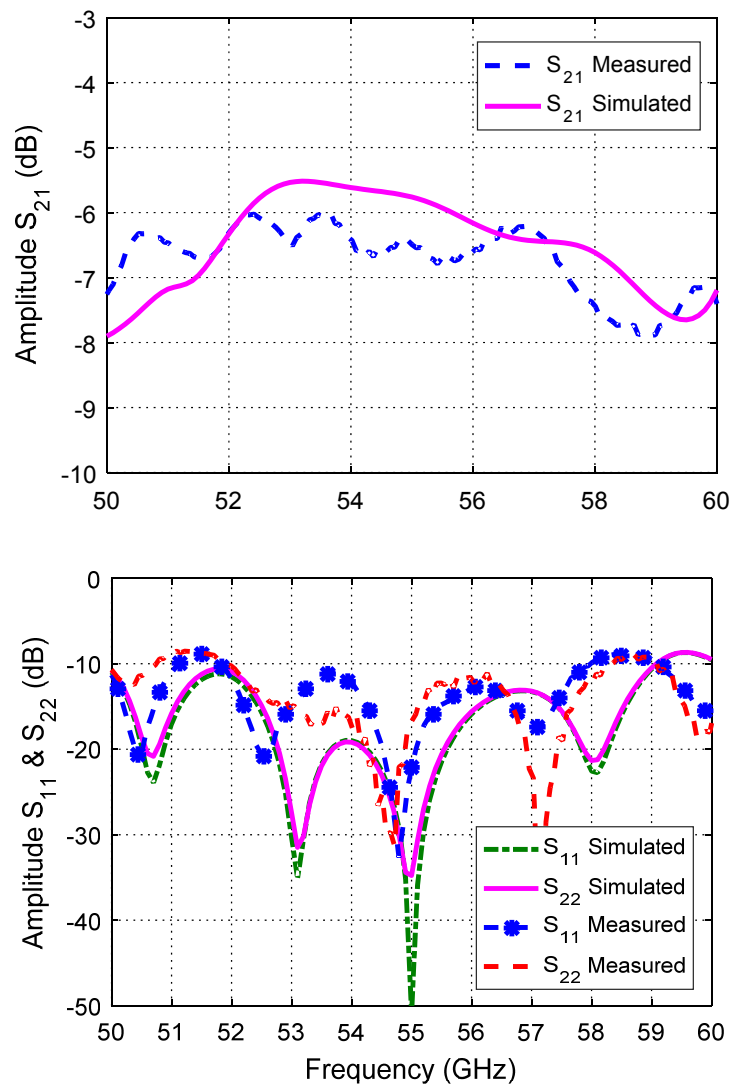


Figure 5.1.27: Measured S parameters for the fabricated prototype.

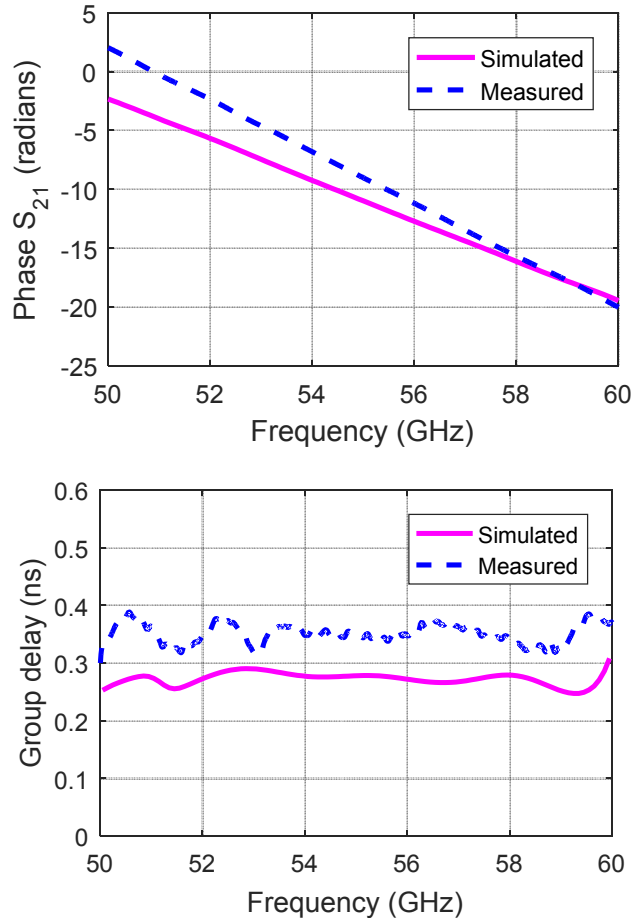


Figure 5.1.28: Measured Phase and Group Delay

Fig. 5.1.28 shows the measured phase and group delay; a fair agreement with simulated results is observed. The linear phase and constant group delay indicate a dispersive free channel behaviour. The fabrication and measurement at 60 GHz are very challenging; the effect of the glue and the tolerance in the material and structure dimensions are very severe. At RF frequencies and even up to 10 GHz, we expect better agreement. However, at 60 GHz, a few tiny deviations in the fabricated prototype produce a significant difference in the results. Not to mention the effect of the surrounding environment, especially for such an open structure, where ideally the measurement should be done in an anechoic chamber, to be in line with the simulation that assumes open free space around the structure. However, the results show good agreement for such low-cost fabrication at 60 GHz, further refinement through several prototypes in a more accurate fabrication facility for industrial and commercial purposes is still possible. Nonetheless, the results are very acceptable for verification purposes.

5.2 One-To-Two Wireless Inter-Chip Communication Link

5.2.1 Introduction

In this section, we study wireless inter-chip communication between adjacent ICs in extreme conditions, where the communicating antennas are misaligned, and the communication link is bent at a 90-degree angle. The study is also extended to include 1:2 wireless inter-chip links, where one transmitting antenna can communicate with two receivers simultaneously.

5.2.2 90-Degree Bend Path

In section 5.1 an inter-chip link structure between two aligned antennas operating between 50-60 GHz was proposed [103]; the structure uses symmetrical layers concept, and soft surfaces to enhance the link budget [85]. The structure is composed of three substrates, all of Rogers 3003, with a dielectric constant of 3. The antennas are dipoles fed differentially through baluns. The three substrates allow the antenna to be symmetrically sandwiched between two equal thickness substrates [93]. Substrate 2 is used for the balun and antenna feed. The balun ground plane is tapered to provide a smooth matching transition; the tapered ground plane also assists in increasing the aperture area of the antenna by capturing more energy at the edge discontinuity of substrates 1 and 3. The dipoles are also backed by reflectors sheets located on top of substrate 1 and bottom of substrate 3. The sheets can be considered as a parallel plate waveguide with its TE cutoff frequency much higher than the operating frequency. Therefore, they suppress backward radiation from the antenna towards the feed. Thus, focusing the antenna radiation towards the receiving antenna. The designed balun exhibits around 1-dB loss, which is equivalent to a 2-dB loss in the link budget due to the two Baluns at the transmitter and receiver. Such loss takes the form of radiation losses, which is expected, especially for the microstrip line technology in the 60 GHz band.

In this section, we consider an extreme condition of misaligned antennas by introducing a 90-degree bend (polarization mismatch [72]). In such case the polarization mismatch is high, however, by employing the hard-soft PEC structure [68], [102], the transmitted energy can be redirected to

the receiving antenna at a 90-degree angle, where the surrounding PEC hard edges guide the waves similar to a typical guiding structure. Fig. 5.2.1 shows the proposed 90-degree bend structures. The path length is $2D_x$ ($D_x = 12\text{mm}$). Two cases are considered. The first case uses the PEC hard/soft surface structure in [103] bent at a 90-degree angle. The second case uses the same structure with an Electromagnetic Band Gap (EBG) periodic structure on the sides of the 90-degree bend. Fig. 5.2.2 shows the electric field heat map for each structure. It is noted from the heat map that the leakage is less in the EBG case. As expected, the EBG structure eliminates the existence of any propagating modes within its bandgap [68]. On the other hand, the soft surface only eliminates the tangential component to the surface.

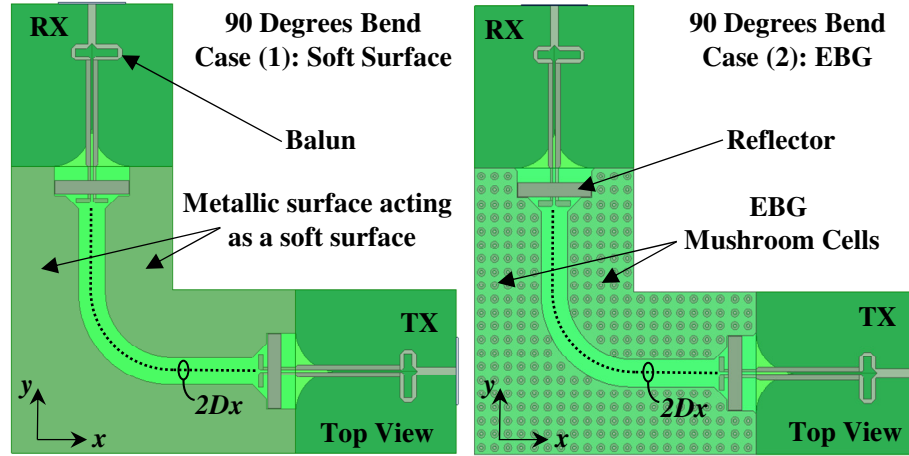


Figure 5.2.1: 90-degree bend structures, left (Case (1): Soft Surface), and right (Case (2): EBG).

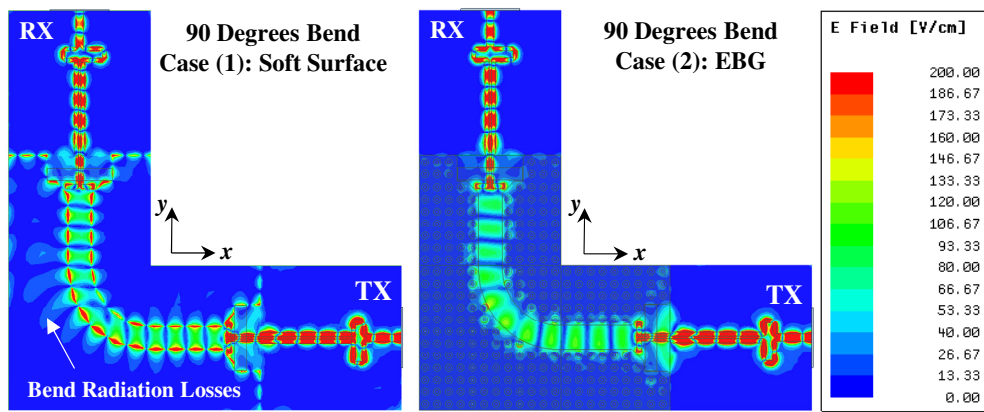


Figure 5.2.2: 90-degree bend structures electric field intensity heat map at 55 GHz, left (Case (1): Soft Surface), and right (Case (2): EBG).

Fig. 5.2.3 shows the S-parameters for both cases. From the S-parameters, it can be noticed that the EBG structure S_{21} value is almost 1-dB higher than the soft surface structure. As well as Fig. 5.2.3 shows that the 90-degree bend S_{21} value is 3 dB lower than the straight case. The 3-dB loss of the 90-degree bend is attributed to the radiation losses at the bend location and the fact that the H-planes of the antennas are not coupled as in the straight case. Fig. 5.2.4 shows the heat map of the electric field in the H-plane for the 90-degree soft surface bend. The intensity of the field drops at the corner point of the link due to the leakage as expected.

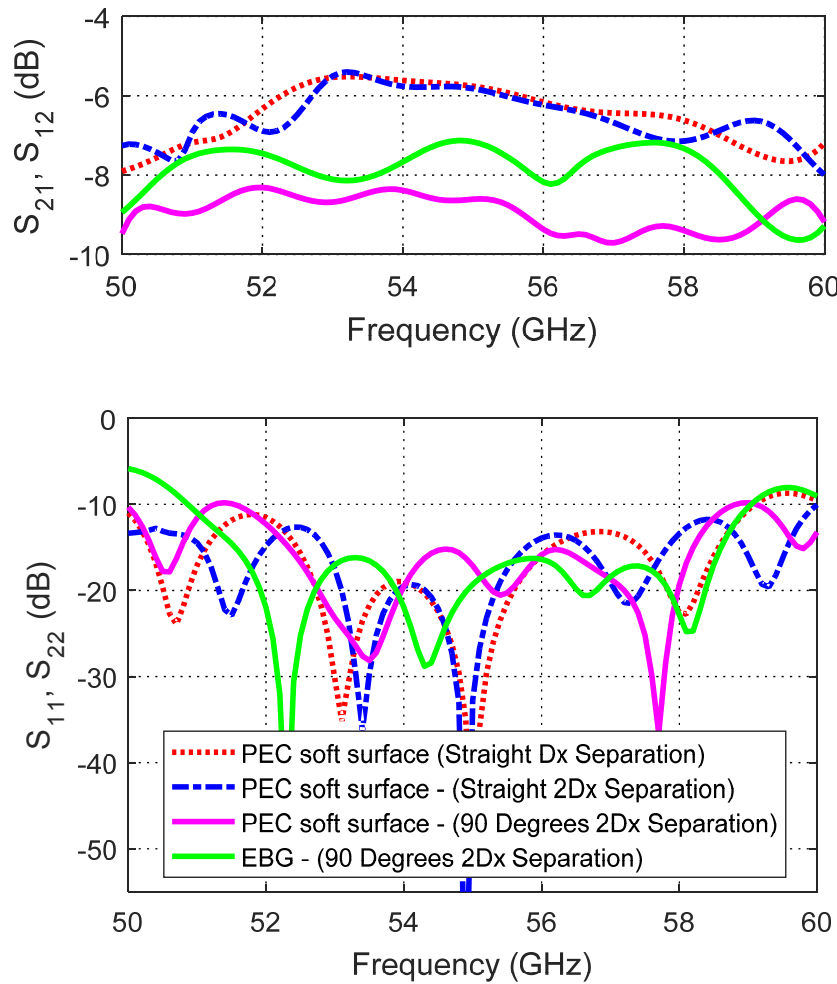


Figure 5.2.3: Doubling the distance and the 90-degree bend S-parameters.

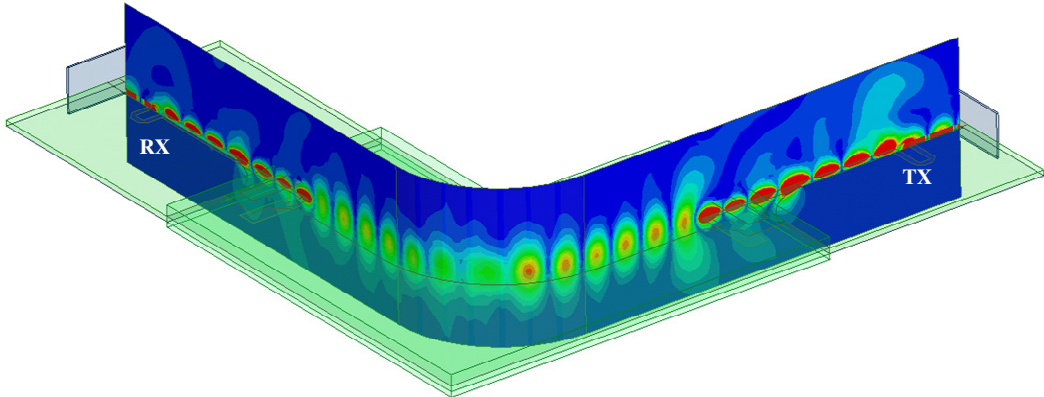


Figure 5.2.4: Electric field heat map in the H-plane for the 90-degree bend (soft surface structure case) at 55 GHz, E-field scale is the same as in Fig. 5.2.2.

5.2.3 1:2 Wireless Inter-Chip Link structures

Fig. 5.2.5 shows three proposed structures for the 1:2 wireless inter-chip communication links, the first two links are T-shape, and the third is a Y-shape structure. The PEC 1:2 T-shape structure generates vertical component modes at the bend location, such generated modes can leak over the PEC surface and contribute significantly to the link budget losses. In such a case, the S_{21} , S_{31} value goes down to -20 dB. The EBG T-shape structure suppresses all types of modes within its band gap. Therefore, the link budget, in this case, is almost 3-dB below the 1:1 bent structure, where the 3-dB here is the division factor between port 2 and 3. In such case, S_{21} and S_{31} value is around -11.5 dB. To avoid using an EBG structure, the PEC structure can be brought up to the level of the EBG structure by having a Y-shape junction. The Y-shape PEC structure reduces the number of vertical component modes generated from the discontinuity, as can be observed from Fig. 5.2.6, and hence reduces the losses in the link budget. The S-Parameters in Fig. 5.2.7 shows that the EBG T-shaped junction and the PEC Y-shaped junction have almost the same S_{21} and S_{31} level.

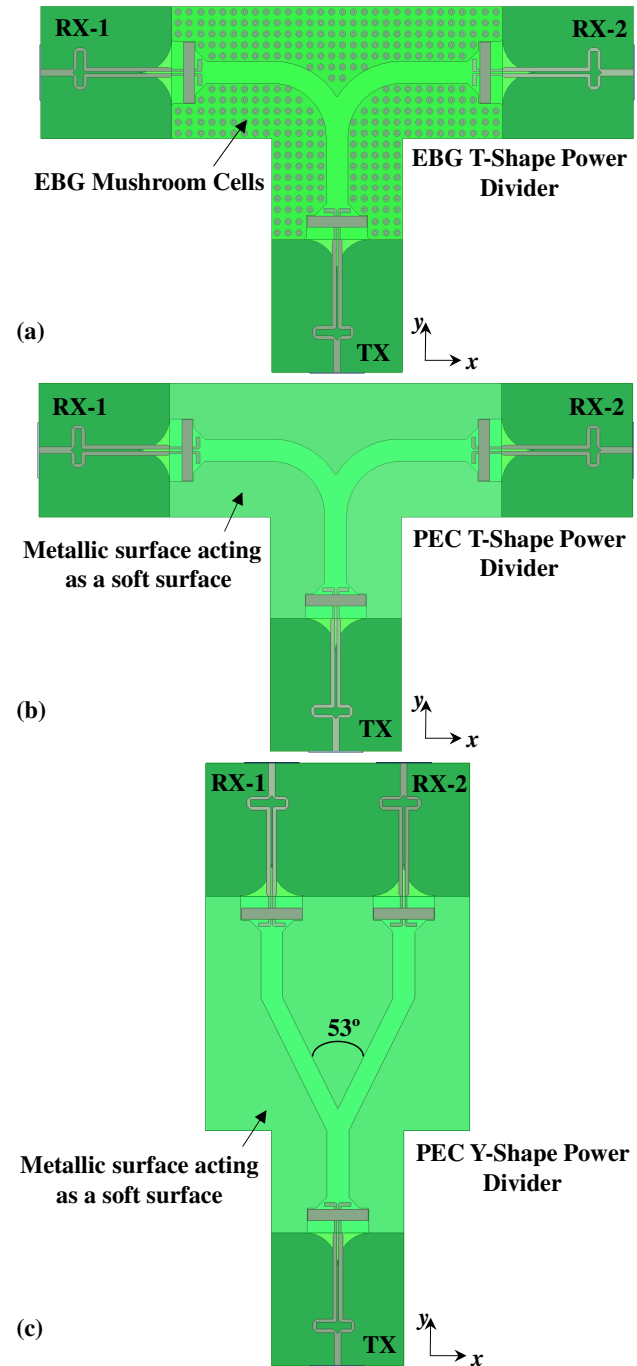


Figure 5.2.5: Proposed 1:2 wireless inter-chip link structures, Port 1 is TX, Port 2 and 3 are RXs,
 (a) EBG T-shape power divider, (b) PEC T-shape power divider, and (c) PEC Y-shape power
 divider.

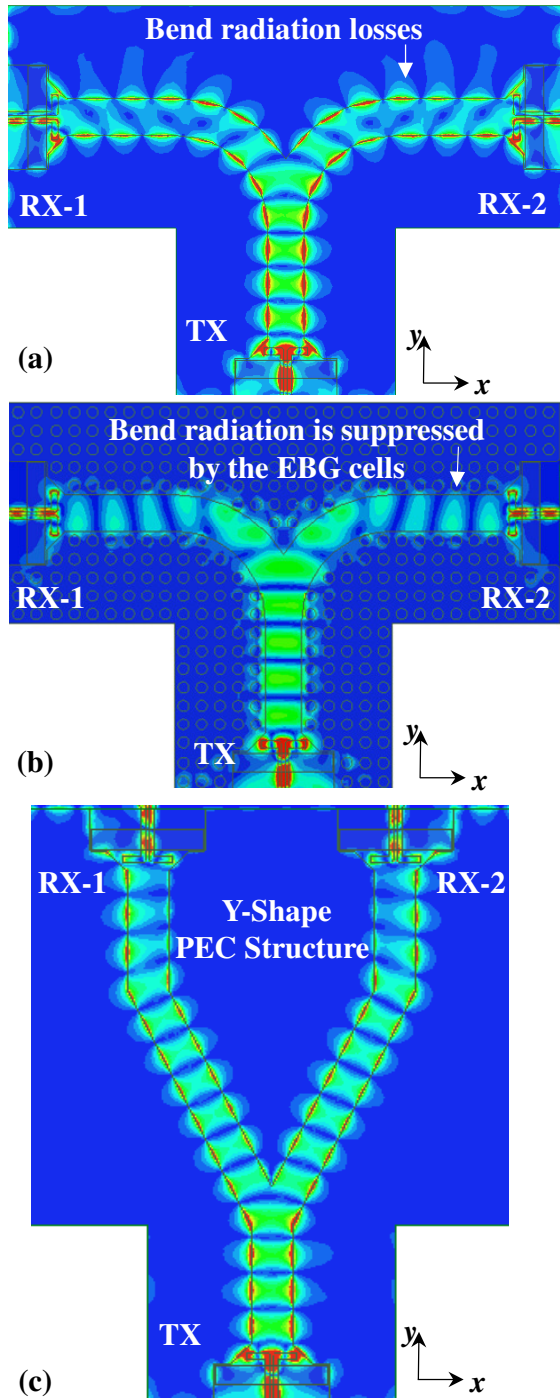


Figure 5.2.6: Proposed 1:2 wireless inter-chip link structures electric field heat maps at 55 GHz.
 (a) EBG T-shape power divider, (b) PEC T-shape power divider, and (c) PEC Y-shape power divider. E-Field scale is the same as in Fig. 5.2.2.

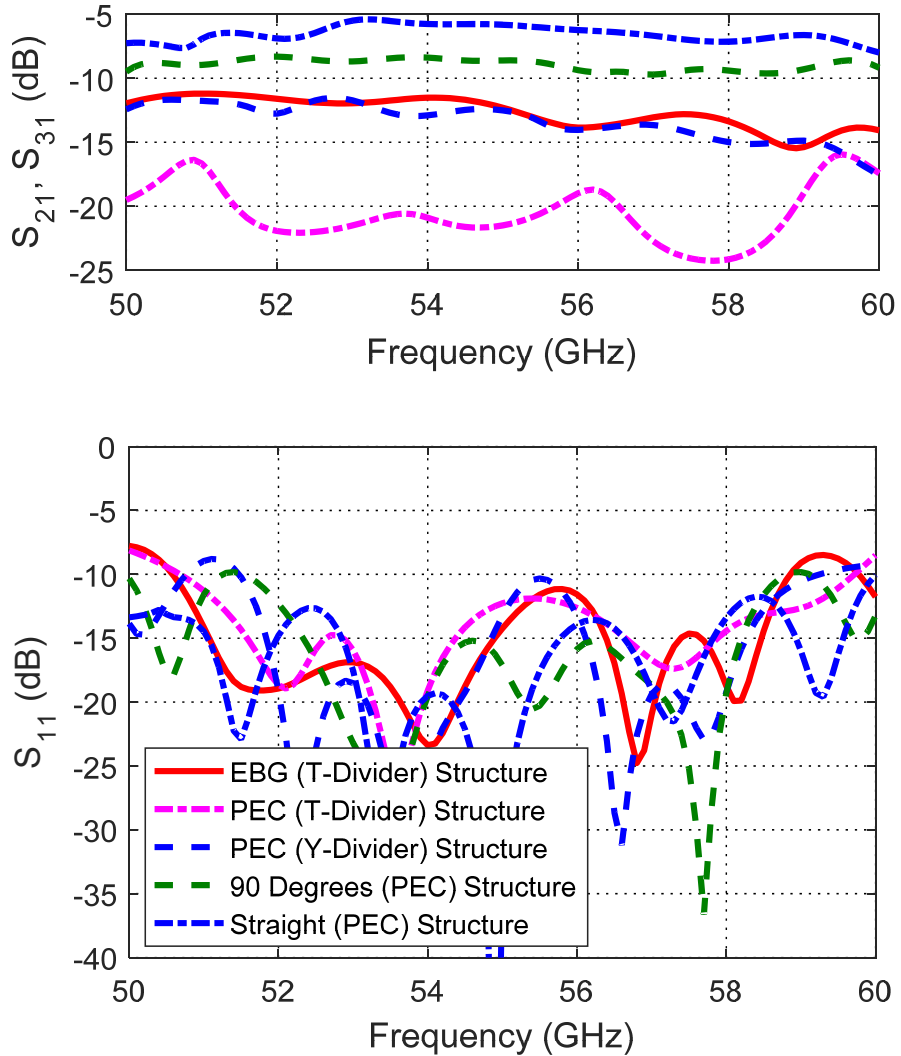


Figure 5.2.7: Proposed 1:2 wireless inter-chip link structures S-parameters.

Fig. 5.2.8 shows the fabricated prototype for the Y-shape structure. The experimental setup consists of a Vector Network Analyzer (VNA), to measure the S-parameters of the Device under Test (Y-shape structure). Fig. 5.2.9 compares the measured values with the simulated results, reasonably good agreement between both is noticed.

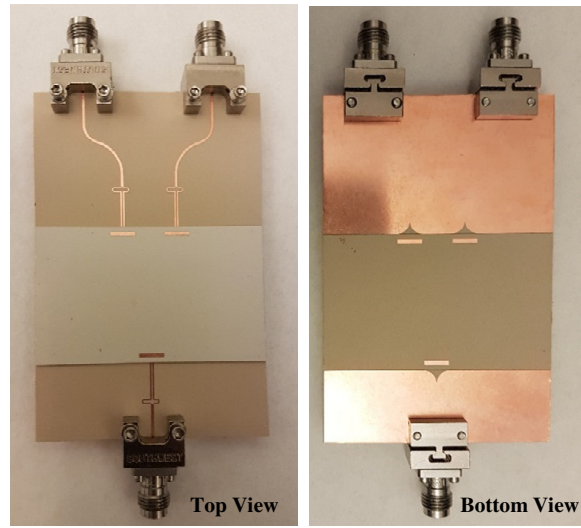


Figure 5.2.8: Fabricated prototype.

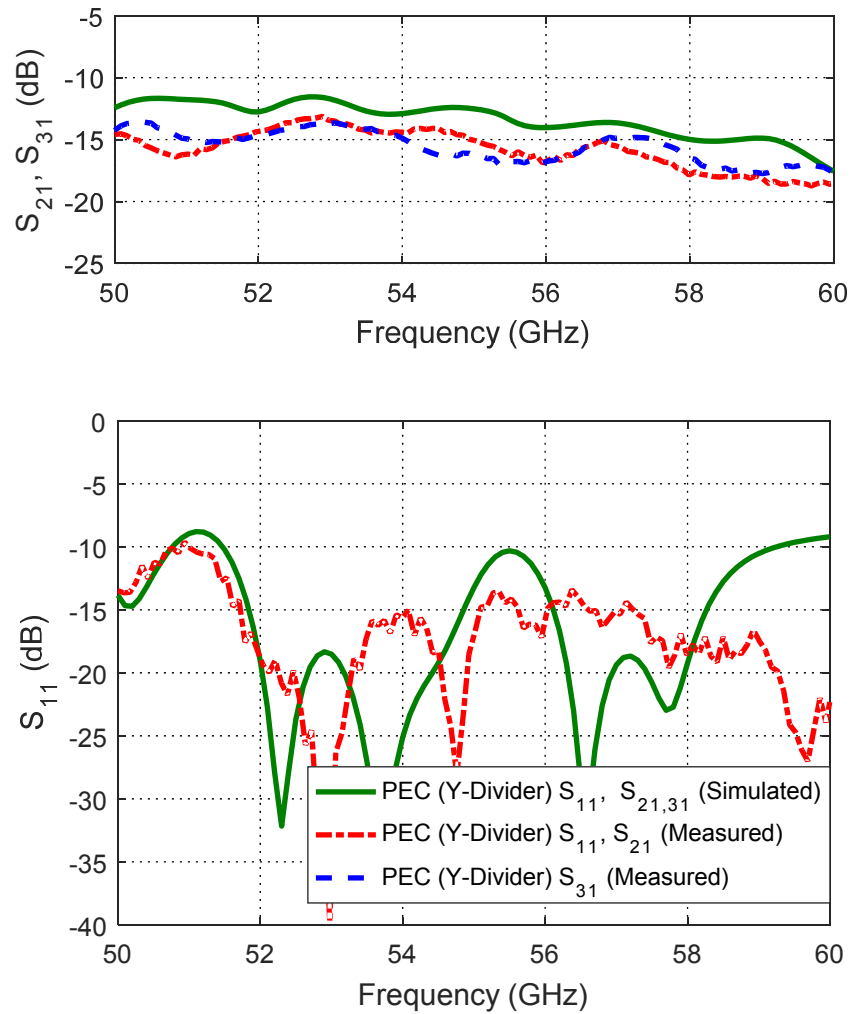


Figure 5.2.9: Proposed 1:2 wireless inter-chip link structure measured S-parameters.

CHAPTER 6

CONCLUSION AND FUTURE WORK

6.1 Conclusion

Adapting to the current requirements for future generations of wireless technologies at millimeter-wave frequencies, our designs have focused on the design of low-cost, low-profile, planar, and high gain antennas at 60 GHz. The proposed structures suit short range, low power applications, such as wireless personal area networks (WPAN). The proposed structures can be realized in any modest fabrication facility. The first antenna proposed a new design perspective, which utilizes microstrip line discontinuities radiation, to create an efficient, high gain, 60 GHz low-profile antenna. The proposed antenna uses only a single substrate and has a high gain of 11.5 dBi; the antenna can be used in a linear array with the separation distance between the elements in the order of a wavelength without generating grating lobes. The compelling feature of the proposed structures is the simplicity, and low-cost (single substrate with no vias), while at the same time maintaining a very high gain at the element level and a decent bandwidth. The second proposed antenna utilized the diffracted fields from plane metallic sheets to achieve a gain of 11 dBi. The antenna has a matching bandwidth of 7 GHz (from 57 to 64) to cover the 60 GHz ISM band. The antenna can be employed in a linear array with around one wavelength distance between the feed points without generating any grating lobes. A new design procedure was proposed; the proposed design procedure can transform the radiation characteristics of an electric or magnetic current element to ME dipole characteristics. The proposed procedure doesn't require the orthogonal combination of the magnetic and electric current elements. Hence, the procedure possesses a significant advantage, where it avoids the need for a quarter free-space wavelength spacing between the current element and the metallic ground plane, making a low-cost, and high-performance solution. A novel technique was proposed to enhance the gain of a DRA antenna over

a wideband range of frequencies, producing a high gain low-cost solution. A study of several aspects of wireless inter-chip communication between adjacent ICs at mm-wave frequencies was provided. The symmetrical layers concept was introduced as a general approach to eliminate the destructive interference and redirect the wasted radiated energy to free space towards the receiving antenna. In addition, the use of hard/soft surfaces and EBG structures to focus the radiated energy towards the receiving antenna was studied thoroughly. The use of such concepts had tremendous advantages, in focusing the energy towards the receiving antenna and eliminating the spherical spreading losses introduced by the radiated spherical wave nature. The incorporation of the symmetrical layers with hard/soft surfaces led to novel compact, low-cost wireless inter-chip structures with enhanced link budget performance.

6.2 Future Work

The scope of future work is vast. This work targeted low-cost planar antenna structures. Many possibilities of developing new structures are still possible with different printed technologies such as substrate integrated waveguide (SIW) technology. SIW cavity antennas are known for wideband performance. Using slots-cavity printed antennas instead of high-Q resonant antennas can have a significant improvement on the bandwidth.

The concept of diffracted fields and using secondary sources to reduce the number of feeding points, relax the feeding network complexity design, and boost the gain with reduced side-lobe level, has been generalized. Thus, the use of PEC, PMC, and Dielectric materials is valid with various type of sources. This suggests many various possible other realizations, with different AMC novel surfaces, and different type of sources. In such a case, the gain, side-lobe level, and bandwidth metrics can be tailored to satisfy the required specifications, taking into consideration a low-cost solution.

Antennas are a crucial part of any transceiver front end; it is usually integrated with filters and amplifier circuits. The co-design of filters, amplifiers, and antennas is highly desirable. The antenna impedance and frequency response can be co-designed in a complementary fashion to achieve the overall system required specifications. The antenna geometry can be designed to satisfy both radiation and filtration requirement (single structure acting as both antenna and filter

at the same time). The study can be extended to minimize the cost and optimize the performance of the whole transceiver chain.

The antenna input impedance can be redesigned to match the output of an amplifier or a filter circuit. The input impedance can be altered from the typical 50 Ohm value. The value that optimizes the performance metrics (gain, bandwidth, etc.) is worth studying.

Furthermore, modifying the currently proposed antennas to operate as circularly polarized antennas is highly desirable. Integrating the proposed structures at the chip level is highly recommended. More rigorous mathematical models for the proposed structures are also of high value. The study of the packaging of inter-chip links is also suggested as future work. The study of integrating the proposed antenna elements with Frequency Selective Surfaces (FSS) and beamforming networks could lead to enhanced novel steering solutions.

Appendix A

Derivation of the total electric field using UTD

The parameters for the reciprocal problem shown in Fig. 3.2 are given as follows:

$$\varphi_1 = \varphi_2 = \pi, \varphi'_1 = \varphi, \varphi'_2 = \pi - \varphi, L_i = \rho_i, \rho_1 = \rho_2 = D_s$$

Using these parameters, the diffraction formulation in (3.2) - (3.4) becomes:

The incident electric field at the edges can be written as:

$$E_x^{inc}(Q_1) = E_0 e^{jk\rho_1 \cos(\varphi)} \quad (\text{A.1})$$

$$E_x^{inc}(Q_2) = E_0 e^{-jk\rho_2 \cos(\varphi)} \quad (\text{A.2})$$

For boresight ($\phi = 90^\circ$), the derivation of (A.3-A.6) can be obtained as follows:

$$D_{so1} = D_{so2} = D_{so} \quad (\text{A.3})$$

$$E_x^{inc}(Q_1) = E_x^{inc}(Q_2) = E_0 \quad (\text{A.4})$$

$$E_x^{inc}(0,0) = E_0 \quad (\text{A.5})$$

$$E_x^{d_i} = E_0 D_{so} \frac{e^{-jkD_s}}{\sqrt{D_s}} \quad (\text{A.6})$$

$$D_{so} = \frac{-e^{-j\pi/4}\sqrt{\lambda}}{8\pi} F(kD_s) \begin{pmatrix} \cot\left(\frac{3\pi}{8}\right) + \cot\left(\frac{\pi}{8}\right) \\ -\cot\left(\frac{5\pi}{8}\right) - \cot\left(\frac{-\pi}{8}\right) \end{pmatrix} \quad (\text{A.7})$$

$$D_{so} = \frac{-e^{-j\pi/4}\sqrt{\lambda/2}}{\pi} F\left(2\pi \frac{D_s}{\lambda}\right) \quad (\text{A.8})$$

$$E_x^{tot} = E_x^{inc} + E_x^{d_1} + E_x^{d_2} \quad (\text{A.9})$$

$$E_x^{tot} = E_0 + 2E_0 D_{so} \frac{e^{-jkD_s}}{\sqrt{D_s}} = E_0 \left(1 + 2D_{so} \frac{e^{-jkD_s}}{\sqrt{D_s}} \right) \quad (\text{A.10})$$

This concludes that the total electric field in the boresight direction as a function of D_s can be written as given by (A.11).

$$E_x^{tot} = E_0 \left(1 - F \left(2\pi \frac{D_s}{\lambda} \right) \frac{\sqrt{2\lambda/D_s}}{\pi} e^{-j(kD_s + \pi/4)} \right) \quad (\text{A.11})$$

The second term of (A.11) resembles a Lituus spiral. In this case, the trace of the spiral can be roughly approximated with concentric circles centered at the spiral center. Hence, the approximate maximum of (A.11) can be obtained when the second term phase is an odd integer multiple of π , and the approximate minimum when it is even multiple integers of π . Hence, the peaks and the dips in the gain as a function of the distance from the dipole can be written as follows:

For the peaks $\rightarrow kD_s + \pi/4 = n_o \pi$

Where n_o is a non-zero odd integer number ($n_o = 1, 3, 5, \dots$)

$$D_s = \frac{(4n_o - 1)}{8} \lambda \rightarrow D_{s\max} = 0.375\lambda, 1.375\lambda, 2.375\lambda, \dots$$

For the dips $\rightarrow kD_s + \pi/4 = n_e \pi$

Where n_e is a non-zero even integer number ($n_e = 2, 4, 6, \dots$)

$$D_s = \frac{(4n_e - 1)}{8} \lambda \rightarrow D_{s\min} = 0.875\lambda, 1.875\lambda, 2.875\lambda, \dots$$

Appendix B

Multilayer Transmission Line Analysis

Fig. B.1 shows the steady-state analysis of a plane wave impinging on a dielectric slab. This problem can be equivalently solved with the transmission line model shown directly below. The characteristic impedance of each section and the load value are given by Equations (B.1) - (B.3) where the intrinsic impedance of the free space is given by $\eta_0 = 377 \Omega$. Using Snell's law and the input impedance equations from the transmission line theory, Equations (B.4) - (B.8), the input reflection coefficient can be calculated. Fig. B.2 shows the calculated reflection coefficient magnitude versus the slab thickness, as can be seen, maximum reflection and minimum transmission can be achieved when the slab thickness is multiple odd integers of a quarter guided wavelength. The used dielectric constant of the slab in this calculation is 10.2. Fig. B.3 shows the reflection coefficient for a quarter guided wavelength slab for all the angles of incidence [29], [64].

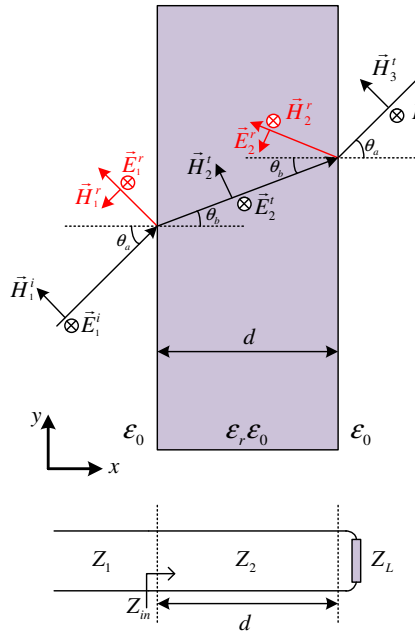


Fig. B.1: Steady-state analysis of a plane wave impinging on a dielectric slab.

$$Z_1 = \frac{\eta_0}{\cos(\theta_a)} \quad (\text{B.1})$$

$$Z_2 = \frac{\eta_0}{\sqrt{\epsilon_r} \cos(\theta_b)} \quad (\text{B.2})$$

$$Z_L = \frac{\eta_0}{\cos(\theta_a)} \quad (\text{B.3})$$

$$k_1 \sin(\theta_a) = k_2 \sin(\theta_b) \quad (\text{B.4})$$

$$k_1 = \frac{\omega}{c} \quad (\text{B.5})$$

$$k_2 = \frac{\omega \sqrt{\epsilon_r}}{c} \quad (\text{B.6})$$

$$Z_{in} = Z_2 \frac{Z_L + jZ_2 \tan(k_2 d)}{Z_2 + jZ_L \tan(k_2 d)} \quad (\text{B.7})$$

$$\Gamma = \frac{Z_{in} - Z_1}{Z_{in} + Z_1} \quad (\text{B.8})$$

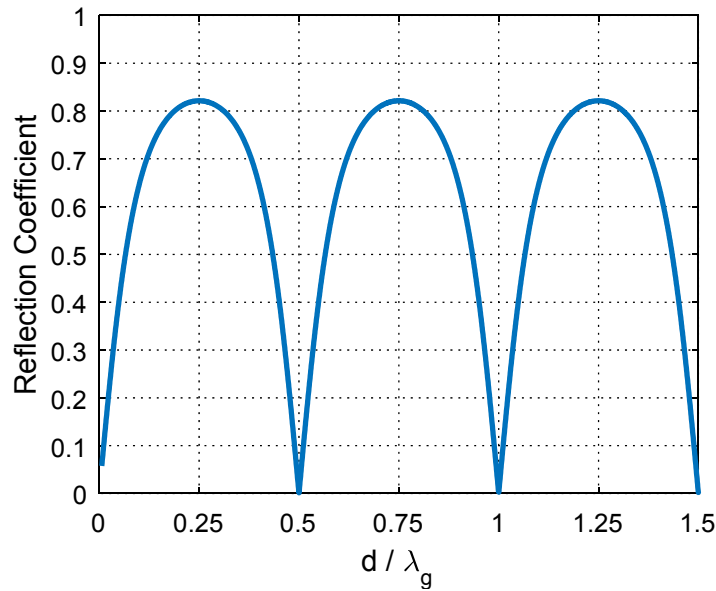


Fig. B.2: Calculated reflection coefficient magnitude versus the slab thickness

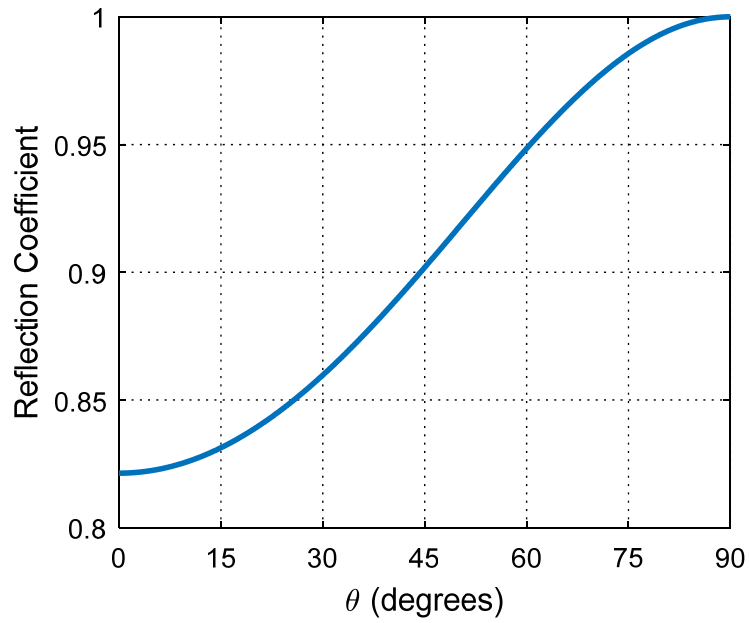


Fig. B.3: Reflection coefficient of a quarter guided wavelength slab versus angle of incidence.

Bibliography

- [1] F. A. Wyczalek, *Millimeter Wave Technology in Wireless PAN, LAN, and MAN*. Auerbach Publications, 2008.
- [2] D. Liu, B. Gaucher, U. Pfeiffer, and J. Grzyb, *Advanced Millimeter-Wave Technologies*. Chichester, UK: John Wiley & Sons, Ltd, 2009.
- [3] L. Lu, K. Ma, F. Meng, and K. S. Yeo, “Design of a 60-GHz Quasi-Yagi Antenna With Novel Ladder-Like Directors for Gain and Bandwidth Enhancements,” *IEEE Antennas Wirel. Propag. Lett.*, vol. 15, pp. 682–685, 2016.
- [4] I. Mohamed, Z. Briqech, and A. Sebak, “Antipodal fermi tapered slot antenna for 60-GHz band applications,” *IEEE Antennas Wirel. Propag. Lett.*, vol. 14, pp. 96–99, 2015.
- [5] T. H. Jang, H. Y. Kim, and C. S. Park, “A 60 GHz Wideband Switched-Beam Dipole-Array-Fed Hybrid Horn Antenna,” *IEEE Antennas Wirel. Propag. Lett.*, vol. 17, no. 7, pp. 1344–1348, 2018.
- [6] M. Sharifi Sorkherizi, A. Dadgarpour, and A. A. Kishk, “Planar high-efficiency antenna array using new printed ridge gap waveguide technology,” *IEEE Trans. Antennas Propag.*, vol. 65, no. 7, pp. 3772–3776, 2017.
- [7] Y. Hong and J. Choi, “60 GHz Patch Antenna Array With Parasitic Elements for Smart Glasses,” *IEEE Antennas Wirel. Propag. Lett.*, vol. 17, no. 7, pp. 1252–1256, 2018.
- [8] T. Zhang, L. Li, H. Xia, X. Ma, and T. J. C. Cui, “A low-cost and high-gain 60-GHz differential phased array antenna in PCB process,” *IEEE Trans. Components, Packag. Manuf. Technol.*, vol. 8, no. 7, pp. 1281–1291, 2018.
- [9] H. Chu, J. X. Chen, and Y. X. Guo, “An Efficient Gain Enhancement Approach for 60-GHz Antenna Using Fully Integrated Vertical Metallic Walls in LTCC,” *IEEE Trans. Antennas Propag.*, vol. 64, no. 10, pp. 4513–4518, 2016.
- [10] N. Celik and M. F. Iskander, “Genetic-algorithm-based antenna array design for a 60-GHz hybrid smart antenna system,” *IEEE Antennas Wirel. Propag. Lett.*, vol. 7, pp. 795–798, 2008.
- [11] C. Kärnfelt, P. Hallbjörner, H. Zirath, and A. Alping, “High gain active microstrip antenna for 60-GHz WLAN/WPAN applications,” *IEEE Trans. Microw. Theory Tech.*, vol. 54, no. 6, pp. 2593–2602, 2006.
- [12] X. P. Chen, K. Wu, L. Han, and F. He, “Low-cost high gain planar antenna array for 60 GHz band applications,” *IEEE Trans. Antennas Propag.*, vol. 58, no. 6, pp. 2126–2129, 2010.
- [13] Y. J. Cheng, *Substrate Integrated Antennas and Arrays*, 1st Ed. Boca Raton: CRC Press, 2015.
- [14] K. S. Chin, W. Jiang, W. Che, C. C. Chang, and H. Jin, “Wideband LTCC 60-GHz antenna

array with a dual-resonant slot and patch structure,” *IEEE Trans. Antennas Propag.*, vol. 62, no. 1, pp. 174–182, 2014.

- [15] A. A. Qureshi, D. M. Klymyshyn, M. Tayfeh, W. Mazhar, M. Borner, and J. Mohr, “Template-Based Dielectric Resonator Antenna Arrays for Millimeter-Wave Applications,” *IEEE Trans. Antennas Propag.*, vol. 65, no. 9, pp. 4576–4584, Sep. 2017.
- [16] M. Li and K. Luk, “Wideband Magneto-Electric Dipole Antenna for 60-GHz Millimeter-Wave Communications,” *IEEE Trans. Antennas Propag.*, vol. 63, no. 7, pp. 3276–3279, Jul. 2015.
- [17] R. A. Alhalabi and G. M. Rebeiz, “Differentially-fed millimeter-wave yagi-uda antennas with folded dipole feed,” *IEEE Trans. Antennas Propag.*, vol. 58, no. 3, pp. 966–969, 2010.
- [18] R. A. Alhalabi and G. M. Rebeiz, “High-efficiency angled-dipole antennas for millimeter-wave phased array applications,” *IEEE Trans. Antennas Propag.*, vol. 56, no. 10, pp. 3136–3142, 2008.
- [19] Z. Chen, H. Liu, J. Yu, and X. Chen, “High gain, broadband and dual-polarized substrate integrated waveguide cavity-backed slot antenna array for 60 GHz band,” *IEEE Access*, vol. 6, pp. 31012–31022, 2018.
- [20] J. Zhu, C. Chu, L. Deng, C. Zhang, Y. Yang, and S. Li, “mm-Wave High Gain Cavity-Backed Aperture-Coupled Patch Antenna Array,” *IEEE Access*, vol. 6, pp. 44050–44058, 2018.
- [21] S. B. Yeap, Z. N. Chen, and X. Qing, “Gain-enhanced 60-GHz LTCC antenna array with open air cavities,” *IEEE Trans. Antennas Propag.*, vol. 59, no. 9, pp. 3470–3473, 2011.
- [22] J. Zhang, X. Zhang, and A. A. Kishk, “Broadband 60 GHz Antennas Fed by Substrate Integrated Gap Waveguides,” *IEEE Trans. Antennas Propag.*, vol. 66, no. 7, pp. 3261–3270, 2018.
- [23] F. J. Huang, C. M. Lee, C. Y. Kuo, and C. H. Luo, “mmW Antenna in IPD process for 60-GHz WPAN applications,” *IEEE Antennas Wirel. Propag. Lett.*, vol. 10, pp. 565–568, 2011.
- [24] M. Sun, X. Qing, and Z. N. Chen, “60-GHz end-fire fan-like antennas with wide beamwidth,” *IEEE Trans. Antennas Propag.*, vol. 61, no. 4, pp. 1616–1622, 2013.
- [25] A. Toda and F. Flaviis, “60-GHz Substrate Materials Characterization Using the Covered Transmission-Line Method,” *IEEE Trans. Microw. Theory Tech.*, vol. 63, no. 3, pp. 1063–1075, Mar. 2015.
- [26] P. Kildal, *Foundations for Antenna Engineering*. Artech House, 2015.
- [27] Y. T. Lo and S. W. Lee, Eds., *Antenna Handbook*. Boston, MA: Springer US, 1988.
- [28] Y. Al-Alem and A. A. Kishk, “Low-Profile Low-Cost High Gain 60 GHz Antenna,” *IEEE Access*, vol. 6, pp. 13376–13384, 2018.
- [29] D. Pozar, *Microwave Engineering Fourth Edition*, Fourth Ed. John Wiley & Sons, 2012.
- [30] Z. G. Liu, “Fabry-Perot Resonator antenna,” *J. Infrared, Millimeter, Terahertz Waves*, vol.

31, no. 4, pp. 391–403, 2010.

- [31] H. Attia, L. Yousefi, and O. Ramahi, “High gain microstrip antennas loaded with high characteristic impedance superstrates,” *IEEE Antennas Propag. Soc. AP-S Int. Symp.*, vol. 10, pp. 1258–1261, 2011.
- [32] A. A. Kishk and L. Shafai, “Gain enhancement of antennas over finite ground plane covered by a dielectric sheet,” *IEE Proc. H Microwaves, Antennas Propag.*, vol. 134, no. 1, pp. 60–64, 1987.
- [33] H. Nakano, *Low-Profile Natural and Metamaterial Antennas*. Hoboken, NJ, USA: John Wiley & Sons, Inc., 2016.
- [34] L. Kwai-man, H. Wong, K. Luk, and H. Wong, “A New Wideband Unidirectional Antenna Element,” *Int. J. Microw. Opt. Technol.*, vol. 1, no. 1, pp. 35–44, 2006.
- [35] E. J. Denlinger, “Losses of Microstrip Lines,” *IEEE Trans. Microw. Theory Tech.*, vol. 28, no. 6, pp. 513–522, 1980.
- [36] C. A. Balanis, *Advanced engineering electromagnetics*, 2nd ed. John Wiley & Sons, 2012.
- [37] C. A. Balanis, Ed., *Modern Antenna Handbook*, 1st ed. Hoboken, NJ, USA: John Wiley & Sons, Inc., 2008.
- [38] T. A. Milligan, *Modern Antenna Handbook*. Hoboken, NJ, USA: John Wiley & Sons, Inc., 2008.
- [39] Y. Al-Alem and A. A. Kishk, “Efficient Millimeter-Wave Antenna Based On the Exploitation of Microstrip Line Discontinuity Radiation,” *IEEE Trans. Antennas Propag.*, vol. 66, no. 6, pp. 2844–2852, 2018.
- [40] T. C. Edwards and M. B. Steer, *Foundations for Microstrip Circuit Design*. Chichester, UK: John Wiley & Sons, Ltd, 2016.
- [41] H. Sobol, “Radiation Conductance of Open-Circuit Microstrip,” *IEEE Trans. Microw. Theory Tech.*, vol. 19, no. 11, pp. 885–887, 1971.
- [42] M. Sharifi Sorkherizi and A. A. Kishk, “Fully Printed Gap Waveguide with Facilitated Design Properties,” *IEEE Microw. Wirel. Components Lett.*, vol. 26, no. 9, pp. 657–659, 2016.
- [43] D. Sievenpiper, “High-impedance electromagnetic surfaces,” University of California, 1999.
- [44] E. Pucci, E. Rajo-Iglesias, J. L. Vázquez-Roy, and P. S. Kildal, “Planar dual-mode horn array with corporate-feed network in inverted microstrip gap waveguide,” *IEEE Trans. Antennas Propag.*, vol. 62, no. 7, pp. 3534–3542, 2014.
- [45] K. Gong, Z. N. Chen, X. Qing, P. Chen, and W. Hong, “Substrate integrated waveguide cavity-backed wide slot antenna for 60-GHz bands,” *IEEE Trans. Antennas Propag.*, vol. 60, no. 12, pp. 6023–6026, 2012.
- [46] J. Xu, Z. N. Chen, X. Qing, and W. Hong, “Bandwidth Enhancement for a 60 GHz Substrate

Integrated Waveguide Fed Cavity Array Antenna on LTCC,” *IEEE Trans. Antennas Propag.*, vol. 59, no. 3, pp. 826–832, 2011.

- [47] A. E. I. Lamminen, J. Säily, and A. R. Vimpari, “60-GHz Patch Antennas and Arrays on LTCC With Embedded-Cavity Substrates,” *IEEE Trans. Antennas Propag.*, vol. 56, no. 9, pp. 2865–2874, 2008.
- [48] H. Sun, Y. Guo, and Z. Wang, “60-GHz Circularly Polarized U-Slot Patch Antenna Array on LTCC,” *IEEE Trans. Antennas Propag.*, vol. 61, no. 1, pp. 430–435, 2013.
- [49] S. Liao, P. Chen, P. Wu, K. M. Shum, and Q. Xue, “Substrate-Integrated Waveguide-Based 60-GHz Resonant Slotted Waveguide Arrays With Wide Impedance Bandwidth and High Gain,” *IEEE Trans. Antennas Propag.*, vol. 63, no. 7, pp. 2922–2931, 2015.
- [50] M. Li and K. Luk, “Low-Cost Wideband Microstrip Antenna Array for 60-GHz Applications,” *IEEE Trans. Antennas Propag.*, vol. 62, no. 6, pp. 3012–3018, 2014.
- [51] H. Jin, W. Che, K. Chin, W. Yang, and Q. Xue, “Millimeter-Wave TE20-Mode SIW Dual-Slot-Fed Patch Antenna Array With a Compact Differential Feeding Network,” *IEEE Trans. Antennas Propag.*, vol. 66, no. 1, pp. 456–461, 2018.
- [52] Z. Gan, Z. Tu, Z. Xie, Q. Chu, and Y. Yao, “Compact Wideband Circularly Polarized Microstrip Antenna Array for 45 GHz Application,” *IEEE Trans. Antennas Propag.*, vol. 66, no. 11, pp. 6388–6392, 2018.
- [53] M. Asaadi and A. Sebak, “High-Gain Low-Profile Circularly Polarized Slotted SIW Cavity Antenna for MMW Applications,” *IEEE Antennas Wirel. Propag. Lett.*, vol. 16, pp. 752–755, 2017.
- [54] L. Wang, Y. Guo, and W. Sheng, “Wideband High-Gain 60-GHz LTCC L-Probe Patch Antenna Array With a Soft Surface,” *IEEE Trans. Antennas Propag.*, vol. 61, no. 4, pp. 1802–1809, 2013.
- [55] T. Mikulasek, J. Puskely, J. Lacik, and Z. Raida, “Design of aperture-coupled microstrip patch antenna array fed by SIW for 60 GHz band,” *IET Microwaves, Antennas Propag.*, vol. 10, no. 3, pp. 288–292, 2016.
- [56] K. Wincza and S. Gruszczynski, “Microstrip antenna arrays fed by a series-parallel slot-coupled feeding network,” *IEEE Antennas Wirel. Propag. Lett.*, vol. 10, pp. 991–994, 2011.
- [57] Z. Liu, “Fabry-Perot Resonator Antenna,” *J. Infrared, Millimeter, Terahertz Waves*, vol. 31, no. 4, pp. 391–403, Dec. 2009.
- [58] A. A. Kishk, “One-dimensional electromagnetic bandgap for directivity enhancement of waveguide antennas,” *Microw. Opt. Technol. Lett.*, vol. 47, no. 5, pp. 430–434, 2005.
- [59] A. A. Kishk and L. Shafai, “Gain enhancement of antennas over finite ground plane covered by a dielectric sheet,” *IEE Proc. H Microwaves, Antennas Propag.*, vol. 134, no. 1, pp. 60–64, 1987.
- [60] H. Vettikalladi, O. Lafond, and M. Himdi, “High-Efficient and High-Gain Superstrate Antenna for 60-GHz Indoor Communication,” *IEEE Antennas Wirel. Propag. Lett.*, vol. 8,

pp. 1422–1425, 2009.

- [61] H. Attia, M. L. Abdelghani, and T. A. Denidni, “Wideband and High-Gain Millimeter-Wave Antenna Based on FSS Fabry–Perot Cavity,” *IEEE Trans. Antennas Propag.*, vol. 65, no. 10, pp. 5589–5594, Oct. 2017.
- [62] A. Hosseini, F. Capolino, and F. De Flaviis, “Gain enhancement of a V-band antenna using a fabry-pérot cavity with a self-sustained all-metal cap with FSS,” *IEEE Trans. Antennas Propag.*, vol. 63, no. 3, pp. 909–921, 2015.
- [63] A. Hosseini, F. De Flaviis, and F. Capolino, “A 60 GHz simple-to-fabricate single-layer planar Fabry–Pérot cavity antenna,” *IET Microwaves, Antennas Propag.*, vol. 9, no. 4, pp. 313–318, Mar. 2015.
- [64] R. Paknys, *Applied Frequency-Domain Electromagnetics*. Chichester, UK: John Wiley & Sons, Ltd, 2016.
- [65] R. G. Kouyoumjian and P. H. Pathak, “A uniform geometrical theory of diffraction for an edge in a perfectly conducting surface,” *Proc. IEEE*, vol. 62, no. 11, pp. 1448–1461, 1974.
- [66] Y. Al-Alem and A. A. Kishk, “Simple High Gain 60 GHz Antenna,” in *2018 IEEE International Symposium on Antennas and Propagation & USNC/URSI National Radio Science Meeting*, 2018, vol. 6, pp. 1693–1694.
- [67] L. B. Felsen, “Evanescent waves*,” *J. Opt. Soc. Am*, vol. 66, no. 8, pp. 751–760, 1976.
- [68] P. S. Kildal, A. A. Kishk, and S. Maci, “Special Issue on Artificial Magnetic Conductors, Soft/Hard Surfaces, and Other Complex Surfaces,” *IEEE Trans. Antennas Propag.*, vol. 53, no. 1, pp. 2–7, Jan. 2005.
- [69] A. Vallecchi, J. R. De Luis, F. Capolino, and F. De Flaviis, “Low profile fully planar folded dipole antenna on a high impedance surface,” *IEEE Trans. Antennas Propag.*, vol. 60, no. 1, pp. 51–62, 2012.
- [70] Z. Zhang and K. Wu, “A Wideband Dual-Polarized Dielectric Magneto-Electric Dipole Antenna,” *IEEE Trans. Antennas Propag.*, 2018.
- [71] X. Ruan, K. B. Ng, and C. H. Chan, “A Differentially-Fed Transmission-Line-Excited Magneto-Electric Dipole Antenna Array for 5G Applications,” *IEEE Trans. Antennas Propag.*, vol. 66, no. 10, pp. 5224–5230, 2018.
- [72] C. A. Balanis, *Antenna Theory Analysis and Design Third Edition*. John Wiley & Sons, 2005.
- [73] K. M. Luk and K. W. Leung, *Dielectric Resonator Antennas*. Research Studies Pr Ltd., 2002.
- [74] A. Petosa and A. Ittipiboon, “Dielectric Resonator Antennas : A Historical Review and the Current State of the Art,” *IEEE Antennas Propag. Mag.*, vol. 52, no. 5, 2010.
- [75] L. Ohlsson *et al.*, “Slot-Coupled Millimeter-Wave Dielectric Resonator Antenna for High-Efficiency Monolithic Integration,” *IEEE Trans. Antennas Propag.*, vol. 61, no. 1, pp. 1599–1607, 2013.

- [76] Q. Lai *et al.*, “60 GHz Aperture-Coupled Dielectric Resonator Antennas Fed by a Half-Mode Substrate Integrated,” *IEEE Trans. Antennas Propag.*, vol. 58, no. 6, pp. 1856–1864, 2010.
- [77] M. J. Al-Hasan, T. A. Denidni, and A. R. Sebak, “Millimeter-Wave EBG-Based Aperture-Coupled Dielectric Resonator Antenna,” *IEEE Trans. Antennas Propag.*, vol. 61, no. 8, pp. 4354–4357, 2013.
- [78] M. O. Sallam *et al.*, “Micromachined On-Chip Dielectric Resonator Antenna Operating at 60 GHz,” *IEEE Trans. Antennas Propag.*, vol. 63, no. 8, pp. 3410–3416, 2015.
- [79] Y.-X. Sun and K. W. Leung, “Circularly Polarized Substrate-Integrated Cylindrical Dielectric Resonator Antenna Array for 60 GHz Applications,” *IEEE Antennas Wirel. Propag. Lett.*, vol. 17, no. 8, pp. 1401–1405, 2018.
- [80] A. A. Kishk, “Directive Yagi-Uda dielectric resonator antennas,” *Microw. Opt. Technol. Lett.*, vol. 44, no. 5, pp. 451–453, 2005.
- [81] A. A. Kishk, “Enhanced gain of scanning DRA array,” in *2016 10th European Conference on Antennas and Propagation, EuCAP 2016*, 2016.
- [82] H. Attia and A. A. Kishk, “Transmission Line Model of RGW Slot Antenna Covered with Superstrate at 60 GHz,” in *2015 IEEE International Symposium on Antennas and Propagation & USNC/URSI National Radio Science Meeting*, 2015.
- [83] A. A. Kishk, “DRA-array with 75% reduction in elements number,” in *IEEE Radio and Wireless Symposium, RWS*, 2013, pp. 70–72.
- [84] Y. Al-Alem and A. A. Kishk, “Antenna Gain and Bandwidth Enhancement Using a Dielectric Superstrate at 60 GHz,” in *2018 18th International Symposium on Antenna Technology and Applied Electromagnetics (ANTEM)*, 2018.
- [85] Y. Al-Alem and A. A. Kishk, “High-Gain 60 GHz Slot Antenna with Symmetric Radiation Characteristics,” *IEEE Trans. Antennas Propag.*, vol. 67, no. 5, pp. 2971–2982, May 2019.
- [86] J. Volakis, *Antenna Engineering Handbook*, Fourth. US: McGraw-Hill Professional, 2007.
- [87] S. I. Shams and A. A. Kishk, “Printed Texture With Triangle Flat Pins for Bandwidth Enhancement of the Ridge Gap Waveguide,” *IEEE Trans. Microw. Theory Tech.*, vol. 65, no. 6, pp. 2093–2100, 2017.
- [88] S. I. Shams and A. A. Kishk, “Design of 3-dB Hybrid Coupler Based on RGW Technology,” *IEEE Trans. Microw. Theory Tech.*, vol. 65, no. 10, pp. 3849–3855, 2017.
- [89] M. Sharifi Sorkherizi, A. Dadgarpour, and A. A. Kishk, “Planar high-efficiency antenna array using new printed ridge gap waveguide technology,” *IEEE Trans. Antennas Propag.*, vol. 65, no. 7, pp. 3772–3776, 2017.
- [90] A. Perron, T. A. Denidni, and A.-R. Sebak, “High-Gain Hybrid Dielectric Resonator Antenna for Millimeter-Wave Applications: Design and Implementation,” *IEEE Trans. Antennas Propag.*, vol. 57, no. 10, pp. 2882–2892, Oct. 2009.
- [91] M. Nitta and T. Kikkawa, “Interference of digital noise with integrated dipole antenna for

inter-chip signal transmission in ULSI,” in *2005 IEEE Antennas and Propagation Society International Symposium*, 2005, vol. 3B, pp. 264–267.

- [92] T. Kikkawa, K. Kimoto, and S. Watanabe, “Ultrawideband characteristics of fractal dipole antennas integrated on Si for ULSI wireless interconnects,” *IEEE Electron Device Lett.*, vol. 26, no. 10, pp. 767–769, Oct. 2005.
- [93] Y. Al-Alem, R. M. Shubair, and A. Kishk, “Efficient on-chip antenna design based on symmetrical layers for multipath interference cancellation,” in *2016 16th Mediterranean Microwave Symposium (MMS)*, 2016.
- [94] K. Kim, “Design and characterization of RF components for inter- and intra-chip wireless communications,” University of Florida, 2000.
- [95] K. Kim *et al.*, “The feasibility of on-chip interconnection using antennas,” in *IEEE/ACM Int'l Conf. Computer-Aided Design (ICCAD '05)*, 2005, pp. 979–984.
- [96] B. A. Floyd, C. Hung, and K. K. O, “Intra-chip wireless interconnect for clock distribution implemented with integrated antennas, receivers, and transmitters,” *IEEE J. Solid-State Circuits*, vol. 37, no. 5, pp. 543–552, May 2002.
- [97] K. K. O *et al.*, “On-Chip Antennas in Silicon ICs and Their Application,” *IEEE Trans. Electron Devices*, vol. 52, no. 7, pp. 1312–1323, Jul. 2005.
- [98] M. Sun, Y. P. Zhang, G. X. Zheng, and W. Yin, “Performance of intra-chip wireless interconnect using on-chip antennas and UWB radios,” *IEEE Trans. Antennas Propag.*, vol. 57, no. 9, pp. 2756–2762, Sep. 2009.
- [99] W. Wang *et al.*, “Wireless Inter/Intra-Chip Communication Using an Innovative PCB Channel Bounded by a Metamaterial Absorber,” *IEEE Antennas Wirel. Propag. Lett.*, vol. 15, pp. 1634–1637, 2016.
- [100] J. Wu, A. Kodi, S. Kaya, A. Louri, and H. Xin, “Monopoles Loaded with 3-D-Printed Dielectrics for Future Wireless Intra-Chip Communications,” *IEEE Trans. Antennas Propag.*, vol. 65, no. 12, pp. 6838–6846, 2017.
- [101] M. Sun, Y. P. Zhang, and G. X. Zheng, “Modeling and measurement of the on-chip meander antenna pair,” in *2005 Asia-Pacific Microwave Conference Proceedings*, 2005, vol. 4, pp. 1–3.
- [102] P. S. Kildal and A. Kishk, “EM modeling of surfaces with stop or go characteristics - Artificial magnetic conductors and soft and hard surfaces,” *Appl. Comput. Electromagn. Soc. J.*, vol. 18, no. 1, pp. 32–40, 2003.
- [103] Y. Al-Alem, A. Kishk, and R. Shubair, “Enhanced Wireless Inter-Chip Communication Performance Using Symmetrical Layers and Soft/Hard Surface Concepts,” *IEEE Trans. Microw. Theory Tech.*, 2019.